Università degli Studi di Modena e Reggio Emilia

DIPARTIMENTO DI SCIENZE FISICHE INFORMATICHE E MATEMATICHE
Dottorato di Ricerca in Physics and Nanosciences

Ciclo XXXV

The effects of strain and lattice vibrations on the excitonic properties of quasi-2D semiconductors

Relatore:
Prof. Elisa Molinari

Candidato:
Matteo Zanfrognini

Correlatori:
Dott. Daniele Varsano
Dott. Fulvio Paleari

Coordinatore del Corso di Dottorato:
Prof. Marco Affronte

Anno Accademico 2021/2022

Abstract

This thesis centers on the effects of lattice dynamics and structural distortions on the excited-state properties of quasi two-dimensional (2D) semiconductors from a theoretical point of view: a new avenue of research which only recently is becoming amenable to predictive computational approaches. We analyse the coupling between excitonic resonances and vibrations, and show its importance for the accurate spectroscopic characterization of prototype systems. The fundamental understanding of the microscopic physical mechanisms governing light-matter interaction, including the effects of strain, is expected to be of key relevance for the design of innovative optoelectronic devices based on such materials.

To gain deep insight in these mechanisms, we combine accurate first-principles calculations –based on Density Functional Theory and Many Body Perturbation Theory– with judicious quantitative models. We then develop simple computational schemes to obtain accurate predictions, while greatly increasing the efficiency with respect to state-of-the-art *ab initio* methods. In this way, we are able to study complex systems that would otherwise be out of reach. We focus on the effects of strain, stacking geometries, lattice vibrations and pressure in selected relevant systems, and analyse and understand recent cathodoluminescence (CL) and inelastic X-ray scattering (IXS) experiments.

First, we investigate graphene-like 2D polyaniline (also known as C_3N), focusing on how uniaxial strain can tune its optical properties. We compute excitonic resonances by solving the Bethe-Salpeter equation in a tight-binding model for the electronic bands including a simplified description of the electronic screening. This model retains the accuracy of our fully *ab initio* calculations at greatly decreased computational cost. We also classify excitons according to the symmetries of the systems, explain the optical anisotropy of the perturbed monolayer and the non-analytic behaviour of the excitonic bands. Our analysis on C_3N progresses with the *ab-initio* characterisation of bilayers in different stacking motifs (namely AB, AB$'$ and AA$'$), where we explain the anomalous quenching of the optical absorption spectrum as induced by the interlayer coupling.

Second, we implement a scheme to predict luminescence spectra, based on calculated exciton-phonon coupling terms. We analyse CL experiments on bulk Boron Nitride (BN) in two stacking motifs: AA$'$ (hBN) and ABC (rhombohedral BN). Our calculations accurately reproduce the fine structure of the observed CL signal and explain the differences in the spectra by revealing the role of out-of-plane phonon branches involved in the photon emission process.

Finally, we develop a tool to simulate the dynamical structure factor of IXS, starting from phonon dispersions DFT Density Functional Perturbation Theory. We employ this tool to provide guidance and a sound interpretation of ultra-high pressure IXS experiments and related structural transitions in MoS_2.

Contents

Ai miei genitori, Miller e Cladis

Introduction

The experimental synthesis of high-quality graphene monolayers by Novoselov *et al.*[1] in 2004 has paved the way to a new research line in the field of condensed matter, i.e. the physics of 2D materials. Despite many exceptional properties (both mechanical and electronic), graphene is characterized by a gapless electronic ground state, making it hardly ideal for applications in the context of opto-electronic devices, which necessarily require finite-gap semiconductors. This has stimulated a huge experimental and theoretical effort in the design of new systems satisfying this requirement.
The optical properties of 2D semiconducting materials are characterised by strong excitonic effects as a consequence of the much stronger electron-hole interaction with respect to their bulk counterparts – a consequence of reduced electronic screening and increased spatial confinement of charge carriers in atomic-size structures. These excitations can be nowadays characterised using state-of-the-art *ab initio* methods, which can be employed both to interpret experimental results and to predict the properties of novel materials, guiding the design of innovative devices.
In this Thesis, we have combined many-body perturbation theory methods with density functional theory approaches to analyze 2D materials and wide-gap bulk layered systems where excitonic effects play a central role in the optical response. First principles results are also combined with simpler theoretical models to better clarify the results obtained numerically. This Thesis is about modelling the effects of lattice dynamics and structural distortions on the excited-state properties of quasi-2D semiconductors. This represents a promising new avenue of research which only recently became amenable to first-principles computational and theoretical techniques.

In the first part of this work, we have focused our attention on monolayer C_3N, a recently synthesized 2D system with a graphene-like honeycomb structure and a semiconducting ground state.
In its pristine single-layer form, C_3N is expected to show intense optical absorption in a narrow spectral range around 2 eV, due to strongly bound electron-hole pairs. Furthermore, because of the strong covalent bonding between carbon and nitrogen atoms, this system is also expected to sustain large mechanical stresses without structural failure. Therefore, it is a good candidate for the coexistence of the remarkable mechanical properties of graphene with a finite electronic band gap. For this reason, in Chapter 2, we theo-

retically explore the effect of uniaxial strain on the excitonic properties of single-layer C_3N, strain being a possible handle to externally tune its optical response. Our results indicate that the symmetry-breaking effect of uniaxial strain induces a strongly anisotropic behaviour in the optical absorption spectrum (even for small applied strain), which is totally absent in the unperturbed monolayer.

From a computational point of view, this analysis has been carried out developing a model solution of the Bethe-Salpeter Equation – which describes bound electron-hole pairs – starting from an *ab initio* description of the electronic screening and combining it with a tight-binding representation of single-particle properties. This methodology, which is easily generalizable to other 2D systems, strongly reduces the computational complexity with respect to fully *ab initio* calculations, while crucially keeping the same degree of accuracy. Furthermore, it also allows us to explore small-momentum excitonic dispersion, which is hardly accessible using fully first-principles methods. Our analysis emphasizes that uniaxial strain is responsible for anisotropy also in the exciton dispersions curves, suggesting the possibility of controlling exciton propagation via external light polarization.

In addition to its interesting properties as a single layer, C_3N can also be considered as a fundamental building block for the fabrication of multilayer structures, where several C_3N-sheets are kept together via Van der Waals interactions.
In a recent experimental work, Wei and collaborators[2] have succeeded in synthesising bilayer C_3N samples with the individual layers arranged in different geometrical motifs (called AA′ and AB′). Exploiting scanning tunnelling spectroscopy, they also demonstrate that the interlayer coupling among the layers induces a strong modulation of the electronic properties compared to the constituent building blocks. In particular, the electronic gaps exhibit important variations with the stacking pattern.
These experimental advances motivated us to investigate the optical properties of bilayer (BL) C_3N from a fully first principles perspective. Interestingly, the *ab initio* analysis proposed in Chapter 3 reveals a strong quenching of the low-energy optical absorption in bilayer C_3N for all the considered stacking patterns (i.e. AB, AB′ and AA′). This is a consequence of the negligible oscillator strengths associated to the lowest-energy bound excitons. We have explained this peculiar behaviour (not observed in other well-studied homobilayers such as BL-hBN, BL-MoS_2 and BL-phosphorene) in terms of the small interband dipole associated to the valence-conduction electronic transitions making up these low-energy excitons. Furthermore, by developing a tight binding model for the electronic states of interest, we have demonstrated that the observed low interband dipole is caused by destructive interference between the contributions of single-layer components.

In the second part of this work, we applied fully *ab initio* approaches to interpret recent cathodoluminescence experiments on boron nitride polytypes

and Inelastic X-ray scattering in compressed MoS_2.
Layered boron nitride (BN) is a wide-gap insulator which exhibits intense luminescence in the ultraviolet (UV) regime due to strongly bound excitons. This material has many practical applications, from UV lasers to its use in the encapsulation of other 2D materials to protect them from external environmental influence while leaving unaltered their electronic properties.
Among the possible layered bulk BN crystals obtained by stacking together different hexagonal BN monolayers, the most stable polytypes are those with AA′ (hBN) and ABC (rBN) motifs. These polymorphs can coexist in the experimentally synthesized sample, and since they differ only in the stackings of monolayer building blocks, their distinction via conventional diffraction approaches is difficult, as these systems only differ by the way in which analogous monolayer building blocks are stacked together.
As both these materials are characterized by an indirect band gap, their low-energy emission in the UV range can be only explained in terms of phonon-assisted processes, made possible by the coupling between finite-momentum excitons and lattice vibrations leading to a second-order process of radiative recombination. Cathodoluminescence (CL) experiments performed by our experimental collaborators at University Paris-Saclay and ONERA suggest that different phonon modes are involved in the CL signals of hBN and rBN, making this spectroscopic technique an ideal probe to identify these two polytypes. To better clarify the observed experimental differences, we implement a computational scheme combining a many-body description of electronic excitations with density functional perturbation theory calculations for lattice vibrations, yielding fully *ab initio* CL spectra. Our approach (discussed in Chapter 4) works in general for indirect-gap materials and overcomes the difficulties present in the currently available schemes for exciton-phonon coupling, which suffer from a phase mismatch between excitonic wavefunctions and electron-phonon matrix elements.
The resulting theoretical emission spectra enabled us to unambiguously identify the different phonon modes responsible for the indirect exciton emission. In particular, we find that out-of-plane lattice vibrations take part in the phonon-assisted emission of rBN but not in hBN, giving rise to characteristic differences in the observed CL spectra.

Finally, Chapter 5 has been devoted to the interpretation of preliminary inelastic X-ray scattering (IXS) experiments on bulk MoS_2 under high pressure at room temperature. These measurements (done by the group of Prof. Luigi Paolasini at ESRF) aimed at characterising the phonon dispersion of single MoS_2 crystals as a function of pressure and testing its behaviour under ultra-high pressure (above 30 GPa). These measurements will be followed by future experimental investigations (beamtime already approved) at low temperature, aimed at spotting experimental fingerprints of the recently theoretically proposed excitonic-insulator phase, which should be induced in this material via external pressure.

To this end, we have developed a computational tool for the contribution of vibrational modes to low-energy inelastic X-ray spectra, starting from a fully *ab initio* description of phonon properties within density functional perturbation theory. Direct comparison between theoretical and experimental spectra allows for the characterization of phonon modes under pressure and the definition of proper experimental configurations for future low-temperature experiments. Most importantly, our *ab initio* results permit to identify IXS-spectral signatures of the structural phase transition $2H_c \rightarrow 2H_a$ occurring in bulk MoS_2 at intermediate pressure (around 20 GPa).

Chapter 1

Computational Methods

Interacting electrons in a condensed matter system can be described by the Hamiltonian operator

$$\hat{H} = \hat{T}_e + \hat{V}_{e-I} + \hat{V}_{e-e} \tag{1.1}$$

where

$$\hat{T}_e = -\frac{\hbar^2}{2}\sum_i^{N_e} \nabla_i^2 \tag{1.2}$$

is the electron kinetic energy operator,

$$\hat{V}_{e-I} = -\sum_I^{N_{at}}\sum_i^{N_e} \frac{Z_I}{|\mathbf{r}_i - \mathbf{R}_I|} \tag{1.3}$$

represents the coupling between electrons and nuclei and

$$\hat{V}_{e-e} = \frac{1}{2}\sum_{i,j}^{N_e} \frac{1}{|\mathbf{r}_i - \mathbf{r}_j|} \tag{1.4}$$

stands for the electron-electron Coulomb interaction[1].
In Equation (1.1) we are implicitly assuming Born-Oppenheimer (BO) approximation, by which is possible to decouple electrons and lattice dynamics: in other words, as the mass of the nuclei is larger than the one of the electrons, the nuclear dynamics is slower than the electronic one, so that atoms can be assumed fixed in space w.r.t. the electrons.
Starting from the Hamiltonian defined by Eq.(1.1), the electronic state is therefore determined by a wavefunction $\Psi_\lambda(\mathbf{r}_1, \mathbf{r}_2, ..., \mathbf{r}_{N_e})$ obtained as

$$\hat{H}\Psi_\lambda(\mathbf{r}_1, \mathbf{r}_2, ..., \mathbf{r}_{N_e}) = E_\lambda \Psi_\lambda(\mathbf{r}_1, \mathbf{r}_2, ..., \mathbf{r}_{N_e}) \tag{1.5}$$

being E_λ the energy of the accessible many-body electronic states λ, represented by wavefunctions $\Psi_\lambda(\mathbf{r}_1, \mathbf{r}_2, ..., \mathbf{r}_{N_e})$.

[1] In the following we will always assume $m_e = e = 4\pi\varepsilon_0 = 1$ and we will neglect the spinorial degrees of freedom.

Computing the electronic states of a realistic system using Eq.(1.5) is, unfortunately, practically impossible: the reason is that the functions Ψ_λ depend on the positions of the N_e electron in the system: as in condensed matter systems, N_e is approximately equal to the Avogadro number, a straightforward solution of Eq.(1.5) cannot be afforded.
In this Chapter we will summarize the state-of-the-art methods adopted in this Thesis to compute electronic ground and excited states in realistic condensed matter systems: in practice, we will discuss Density Functional Theory (DFT) (Section 1.1) to compute ground state properties, and Many Body Perturbation Theory (MBPT) approaches (Sections 1.2 and 1.3) to obtain realistic electronic bandstructures and optical properties. Finally, we briefly discuss simulation of lattice vibrations in solids via Density Functional Perturbation Theory (DFPT) in Section 1.4.

1.1 Density Functional Theory

Density Functional Theory (DFT)[3] is a theoretical approach, which provides a formally exact description of the ground state properties of an electronic system.
Such theory is grounded on two fundamental theorems by Hohenberg and Kohn[4]. The first theorem states that, given a system of N_e interacting electrons under the action of an external potential V, the potential giving a certain electronic density $n(\mathbf{r})$ is unique (except for a constant).
A straightforward consequence of this theorem is that the total energy of the system is a functional of the charge density: formally

$$E[n(\mathbf{r})] = \langle\Psi_0|\hat{T}_e|\Psi_0\rangle + \langle\Psi_0|\hat{V}_{e-e}|\Psi_0\rangle + \int \mathrm{d}\mathbf{r}\ n(\mathbf{r})V(\mathbf{r}) \tag{1.6}$$

where V is the 'external' potential which corresponds to the electron-ion interaction while Ψ_0 is the (unknown) many-body electronic state. In general, the expectation values of $\hat{T}_e$ and $\hat{V}_{e-e}$ are written as

$$F[n(\mathbf{r})] = \langle\Psi_0|\hat{T}_e|\Psi_0\rangle + \langle\Psi_0|\hat{V}_{e-e}|\Psi_0\rangle \tag{1.7}$$

F being a universal functional of the sole electronic charge density.
Starting from Eqs.(1.6)-(1.7), we can directly state the second Hohenberg-Kohn theorem: the ground state electronic charge density is the function $n_0(\mathbf{r})$ which minimizes the total energy functional $E[n(\mathbf{r})]$ defined in Eq.(1.6).
Such second theorem gives an important conceptual advantage: to fully describe the electronic ground state, the explicit knowledge of the intractable many body wavefunction $\Psi_0(\mathbf{r}_1, \mathbf{r}_2, ..., \mathbf{r}_{N_e})$ is unnecessary, as we only need the ground state charge density $n_0(\mathbf{r})$ which is a much simpler function of only three spatial coordinates $\mathbf{r} = [x, y, z]$.
Despite their fundamental importance, Hohenberg-Kohn theorems do not provide a practical recipe to compute such ground state charge density: this gap

was closed by the work of Kohn and Sham[5]. Kohn-Sham (KS) approach maps the fully interacting system with ground state density $n_0(\mathbf{r})$ onto a fictitious system of non-interacting electrons having the same charge density of the real interacting system: the fictitious particles are subject to the action of an unknown external potential, called the KS potential $V_{KS}(\mathbf{r})$.
Defining as

$$E_S[n(\mathbf{r})] = T_S[n(\mathbf{r})] + \int \mathrm{d}\mathbf{r}\ n(\mathbf{r}) V_{KS}(\mathbf{r}) \tag{1.8}$$

the total energy functional of the KS auxiliary system, where $T_S[n(\mathbf{r})]$ is the kinetic energy contribution, we can use Hohenberg-Kohn theorems to state that the external KS potential is unique and defined by

$$V_{KS}(\mathbf{r}) + \left.\frac{\delta T_s}{\delta n}\right|_{n_0} = \Lambda. \tag{1.9}$$

Equation (1.9) is found by minimizing $E_S[n(\mathbf{r})]$ w.r.t. the charge density n, while including the constraint $N_e = \int d\mathbf{r} n(\mathbf{r})$ to guarantee charge conservation (here Λ is a Lagrange multiplier).
Now, within KS approach, the total-energy functional $E[n]$ of the interacting system is written as

$$E[n(\mathbf{r})] = T_S[n(\mathbf{r})] + E_H[n(\mathbf{r})] + \int \mathrm{d}\mathbf{r}\ n(\mathbf{r}) V(\mathbf{r}) + E_{xc}[n(\mathbf{r})] \tag{1.10}$$

being $E_H[n(\mathbf{r})]$ the (classic) electrostatic Hartree energy, $T_S[n]$ the kinetic energy of the auxiliary system and E_{xc} the exchange-correlation energy, whose expression is unknown. Minimizing this new expression of $E[n(\mathbf{r})]$ with the same charge-conservation constraint applied before, we can obtain

$$\left.\frac{\delta T_s}{\delta n}\right|_{n_0} + V_H(\mathbf{r}) + V(\mathbf{r}) + V_{xc}(\mathbf{r}) = \Lambda \tag{1.11}$$

where

$$V_H(\mathbf{r}) = \int \mathrm{d}\mathbf{r}'\ v_c(\mathbf{r} - \mathbf{r}') n(\mathbf{r}') \tag{1.12}$$

is the Hartree potential (being $v_c(\mathbf{r} - \mathbf{r}')$ the Coulomb electron-electron interaction), V is the 'external' electron-ion interaction and

$$V_{xc}(\mathbf{r}) = \left.\frac{\delta E_{xc}}{\delta n}\right|_{n_0} \tag{1.13}$$

is the exchange-correlation potential.
Comparing Eq.(1.9) with Eq.(1.11), we can immediately find the effective KS potential, i.e.

$$V_{KS}(\mathbf{r}) = V(\mathbf{r}) + V_H(\mathbf{r}) + V_{xc}(\mathbf{r}) \tag{1.14}$$

In practice, KS scheme allows to compute the ground state charge density $n_0(\mathbf{r})$ of the interacting system starting from an auxiliary set of independent electrons, subject to a single-particle potential V_{KS} defined by Eq.(1.14).
The electronic states accessible to these auxiliary electrons can be obtained by solving KS equations

$$\Big[-\frac{\hbar^2}{2}\nabla^2 + V_{KS}(\mathbf{r})\Big]\phi_j(\mathbf{r}) = \epsilon_j^{KS}\phi_j(\mathbf{r}) \tag{1.15}$$

where the index j runs over the auxiliary-single particle KS states $\phi_j(\mathbf{r})$, with energy ϵ_j^{KS}. In practice, these equations have to be solved self-consistently, and this is what is generally done in a conventional ground state DFT calculation. More precisely, one starts from an initial ansatz for the electronic charge density in the system, i.e. $n^{(i)}(\mathbf{r})$, and computes $V_{KS}^{(i)}$ using Eq.(1.14), after choosing an approximate expression for the KS potential, as we will discuss below. Then, the obtained KS potential is used to construct and solve Eq.(1.15), from which a first set of KS state $\phi_j^i(\mathbf{r})$ are obtained. Finally, a refined approximation for the charge density is computed starting from the occupied KS states, i.e.

$$n^{(i+1)}(\mathbf{r}) = \sum_{j}^{occ} |\phi_j^i(\mathbf{r})|^2 \tag{1.16}$$

The obtained charge density $n^{(i+1)}(\mathbf{r})$ is then used to re-evaluate the KS potential and, subsequently to obtain new KS states: such iterative procedure is repeated up to when self-consistency is reached.
As anticipated, this self-consistent scheme requires the knowledge of the exchange-correlation potential. We underline that this is the step at which approximations has to be included to proceed further: in fact, provided the exact expression of V_{xc}, the self-consistent solution of KS equation would give the exact electronic charge density.
We now briefly discuss the two main approximations used in this Thesis for E_{xc}, i.e. Local Density Approximation (LDA) and Generalized-Gradient-approximation (GGA).
The core idea behind LDA is to assume that a small volume $d\mathbf{r}$ centered at $\mathbf{r}$ in an in-homogeneous system of electrons, in which the electron density is $n = n(\mathbf{r})$, contributes to the total exchange-correlation energy as the same volume of a homogeneous electron gas with a uniform density n. This can be written in mathematical terms as

$$E_{xc}^{LDA}[n(\mathbf{r})] = \int \mathrm{d}\mathbf{r}\; n(\mathbf{r})\epsilon_{xc}^{hom}(n) \tag{1.17}$$

with ϵ_{xc}^{hom} being the exchange-correlation energy per electron in an homogeneous electron gas, which a function (instead of a functional) of the charge

density: this is a known quantity, accessible via parametrization of Monte Carlo results on the interacting homogeneous electron gas[6].
Despite its simplicity, LDA works reasonably well for solids, where the used approximation of slowly varying charge density turns out to be generally (even if not always) reasonable. However LDA still exhibits practical problems: for example it tends to overestimate the strength of chemical bonding between atoms, giving underestimated lattice parameters in crystals, once compared to the experimental ones.
A different approximation (which generally solves the lattice parameter problem just discussed) is given by Generalized Gradient Approximation (GGA)[7, 8, 9, 10]. The central idea for these functionals is to go beyond LDA by considering the role of local charge density gradient, i.e.

$$E_{xc}^{GGA}[n(\mathbf{r})] = \int \mathrm{d}\mathbf{r}\ n(\mathbf{r})\epsilon_{xc}^{GGA}(n(\mathbf{r}), \nabla n(\mathbf{r})) \tag{1.18}$$

A detailed discussion of the possible expressions used for ϵ_{xc}^{GGA} is beyond the scope of this short introduction: here we only point out that, in the following, we will adopt the Perdew-Burke-Ernzerhof (PBE) treatment of GGA as presented in the fundamental Reference [10].
All DFT calculations presented in this Thesis have been performed using `Quantum Espresso` package[11, 12]. This code is based on a plane-wave basis set description of KS states and exploits norm-conserving Pseudopotentials[13] to model core electrons not involved in the chemical bonding.
In periodic crystals, the KS potential is a periodic function and consequently KS states are Bloch states characterized by quantum numbers $(n, \mathbf{k})$, given by

$$\phi_j(\mathbf{r}) \rightarrow \phi_{n\mathbf{k}}(\mathbf{r}) = e^{i\mathbf{k}\cdot\mathbf{r}} u_{n\mathbf{k}}(\mathbf{r}) \tag{1.19}$$

being n the band index, $\mathbf{k}$ the crystal momentum (in the Brillouin Zone) and $u_{n\mathbf{k}}$ the lattice periodic part of KS states. In `Quantum Epsresso` such periodic functions are written on a plane wave basis set $\left\{\frac{1}{\sqrt{V}} e^{i\mathbf{G}\cdot\mathbf{r}}\right\}$, where $\mathbf{G}$ are reciprocal lattice vectors: each function $u_{n\mathbf{k}}$ is represented by the coefficients

$$c_{n\mathbf{k}}(\mathbf{G}) = \int_{u.c.} \mathrm{d}\mathbf{r}\ e^{-i\mathbf{G}\cdot\mathbf{r}} u_{n\mathbf{k}}(\mathbf{r}) \tag{1.20}$$

which can be efficiently computed using Fast Fourier Transform algorithm (in Eq. (1.20) 'u.c.' indicates integration over the crystal unit cell).
In practical terms, a relevant parameter, which needs to be checked in conventional DFT calculations, is the so called cutoff energy E_{cut}: it basically determines the shortest wavelenght used to describe KS states for each $\mathbf{k}$ point, i.e.

$$c_{n\mathbf{k}}(\mathbf{G}) = 0 \text{ if } \frac{\hbar^2}{2}|\mathbf{k}+\mathbf{G}|^2 > E_{cut} \tag{1.21}$$

Together with E_{cut}, another important quantity that has to be set in general

DFT calculations is the **k**-grid sampling the Brillouin Zone (BZ): to better understand this point, we remind that the electronic charge density is written in terms of KS states as

$$n(\mathbf{r}) = \sum_{n}^{occ} \sum_{\mathbf{k}}^{BZ} |u_{n\mathbf{k}}(\mathbf{r})|^2 \tag{1.22}$$

therefore, properly converged results require a accurate sampling of the BZ: in the following presented results we will always use Monkhorst-Pack[14] grids as regular meshes to sample the BZ and we choose the grid size by checking convergence of physical properties (e.g. relative total energies or lattice parameters) w.r.t. the **k**-points sampling.

1.2 GW Approximation and Quasi-Particle effects

In the precedent section we have discussed DFT as the approach by which a robust description of ground state properties is accessible. We now turn our attention to the evaluation of the excited states of an interacting-electron system.
We start here focusing on the case of single-particle excitations, which correspond to the addition or removal of an electron to the system: these excitations are, for example, probed experimentally via electronic transport measurements (such as Scannning Tunnelling Spectroscopy) or by photoemission techniques (e.g. ARPES). In the following we will discuss how to compute the energies of these excitations within Many Body Perturbation Theory (MBPT)[15, 16, 17], in order to derive the so-called Quasi-Particle (QP) electronic bandstructures.
In this context, a central role is played by single particle Green Function[18] $G(\mathbf{r}, t; \mathbf{r}', t')$ which is defined as

$$G(\mathbf{r}, t; \mathbf{r}', t') = -i\langle \Psi_0^N | \hat{T}\big[\hat{\psi}(\mathbf{r}, t)\hat{\psi}^\dagger(\mathbf{r}', t')\big] | \Psi_0^N \rangle \tag{1.23}$$

where we take $\hbar = 1$ in the following, to simplify the notation. $|\Psi_0^N\rangle$ is the many-body ground state for a system of N interacting electrons, $\hat{\psi}(\mathbf{r}, t)$ ($\hat{\psi}^\dagger(\mathbf{r}, t)$) is the annihilation (creation) operator for an electron at $\mathbf{r}$ at time t in Heisenberg representation and $\hat{T}$ is the time ordering operator for fermionic operators. In practice, if $t > t'$, G describes the probability amplitude to find at time t and at position $\mathbf{r}$ an electron once a charge e^- has been added to the system at time t' and at position $\mathbf{r}'$; if $t < t'$, a similar definition can be provided for holes.
If the system is isolated and not subject to external perturbations, it can be shown[18] that G depends on the difference $t - t'$ and not on t and t' separately. Therefore, by taking the Fourier transform of $G(\mathbf{r}, \mathbf{r}', t - t')$ with respect to

$t - t'$ we can define the Lehmann representation for the single particle Green function, i.e.

$$G(\mathbf{r}, \mathbf{r}', \omega) = \sum_{\lambda} \frac{f_\lambda(\mathbf{r}) f_\lambda^*(\mathbf{r}')}{\omega - \epsilon_\lambda + i\eta sgn(\varepsilon_\lambda - \mu)} \tag{1.24}$$

λ being an index running over all excited states $|\Psi_\lambda^{N\pm1}\rangle$ of the system with $N \pm 1$ electrons (N is the number of electrons in the ground state), while

$$f_\lambda(\mathbf{r}) = \begin{cases} \langle \Psi_0^N | \hat{\psi}(\mathbf{r}) | \Psi_\lambda^{N+1} \rangle & \text{if } \epsilon_\lambda > \mu \\ \langle \Psi_\lambda^{N-1} | \hat{\psi}(\mathbf{r}) | \Psi_0^N \rangle & \text{if } \epsilon_\lambda < \mu \end{cases} \tag{1.25}$$

are the Lehmann amplitudes and

$$\epsilon_\lambda = \begin{cases} E_\lambda^{N+1} - E_0^N & \text{if } \epsilon_\lambda - \mu > 0 \\ E_0^N - E_\lambda^{N-1} & \text{if } \epsilon_\lambda - \mu < 0 \end{cases} \tag{1.26}$$

are the excitation energies for adding ($\epsilon_\lambda - \mu > 0$) or removing ($\epsilon_\lambda - \mu < 0$) an electron from the system, with chemical potential μ. Furthermore, η is an infinitesimal number, i.e. $\eta \to 0^+$.

This representation of G is extremely useful to clarify one of the most important information provided by the single-particle Green function: in fact, looking at the denominator of Eq.(1.24) it is immediate to realize that the time-Fourier transform of G has its poles at the single particle excitation energies of the system.

Suppose now to consider the case of adding an electron to a material: while propagating in the system, this particle will be surrounded by a positively polarized region due to the repulsion among the electrons: the combination of the electron and this induced polarization cloud can be thought as a Quasi-Particle (in this case a quasi-electron). A similar reasoning can be carried out in the case of electron removal, where the created quasiparticle is referred to as a quasi-hole. The energies ϵ_λ and the corresponding Lehmann amplitudes f_λ can be respectively thought as the excitation energies and wavefunctions of these quasiparticles, at least approximately. Such interpretation is fully consistent to the simpler case of a system of independent particles, as the KS auxiliary system. In this case using the definitions (1.25)-(1.26), it is straightforward to demonstrate that $\epsilon_\lambda \equiv \epsilon_{n\mathbf{k}}$, i.e. they correspond to the energies of the single particle levels $(n, \mathbf{k})$ accessible in the system, while the Lehmann amplitudes $f_\lambda(\mathbf{r})$ will coincide with the corresponding single particle wavefunctions $\phi_{n\mathbf{k}}(\mathbf{r})$.

We now discuss the procedure by which we can compute these single particle excitation energies from a fully *ab initio* perspective in realistic materials.

To this purpose, it is useful to consider the equation of motion of G: starting from the Heisenberg equations for $\hat{\psi}(\mathbf{r}, t)$ and $\hat{\psi}^\dagger(\mathbf{r}', t')$ it is possible to derive[19]

$$\left[i\frac{\partial}{\partial \tau} - \hat{h}(1) \right] G(1,2) - \int \mathrm{d}3 \; \Sigma(1,3) G(3,2) = \delta(1,2) \tag{1.27}$$

where '1' is a compact notation for $(\mathbf{r}_1, t_1)$, $\tau = t - t'$ and

$$\hat{h} = \frac{1}{2}\nabla^2 + \hat{V} + \hat{V}_H \tag{1.28}$$

is the single particle Hamiltonian which contains the kinetic energy operator, the electron-ion coupling potential $\hat{V}$ and the Hartree interaction. Eq.(1.27) depends on the electron-self energy Σ, which accounts for the electron-electron interaction, beyond the classical Hartree term.
Taking the time Fourier transform w.r.t. τ of Eq.(1.27), using the Lehmann representation (1.24) for the Green function and considering the limit $\omega \to \epsilon_\lambda$, we obtain

$$\hat{h} f_\lambda(\mathbf{r}) + \int \mathrm{d}\mathbf{r}' \; \Sigma(\mathbf{r}, \mathbf{r}'; \epsilon_\lambda) f_\lambda(\mathbf{r}') = \epsilon_\lambda f_\lambda(\mathbf{r}) \tag{1.29}$$

Adding and subtracting the quantity

$$\int \mathrm{d}\mathbf{r}' \; V_{xc}(\mathbf{r}') f_\lambda(\mathbf{r}') \delta(\mathbf{r} - \mathbf{r}') \tag{1.30}$$

to the l.h.s. of Eq.(1.29) we finally obtain

$$\hat{h}_{KS} f_\lambda(\mathbf{r}) + \int \mathrm{d}\mathbf{r}' \left[\Sigma(\mathbf{r}, \mathbf{r}'; \epsilon_\lambda) - V_{xc}(\mathbf{r}') \delta(\mathbf{r} - \mathbf{r}') \right] f_\lambda(\mathbf{r}') = \epsilon_\lambda f_\lambda(\mathbf{r}) \tag{1.31}$$

where $\hat{h}_{KS}$ is the Kohn-Sham hamiltonian operator appearing in Eq.(1.15), whose eigenstates (eigenvalues) correspond to the KS wavefunction (energies). Following Hybertsen and Louie[20], we can interpret the non local and energy dependent operator $\hat{\Sigma} - \hat{V}_{xc}$ as a perturbation of the KS hamiltonian. As a result, we can express the quasi-particle energies ε_λ with first order perturbation theory, i.e.

$$\epsilon_\lambda^{QP} = \epsilon_\lambda^{KS} + \langle \phi_\lambda^{KS} | \hat{\Sigma}(\epsilon_\lambda^{QP}) - \hat{V}_{xc} | \phi_\lambda^{KS} \rangle \tag{1.32}$$

We emphasise that this approach is reasonable if KS states, obtained within DFT, can be considered good approximations of the quasiparticle wavefunctions f_λ; in these cases many body effects encoded in the self energy operator, can be properly included by simply adding to the DFT energies ϵ_λ^{KS} the expectation value of $\hat{\Sigma} - \hat{V}_{xc}$ on the corresponding KS states.
As the electron self-energy depends on the QP energies, Eq.(1.32) would in principle require a self-consistent solution. In practical calculations, such energy dependence is simplified by considering the linearized self energy in proximity of the KS eigenvalue, i.e.

$$\hat{\Sigma}(\epsilon_\lambda^{QP}) \approx \hat{\Sigma}(\epsilon_\lambda^{KS}) + \left. \frac{\partial \Sigma}{\partial \epsilon} \right|_{\epsilon_\lambda^{KS}} (\epsilon_\lambda^{QP} - \epsilon_\lambda^{KS}) \tag{1.33}$$

In this way the self energy and its first derivative need to be computed only once, in correspondence of the KS energy.
Collecting Eqs.(1.32)-(1.33) we can easily obtain

$$\epsilon_{n\mathbf{k}}^{QP} = \epsilon_{n\mathbf{k}}^{KS} + Z_{n\mathbf{k}} \langle \phi_{n\mathbf{k}}^{KS} | \hat{\Sigma}(\epsilon_{n\mathbf{k}}^{KS}) - \hat{V}_{xc} | \phi_{n\mathbf{k}}^{KS} \rangle \tag{1.34}$$

where we have done the substitution $\lambda \to (n\mathbf{k})$, as we generally work with periodic systems where KS states are labeled according to band and momentum indexes, and we have defined

$$Z_{n\mathbf{k}} = \frac{1}{1 - \frac{\partial \Sigma}{\partial \varepsilon}\Big|_{\epsilon^{KS}_{n\mathbf{k}}}} \tag{1.35}$$

usually referred to as renormalization factors. Equation (1.34) is the expression used in this Thesis to evaluate Quasi-Particle corrected electronic bands starting from DFT eigenenergies.
To evaluate Eq.(1.34), we need a method to compute the matrix element of the electron self energy on KS states. We now outline the main approximations adopted in this work, together with the practical steps needed to effectively evaluate quasi-particle corrections.
In his fundamental work[21], Lars Hedin derived a set of self-consistent equations by which it is in principle possible to obtain the self energy Σ, i.e.

$$\Sigma(1,2) = i \int \mathrm{d}34 \; G(1,4) W(1^+,3) \tilde{\Gamma}(4,2;3) \tag{1.36}$$

$$W(1,2) = v(1,2) + \int \mathrm{d}34 \; v(1,3) P(3,4) W(4,2) \tag{1.37}$$

$$P(1,2) = -i \int \mathrm{d}34 \; G(1,3) G(4,1) \tilde{\Gamma}(3,4;2) \tag{1.38}$$

$$\tilde{\Gamma}(1,2;3) = \delta(1,2)\delta(1,3) + \int \mathrm{d}4567 \; \frac{\delta \Sigma(1,2)}{\delta G(4,5)} G(4,6) G(7,5) \tilde{\Gamma}(6,7;3) \tag{1.39}$$

$$G(1,2) = G^0(1,2) + \int \mathrm{d}34 \; G^0(1,3) \Sigma(3,4) G(4,2) \tag{1.40}$$

A formal proof of these Equations is beyond the scope of this introduction, and we refer to relevant literature for their derivation[21, 15, 17]. We point out here that P and $\tilde{\Gamma}$ are respectively referred to as the irreducible polarizability and vertex function. Furthermore, W is the electron-electron screened interaction, describing the bare Coulomb coupling v between electrons, screened by the other carriers in the material. Finally, G^0 is the single particle Green function, associated to the single particle Hamiltonian defined in Eq.(1.28).
In this Thesis we adopt the GW approximation for the self-energy. It corresponds to approximate the irreducible vertex as

$$\tilde{\Gamma}(1,2;3) \approx \delta(1,2)\delta(1,3) \tag{1.41}$$

to obtain, for the self-energy,

$$\Sigma(1,2) \approx i G(1,2) W(1^+,2) \tag{1.42}$$

Apart from its mathematical definition, provided by Eqs.(1.41) and (1.42), GW approximation is based on the assumption that the terms proportional

to W^n, with $n > 1$, appearing in the vertex function of Eq.(1.36) are negligible w.r.t. the contribution linear in W, as a consequence of the electronic screening of the bare Coulomb interaction.
Using Eq.(1.41), we also obtain a simplified expression for the irreducible polarizability,

$$P(1,2) \approx -iG(2,1^+)G(1,2^+) \tag{1.43}$$

which becomes the product of two interacting-single-particle Green functions describing an electron-hole pair, not coupled with each other.
Even within GW approximation, Hedin's equations still require a self-consistent solution, where G, W and Σ need to be iteratively evaluated up to convergence.
In this Thesis we adopt a simplified approach called G_0W_0-single-shot method to compute the self energy operator, which consists on performing a first iteration of Hedin's equations, starting from Green function constructed from KS wavefunctions and energies. To clarify this methodology, we summarize below the steps followed in a G_0W_0 calculation.
Firstly, we exploit the KS wavefunctions and energies obtained at the DFT level to construct a non-interacting single particle Green function G^{KS}, which is then used to compute the irreducible polarizability $P_0 \approx -iG^{KS}(2,1^+)G^{KS}(1,2^+)$. Notice that this is an approximation for Eq.(1.43), as we are substituting the interacting Green function with a non-interacting one.
The screened electron-electron interaction W is evaluated as

$$W(1,2) = \int \mathrm{d}3\ \varepsilon^{-1}(1,3)v(2,3) \tag{1.44}$$

where the inverse dielectric function ε^{-1} satisfies the equation

$$\varepsilon^{-1}(1,2) = \delta(1,2) + \int \mathrm{d}3\chi(1,3)v(3,2) \tag{1.45}$$

$\chi(1,3)$ being the reducible polarizability related to the irreducible polarizability by the Dyson equation

$$\chi(1,2) = P(1,2) + \int \mathrm{d}34\ P(1,3)v(3,4)\chi(4,2) \tag{1.46}$$

To proceed further, we introduce the Random Phase Approximation (RPA), i.e. we approximate P in Eq.(1.46) with P_0, obtained from the non interacting Green functions G^{KS}.
From Eqs.(1.44)-(1.46) we obtain the screened electron-electron interaction, which is then combined with KS Green-function to obtain the electron self energy as

$$\Sigma(1,2) \approx iG^{KS}(1,2)W(1^+,2) \tag{1.47}$$

After taking the time Fourier transform, this self energy Σ_{GW} is then used in Eq.(1.34) to compute quasi-particle energies using first order perturbation

theory.
In the following, we provide few more details about the implementation of this procedure within `Yambo` code[22, 23], to make clearer the parameters which has to be carefully converged to obtain meaningful QP energies.
Our aim is compute the matrix element

$$\Sigma_{n\mathbf{k}}(\omega) = \langle \phi^{KS}_{n\mathbf{k}} | \hat{\Sigma}(\omega) | \phi^{KS}_{n\mathbf{k}} \rangle \tag{1.48}$$

where ω is fixed to the KS energy $\epsilon^{KS}_{n\mathbf{k}}$. Such matrix element can be written as the sum of two terms,

$$\Sigma^{x}_{n\mathbf{k}} = -\sum_{v}\sum_{\mathbf{G}}\int \frac{\mathrm{d}\mathbf{q}}{(2\pi)^3}\, v(\mathbf{q}+\mathbf{G})|\rho_{nv\mathbf{k}}(\mathbf{q},\mathbf{G})|^2 \tag{1.49}$$

$$\Sigma^{c}_{n\mathbf{k}}(\omega) = i\sum_{m}\sum_{\mathbf{G}\mathbf{G}'}\int \frac{\mathrm{d}\mathbf{q}}{(2\pi)^3}\, v(\mathbf{q}+\mathbf{G})\rho_{nm\mathbf{k}}(\mathbf{q},\mathbf{G})\rho^{*}_{nm\mathbf{k}}(\mathbf{q},\mathbf{G}')\cdot \int d\omega' G^{KS}_{m,\mathbf{k}-\mathbf{q}}(\omega-\omega')\varepsilon^{-1}_{\mathbf{G}\mathbf{G}'}(\mathbf{q},\omega') \tag{1.50}$$

$\mathbf{G}$ and $\mathbf{G}'$ being reciprocal lattice vectors.
Equation (1.49) gives the exchange contribution to the electron self-energy. This term is frequency-independent and comes from the Hartree-Fock contribution to the self-energy, i.e. $\Sigma_{HF} = iGv$. We note that in Eq.(1.49) the sum over bands is performed only on occupied states v, while the functions ρ are defined as

$$\rho_{nm\mathbf{k}}(\mathbf{q},\mathbf{G}) = \langle \phi^{KS}_{n\mathbf{k}} | e^{i(\mathbf{q}+\mathbf{G})\cdot\mathbf{r}} | \phi^{KS}_{m\mathbf{k}-\mathbf{q}} \rangle \tag{1.51}$$

which are computed using Fast Fourier Transform algorithms, starting from KS states.
The second contribution to the electron self energy is given by the correlation term provided by Eq.(1.50), which is frequency dependent, differently from $\Sigma^{x}_{n\mathbf{k}}$. Also in this case, we notice the presence of a summation over bands, denoted by the index m in Eq.(1.50). In this case, the states to be included are both occupied and unoccupied and their number must be carefully chosen to properly converge the QP corrections. We recall that numerical approaches which reduce the needed number of bands to be included in this summation are available in the literature[24].
In Eq. (1.50), $G^{KS}_{m,\mathbf{k}-\mathbf{q}}$ is the time-Fourier transform of the KS Green function, written in the KS basis, i.e.

$$G^{KS}_{m,\mathbf{k}}(\omega) = \frac{f_{m\mathbf{k}}}{\omega - \epsilon^{KS}_{m\mathbf{k}} - i\eta} + \frac{1-f_{m\mathbf{k}}}{\omega - \epsilon^{KS}_{m\mathbf{k}} + i\eta} \tag{1.52}$$

where $f_{m\mathbf{k}}$ is the Fermi-Dirac distribution computed at the KS energy $\epsilon^{KS}_{m\mathbf{k}}$. Finally, $\epsilon^{-1}_{\mathbf{G}\mathbf{G}'}(\mathbf{q},\omega)$ is the frequency-dependent inverse dielectric function, i.e.

the space and time Fourier transform of $\varepsilon^{-1}(1,2)$ defined by Eq.(1.45), with χ evaluated within RPA approximation. In a conventional G_0W_0 calculation in `Yambo`, the first step is the evaluation (in Fourier space) of the irreducible polarizability P_0, using KS Green functions. This provides

$$P_{0,\mathbf{GG'}}(\mathbf{q},\omega) = 2\int \frac{\mathrm{d}\mathbf{k}}{(2\pi)^3} \sum_{nm} \rho_{nm\mathbf{k}}(\mathbf{q},\mathbf{G})\rho^*_{nm\mathbf{k}}(\mathbf{q},\mathbf{G'}) \cdot \left[\frac{f_{m\mathbf{k}}(1-f_{n,\mathbf{k}-\mathbf{q}})}{\omega-(\epsilon^{KS}_{m\mathbf{k}}-\epsilon^{KS}_{n\mathbf{k}-\mathbf{q}})-i\eta} - \frac{f_{m\mathbf{k}}(1-f_{n,\mathbf{k}-\mathbf{q}})}{\omega-(\epsilon^{KS}_{n\mathbf{k}-\mathbf{q}}-\epsilon^{KS}_{m\mathbf{k}})+i\eta}\right] \tag{1.53}$$

The calculation of P_0 requires a summation over both occupied and unoccupied states (m and n respectively in Eq.(1.53)); the number of empty bands included in the construction of P_0 is a relevant convergence parameter in practical calculations. Once the independent particle polarizability is known, the reducible χ is evaluated by numerical inversion of Eq.(1.46), once written in Fourier space, i.e.

$$\chi^{RPA}_{\mathbf{GG'}}(\mathbf{q},\omega) = P_{0,\mathbf{GG'}}(\mathbf{q},\omega) + \sum_{\mathbf{G}_1} P_{0,\mathbf{GG}_1}(\mathbf{q},\omega)v(\mathbf{q}+\mathbf{G}_1)\chi^{RPA}_{\mathbf{G}_1\mathbf{G'}}(\mathbf{q},\omega) \tag{1.54}$$

for each $\mathbf{q}$ scattering wave-vector in the Brillouin zone and, in principle, for each frequency ω. Finally, the dielectric screening matrix is obtained as

$$\varepsilon^{-1}_{\mathbf{GG'}}(\mathbf{q},\omega) = \delta_{\mathbf{GG'}} + \chi^{RPA}_{\mathbf{GG'}}(\mathbf{q},\omega)v(\mathbf{q}+\mathbf{G}) \tag{1.55}$$

We remind here that a cut-off is applied on the $(\mathbf{G},\mathbf{G'})$ reciprocal lattice vectors appearing in Eq.(1.54): similarly to the number of bands included in the polarizability P_0, such cut-off needs to be chosen with care, as it strongly affects the obtained description of the electronic screening.
Equation (1.50) requires a frequency-space integration, over the variable ω', which would make in principle necessary the evaluation of the inverse dielectric function at different frequencies. The calculation of Eq.(1.53) on a fine frequency grid is extremely demanding, therefore a frequency-interpolation of the dielectric screening is needed. The simple approach used in this Thesis is the so called Plasmon-Pole-Approximation (PPA), following Godby-Needs scheme[25]. In this model, the dielectric function is written as[15]

$$Re[\varepsilon^{-1}_{\mathbf{GG'}}(\mathbf{q},\omega)] = \delta_{\mathbf{GG'}} + \frac{2}{\pi}\frac{A_{\mathbf{GG'}}(\mathbf{q})\tilde{\omega}_{\mathbf{GG'}}(\mathbf{q})}{\omega^2-\tilde{\omega}^2_{\mathbf{GG'}}(\mathbf{q})} \tag{1.56}$$

$$Im[\varepsilon^{-1}_{\mathbf{GG'}}(\mathbf{q},\omega)] = -A_{\mathbf{GG'}}(\mathbf{q})\left[\delta(\omega-\tilde{\omega}_{\mathbf{GG'}}(\mathbf{q})) + \delta(\omega+\tilde{\omega}_{\mathbf{GG'}}(\mathbf{q}))\right] \tag{1.57}$$

In practice, the dielectric function $\varepsilon^{-1}_{\mathbf{GG'}}(\mathbf{q},\omega)$ is explicitly evaluated for all $\mathbf{q}$, $\mathbf{G}$ and $\mathbf{G'}$) at two frequencies, i.e. $\omega = 0$ and $\omega = i\omega_p$: then the model parameters $A_{\mathbf{GG'}}(\mathbf{q})$ and $\tilde{\omega}_{\mathbf{GG'}}(\mathbf{q})$ are chosen so that the model function expressed

by Eqs.(1.56)-(1.57) reproduce the *ab initio* results at these two frequencies. In all the calculation presented in the following we have kept fixed the frequency ω_p to its default value chosen in `Yambo` code, i.e. $\omega_p = 1$Ry.
Substitution of Eqs.(1.56)-(1.57) in the correlation part of the electron self-energy, Eq.(1.50), provides an analytical solution of the integral on frequencies.
We point out that relevant variations of QP corrections under small changes of the value of ω_p reflect the inadequacy of PPA for the system under study. In that cases one should adopt a more refined treatment of the frequency dependence of the dielectric screening either using a full-frequency approach, or adopting more advanced frequency interpolation techniques as the one proposed in Ref.[26].
All the integrals over the scattering vectors $\mathbf{q}$ in the Brillouin Zone are numerically discretized on a uniform $\mathbf{q}$ Monkhorst-Pack mesh sampling the BZ. QP corrections are extremely sensitive to the $\mathbf{q}$-sampling of the BZ and properly converged results usually require much denser grids than those used to sample the BZ in self consistent calculations in DFT. There exists methods which enable accelerated convergence w.r.t. the BZ sampling, performing more refined evaluations of the integrals over $\mathbf{q}$: a recent implementation of one of these approaches has been adopted in Chapter 3 to compute QP corrections to DFT energies in Bilayer C_3N[27, 28].
We complete this introduction to GW approximation for the evaluation of QP energies considering a fundamental aspect that must be taken into account in QP-calculation in low dimensional systems. We focus here on the case of 2D materials, which are the low dimensional systems considered in this work. Within a plane-wave basis-set framework, they are represented using a supercell technique, i.e. considering a 3D crystal characterized by a unit cell having size L along the non-periodic direction sufficiently large to avoid unphysical interaction between the periodic copies of the 2D system. Within a DFT description, these spurious interactions can be removed by choosing relatively small values of L: in general a vacuum region of 15-20 Å between periodic copies is enough to decouple periodic images of the 2D material, as a consequence of the short-range nature of the exchange-correlation potential V_{xc}, within local (LDA) or semi-local (GGA-PBE) approximations. As bare Coulomb interaction is long-ranged, in *GW* calculations one generally needs to use impractically large supercells along the non-periodic direction, to make sure that periodic repetitions are not coupled by Coulomb interaction.
The solution to this problem is to adopt a real-space cut-off for the Coulomb potential: as detailed in Refs.[29, 30], this corresponds to define the electron-electron potential as

$$\bar{v}(\mathbf{r}) = \begin{cases} v(\mathbf{r}), & \text{if } |z| < \frac{L}{2} \\ 0 & \text{otherwise} \end{cases} \tag{1.58}$$

i.e. the Coulomb interaction between points separated, along the non-periodic direction, more than the supercell size L is manually set to zero. In this way, properly converged QP corrections can be obtained using supercells with length L along the non-periodic direction comparable to those needed in DFT calculations.

1.3 Neutral excitations from Bethe-Salpeter Equation

In this Section we discuss neutral excitations in interacting electron systems, corresponding to excited states in which the number of particle is left unchanged w.r.t. the one of the ground state.
A simple example of this type of excitations is the electron-hole pair created by absorption of an optical photon. These two quasi-particles (i.e. the created quasi-electron and the quasi-hole) interact among each other and therefore constitute a correlated pair, generally referred to as an exciton. As the electron-hole interaction is mainly attractive, the energy of this composite quasi-particle can be lower than the one of the free pair, so that exciton is considered as bound. This interaction is not captured by GW approximation, therefore an *ab initio* investigation of this type of excitation requires a different treatment, which we now summarize in the following. Such treatment enables an accurate description of many experimental observables, like optical absorption and electron energy loss spectroscopy.
Neutral excitations can be obtained from the two-particle correlation function $L(12,1'2')$, which satisfies the Dyson-like Bethe Salpeter Equation (BSE)[31, 32, 16, 15]

$$L(12,1'2') = L_0(12,1'2') + \int \mathrm{d}3456\ L_0(14,1'3)\Xi(35,46)L(62,52') \tag{1.59}$$

where L_0 describes the propagation of a pair of non-interacting particles, i.e.

$$L_0(12,1'2') = -iG(12')G(21') \tag{1.60}$$

while Ξ is the BSE kernel, which accounts for the interaction among these two particles

$$\Xi(35,46) = -i\delta(34)\delta(56)v(35) + \frac{\delta\Sigma(34)}{\delta G(65)} \tag{1.61}$$

where Σ is the electron self-energy discussed in Sec.1.2. Following Ref.[33], we know that L depends on three time differences, i.e.

$$\tau_1 = \frac{1}{2}[t_1 - t_{1'} - t_2 - t_{2'}]$$

$$\tau_2 = t_1 - t_{1'}$$

$$\tau_3 = t_2 - t_{2'}$$

In the following we will restrict our attention to the simultaneous propagation of an electron-hole pair: in this case $\tau_2 = 0$ and $\tau_3 = 0$ and only the time dependence on τ_1 is considered, with τ_1 representing the propagation time of the correlated pair.
In frequency space, this means that the energy of the electron-hole pairs can be obtained as the poles of

$$L(\omega) = \int \mathrm{d}\omega' \int \mathrm{d}\omega'' \; L(\omega, \omega', \omega'') \tag{1.62}$$

where

$$L(\omega, \omega', \omega'') = L_0(\omega, \omega', \omega'') + \frac{1}{(2\pi)^4} \int \mathrm{d}\omega_3 \int \mathrm{d}\omega_4 \; L_0(\omega, \omega', \omega_3) \Xi(\omega, \omega_3, \omega_4) L(\omega, \omega_4, \omega'') \tag{1.63}$$

is obtained by time Fourier transform of Eq.(1.59) (here, we do not make explicit the dependence on spatial coordinates to simplify the notation).
Starting from Eq.(1.61) and using GW approximation (1.42) for the electron self-energy, we can find

$$\frac{\delta \Sigma_{GW}(34)}{\delta G(65)} = iW(34)\delta(36)\delta(45) + iG(34)\frac{\delta W(34)}{\delta G(65)} \tag{1.64}$$

By neglecting the second term in Eq.(1.64) (as it depends on W^n, with $n > 1$), we can write the BSE kernel as

$$\Xi(35, 46) \approx -i\delta(34)\delta(65)v(35) + i\delta(36)\delta(45)W(34) \tag{1.65}$$

and taking the time Fourier transform we obtain

$$\Xi(\omega, \omega_3, \omega_4) \approx -iv + iW(\omega_3 - \omega_4) \tag{1.66}$$

Looking at Eq.(1.66), we can notice the frequency dependence of the electron-electron screened interaction. In the following we will use the static-screening approximation, by which we approximate $W(\omega_3 - \omega_4)$ with its static ($\omega = 0$) component, denoted in the following as W_s. This approximation is generally valid if the excitation energies of electron-hole pairs are smaller than the plasmon frequency characterizing the system.
Substitution of Eq.(1.66) (with static approximation) in Eq.(1.63) and computing the integrals over ω and ω' (see Eq.(1.62)) we finally obtain

$$L(\omega) = L_0(\omega) + L_0(\omega)\big[-iv + iW_s\big]L(\omega) \tag{1.67}$$

where

$$L_0(\omega) = -i \int \mathrm{d}\omega' \; G(\omega' + \frac{\omega}{2})G(\omega' - \frac{\omega}{2}) \tag{1.68}$$

To proceed further, we now write L and L_0 on the basis of independent particle states. In practice, we assume that the single particle Green functions appearing in L_0 are given by

$$G(\mathbf{r}_1, \mathbf{r}_2, \omega) = \sum_{n_i} \frac{\phi^{KS}_{n_i}(\mathbf{r}_1)\phi^{KS*}_{n_i}(\mathbf{r}_2)}{\omega - \epsilon^{QP}_{n_i} + i\eta sgn(\epsilon^{QP}_{n_i} - \mu)} \tag{1.69}$$

where we have made explicit the dependence on spatial coordinates and used the compact notation $n_i \equiv (n\mathbf{k})$. The Green function given by Eq.(1.69) describes the propagation of quasi-particles (electron and holes) having as wavefunctions the KS states and energies equal to quasi-particle corrected KS eigenvalues.
By defining the basis transformation of 4-variables functions $F(\mathbf{r}_1, \mathbf{r}_2, \mathbf{r}_3, \mathbf{r}_4, \omega)$ as

$$F_{n_1n_2n_3n_4}(\omega) = \int \mathrm{d}\mathbf{r}_1\mathrm{d}\mathbf{r}_2\mathrm{d}\mathbf{r}_3\mathrm{d}\mathbf{r}_4\, \phi^{KS*}_{n_1}(\mathbf{r}_1)\phi^{KS*}_{n_2}(\mathbf{r}_2)F(\mathbf{r}_1, \mathbf{r}_2, \mathbf{r}_3, \mathbf{r}_4, \omega)\phi^{KS}_{n_3}(\mathbf{r}_3)\phi^{KS}_{n_4}(\mathbf{r}_3) \tag{1.70}$$

we can project Eq.(1.67) on the basis of single particle KS states: via algebraic manipulation we obtain

$$L_{n_1n_2n_3n_4}(\omega) = 2i\Big[H^{exc} - \omega\Big]_{n_1n_2n_3n_4}(f_{n_2} - f_{n_4}) \tag{1.71}$$

where we have introduced the excitonic Hamiltonian

$$H^{exc}(n_1n_2n_3n_4) = (\epsilon^{QP}_{n_2} - \epsilon^{QP}_{n_1})\delta_{n_1n_4}\delta_{n_2n_3} + (f_{n_1} - f_{n_3})\Xi(n_1n_2n_3n_4) \tag{1.72}$$

n_i being the indexes running over KS states while f_{n_i} is the occupation factor for state n_i.
To make clearer the expression of H^{exc}, we make explicit the indeces n_i by associating to each of them a conduction c or a valence v band index, according to the occupation factors f, assuming $T = 0$ K. In this way, we can express the excitonic Hamiltonian as a block-matrix

$$H^{exc} = \begin{bmatrix} H^{res}(vc, v'c') & H^{coupl}(vc, v'c') \\ -H^{coupl*}(vc, v'c') & -H^{res*}(vc, v'c') \end{bmatrix} \tag{1.73}$$

In all the calculations presented in this Thesis we will apply Tamm-Dancoff approximation[34, 18], which corresponds to neglect the out-of-diagonal blocks of the excitonic Hamiltonian, therefore approximating $H^{exc} \approx H^{res}$ (the apex 'res' stands for resonant). It has been demonstrated that this approximation provides a proper description of the optical properties in solids, therefore we will not discuss coupling terms H^{coupl} in the following.
H^{res} is an hermitian matrix, whose eigenvalues corresponds to the energies of

the correlated electron-hole pairs accessible in the system. Using the extended notation $(n, \mathbf{k})$ for the KS states, we can write

$$H^{res}(vc\mathbf{k}, v'c'\mathbf{k}') = (\epsilon^{QP}_{c\mathbf{k}} - \epsilon^{QP}_{v\mathbf{k}})\delta_{cc'}\delta_{vv'}\delta_{\mathbf{k}\mathbf{k}'} + K^d(vc\mathbf{k}, v'c'\mathbf{k}') + K^x(vc\mathbf{k}, v'c'\mathbf{k}') \tag{1.74}$$

where

$$K^d(vc\mathbf{k}, v'c'\mathbf{k}') = -\int \mathrm{d}\mathbf{r} \int \mathrm{d}\mathbf{r}' \; \phi^{KS*}_{c\mathbf{k}}(\mathbf{r})\phi^{KS}_{c'\mathbf{k}'}(\mathbf{r})W_s(\mathbf{r}\mathbf{r}')\phi^{KS}_{v\mathbf{k}}(\mathbf{r}')\phi^{KS*}_{v'\mathbf{k}'}(\mathbf{r}') \tag{1.75}$$

is called direct BSE kernel, while

$$K^x(vc\mathbf{k}, v'c'\mathbf{k}') = 2\int \mathrm{d}\mathbf{r} \int \mathrm{d}\mathbf{r}' \; \phi^{KS*}_{c\mathbf{k}}(\mathbf{r})\phi^{KS}_{v\mathbf{k}}(\mathbf{r})v(\mathbf{r}-\mathbf{r}')\phi^{KS}_{c'\mathbf{k}'}(\mathbf{r}')\phi^{KS*}_{v'\mathbf{k}'}(\mathbf{r}') \tag{1.76}$$

is the exchange component. Notice that the excitonic Hamiltonian given by Eq.(1.74) is valid for system with negligible spin-orbit-coupling. In these cases, excitons can have a singlet (triplet) spin structure, where the electron and the hole have equal (opposite) spin projections. As optically active excitons must be of singlet type, in the following we will only focus on the this particular spin-configuration, for which the exchange term is different from zero. We point out that triplet-exciton energies can be obtained from Eq.(1.74) by neglecting the exchange kernel contribution[17, 32].
Looking at Eq.(1.74)-(1.76), the physical meaning of H^{res} is transparent. The first term in Eq.(1.74) corresponds to the energies of the independent, single-particle transitions from a valence state $(v\mathbf{k})$ to a conduction state $(c\mathbf{k})$; the direct kernel K^d accounts for the attractive coupling between the electron and the hole, governed by the static-screened interaction W_s, while the exchange kernel K^x represents gives a small repulsive term.
Diagonalization of Eq.(1.74), i.e.

$$\sum_{v',c',\mathbf{k}'} H^{res}(vc\mathbf{k}, v'c'\mathbf{k}')A_\lambda(v'c'\mathbf{k}') = E_\lambda A_\lambda(vc\mathbf{k}) \tag{1.77}$$

provides the exciton energies E_λ (λ is the index identifying different excitonic states) together with the envelope functions $A_\lambda(vc\mathbf{k})$: for a given exciton λ, the square modulus of A_λ defines the weight of the single particle transition $(v\mathbf{k}) \to (c\mathbf{k})$ to the chosen excitonic state.
Starting from the spectrum of H^{res}, it is possible to derive the macroscopic dielectric function $\varepsilon_M(\omega)$, whose imaginary part is proportional to the absorption spectrum obtained in optical spectroscopy.[2] We notice that, when the macroscopic dielectric function is evaluated, the bare Coulomb interaction appearing in the exchange kernel (Eq.(1.76)) is substituted by a potential not

[2]More precisely, the absorption signal is defined by the absorption coefficient $\alpha(\omega) \propto \omega\frac{\mathrm{Im}[\epsilon_M(\omega)]}{\mathrm{Re}[n(\omega)]}$, being n the refractive index. Anyhow, in general, its frequency dependence is generally well captured by the sole $\mathrm{Im}[\epsilon_M(\omega)]$.

including the long range contribution[16], i.e. $v(\mathbf{q}+\mathbf{G})$ is set to zero for each $\mathbf{q}$, if $\mathbf{G}=\mathbf{0}$. This accounts for the fact that optical spectroscopy describes the macroscopic response of the system to an external perturbation.

In practice, this quantity is evaluated as

$$\varepsilon_M^j(\omega) = 1 - \frac{8\pi}{\Omega}\sum_\lambda \frac{|D_\lambda^j|^2}{\omega - E_\lambda + i\eta} \tag{1.78}$$

where Ω is the unit cell volume, λ runs over the excitonic eigenstates with energy E_λ and

$$D_\lambda^j = \sum_{vc\mathbf{k}} A_\lambda(vc\mathbf{k})\left(\hat{\mathbf{j}}\cdot\mathbf{d}_{vc\mathbf{k}}\right) \tag{1.79}$$

is the dipole strength for exciton λ, assuming light polarized along direction $\hat{\mathbf{j}}$. This quantity determines if a given exciton can be optically excited by electromagnetic radiation, with a certain polarization. We notice that Eq.(1.79) is an average of the single-particle transitions interband dipole $\mathbf{d}_{vc\mathbf{k}}$ weighted by the contribution of each transition $(v\mathbf{k})\rightarrow(c\mathbf{k})$ to the chosen exciton. The interband dipoles are directly computed using Kohn Sham states[35], i.e.

$$\mathbf{d}_{vc\mathbf{k}} = \frac{1}{\epsilon_{c\mathbf{k}}^{KS}-\epsilon_{v\mathbf{k}}^{KS}}\left(\langle\phi_{v\mathbf{k}}^{KS}|\mathbf{p}|\phi_{c\mathbf{k}}^{KS}\rangle + \langle\phi_{v\mathbf{k}}^{KS}|[\mathbf{r},\hat{V}_{NL}]|\phi_{c\mathbf{k}}^{KS}\rangle\right) \tag{1.80}$$

where $\hat{V}_{NL}$ is the non-local part of the KS potential, due to the non-locality of pseudopotentials and $\mathbf{p}$ is the linear momentum.
In this Thesis, BSE is solved using `Yambo` package: in practice, via a DFT calculation KS states and energies are computed and used to construct the static screened interaction W_s, using RPA approximation, as outlined in Section 1.2. Then, starting from the same set of KS states, the hermitian excitonic Hamiltonian is constructed using Eqs.(1.74)-(1.76), where QP energies are obtained from KS values using Eq.(1.34)[3]. From a numerical perspective, it is extremely important to properly choose both the number of valence-conduction states included in the excitonic Hamiltonian together with the sampling of the BZ in order to obtain properly converged optical spectra.
In the following chapter we will discuss an alternative simplified implementation of the excitonic Hamiltonian, obtained considering a Tight-Binding description of the single particle states. Furthermore, we also generalize Eq.(1.74) to obtain the energies of finite-momentum excitons, i.e. electron-hole pairs composed by single particle states having different wave-vectors, and so carrying a finite center-of-mass momentum. Although such excitons cannot be probed by optical spectroscopy, because of momentum conservation,

[3]In general, to obtain properly converged exciton energies, one needs denser $\mathbf{k}$-grid than those used in G_0W_0 calculations, where QP corrections are computed. To model QP corrections on points where they have not been explicitly evaluated, we have made use of scissor-streching approximation, whenever meaningful.

they play a fundamental role in determining many observable properties: in particular, in indirect-gap materials they are responsible for light emission, due to their phonon-assisted recombination (as discussed in Chapter 4).

1.4 *Ab initio* simulation of lattice vibrations

After presenting state-of-the-art methods to simulate excited electronic states in interacting electron systems, we now turn out attention to a fully *ab initio* description of lattice vibrations, by which we will evaluate phonon dispersions and the corresponding atomic displacements in Chapter 4 and 5.
We start considering a periodic crystal with lattice vectors $\mathbf{R}$ and with N_{at} atoms per unit cell. The atomic equilibrium positions will be denoted as $\mathbf{R}+\tau_s$, where s is a progressive index running over the atoms in the unit cell, while the compact notation $l \equiv (\mathbf{R}, s)$ will be also used to refer a specific atom at $\tau_l \equiv \mathbf{R}+\tau_s$. Furthermore, $\mathbf{u}_l$ denotes a small displacement of atom l from its equilibrium position.
Lattice dynamics is described within Born-Oppenheimer approximation: as already discussed, this assumption decouples the nuclear and the electronic dynamics, so that the Hamiltonian describing the nuclear motion can be written as

$$\hat{H}_N = \hat{T}_N + E(\{\mathbf{u}\}) \tag{1.81}$$

where $\hat{T}_N$ is the nuclei-kinetic-energy operator, while $E(\{\mathbf{u}\})$ is the electronic ground state energy when nuclei are fixed at positions $\tau_l + \mathbf{u}_l$ summed to the nuclei-nuclei Coulomb interaction (defined in the following as V_{II}). As the atomic displacements from equilibrium positions are generally small (i.e. $|\mathbf{u}_l| << |\tau_l|$) we can introduce the harmonic approximation for the function E, i.e.

$$E(\{\mathbf{u}\}) \approx E_0 + \frac{1}{2}\sum_{l,l'}\sum_{\alpha,\beta}\frac{\partial^2 E}{\partial u_l^\alpha \partial u_{l'}^\beta}\Big|_{eq} u_l^\alpha u_{l'}^\beta \tag{1.82}$$

where the indices α and β run over the cartesian directions (x, y, z). The second derivative of E is evaluated at equilibrium (as pointed out by the 'eq' suffix), while first order derivatives are null as atomic forces are zero once atoms are clamped at their equilibrium positions. Substituting Eq.(1.82) in Eq.(1.81) and expressing the nuclear kinetic energy as

$$T_N = \sum_l \frac{\mathbf{P}_l^2}{2M_l}$$

M_l being the mass of atom l, the Hamilton equations of motion for the atoms are obtained

$$M_l \ddot{u}_l^\alpha = -\sum_{l'\beta}\frac{\partial^2 E}{\partial u_l^\alpha \partial u_{l'}^\beta} u_{l'}^\beta \tag{1.83}$$

We now look for the normal modes of oscillations for the lattice, i.e. solutions of Eq.(1.83) in the form

$$\xi^{\alpha}_{\mathbf{R}s}(\nu,\mathbf{q};t) = \frac{1}{\sqrt{M_s}}\xi^{\alpha}_{s}(\nu,\mathbf{q})e^{i[\mathbf{q}\cdot\mathbf{R}-\omega_{\nu\mathbf{q}}t]} \tag{1.84}$$

These modes (generally called phonons) are identified by the pair of indexes $(\nu,\mathbf{q})$, where ν is the phonon branch while $\mathbf{q}$ is the phonon wave-vector characterizing the lattice vibration; substitution of Eq.(1.84) in Eq.(1.83) gives

$$\sum_{s'\beta} D_{s\alpha,s'\beta}(\mathbf{q})\xi^{\beta}_{s'}(\nu,\mathbf{q}) = \omega^2_{\nu\mathbf{q}}\xi^{\alpha}_{s}(\nu,\mathbf{q}) \tag{1.85}$$

In practice, phonon displacements $\xi^{\alpha}_{s}(\nu,\mathbf{q})$ (describing how atoms are displaced in the unit cell at $\mathbf{R}=\mathbf{0}$ within phonon $(\nu,\mathbf{q})$) are obtained as the eigenstates of the Dynamical matrix $D_{s\alpha,s'\beta}(\mathbf{q})$ defined, at each $\mathbf{q}$, as

$$D_{s\alpha,s'\beta}(\mathbf{q}) = \frac{1}{N}\frac{1}{\sqrt{M_sM'_s}}\sum_{\mathbf{R}\mathbf{R}'}\frac{\partial^2 E}{\partial u^{\alpha}_{\mathbf{R}s}\partial u^{\beta}_{\mathbf{R}'s'}}e^{i\mathbf{q}\cdot(\mathbf{R}'-\mathbf{R})} = \frac{1}{\sqrt{M_sM'_s}}\sum_{\mathbf{R}_1} e^{-i\mathbf{q}\cdot\mathbf{R}_1}C^{\alpha,\beta}_{ss'}(\mathbf{R}_1) \tag{1.86}$$

where $C^{\alpha,\beta}_{ss'}(\mathbf{R}_1)$ is the force-constants matrix in real space. Furthermore, the square of the allowed phonon frequencies $\omega_{\nu\mathbf{q}}$ correspond to the eigenvalues of D.

The Dynamical matrix at a general $\mathbf{q}$ is evaluated fully *ab initio* using Density Functional Perturbation Theory (DFPT)[36, 37, 38, 39], as implemented in `Quantum Espresso` package. We summarize in the following the main steps needed to evaluate the Dynamical matrices and how we can obtain phonon energies and displacements over the entire Brillouin zone.

Starting from Eq.(1.10), adding the nuclei-nuclei Coulomb coupling and using Hellman-Feynman theorem[40], we can write

$$\frac{\partial^2 E}{\partial u^{\alpha}_{\mathbf{R}s}\partial u^{\beta}_{\mathbf{R}'s'}} = \int \mathrm{d}\mathbf{r}\; n_0(\mathbf{r})\frac{\partial^2 V(\mathbf{r})}{\partial u^{\alpha}_{\mathbf{R}s}\partial u^{\beta}_{\mathbf{R}'s'}} + \int \mathrm{d}\mathbf{r}\;\frac{\partial V(\mathbf{r})}{\partial u^{\alpha}_{\mathbf{R}s}}\frac{\partial n(\mathbf{r})}{\partial u^{\beta}_{\mathbf{R}'s'}} + \frac{\partial V_{II}}{\partial u^{\alpha}_{\mathbf{R}s}\partial u^{\beta}_{\mathbf{R}'s'}} \tag{1.87}$$

where n_0 is the ground state electronic density, V is the electron-ion potential and all the derivatives are evaluated assuming the nuclei fixed at their equilibrium positions. By substitution of Eq.(1.87) in Eq.(1.86) the Dynamical matrix can be written as

$$\begin{aligned} D_{s\alpha,s'\beta}(\mathbf{q}) = {} & \frac{1}{N\sqrt{M_sM'_s}}\int \mathrm{d}\mathbf{r}\; n_0(\mathbf{r})\sum_{\mathbf{R}\mathbf{R}'}\frac{\partial^2 V}{\partial u^{\alpha}_{\mathbf{R}s}\partial u^{\beta}_{\mathbf{R}'s'}}e^{i\mathbf{q}\cdot(\mathbf{R}'-\mathbf{R})} \\ & + \frac{1}{N\sqrt{M_sM'_s}}\int \mathrm{d}\mathbf{r}\;\sum_{\mathbf{R}\mathbf{R}'}\frac{\partial V}{\partial u^{\alpha}_{\mathbf{R}s}}\frac{\partial n}{\partial u^{\beta}_{\mathbf{R}'s'}}e^{i\mathbf{q}\cdot(\mathbf{R}'-\mathbf{R})} \\ & + D^{II}_{s\alpha,s'\beta}(\mathbf{q}) \end{aligned} \tag{1.88}$$

where D^{II} is the contribution to the Dynamical matrix coming from the derivative of the nuclei-nuclei interaction. The derivatives of the electron-ion potential w.r.t. the atomic displacements can be computed directly, starting from the expression of V, i.e. the sum of the potentials due to all the atoms in the crystal (see for example [36]). Therefore, in the following our focus will be on the second term of Eq.(1.88), which we call $\tilde{D}_{s\alpha,s'\beta}(\mathbf{q})$.
Given a general function $f(\mathbf{r})$, crystal-periodic in equilibrium conditions, we define

$$\partial^{\mathbf{q}}_{s\alpha} f(\mathbf{r}) = e^{-i\mathbf{q}\cdot\mathbf{r}} \sum_{\mathbf{R}} \frac{\partial f(\mathbf{r})}{\partial u^{\alpha}_{\mathbf{R}s}} e^{i\mathbf{q}\cdot\mathbf{R}} \tag{1.89}$$

which is also a crystal-periodic function. With this definition,

$$\tilde{D}_{s\alpha,s'\beta}(\mathbf{q}) = \frac{1}{N\sqrt{M_s M'_s}} \int \mathrm{d}\mathbf{r}\ \partial^{\mathbf{q}*}_{s\alpha} V(\mathbf{r}) \partial^{\mathbf{q}}_{s'\beta} n(\mathbf{r}) \tag{1.90}$$

As already pointed out, $\partial^{\mathbf{q}*}_{s\alpha} V(\mathbf{r})$ only depends on the electron-ion interaction, which can be computed directly: the variation of electronic charge density $\partial^{\mathbf{q}}_{s'\beta} n(\mathbf{r})$ is, instead, unknown, and is computed via DFPT. To evaluate $\partial^{\mathbf{q}}_{s'\beta} n(\mathbf{r})$, we start computing

$$\frac{\partial n(\mathbf{r})}{\partial u^{\beta}_{\mathbf{R}'s'}} = 2\sum_{v\mathbf{k}} \phi^*_{v\mathbf{k}}(\mathbf{r}) \frac{\partial \phi_{v\mathbf{k}}(\mathbf{r})}{\partial u^{\beta}_{\mathbf{R}'s'}} + 2\sum_{v\mathbf{k}} \phi_{v\mathbf{k}}(\mathbf{r}) \frac{\partial \phi^*_{v\mathbf{k}}(\mathbf{r})}{\partial u^{\beta}_{\mathbf{R}'s'}} \tag{1.91}$$

It is possible to show[36] that $\frac{\partial n(\mathbf{r})}{\partial u^{\beta}_{\mathbf{R}'s'}}$ only depends on the variation of KS states projected on the manifold of un-occupied states. Therefore, using this information combined with time-reversal symmetry property for which $\phi^*_{v\mathbf{k}}(\mathbf{r}) = \phi_{v-\mathbf{k}}(\mathbf{r})$ it is possible to obtain

$$\frac{\partial n(\mathbf{r})}{\partial u^{\beta}_{\mathbf{R}'s'}} = 4\sum_{v\mathbf{k}} \phi^*_{v\mathbf{k}}(\mathbf{r}) \left[\hat{P}_c \frac{\partial \phi_{v\mathbf{k}}}{\partial u^{\beta}_{\mathbf{R}'s'}} \right](\mathbf{r}) \tag{1.92}$$

where $\hat{P}_c$ is the projection operator on the manifold of conduction-unoccupied states[4]. By substitution of Eq.(1.92) in Eq.(1.89) for the charge density and writing KS states as $\phi_{v\mathbf{k}}(\mathbf{r}) = e^{i\mathbf{k}\cdot\mathbf{r}} u_{n\mathbf{k}}(\mathbf{r})$, it is possible to obtain

$$\partial^{\mathbf{q}}_{s'\beta} n(\mathbf{r}) = 4\sum_{v\mathbf{k}} u^*_{v\mathbf{k}}(\mathbf{r}) \left[\hat{P}^{\mathbf{k}+\mathbf{q}}_c \partial^{\mathbf{q}}_{s'\beta} u_{v\mathbf{k}} \right](\mathbf{r}) \tag{1.93}$$

where $\hat{P}^{\mathbf{k}+\mathbf{q}}_c$ is the projector on the manifold of unoccupied states with momentum $\mathbf{k}+\mathbf{q}$, while $\partial^{\mathbf{q}}_{s'\beta} u_{v\mathbf{k}}$ is the variation of the periodic-part of KS states,

[4]The notation $\left[\hat{P}_c \frac{\partial \phi_{v\mathbf{k}}}{\partial u^{\beta}_{\mathbf{R}'s'}} \right](\mathbf{r})$ corresponds to the matrix element $\langle \mathbf{r} | \hat{P}_c | \frac{\partial \phi_{v\mathbf{k}}}{\partial u^{\beta}_{\mathbf{R}'s'}} \rangle$

according to the definition of Eq.(1.89). This last term is evaluated using Sternheimer equation, obtained by simple first-order perturbation theory, i.e.

$$\left\{\hat{H}_{KS}^{\mathbf{k}+\mathbf{q}} - \epsilon_{v\mathbf{k}}^{KS}\right\}\left[\hat{P}_c^{\mathbf{k}+\mathbf{q}}(\partial_{s'\beta}^{\mathbf{q}} u_{v\mathbf{k}})\right](\mathbf{r}) = -\left[\hat{P}_c^{\mathbf{k}+\mathbf{q}}(\partial_{s'\beta}^{\mathbf{q}} V_{KS}) u_{v\mathbf{k}}\right](\mathbf{r}) \tag{1.94}$$

where the variation of the KS potential is given by

$$\partial_{s'\beta}^{\mathbf{q}} V_{KS}(\mathbf{r}) = \partial_{s'\beta}^{\mathbf{q}} V(\mathbf{r}) + \int \mathrm{d}\mathbf{r}'\, e^{i\mathbf{q}\cdot(\mathbf{r}-\mathbf{r}')} v(\mathbf{r}-\mathbf{r}') \partial_{s'\beta}^{\mathbf{q}} n(\mathbf{r}') + \frac{\partial V_{xc}}{\partial n} \partial_{s'\beta}^{\mathbf{q}} n(\mathbf{r}) \tag{1.95}$$

and $\hat{H}_{KS}^{\mathbf{k}+\mathbf{q}} = e^{-i(\mathbf{k}+\mathbf{q})\cdot\hat{\mathbf{r}}} \hat{H}_{KS} e^{i(\mathbf{k}+\mathbf{q})\cdot\hat{\mathbf{r}}}$.
Equations (1.93)-(1.95) are the core of DFPT: in practice, starting from an initial guess for the charge-density variation, the quantity $\partial_{s'\beta}^{\mathbf{q}} V_{KS}(\mathbf{r})$ is computed using Eq.(1.95) and then a new approximation for $\partial_{s'\beta}^{\mathbf{q}} u_{v\mathbf{k}}$ is obtained by solving Eq.(1.94) from which the charge variation is refined using Eq.(1.93). This iterative procedure is repeated up to when a converged charge-density variation is obtained. Finally, using Eqs.(1.88) and (1.90), the Dynamical matrix can be then computed.
As Eq.(1.94) involves only crystal periodic functions, it can be directly implemented in a plane-wave-basis-set description, as discussed for DFT in Section 1.1; furthermore, the solution of Eqs. (1.93)-(1.95) does not require the knowledge of the full spectrum of the KS Hamiltonian at equilibrium, as $\hat{P}_c^{\mathbf{k}+\mathbf{q}} = 1 - \hat{P}_v^{\mathbf{k}+\mathbf{q}}$, $\hat{P}_v^{\mathbf{k}+\mathbf{q}}$ being the projector on the occupied KS manifold at $\mathbf{k}+\mathbf{q}$.
In order to obtain phonon dispersion and displacements over the entire BZ, Dynamical matrices are computed on a regular coarse grid of $\mathbf{q}$ points. By inverse Fourier transformation, the interatomic force constants in real space are evaluated as

$$C_{ss'}^{\alpha\beta}(\mathbf{R}) = \sqrt{M_s M_{s'}} \frac{1}{N_{\mathbf{q}}} \sum_{i=1}^{N_{\mathbf{q}}} D_{s\alpha,s'\beta}(\mathbf{q}_i) e^{i\mathbf{q}_i\cdot\mathbf{R}} \tag{1.96}$$

$\mathbf{q}_i$ being the points of the considered BZ sampling. In general, the Dynamical matrices at $\mathbf{q}$ points not included in the original grid can be evaluated by Fourier interpolation, i.e.

$$D_{s\alpha,s'\beta}(\mathbf{q}) = \frac{1}{\sqrt{M_s M_{s'}}} \sum_{\mathbf{R}} C_{s,s'}^{\alpha,\beta}(\mathbf{R}) e^{-i\mathbf{q}\cdot\mathbf{R}} \tag{1.97}$$

from which phonon frequencies and displacements can be easily computed via Eq.(1.85). The validity of this procedure is justified by the short-range nature of force constants in real space: as a consequence, a small number of $\mathbf{R}$ vectors (and therefore of $\mathbf{q}_i$ points) is needed to properly interpolate $D_{s\alpha,s'\beta}(\mathbf{q})$ at points where DFPT calculations were not explicitly carried out.

In general, $\mathbf{q}_i$ grids comparable to the $\mathbf{k}$ grid used to sample the BZ in the ground state calculations are enough to guarantee a correct interpolation of phonon dispersions. We note that these considerations are generally valid in non-polar insulators. Special attention must be paid in case of Kohn anomalies in metals or in polar insulators.

Chapter 2

Effect of uniaxial strain on the excitonic properties of monolayer C_3N

Since its experimental realization [41, 42], monolayer C_3N (ML-C_3N) has been intensively studied from a theoretical point of view, to fully characterize its electronic [43], optical [44, 45], mechanical, [46, 47, 48] and electrochemical properties [49, 50, 51, 52, 53]. As ML-C_3N is a 2D material, the combination of electron confinement and enhanced electron-hole interaction (due to reduced electronic screening) gives rise to strong excitonic effects, which characterize its optical response [44, 45]. At the same time, DFT and molecular dynamics calculations [46] have predicted the capability of ML-C_3N to sustain strong uniaxial strains, up to about 10%, without failure.
Motivated by recent advances in the experimental application of relatively intense mechanical stresses to 2D materials [54, 55, 56], in this Chapter we discuss how the excitonic properties of ML-C_3N are modified by external uniaxial strain, when applied along high symmetry directions, such as zig-zag and armchair, as shown in Figure 2.1. As fully *ab initio* calculations of excitonic effects are computationally very demanding, especially for 2D materials, here we develop a simpler approach to solve the Bethe Salpeter equation[31, 32, 16] and apply it to the case of ML-C_3N subject to different strain conditions. This model describes the single particle states involved in the lowest lying excitons through a tight binding (TB) Hamiltonian and approximates the electron-hole interaction using quantities derived from *ab initio* calculations [57, 58, 43, 59]. Based on this model, we discuss the appearance of excitons in strained C_3N with strong optical anisotropy, and we have provided a rationale for this behaviour through group theory arguments. Furthermore, taking advantage of the computational simplicity of the model, we have analyzed the small momentum excitonic dispersion, both in pristine and strained C_3N, revealing the effect of uniaxial strain on the small-momentum linear non-analytic dispersion. These calculations demonstrate that the presence of a few percent

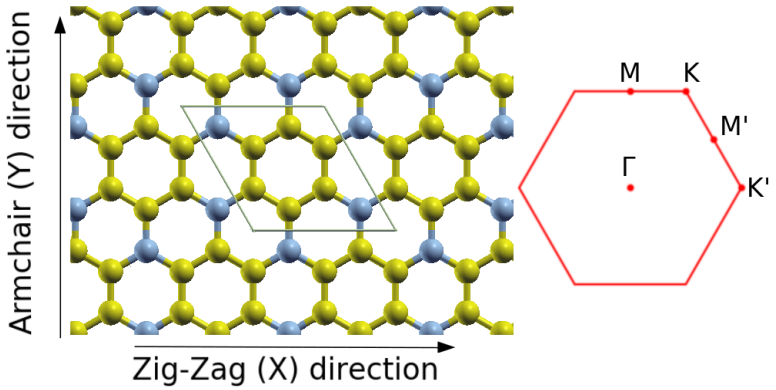

Figure 2.1: Left: crystal structure of C_3N, where yellow (light-blue) spheres represent Carbon (Nitrogen) atoms. High symmetry armchair and zig-zag directions where strain is applied are also highlighted. Right: hexagonal Brillouin zone of pristine C_3N, with the high symmetry points considered in this work.

strain is already able to induce a strong anisotropy in the exciton dispersion close to Γ regarding the direction of applied strain, and furthermore leading to anisotropic brightening of some of the low-lying excitons.

The content of this Chapter is reported in part in the publication *Effect of uniaxial strain on the excitonic properties of monolayer C_3N: A symmetry-based analysis*[60], and started with our work appeared in the publication *Excitonic effects in graphene-like C_3N*[45].

2.1 Model solution of BSE

In this Section we present the method used to study the excitonic properties of pristine and strained ML-C_3N. More precisely, in Section 2.1.1 we discuss the modeling of single particle states via a fully *ab initio* Tight Binding (TB) model, while in Section 2.1.2 we will focus on describing the approximations adopted in the solution of the BSE.

2.1.1 Tight Binding Model

As previous works [43, 44, 45] have shown that the valence and conduction states involved in the formation of the lowest lying excitons have π character, we have modelled these bands through a TB Hamiltonian [61] considering one $2p_z$ orbital for each atom in the unit cell:

$$H_{\alpha\beta}(\mathbf{k}) = \sum_{\mathbf{R}} e^{i\mathbf{k}\cdot\mathbf{R}} \langle \alpha 0 | \hat{H} | \beta \mathbf{R} \rangle. \tag{2.1}$$

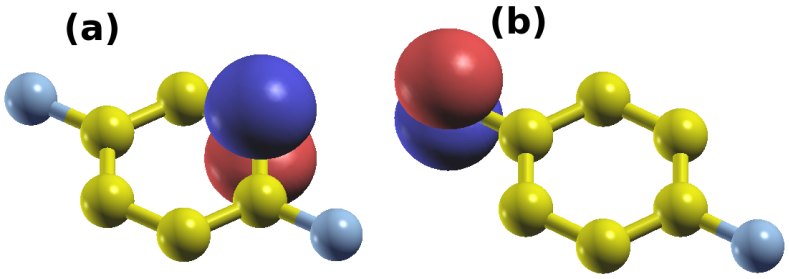

Figure 2.2: Example of Maximally Localized Wannier Functions (MLWF) localized on carbon (a) and nitrogen atoms (b). The obtained Wannier functions exhibit a $2p_z$-like character, with comparable spatial spreads.

In Eq. (2.1), $\mathbf{R}$ is a lattice vector, $\mathbf{k}$ is a point sampling the 2D Brillouin Zone, and $t(\alpha 0; \beta \mathbf{R}) = \langle \alpha 0 | \hat{H} | \beta \mathbf{R} \rangle$ corresponds to the hopping between a $2p_z$ orbital localized on atom α in the unit cell at $\mathbf{R} = 0$ and a $2p_z$ orbital localized on atom β in the unit cell at $\mathbf{R}$. The hopping parameters have been evaluated fully *ab initio* adopting the following procedure.
Firstly, we relax the atomic positions in presence of uniaxial strain along zig-zag or armchair direction following the approach of Lechifflart *et al.* [62]. In practice we have constructed a rectangular unit cell containing 16 atoms, such that the in-plane unit cell basis vectors were oriented along the armchair (y) and the zig-zag (x) directions respectively. We then increased the length of the cell side along the direction in which we wanted to apply the strain, and we relaxed both the atomic positions and the unit cell while keeping fixed the length of the strained cell side. This relaxation step was performed using DFT with PBE approximation[10] for the exchange-correlation potential and norm-conserving ONCV pseudopotentials [63]. The kinetic energy cutoff was set to 100 Ry, while the rectangular BZ was sampled with a 12x12x1 Monkhorst-Pack grid, using a supercell with a length of 18 Angstrom along the z direction. The relaxation step was interrupted once forces acting on atoms were less that 10^{-5} a.u.
From these relaxed orthogonal cells, we then obtained pseudo-hexagonal unit cells, containing only eight atoms, as in the case of pristine C_3N. After this process we always checked that the forces acting on each atom were still smaller than 10^{-5} a.u.
For each strain configuration, we have computed single particle electronic states and energies at the DFT level on a 24x24x1 $\mathbf{k}$-grid and we extracted Maximally Localized Wannier Functions (MLWFs) [61, 64] with the `Wannier90` code [65, 66, 67], making use of the band disentanglement method [68]. As expected, the obtained MLWFs exhibit a $2p_z$-like character, as shown in Fig. 2.2. Finally, the hopping parameters appearing in Eq. (2.1) have been obtained as the Hamiltonian matrix elements on the computed MLWF basis.

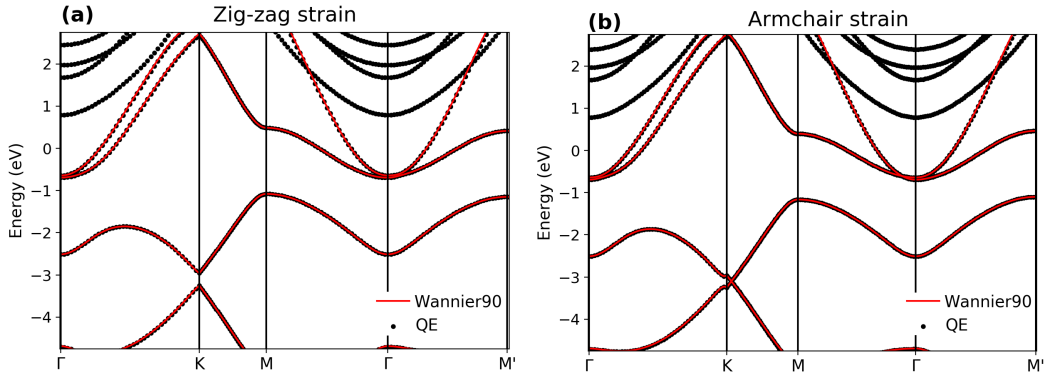

Figure 2.3: Comparison between electronic bandstructures computed with DFT-PBE (black dots) and those interpolated using $2p_z$ like MLWFs. a) (b) refers to a zig-zag strain (armchair strain) of 2.0 %. The bands not captured by the Wannier interpolation are those characterized by a character which is not of type π, so that they cannot be reproduced using $2p_z$-like MLWF only.

The diagonalization of $H_{\alpha\beta}(\mathbf{k})$ gives access to single particle energies and states: more precisely, we have solved the eigenvalue problem

$$\sum_{\beta} H_{\alpha\beta}(\mathbf{k}) c_{\beta}(n\mathbf{k}) = \epsilon_{n\mathbf{k}}\, c_{\alpha}(n\mathbf{k}) \tag{2.2}$$

obtaining $\epsilon_{n\mathbf{k}}$ (the energy of the n-th band at point $\mathbf{k}$) and $c_{\alpha}(n\mathbf{k})$, the projection of Bloch state $|n\mathbf{k}\rangle$ on the MLWF α, i.e.

$$|\psi_{n\mathbf{k}}\rangle = \frac{1}{\sqrt{N_c}} \sum_{\alpha} c_{\alpha}(n\mathbf{k}) \sum_{\mathbf{R}} e^{i\mathbf{k}\cdot\mathbf{R}} |\alpha\mathbf{R}\rangle, \tag{2.3}$$

$|\alpha\mathbf{R}\rangle$ being the $2p_z$-like MLWF localized at $\tau_{\alpha} + \mathbf{R}$, with τ_{α} corresponding to the atomic site of atom α in the unit cell.
In Figure 2.3 we show the comparison between DFT (black dots) and TB (solid red lines) energies computed for a applied strain of 2.0 % along zig-zag and armchair directions. We notice that the quantities $\epsilon_{n\mathbf{k}}$ provide an accurate description of the single particle energies obtained at the DFT level, as the hopping parameters were computed by Wannierizing DFT bands. In the following, we include the effect of quasi-particle corrections using a scissor/stretching operator, as in Ref.[45]. To reduce the computational complexity, in the following we use the scissor/stretching parameters computed in the pristine case for all the considered strain perturbations, assuming a negligible dependence of the quasi-particle corrections on the applied strain here considered (always smaller than 5 %).

2.1.2 Excitonic Hamiltonian at finite momentum

In the following, we will solve BSE within the resonant Tamm-Dancoff approximation, by computing exciton energies and wave-functions diagonalizing the Hermitian excitonic Hamiltonian:

$$H_{\mathbf{Q}}(vc\mathbf{k};v'c'\mathbf{k}') = (\epsilon_{c,\mathbf{k}+\mathbf{Q}} - \epsilon_{v\mathbf{k}})\delta_{c,c'}\delta_{v,v'}\delta_{\mathbf{k},\mathbf{k}'} + K^d_{\mathbf{Q}}(vc\mathbf{k};v'c'\mathbf{k}') + K^x_{\mathbf{Q}}(vc\mathbf{k};v'c'\mathbf{k}') \tag{2.4}$$

Here we generalize the discussion presented in Chapter 1, by considering finite-momentum excitons. In practice, diagonalization of $H_{\mathbf{Q}}$

$$\sum_{v'c'\mathbf{k}'} H_{\mathbf{Q}}(vc\mathbf{k};v'c'\mathbf{k}')A_{\lambda\mathbf{Q}}(v'\mathbf{k},c'\mathbf{k}'+\mathbf{Q}) = E_{\lambda\mathbf{Q}}A_{\lambda\mathbf{Q}}(v\mathbf{k},c\mathbf{k}+\mathbf{Q}) \tag{2.5}$$

provides the energies $E_{\lambda\mathbf{Q}}$ of finite momentum excitons $|\lambda\mathbf{Q}\rangle$, composed by single particle transitions $(v\mathbf{k},c\mathbf{k}+\mathbf{Q})$, which involve states with wave-vectors differing by $\mathbf{Q}$. As in the $\mathbf{Q}=0$ case, the square modulus of $A_{\lambda\mathbf{Q}}(v\mathbf{k},c\mathbf{k}+\mathbf{Q})$ indicate the weight of the single particle transition $(v\mathbf{k},c\mathbf{k}+\mathbf{Q})$ to the excitonic state $|\lambda\mathbf{Q}\rangle$.
All the results presented in the following have been obtained including the last occupied valence and the two lowest unoccupied conduction bands in the construction of the BSE kernel, as the lowest energy excitons in ML-C_3N are mainly composed by transitions among those states. Furthermore, we have always used a 121×121×1 Monkhorst-Pack grid to sample the BZ, as it guarantees exciton energies converged within 1 meV.
We now discuss the evaluation of the direct $K^d_{\mathbf{Q}}$ and exchange $K^x_{\mathbf{Q}}$ BSE kernels, starting from the TB description of independent particle states presented in Section 2.1.1.

Direct part of the BSE kernel

The direct part of the BSE kernel at finite momentum is defined as

$$K^d_{\mathbf{Q}}(vc\mathbf{k};v'c'\mathbf{k}') = -\int d\mathbf{r}\int d\mathbf{r}'\ \psi^*_{c,\mathbf{k}+\mathbf{Q}}(\mathbf{r})\psi_{c',\mathbf{k}'+\mathbf{Q}}(\mathbf{r})W(\mathbf{r},\mathbf{r}')\psi_{v\mathbf{k}}(\mathbf{r}')\psi^*_{v'\mathbf{k}'}(\mathbf{r}') \tag{2.6}$$

where $W(\mathbf{r},\mathbf{r}')$ represents the electron-electron screened interaction and $\psi_{n\mathbf{k}}(\mathbf{r})$ are the Bloch states for valence and conduction bands. Within our TB formalism, we write the electronic wavefunctions on the basis of $2p_z$-like orbitals $w(\mathbf{r}-\mathbf{R}-\tau_\alpha)$ localized on the atomic sites τ_α in the unit cell, i.e. by expressing in real space Eq.(2.3)

$$\psi_{n\mathbf{k}}(\mathbf{r}) = \frac{1}{\sqrt{N}}\sum_{\mathbf{R}} e^{i\mathbf{k}\cdot\mathbf{R}}\sum_{\alpha} c_\alpha(n\mathbf{k})w(\mathbf{r}-\mathbf{R}-\tau_\alpha) \tag{2.7}$$

Here we are implicitly assuming that the MLWF located on different atoms in the unit cell are equal, as the spatial spread obtained *ab initio* for N and C

localized MLWF are very close, with differences smaller than 10 %. In other words, their only dependence on the atomic index α comes from the site τ_α where they are localized.
By substitution of Eq.(2.7) in Eq.(2.6) we obtain

$$K^d_{\mathbf{Q}}(vc\mathbf{k};v'c'\mathbf{k}') = -\frac{1}{N^2}\cdot$$
$$\sum_{\substack{\mathbf{R}_1,\mathbf{R}_2,\mathbf{R}_3,\mathbf{R}_4\\ \alpha,\beta,\gamma,\rho}} e^{-i(\mathbf{k}+\mathbf{Q})\cdot\mathbf{R}_1} e^{i(\mathbf{k}'+\mathbf{Q})\cdot\mathbf{R}_2} e^{i\mathbf{k}\cdot\mathbf{R}_3} e^{-i\mathbf{k}'\cdot\mathbf{R}_4} c^*_\alpha(c,\mathbf{k}+\mathbf{Q}) c_\beta(c',\mathbf{k}'+\mathbf{Q}) c_\gamma(v\mathbf{k}) c^*_\rho(v'\mathbf{k}')$$
$$\cdot \int \mathrm{d}\mathbf{r}\mathrm{d}\mathbf{r}'\; w(\mathbf{r}-\mathbf{R}_1-\tau_\alpha) w(\mathbf{r}-\mathbf{R}_2-\tau_\beta) W(\mathbf{r},\mathbf{r}') w(\mathbf{r}'-\mathbf{R}_3-\tau_\gamma) w(\mathbf{r}'-\mathbf{R}_4-\tau_\rho) \tag{2.8}$$

where we have used of the property of MLWF $w(\mathbf{r}-\mathbf{R}-\tau_\alpha) = w^*(\mathbf{r}-\mathbf{R}-\tau_\alpha)$. Notice that the indeces $[\alpha,\beta,\gamma,\rho]$ runs over the MLWF (or equivalently on the atoms in the unit cell, as we have one Wannier function for each atom), while $[\mathbf{R}_1,\mathbf{R}_2,\mathbf{R}_3,\mathbf{R}_4]$ represent the lattice vectors of the real space lattice.
As the Wannier functions are strongly spatially localized, we neglect the overlap between MLWF localized on different atomic sites, i.e. we use the approximations

$$w(\mathbf{r}-\mathbf{R}_1-\tau_\alpha) w(\mathbf{r}-\mathbf{R}_2-\tau_\beta) \approx \delta_{\alpha,\beta}\delta_{\mathbf{R}_1,\mathbf{R}_2} w(\mathbf{r}-\mathbf{R}_1-\tau_\alpha)^2 \tag{2.9}$$

$$w(\mathbf{r}'-\mathbf{R}_3-\tau_\gamma) w(\mathbf{r}'-\mathbf{R}_4-\tau_\rho) \approx \delta_{\gamma,\rho}\delta_{\mathbf{R}_3,\mathbf{R}_4} w(\mathbf{r}'-\mathbf{R}_3-\tau_\gamma)^2 \tag{2.10}$$

Using these approximations in Eq.(2.8) we obtain for $K^d_{\mathbf{Q}}(vc\mathbf{k};v'c'\mathbf{k}')$ the expression

$$K^d_{\mathbf{Q}}(vc\mathbf{k};v'c'\mathbf{k}') \approx$$
$$-\frac{1}{N^2}\sum_{\mathbf{R}_1,\mathbf{R}_3}\sum_{\alpha,\gamma} e^{i(\mathbf{k}'-\mathbf{k})\cdot\mathbf{R}_1} e^{i(\mathbf{k}-\mathbf{k}')\cdot\mathbf{R}_3} c^*_\alpha(c,\mathbf{k}+\mathbf{Q}) c_\alpha(c',\mathbf{k}'+\mathbf{Q}) c_\gamma(v\mathbf{k}) c^*_\gamma(v'\mathbf{k}')$$
$$\cdot \int \mathrm{d}\mathbf{r} \int \mathrm{d}\mathbf{r}'\; w(\mathbf{r}-\mathbf{R}_1-\tau_\alpha)^2 W(\mathbf{r},\mathbf{r}') w(\mathbf{r}'-\mathbf{R}_3-\tau_\gamma)^2 \tag{2.11}$$

We now solve the double integral over $\mathbf{r}$ and $\mathbf{r}'$. To do this, we start writing the electron-electron screened interaction in terms of its in-plane Fourier transform. More precisely we use

$$W(\mathbf{r},\mathbf{r}') = \frac{1}{4\pi^2}\sum_{\mathbf{q}}\sum_{\mathbf{G}} v_{2D}(\mathbf{q}+\mathbf{G}) e^{i(\mathbf{q}+\mathbf{G})\cdot(\mathbf{r}_\parallel-\mathbf{r}'_\parallel)} \int \mathrm{d}z_1\, \varepsilon^{-1}(\mathbf{q}+\mathbf{G};z,z_1) e^{-|\mathbf{q}+\mathbf{G}|\cdot|z_1-z'|} \tag{2.12}$$

In Eq.(2.12), $\mathbf{r}_\parallel$ and $\mathbf{r}'_\parallel$ are the in-plane components of $\mathbf{r}$ and $\mathbf{r}'$, $\mathbf{q}$ is a vector sampling the 2D Brillouin zone, $\mathbf{G}$ is a planar reciprocal lattice vector, $v_{2D}(\mathbf{q}+\mathbf{G})$ is the Fourier transform of the bare Coulomb interaction in 2D and $\varepsilon^{-1}(\mathbf{q}+$

$\mathbf{G}; z, z_1)$ is the planar Fourier transform of the inverse dielectric function in real space, i.e.

$$\varepsilon^{-1}(\mathbf{r}, \mathbf{r}') = \frac{1}{4\pi^2} \sum_{\mathbf{q},\mathbf{G}} \varepsilon^{-1}(\mathbf{q}+\mathbf{G}; z, z_1) e^{i(\mathbf{q}+\mathbf{G})\cdot(\mathbf{r}_\parallel - \mathbf{r}'_\parallel)} \tag{2.13}$$

It is important to notice that in Eq.(2.13) we are neglecting the in-plane local field effects, i.e. we are assuming that the inverse dielectric function $\varepsilon^{-1}(\mathbf{r}, \mathbf{r}')$ written in real space does not depend on $\mathbf{r}_\parallel$ and $\mathbf{r}'_\parallel$ separately, but only through the difference $\mathbf{r}_\parallel - \mathbf{r}'_\parallel$. However, we are fully considering the non-locality with respect to z of the inverse dielectric function ϵ^{-1}, since it is fundamental to obtain a proper description of electronic screening in 2D materials [57, 69]. Furthermore, to solve the double integral in Eq.(2.11), we adopt a cylindrical approximation for the $2p_z$-like Wannier functions $w(\mathbf{r} - \mathbf{R} - \tau_\alpha)$, i.e.

$$w(\mathbf{r} - \mathbf{R} - \tau_\alpha) \approx f_\alpha(\mathbf{r}_\parallel - \mathbf{R} - \tau_\alpha) h_\alpha(z)\, \mathrm{sgn}(z), \tag{2.14}$$

decoupling the in-plane components $\mathbf{r}_\parallel$ of the position vector $\mathbf{r}$ from the out-of-plane component z[70]. The functions f_α and h_α were obtained using the definitions:

$$f_\alpha(\mathbf{r}_\parallel - \mathbf{R} - \tau_\alpha) = A^f_\alpha \int_{-\infty}^{+\infty} \mathrm{d}z \left| w(\mathbf{r} - \mathbf{R} - \tau_\alpha) \right| = A^f_\alpha\, e^{-B_\alpha |\mathbf{r}_\parallel - \mathbf{R} - \tau_\alpha|}, \left[1 + B_\alpha \left| \mathbf{r}_\parallel - \mathbf{R} - \tau_\alpha \right| \right] \tag{2.15}$$

and,

$$h_\alpha(z) = A^h_\alpha \int \mathrm{d}r_\parallel \left| w(\mathbf{r} - \mathbf{R} - \tau_\alpha) \right| = A^h_\alpha \left[|z| e^{-B_\alpha |z|} \big(1 + B_\alpha |z| \big) \right], \tag{2.16}$$

where A^f_α and A^h_α are normalization constants. In practice, f_α is the average of the modulus of a $2p_z$ orbital along z at fixed planar coordinate $\mathbf{r}_\parallel - \mathbf{R} - \tau_\alpha$, while h_α is its plane average, for each z. Finally, B_α is a parameter related to the spread of the MLWF, which depends in principle on the atomic site τ_α where the Wannier function is localized. As MLWF on C and N are very similar, we have taken B_α as the average among the spreads of the Wannier functions localized on different atoms. With these approximations we can write the double integral appearing in Eq.(2.11) as

$$\begin{aligned} \int \mathrm{d}\mathbf{r} \int \mathrm{d}\mathbf{r}'\; w(\mathbf{r} - \mathbf{R}_1 - \tau_\alpha)^2 W(\mathbf{r}, \mathbf{r}') w(\mathbf{r}' - \mathbf{R}_3 - \tau_\gamma)^2 \approx \frac{1}{4\pi^2} \sum_{\mathbf{q},\mathbf{G}} v_{2D}(\mathbf{q}+\mathbf{G}) I_d(\mathbf{q}+\mathbf{G}) \\ \cdot \left[\int \mathrm{d}\mathbf{r}_\parallel\; e^{i(\mathbf{q}+\mathbf{G})\cdot\mathbf{r}_\parallel} f^2(\mathbf{r}_\parallel - \mathbf{R}_1 - \tau_\alpha) \right] \left[\int \mathrm{d}\mathbf{r}'_\parallel\; e^{-i(\mathbf{q}+\mathbf{G})\cdot\mathbf{r}'_\parallel} f^2(\mathbf{r}'_\parallel - \mathbf{R}_3 - \tau_\gamma) \right] \end{aligned} \tag{2.17}$$

with $I_d(\mathbf{q}+\mathbf{G})$ defined as

$$I_d(\mathbf{q}+\mathbf{G}) = \int \mathrm{d}z\, \mathrm{d}z'\, \mathrm{d}z_1\; e^{-|\mathbf{q}+\mathbf{G}|\cdot|z_1 - z'|} \left| h(z) \right|^2 \varepsilon^{-1}(\mathbf{q}+\mathbf{G}; z, z_1) \left| h(z') \right|^2 \tag{2.18}$$

Performing the variable change

$$\int \mathrm{d}\mathbf{r}_\parallel \; e^{i(\mathbf{q}+\mathbf{G})\cdot\mathbf{r}_\parallel} f^2(\mathbf{r}_\parallel - \mathbf{R}_1 - \tau_\alpha) = e^{i(\mathbf{q}+\mathbf{G})\cdot(\mathbf{R}_1+\tau_\alpha)} \int \mathrm{d}\mathbf{r}_\parallel \; e^{i(\mathbf{q}+\mathbf{G})\cdot\mathbf{r}_\parallel} f^2(\mathbf{r}_\parallel) \tag{2.19}$$

we can write Eq.(2.17) as

$$\int \mathrm{d}\mathbf{r} \int \mathrm{d}\mathbf{r}' \; w(\mathbf{r} - \mathbf{R}_1 - \tau_\alpha)^2 W(\mathbf{r},\mathbf{r}') w(\mathbf{r}' - \mathbf{R}_3 - \tau_\gamma)^2 \approx \\ \frac{1}{4\pi^2} \sum_{\mathbf{q},\mathbf{G}} v_{2D}(\mathbf{q}+\mathbf{G}) \left|F(\mathbf{q}+\mathbf{G})\right|^2 I_d(\mathbf{q}+\mathbf{G}) \cdot e^{i(\mathbf{q}+\mathbf{G})\cdot(\mathbf{R}_1+\tau_\alpha)} e^{-i(\mathbf{q}+\mathbf{G})\cdot(\mathbf{R}_3+\tau_\gamma)} \tag{2.20}$$

with the function $F(\mathbf{q}+\mathbf{G})$ being the 2D Fourier transform of the square modulus of the function f, i.e.

$$F(\mathbf{q}+\mathbf{G}) = \int \mathrm{d}\mathbf{r}_\parallel \; |f(\mathbf{r}_\parallel)|^2 e^{i(\mathbf{q}+\mathbf{G})\cdot\mathbf{r}_\parallel} \tag{2.21}$$

and $v_{2D}(\mathbf{q}+\mathbf{G}) = \frac{2\pi}{|\mathbf{q}+\mathbf{G}|}$.

By substitution of Eq.(2.20) in Eq.(2.11) we obtain

$$K^d_{\mathbf{Q}}(vc\mathbf{k}; v'c'\mathbf{k}') \approx -\frac{1}{(2\pi N)^2} \sum_{\mathbf{q},\mathbf{G}} v_{2D}(\mathbf{q}+\mathbf{G}) \left|F(\mathbf{q}+\mathbf{G})\right|^2 I_d(\mathbf{q}+\mathbf{G}) \\ \sum_{\mathbf{R}_1,\mathbf{R}_3} \sum_{\alpha,\gamma} e^{i(\mathbf{k}'-\mathbf{k})\cdot\mathbf{R}_1} e^{i(\mathbf{k}-\mathbf{k}')\cdot\mathbf{R}_3} e^{i(\mathbf{q}+\mathbf{G})\cdot(\mathbf{R}_1+\tau_\alpha)} e^{-i(\mathbf{q}+\mathbf{G})\cdot(\mathbf{R}_3+\tau_\gamma)} \\ \cdot c^*_\alpha(c, \mathbf{k}+\mathbf{Q}) c_\alpha(c', \mathbf{k}'+\mathbf{Q}) c_\gamma(v\mathbf{k}) c^*_\gamma(v'\mathbf{k}') \tag{2.22}$$

To remove the summations over lattice vectors $\mathbf{R}_1$ and $\mathbf{R}_3$ in Eq.(2.22), we use the property

$$\sum_{\mathbf{R}_1} e^{i(\mathbf{k}'-\mathbf{k}+\mathbf{q}+\mathbf{G})\cdot\mathbf{R}_1} = \sum_{\mathbf{R}_1} e^{i(\mathbf{k}'-\mathbf{k}+\mathbf{q})\cdot\mathbf{R}_1} = N\delta(\mathbf{k}'-\mathbf{k}+\mathbf{q}-\mathbf{G}_0^{\mathbf{k},\mathbf{k}'}) \\ \sum_{\mathbf{R}_3} e^{i(\mathbf{k}-\mathbf{k}'-\mathbf{q}-\mathbf{G})\cdot\mathbf{R}_3} = \sum_{\mathbf{R}_3} e^{i(\mathbf{k}-\mathbf{k}'-\mathbf{q})\cdot\mathbf{R}_3} = N\delta(\mathbf{k}'-\mathbf{k}+\mathbf{q}-\mathbf{G}_0^{\mathbf{k},\mathbf{k}'})$$

where we also exploit $e^{i\mathbf{G}\cdot\mathbf{R}} = 1$ and $\mathbf{G}_0^{\mathbf{k},\mathbf{k}'}$ is a planar reciprocal lattice vector such that

$$\mathbf{q} = \mathbf{k} - \mathbf{k}' + \mathbf{G}_0^{\mathbf{k},\mathbf{k}'}$$

being $\mathbf{q}$,$\mathbf{k}$ and $\mathbf{k}'$ vectors of the BZ. Applying this relations to Eq.(2.22), we find

$$K^d_{\mathbf{Q}}(vc\mathbf{k}; v'c'\mathbf{k}') = -\frac{1}{4\pi^2} \sum_{\mathbf{G}} v_{2\mathrm{D}}(\mathbf{q}+\mathbf{G}) \left|F(\mathbf{q}+\mathbf{G})\right|^2 I_d(\mathbf{q}+\mathbf{G}) \cdot \\ \rho^*_{\mathbf{q}+\mathbf{G}}(c, \mathbf{k}+\mathbf{Q}; c', \mathbf{k}'+\mathbf{Q}) \; \rho_{\mathbf{q}+\mathbf{G}}(v\mathbf{k}; v'\mathbf{k}') \tag{2.23}$$

having introduced the auxiliary quantities

$$\rho_{\mathbf{p}+\mathbf{G}}(n\mathbf{k}; m\mathbf{k}') = \sum_{\alpha} e^{-i\boldsymbol{\tau}_\alpha\cdot(\mathbf{p}+\mathbf{G})} c_\alpha(n\mathbf{k})\, c^*_\alpha(m\mathbf{k}'), \tag{2.24}$$

where $\mathbf{p} = \mathbf{k} - \mathbf{k}'$, the index α runs over the MLWF in the unit cell, and $\boldsymbol{\tau}_\alpha$ identifies the position of the corresponding center.
Equation (2.23) is the expression which has been used in the following to obtain excitonic properties of strained C_3N. We now discuss how functions I_d and F have been evaluated in practice. We point out that the presented approach can be extended to other 2D systems, by properly adapting the following procedure to compute I_d and F to the MLWF of the system of interest.
Function I_d can be interpreted as an effective inverse dielectric function which screens the Coulomb interaction in a 2D system. It is a generalization of the treatment proposed by Latini *et al.* [57], with two main differences. Firstly, we assume an exponential decaying function to represent the WF behaviour along the z direction, instead of a box-like function; secondly, the triple integral over z,z_1 and z' appearing in the definition of I_d is carried out exactly, without introducing the averaging process used by Latini *et al.* to obtain an analytical expressions for the dielectric screening.
We start from the definition of $I_d(\mathbf{q}_1)$ (2.18), defining $\mathbf{q}_1 = \mathbf{q} + \mathbf{G}$ to make the notation more compact. The integrals over z' and z_1 are solved writing

$$\varepsilon^{-1}(\mathbf{q}_1; z, z_1) = \frac{1}{L} \sum_{G_z, G'_z} e^{iG_z\cdot z} e^{-iG'_z\cdot z_1} \varepsilon^{-1}(\mathbf{q}_1; G_z, G'_z) \tag{2.25}$$

where $\varepsilon^{-1}(\mathbf{q}_1; G_z, G'_z)$ is the *ab initio* inverse static dielectric function in reciprocal space, while L is the size of the supercell along the z direction used in first-principles calculations.
Therefore we have

$$\int_{-\frac{L}{2}}^{\frac{L}{2}} \mathrm{d}z' \int_{-\frac{L}{2}}^{\frac{L}{2}} \mathrm{d}z_1\, \varepsilon^{-1}(\mathbf{q}_1; z, z_1) e^{-|\mathbf{q}_1|\cdot|z_1 - z'|} |h(z')|^2 = \sum_{G_z, G'_z} \varepsilon^{-1}(\mathbf{q}_1; G_z, G'_z) \mathbf{T}(\mathbf{q}_1, G'_z) e^{iG_z\cdot z} \tag{2.26}$$

defining

$$\mathbf{T}(\mathbf{q}_1, G'_z) = \frac{1}{L} \int_{-\frac{L}{2}}^{\frac{L}{2}} \mathrm{d}z' \int_{-\frac{L}{2}}^{\frac{L}{2}} \mathrm{d}z_1\; e^{-iG'_z\cdot z_1} e^{-|\mathbf{q}_1|\cdot|z_1 - z'|} |h(z')|^2 \tag{2.27}$$

The function $\mathbf{T}$ can be expressed in terms of the quantity $\mathbf{H}$ given by

$$\mathbf{H}(K) = \int_0^{\frac{L}{2}} \mathrm{d}z\; e^{Kz} |h(z)|^2 \tag{2.28}$$

where K is a general complex number. Using as $h(z)$ the expression given in Eq.(2.16), it is possible to obtain an analytical solution of $\mathbf{H}(K)$. As the

result of this analytical integration is cumbersome (even if the procedure to obtain it is straightforward), we omit the result of this analytical integration. Using the values of $\mathbf{H}$ we can compute $\mathbf{T}$ as

$$\begin{aligned}\mathbf{T}(\mathbf{q}_1, G'_z) = \frac{1}{L}\Bigg\{ & \frac{1}{|\mathbf{q}_1| - iG'_z}\left[\mathbf{H}(iG'_z) - e^{-\frac{L}{2}(|\mathbf{q}_1|-iG'_z)}\mathbf{H}(|\mathbf{q}_1|)\right] - \frac{1}{|\mathbf{q}_1| + iG'_z}\left[\mathbf{H}(-|\mathbf{q}_1|) - \mathbf{H}(iG'_z)\right] \\ & - \frac{1}{|\mathbf{q}_1| + iG'_z}\mathbf{H}(-|\mathbf{q}_1|)\left[e^{-\frac{L}{2}(|\mathbf{q}_1|+iG'_z)} - 1\right] \\ & - \frac{1}{|\mathbf{q}_1| - iG'_z}\mathbf{H}(-|\mathbf{q}_1|)\left[e^{-\frac{L}{2}(|\mathbf{q}_1|-iG'_z)} - 1\right] \\ & + \frac{1}{|\mathbf{q}_1 + iG'_z|}\left[\mathbf{H}(-iG'_z) - e^{-\frac{L}{2}(|\mathbf{q}_1|+iG'_z)}\mathbf{H}(|\mathbf{q}_1|)\right] - \frac{1}{|\mathbf{q}_1| - iG'_z}\left[\mathbf{H}(-|\mathbf{q}_1|) - \mathbf{H}(-iG'_z)\right]\Bigg\}\end{aligned} \tag{2.29}$$

therefore the function $I_d(\mathbf{q}_1)$ can be written starting from Eq.(2.18) and using Eq.(2.26) as

$$I_d(\mathbf{q}_1) = \sum_{G_z, G'_z} \varepsilon^{-1}(\mathbf{q}_1; G_z, G'_z)\mathbf{T}(\mathbf{q}_1, G'_z) \int_{-\frac{L}{2}}^{\frac{L}{2}} \mathrm{d}z \; e^{iG_z \cdot z}|h(z)|^2 \tag{2.30}$$

where the integral over z can be expressed as

$$\int_{-\frac{L}{2}}^{\frac{L}{2}} \mathrm{d}z \; e^{iG_z \cdot z}|h(z)|^2 = \mathbf{H}(-iG_z) + \mathbf{H}(iG_z)$$

using Eq.(2.16) for $h(z)$.
To compute in practice, I_d we have carried out the following steps:

- we have computed the static dielectric function in RPA approximation using the `Yambo` code in the case of pristine C_3N. This calculation has been done starting from Kohn-Sham wavefunctions computed on a Monkhorst-Pack grid 48x48x1 and including 300 states in the sum over bands defining ε^{-1}; further, $\varepsilon^{-1}(\mathbf{q}+\mathbf{G}, \mathbf{q}+\mathbf{G}')$ has been computed for $[\mathbf{G}, \mathbf{G}']$ with modulus smaller or equal to 22 Ry. We also notice that, to avoid spurious interactions between periodically repeated layers, we have used a cutoff for the Coulomb potential(in the calculations we have considered $L = 18.0$ Angstrom);

- using Python post-processing scripts, we have extracted from the `Yambo` databases the quantity $\varepsilon^{-1}(\mathbf{q}_1; G_z, G'_z)$, for all the available pairs (G_z, G'_z) at fixed in plane vector $\mathbf{q}_1 = \mathbf{q} + \mathbf{G}$;

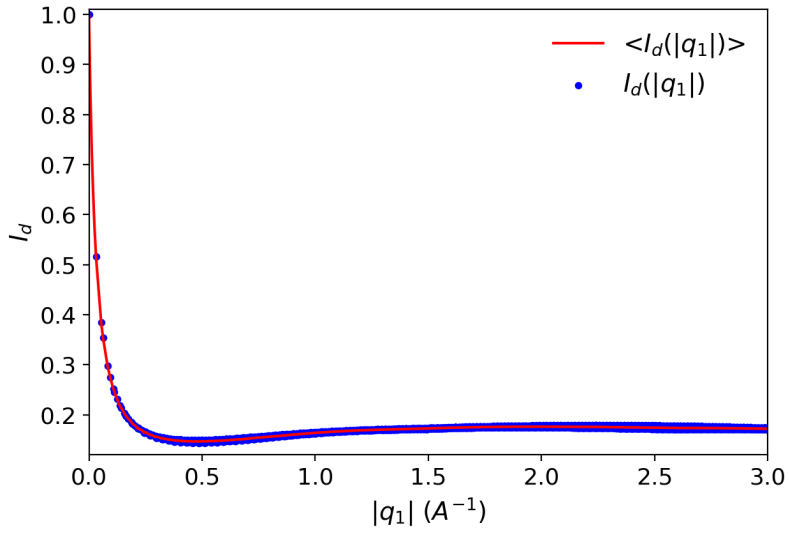

Figure 2.4: Function $I_d(\mathbf{q}_1)$ obtained by post-processing of ab initio RPA calculation of the static dielectric screening in unstrained ML-C_3N. The blue dots are the quantities obtained directly from the ab initio results; the red line represent the data obtained after averaging the value of $I_d(\mathbf{q}_1)$ which are close in modulus but have different directions.

- for each $\mathbf{q}_1 = \mathbf{q} + \mathbf{G}$ we firstly compute the function $\mathbf{T}$ using Eq. (2.29), then we have combined this quantity with $\varepsilon^{-1}(\mathbf{q}_1; G_z, G'_z)$ to finally evaluate $I_d(\mathbf{q}_1)$ through Eq. (2.30), summing over all the possible pairs (G_z, G'_z).

In Fig. 2.4, we present (as blue dots) the function $I_d(\mathbf{q}_1)$ obtained with the procedure just discussed from the *ab initio* data: we notice that with the used q grid of 48x48x1, the behaviour of $I_d(\mathbf{q}_1)$ at small $\mathbf{q}_1$ is not accessible. As this function corresponds to an effective inverse dielectric function for a 2D material, we have extrapolated its behaviour at small-$\mathbf{q}$ using the analytical expression proposed by Cudazzo *et al.* [71]

$$I_d(\mathbf{q}_1 \to 0) = \frac{1}{1 + \alpha_{2D}|\mathbf{q}|}$$

where the value of α_{2D} has been chosen to match the value of $I_d(\mathbf{q}_1)$ computed *ab initio* for the smallest non zero $\mathbf{q}$. To make the calculations easier, we have considered $I_d(\mathbf{q}_1)$ as an average over the direction of the $\mathbf{q}_1$ vector: in practice, as $I_d(\mathbf{q}_1)$ turns out to be mainly dependent on $|\mathbf{q}_1|$ while it is almost constant with respect to the direction of $\mathbf{q}_1$, we have performed the approximation

$$I_d(\mathbf{q}_1) \approx \langle I_d(|\mathbf{q}_1|) \rangle$$

where we have computed $\langle I_d(|\mathbf{q}_1|) \rangle$ taking the average of $I_d(\mathbf{q}_1)$ evaluated for $\mathbf{q}_1$ points which are close in modulus but with different directions. The result

of this averaging procedure is shown as the red continuous line in Fig. 2.4. With this treatment, I_d has become a one-variable function, known on the grid used in the RPA calculation. As the solution of BSE requires much denser grids, we have extrapolated I_d on the 121x121x1 grid used in the main text by simple linear spline interpolation of the results shown in Fig. 2.4. This approach makes sense because of the smoothness of $\langle I_d(|\mathbf{q}_1|)\rangle$ as a function of $|\mathbf{q}_1|$. In the following we will assume as negligible the effect of small strains on the electronic screening: therefore we have used the I_d function computed for the unstrained monolayer for all the low-strain configurations considered in this work.
To complete the calculation of the direct kernel according to Eq.(2.23), we have evaluated functions F by substitution of Eq.(2.15) in Eq.(2.21). By simple algebraic manipulation we find

$$F(\mathbf{q}_1) = F(|\mathbf{q}_1|) = \frac{8}{9}B^2 \int_0^{+\infty} \mathrm{d}r_\parallel \; r_\parallel J_0(|\mathbf{q}_1| r_\parallel) \left[e^{-Br_\parallel}(1 + Br_\parallel) \right]^2 \tag{2.31}$$

where $r_\parallel = |\mathbf{r}_\parallel|$ and J_0 is a Bessel function of the first kind with $n = 0$. Notice that F depends on $|\mathbf{q}_1|$ as a consequence of the cylindrical symmetry of the function f. This 1D integral has been evaluated numerically for the required momenta $|\mathbf{q}_1|$. Furthermore, B, which is related to the spread of the MLWF, is chosen equal to an average of the values obtained from the spreads of the $2p_z$-like orbitals localized on carbon and nitrogen atoms.

Exchange part of the BSE kernel

We now derive the expression of the exchange kernel $K^x_{\mathbf{Q}}$, similarly to what has been done in the precedent section for $K^d_{\mathbf{Q}}$. We start from the definition

$$K^x_{\mathbf{Q}}(vc\mathbf{k}; v'c'\mathbf{k}') = 2 \int \mathrm{d}\mathbf{r} \int \mathrm{d}\mathbf{r}' \; \psi^*_{c,\mathbf{k}+\mathbf{Q}}(\mathbf{r}) \psi_{v\mathbf{k}}(\mathbf{r}) v(\mathbf{r} - \mathbf{r}') \psi_{c',\mathbf{k}'+\mathbf{Q}}(\mathbf{r}') \psi^*_{v'\mathbf{k}'}(\mathbf{r}') \tag{2.32}$$

with the factor 2 in Eq.(2.32) indicating that we are only considering singlet excitons. As in the case of the direct kernel, we write Bloch states for the valence and conduction bands using Eq.(2.7) and we again assume valid the hypothesis of negligible overlap between MLWF localized on different atomic sites (see Eq.(2.9) and Eq.(2.10)). Using these results in Eq.(2.32) we find

$$\begin{aligned} K^x_{\mathbf{Q}}(vc\mathbf{k}; v'c'\mathbf{k}') \approx \frac{2}{N^2} \sum_{\mathbf{R}_1,\mathbf{R}_3} \sum_{\alpha,\gamma} e^{-i\mathbf{Q}\cdot\mathbf{R}_1} e^{i\mathbf{Q}\cdot\mathbf{R}_3} c^*_\alpha(c, \mathbf{k}+\mathbf{Q}) c_\alpha(v\mathbf{k}) c_\gamma(c', \mathbf{k}'+\mathbf{Q}) c^*_\gamma(v'\mathbf{k}') \\ \cdot \int \mathrm{d}\mathbf{r} \int \mathrm{d}\mathbf{r}' \; w(\mathbf{r} - \mathbf{R}_1 - \tau_\alpha)^2 v(\mathbf{r} - \mathbf{r}') w(\mathbf{r}' - \mathbf{R}_3 - \tau_\gamma)^2 \end{aligned} \tag{2.33}$$

To solve the integrals over $\mathbf{r}$ and $\mathbf{r}'$, we introduce the cylindrical approximation for the MLWF as done for the direct kernel and we write the bare Coulomb

interaction in terms of its 2D Fourier transform v_{2D}, i.e.

$$v(\mathbf{r}-\mathbf{r}') = \frac{1}{4\pi^2}\sum_{\mathbf{q},\mathbf{G}} v_{2D}(\mathbf{q}+\mathbf{G}) e^{-|\mathbf{q}+\mathbf{G}|\cdot|z-z'|} e^{i(\mathbf{q}+\mathbf{G})\cdot(\mathbf{r}_\parallel-\mathbf{r}'_\parallel)} \tag{2.34}$$

With these approximations it is possible to write the double integral over $\mathbf{r}$ and $\mathbf{r}'$ as

$$\int \mathrm{d}\mathbf{r} \int \mathrm{d}\mathbf{r}'\; w(\mathbf{r}-\mathbf{R}_1-\tau_\alpha)^2 v(\mathbf{r}-\mathbf{r}') w(\mathbf{r}'-\mathbf{R}_3-\tau_\gamma)^2 \approx \frac{1}{4\pi^2}\sum_{\mathbf{q},\mathbf{G}} v_{2D}(\mathbf{q}+\mathbf{G})\big|F(\mathbf{q}+\mathbf{G})\big|^2 X_{ex}(\mathbf{q}+\mathbf{G}) e^{i(\mathbf{q}+\mathbf{G})\cdot(\mathbf{R}_1+\tau_\alpha)} e^{-i(\mathbf{q}+\mathbf{G})\cdot(\mathbf{R}_3+\tau_\gamma)} \tag{2.35}$$

being $X_{ex}(\mathbf{q}+\mathbf{G})$ defined as

$$X_{ex}(\mathbf{Q}+\mathbf{G}) = \int \mathrm{d}z\, \mathrm{d}z'\; e^{-|\mathbf{Q}+\mathbf{G}|\cdot|z-z'|} |h(z)|^2\, |h(z')|^2 \tag{2.36}$$

After inserting Eq.(2.35) in Eq.(2.33) we remove the summations over $\mathbf{R}_1$ and $\mathbf{R}_3$ using

$$\sum_{\mathbf{R}_3} e^{i\mathbf{R}_1\cdot(-\mathbf{q}-\mathbf{G}+\mathbf{Q})} = N\delta_{\mathbf{q},\mathbf{Q}} \tag{2.37}$$

to finally obtain the expression used within our approach for the exchange kernel, given by

$$\begin{aligned} K^x_{\mathbf{Q}}(vc\mathbf{k}; v'c'\mathbf{k}') = &\frac{2}{4\pi^2}\sum_{\mathbf{G}} v_{2\mathrm{D}}(\mathbf{q}+\mathbf{G})\big|F(\mathbf{Q}+\mathbf{G})\big|^2 X_{ex}(\mathbf{Q}+\mathbf{G})\cdot \\ &\rho^*_{\mathbf{Q}+\mathbf{G}}(c,\mathbf{k}+\mathbf{Q}; v\mathbf{k})\; \rho_{\mathbf{Q}+\mathbf{G}}(c',\mathbf{k}'+\mathbf{Q}; v'\mathbf{k}'), \end{aligned} \tag{2.38}$$

ρ being defined as in Eq.(2.24). We notice that the $\mathbf{G}=0$ term in the exchange kernel is included in all the calculations shown in the following.
The function $X_{ex}(\mathbf{Q}+\mathbf{G})$ has been computed by performing numerically the double integration over z and z' appearing in Eq.(2.36) for fixed $\mathbf{Q}$ and for all the $\mathbf{G}$ vectors included in the summation appearing in Eq.(2.38). The result of this integration is shown in Fig. 2.5.
We complete this section noting that the computational advantage of our method is two-fold: first, the use of a TB model for single particle states permits an accurate mapping of single particle states and energies on small matrices, with dimension equal to the number of used Wannier Functions, from which electronic states and energies can be obtained by simple diagonalizations at all $\mathbf{k}$-points in the BZ. Second, modeling the dielectric screening through the function I_d permits to obtain electron-electron interaction on very fine grids, without explicit calculations for all scattering $\mathbf{q}$-vectors.

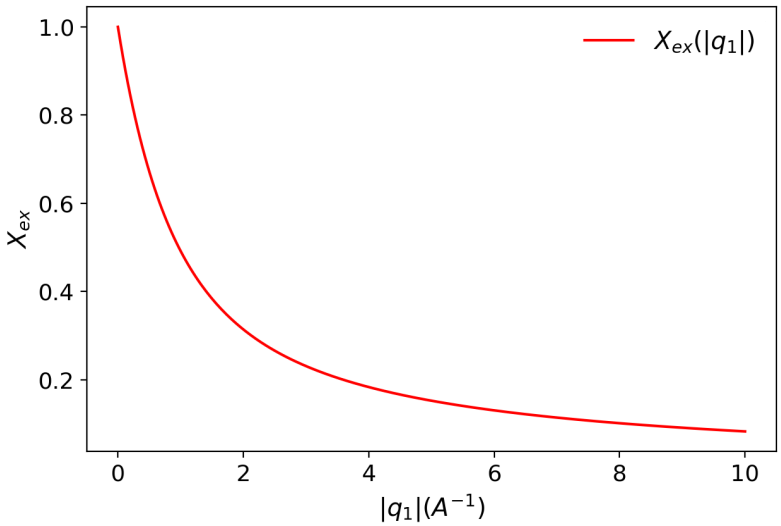

Figure 2.5: Function $X_{ex}(|\mathbf{q}_1|)$ obtained by numerical integration of Eq. (2.36), using as h the functions given by Eq.(2.16)

2.2 Model validation

We now test the validity of the approximations discussed in the preceding Section, by comparing the *ab initio* results recently obtained [45] for $\mathbf{Q} = 0$ excitons in unstrained ML-C_3N ,with those obtained by the TB-BSE approach here presented. In Fig. 2.6 we show the absorption spectrum computed with and without the electron-hole interaction in the BSE kernel (continuous blue line and dashed red line, respectively) together with fully *ab initio* BSE results of Ref.[45] shown as a dotted green line. In agreement with previous results [45, 44], we find an optical spectrum dominated by a single intense peak which corresponds to a pair of degenerate excitons, $e_{4,5}$, exhibiting a large binding energy, of about 0.6 eV. These excitons are mainly due to valence-conduction transitions located along the ΓM directions, as visualized by considering the **k**-resolved contributions to the exciton wavefunctions:

$$A(\mathbf{k}) = \sum_{vc} \sum_{\lambda} \left| A_\lambda(v\mathbf{k}; c\mathbf{k}) \right|^2, \tag{2.39}$$

where the summation over the exciton index λ is present only for degenerate excitons and $A_\lambda(v\mathbf{k}; c\mathbf{k})$ is the exciton envelope function discussed in Chapter 1. These functions are shown for the lowest resonances in the insets of Fig. 2.6. A second structure at an higher energy of 2.219 eV appears in the optical spectrum, due to a pair of degenerate excitons $e_{14,15}$. This structure is also present in the *ab initio* absorption spectrum, at a slightly smaller energy (2.18 eV). This exciton pair will not be further discussed in the following. At energies below the $e_{4,5}$ intense peak, we also find three dark excitations, i.e. a pair of degenerate excitons $e_{1,2}$ and a single resonance e_3.

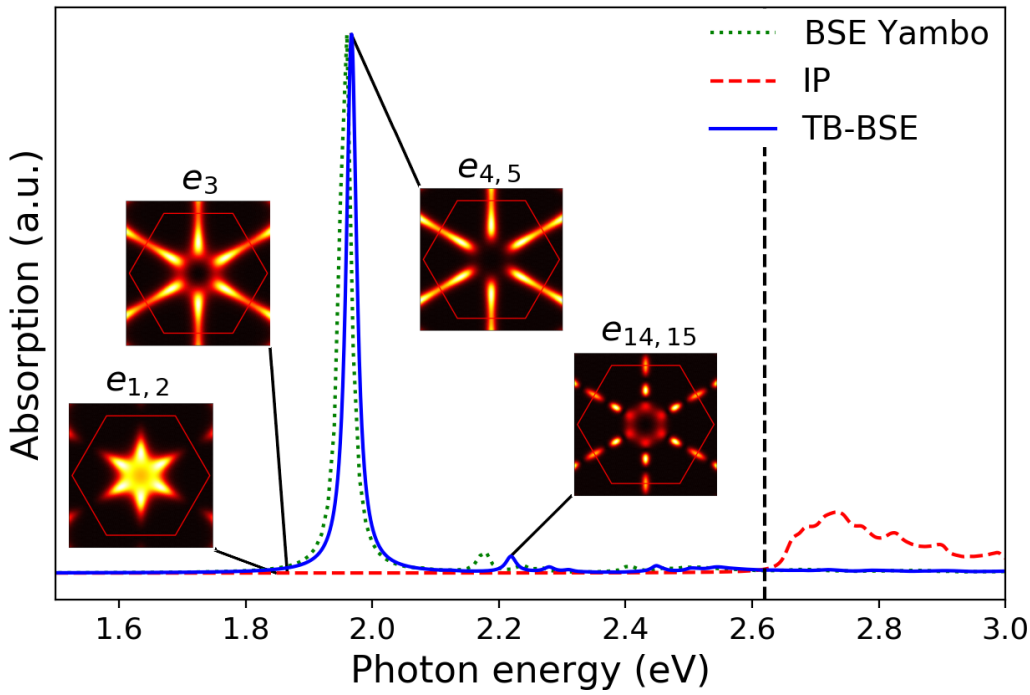

Figure 2.6: Absorption spectrum of monolayer C_3N computed with the model described in Sec. 2.1. The continuous blue line (dashed red line) represents the spectrum computed with (without, independent particle IP) the electron-hole interaction in the BSE kernel.The green dotted line is the fully *ab initio* BSE spectrum obtained in Ref.[45], while the vertical dashed black line indicates the position of the quasi-particle direct band gap corresponding to the onset of independent particle (IP) absorption. These spectra were computed assuming light polarization along the zig-zag direction, and analogous results were found for different polarizations. **k**-resolved contributions to the exciton wavefunctions are shown for the first five lowest energy excitons, and for the resonances responsible for the higher energy absorption peak at about 2.2 eV. All the spectra have been convoluted with a Lorentzian broadening of 10 meV. The labels e_i indicate the excitation energies in ascending order.

To quantify more precisely the comparison between the model and the *ab initio* results, in Tab. 2.1 we collect the excitation energies of the first five excitons in monolayer C_3N computed with *ab initio* methods and with the TB-BSE approach. We note that the model reproduces with high accuracy first principles results, with a small blue shift of exciton energies, which is anyhow smaller than 40 meV. Having validated the TB-BSE model, we now turn our attention to the effect of mechanical strain on these five lowest excitonic resonances, dividing them according to their optical activity in the unstrained monolayer.

Method	$e_{1,2}$	e_3	$e_{4,5}$
Ab initio BSE [45]	1.821	1.854	1.957
Model TB-BSE	1.848	1.866	1.967

Table 2.1: Comparison between ab initio BSE and TB-BSE excitation energies of the first five lowest excitons.

2.3 Effect of strain on bright excitons

We now consider in detail the effect of uniaxial strain on the pair of bright excitons $e_{4,5}$, responsible for the intense absorption peak in pristine C_3N. In Figure 2.7 we plot the absorption spectra for zig-zag (panel a) and armchair (panel b) strains, with strengths in the range 0–3.5 %. We consider the polarization along both the zig-zag (continuous red lines) and armchair (dashed blue lines) directions. We point out that, within our choice of the reference system, the zig-zag direction X coincides with the cartesian direction x while the armchair axis Y corresponds to the direction y in the monolayer plane (see Fig. 2.1).
The effect of strain is two-fold: first, the double degeneracy observed in pristine C_3N is removed, with the appearance of two excitations whose splitting increases linearly with strain, at a rate of about 6.0 $\frac{\text{meV}}{\%}$ for both strain directions. Second, these two resonances exhibit a strong optical anisotropy: in the case of zig-zag strain the lowest energy exciton (here called e_4) is bright for light polarization along x, while it is dark if the incoming electric field is oriented along the y direction. Differently, the highest energy exciton e_5 can only absorb photons with polarization along the armchair direction. This strain-induced optical anisotropy, also proposed in Ref.[72] within a single particle description of C_3N optical properties, is therefore also present once excitonic effects are included.
The situation is exactly the opposite in the case of armchair strain, where e_4 (e_5) becomes dark for incoming light polarization along the zig-zag (armchair) direction. The observed strain-induced optical anisotropy is further highlighted by computing the oscillator strengths D_4 and D_5 as a function of the polarization angle with respect to the zig-zag direction. This is shown in Fig. 2.8, where we consider a strain of 2.0 % for both cases. We see that with zig-zag strain these two excitons have an oscillator strength (OS) characterized by a two-lobed angular pattern, with e_4 having a nodal line along the y direction and e_5 along the x direction. Analogously, in the case of armchair strain the OS patterns have similar features, but the profiles for the two split excitons are exchanged. We remark that the observed optical anisotropy does not depend on the value of the applied strain, as, also for larger strains, the nodal lines at which the OS becomes zero are always present. To properly characterize the excitons e_4 and e_5 we computed the corresponding transition distribution functions $A(\mathbf{k})$, as defined in Eq.(2.39). These are shown in

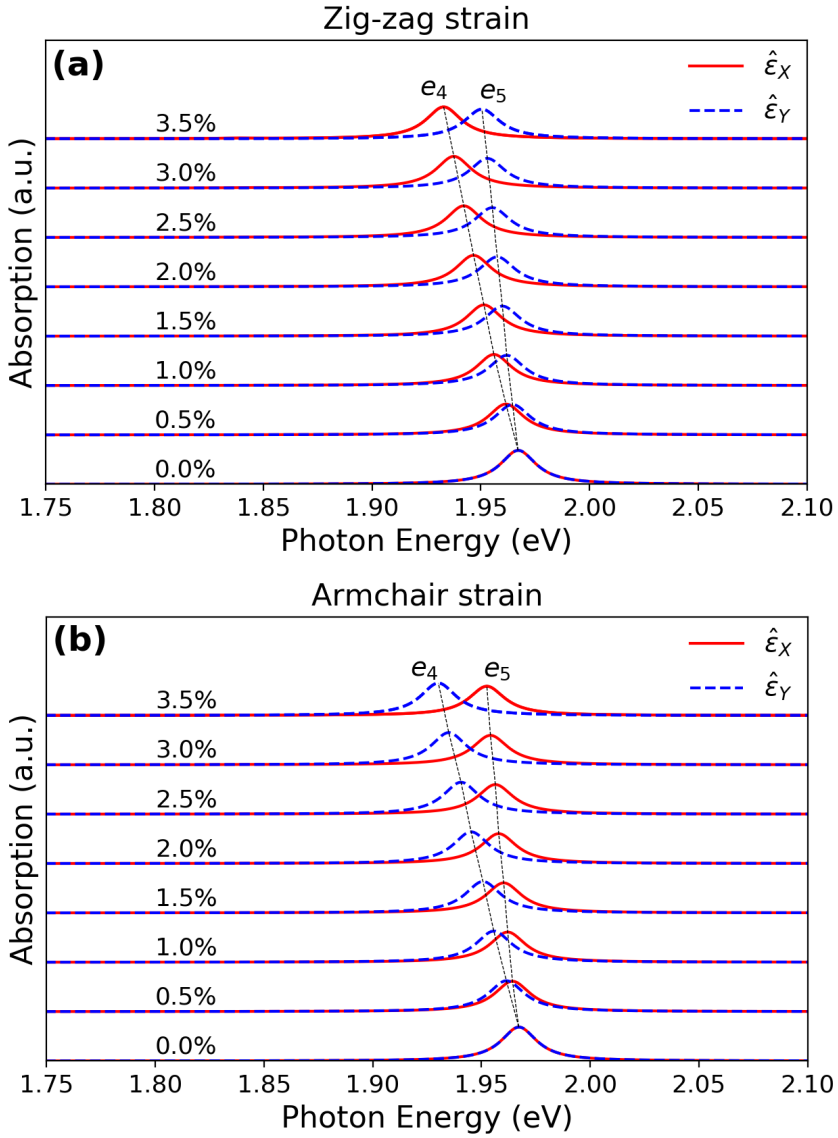

Figure 2.7: (a) Absorption spectra of ML-C_3N under uniaxial strain along the zig-zag direction: continuous red lines correspond to light polarized along the zig-zag (X) direction, while dashed blue lines to light polarized along the armchair (Y) direction. Spectra for different values of applied strain are rigidly shifted vertically to make the plot more readable. The black dashed lines highlight the splitting of the two-fold degenerate exciton $e_{4,5}$ in pristine C_3N into two separate excitons, here called e_4 and e_5. All the spectra are convoluted with a Lorentzian broadening of 10 meV. (b) Same as (a), for externally applied strain along the armchair direction.

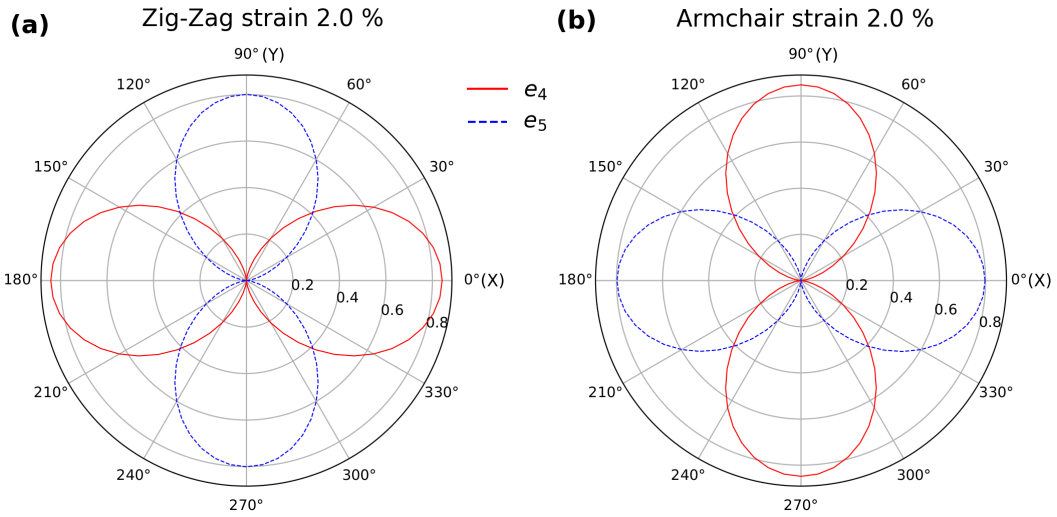

Figure 2.8: Polar plot of the oscillator strenghts D_λ defined in Eq. 1.79 for excitons e_4 and e_5, in the case of zig-zag strain (a) and armchair strain (b) of 2.0 %, as a function of the in-plane light polarization direction, measured starting from the zig-zag (X) axis. Concentric lines represent isovalues for the modulus of the exciton oscillator strength $|D_\lambda|$.

Fig. 2.9 in the case of a 2.0 % strain along both the zig-zag and armchair directions (we checked that the following considerations are valid independently of the value of the applied strain within the considered range). In the case of zig-zag strain, the exciton e_4 is mainly due to transitions along the ΓM direction, while e_5 is characterized by a wavefunction $A(\mathbf{k})$ peaked for $\mathbf{k}$ along ΓM$'$ direction. On the other hand, in the case of armchair strain, the function $A(\mathbf{k})$ for the lowest energy exciton e_4 is non-zero along ΓM$'$, while for e_5 is mainly localized along the ΓM direction. The reason why in zig-zag strained ML-C_3N the lowest exciton is mainly confined along ΓM, while in the case of armchair strain it becomes localized along ΓM$'$, can be understood by considering the effect of strain on the electronic band structure. In Fig. 2.10 we present the electronic bands computed at the DFT-PBE level for zig-zag (a) and armchair (b) strain, both equal to 2.0 %, compared to pristine C_3N, represented by solid black lines. Considering the DFT bands, we see that one of the main effects of uniaxial strain (in both directions) is to induce different electronic band dispersions along the ΓM and the ΓM$'$ directions, otherwise equivalent by symmetry in the pristine case. The connection with the excitonic transition distribution becomes clearer by looking at Fig. 2.10(c-d) where we report the difference $\epsilon_c(\mathbf{k}) - \epsilon_v(\mathbf{k})$ for the last occupied valence band v and the first unoccupied conduction band c along the path M-Γ-M$'$ in the BZ. We see that in zig-zag strained C_3N the lowest transition energies $\epsilon_c(\mathbf{k}) - \epsilon_v(\mathbf{k})$ occur along ΓM. Therefore, the exciton involving transitions along this direction (i.e. e_4) has a smaller excitation energy than the exciton e_5, mainly composed by sin-

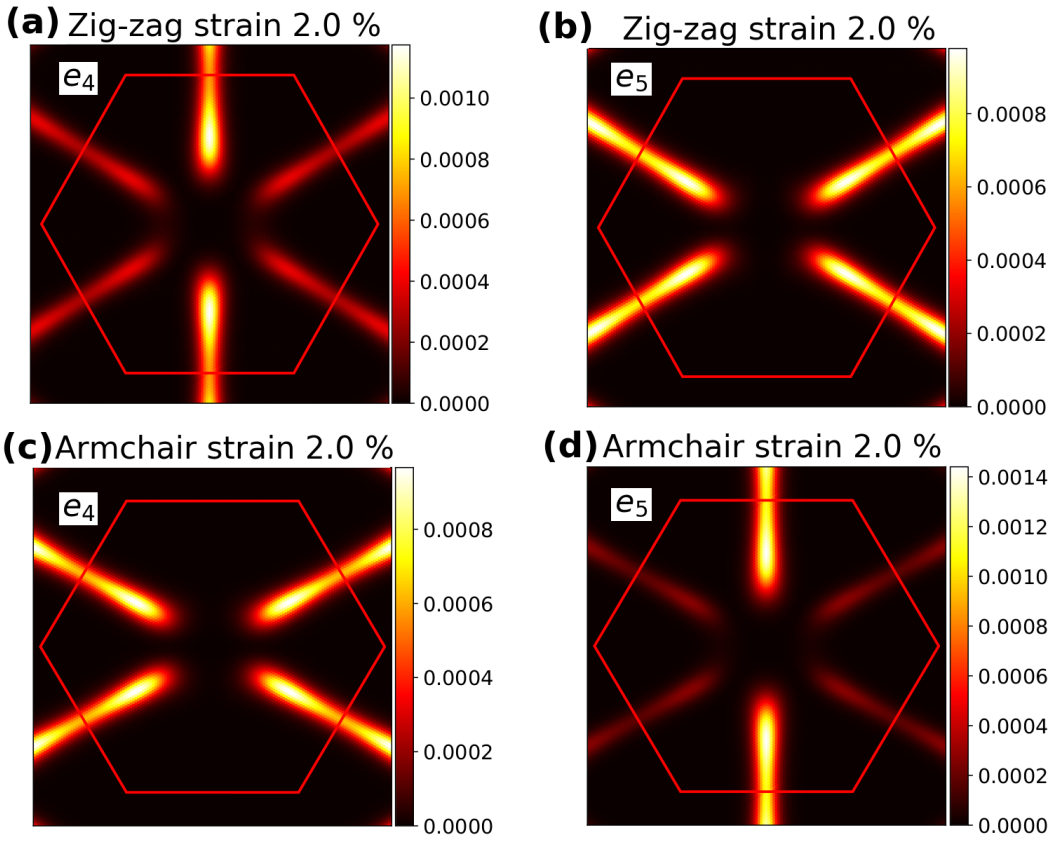

Figure 2.9: Functions $A(\mathbf{k})$ defined in Eq.2.39, computed for exciton e_4 (a) and e_5 (b) in the case of zig-zag strain of 2.0 %. (c) and (d) correspond to the same quantities shown in (a) and (b), but evaluated for ML-C_3N strained along the armchair direction.

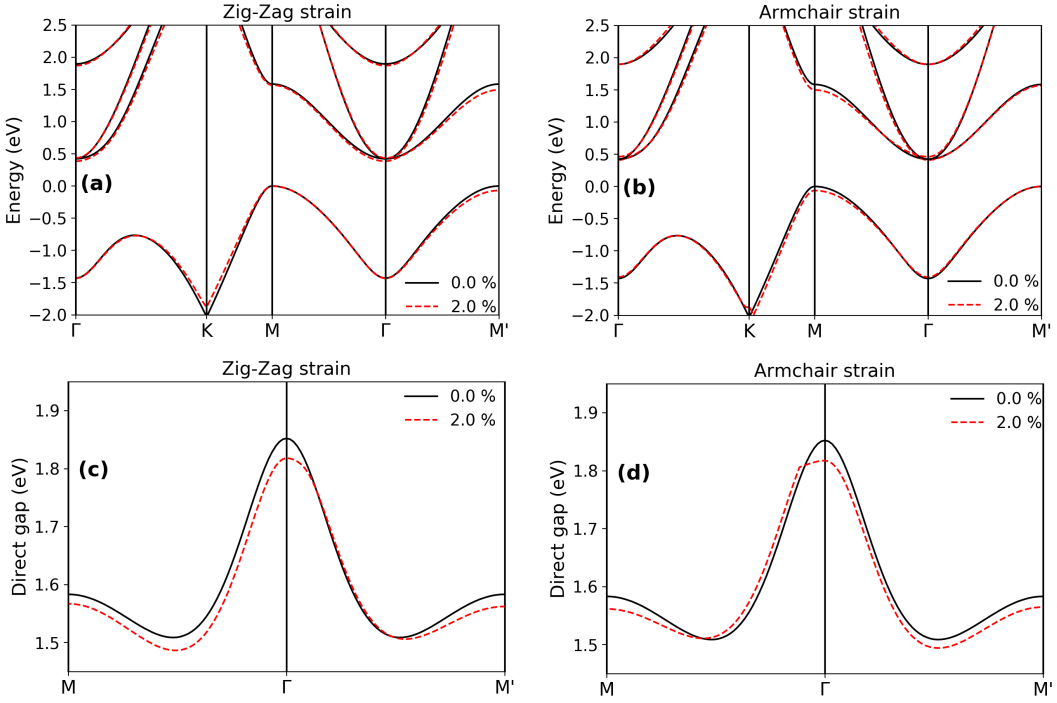

Figure 2.10: (a) DFT-PBE band structure of ML-C_3N in the pristine case (solid black lines) and with a zig-zag strain of 2.0 % (dashed red lines); (b) same as (a), but for a 2.0 % strain along the armchair direction. (c) Energy difference $\epsilon_c(\mathbf{k}) - \epsilon_v(\mathbf{k})$ between the lowest unoccupied conduction c and the highest occupied valence v for $\mathbf{k}$ along the path M-Γ-M' for the unstrained case and for a 2.0 % zig-zag strain; (d) same as (c) for an armchair strain.

gle particle transitions along ΓM′. Analogously, by looking at Fig. 2.10(d), we can see that for armchair strain the minimum of $\epsilon_c(\mathbf{k}) - \epsilon_v(\mathbf{k})$ falls along ΓM′ so that we effectively expect the lowest energy exciton to be mainly composed by transitions along this direction. We point out that the relative energy differences among the directions ΓM and ΓM' could be affected by the addition of quasiparticle effects, but the dispersions along the two directions are expected to remain different as a result of the symmetry breaking effect of applied uniaxial strain. Furthermore, this strain induced change of the electronic bands along ΓM and ΓM' directions can also explain the observed increasing of the splitting among excitons e_4 and e_5 as a function of strain. Considering the case of zig-zag strain, by increasing strain we observe that the difference between the minima of $\epsilon_c(\mathbf{k}) - \epsilon_v(\mathbf{k})$ computed for $\mathbf{k}$ along ΓM and ΓM' progressively increases: as the exciton e_4 is mainly composed by $v - c$ transitions along ΓM while e_5 is localized along ΓM' their energy splitting will increase as a consequence of the increased energy-splitting among the single particle states involved in the two excitons. Similar reasoning can be done in case of armchair strain.

2.3.1 Symmetry analysis of bright excitons

Having described how the main absorption peak in pristine C_3N is modified by the application of strain, we now classify the two resulting excitons e_4 and e_5 in terms of their symmetry properties, starting from the symmetry characterization of excitons in pristine C_3N and then focusing our attention on the strained monolayer. The point group of pristine C_3N is D_{6h}, which contains the in-plane symmetries of a hexagon combined with the mirror symmetry operation σ_h w.r.t. the monolayer plane. Within our approach, we describe the electronic properties (and therefore the excitonic ones) of the system with an effective tight binding model, which is purely planar. Therefore, analogously to the work of Galvani *et al.* [73], in the following we classify excitons considering only the in-plane symmetry operations contained in the point group D_{6h}, which form the subgroup C_{6v}. Once strain is applied to ML-C_3N, the symmetry of the system is lowered and the full point group becomes D_{2h}. Following the reasoning just outlined, we will then classify excitons according to the irreducible representations of the subgroup C_{2v}, only composed by in-plane symmetries.
We start by discussing the degenerate excitons $e_{4,5}$ of pristine C_3N. In order to understand which is the irreducible representation of C_{6v} which transforms as these excitons, for each symmetry operator $\hat{S}$ representing a class of C_{6v} we have computed the character:

$$\chi[\hat{S}] = \sum_{\lambda=\{e_{4,5}\}} \langle\lambda|\hat{S}|\lambda\rangle, \tag{2.40}$$

where the sum over λ runs on the two degenerate excitons $e_{4,5}$. This quantity is the trace of the symmetry operator $\hat{S}$ on the 2D space spanned by these excitons.
We now describe a general approach by which these traces can be computed, starting from the envelope functions obtained from our TB-BSE model.
Starting from Eq.(2.40), an exciton λ is assigned to the irreducible representation Γ if, given a symmetry operation $\hat{S}$ of each class C of the group, we have that

$$\chi_C = \sum_\lambda \chi_S^\lambda = \sum_\lambda \int \mathrm{d}\mathbf{r}_e \mathrm{d}\mathbf{r}_h \, \Psi_\lambda^*(\mathbf{r}_e, \mathbf{r}_h) \hat{S} \Psi_\lambda(\mathbf{r}_e, \mathbf{r}_h) \tag{2.41}$$

is equal to the character of class C for the irreducible representation Γ. In Eq. (2.41) the summation over λ is present only when we consider a manifold of degenerate excitons.
We now discuss how to compute the quantity χ_S^λ for a single exciton λ, also assuming that $\hat{S}$ is a planar symmetry operator, which leaves unchanged the out-of-plane variable z. We start by writing the exciton wavefunction $\Psi_\lambda(\mathbf{r}_e, \mathbf{r}_h)$ in real space as

$$\Psi_\lambda(\mathbf{r}_e, \mathbf{r}_h) = \sum_{vc\mathbf{k}} A_\lambda(v\mathbf{k}; c\mathbf{k}) \, \psi_{v\mathbf{k}}^*(\mathbf{r}_h) \psi_{c\mathbf{k}}(\mathbf{r}_e). \tag{2.42}$$

By defining

$$\psi_{\alpha\mathbf{k}}^W(\mathbf{r}) = \frac{1}{\sqrt{N}} \sum_{\mathbf{R}} e^{i\mathbf{k}\cdot\mathbf{R}} w(\mathbf{r} - \tau_\alpha - \mathbf{R}), \tag{2.43}$$

and writing the conduction and valence states c and v involved in the BSE in terms of the tight-binding coefficients $c_\alpha(n\mathbf{k})$, we can compactly write $\Psi_\lambda(\mathbf{r}_e, \mathbf{r}_h)$ as

$$\Psi_\lambda(\mathbf{r}_e, \mathbf{r}_h) = \sum_{\alpha\beta\mathbf{k}} \bar{A}_\lambda(\alpha\mathbf{k}; \beta\mathbf{k}) \, \psi_{\alpha\mathbf{k}}^{W*}(\mathbf{r}_h) \psi_{\beta\mathbf{k}}^W(\mathbf{r}_e), \tag{2.44}$$

where we have defined

$$\bar{A}_\lambda(\alpha\mathbf{k}; \beta\mathbf{k}) = \sum_{vc} A_\lambda(v\mathbf{k}; c\mathbf{k}) \, c_\alpha^*(v\mathbf{k}) c_\beta(c\mathbf{k}). \tag{2.45}$$

The action of the symmetry operator $\hat{S}$ on a general $\mathbf{r}$-dependent function g is $\hat{S}g(\mathbf{r}) = g(\hat{S}^{-1}\mathbf{r})$, so, by straightforward generalization to two-variable functions, we have

$$\hat{S}\Psi_\lambda(\mathbf{r}_e, \mathbf{r}_h) = \Psi_\lambda(\hat{S}^{-1}\mathbf{r}_e, \hat{S}^{-1}\mathbf{r}_h)$$

and then χ_S^λ becomes

$$\chi_S^\lambda = \int \mathrm{d}\mathbf{r}_e \mathrm{d}\mathbf{r}_h \, \Psi_\lambda^*(\mathbf{r}_e, \mathbf{r}_h) \Psi_\lambda(\hat{S}^{-1}\mathbf{r}_e, \hat{S}^{-1}\mathbf{r}_h). \tag{2.46}$$

Using Eq. (2.44) in Eq. (2.46) we obtain

$$\chi_S^\lambda = \sum_{\alpha_1\beta_1\mathbf{k}_1} \sum_{\alpha\beta\mathbf{k}} \bar{A}^*_\lambda(\alpha_1\mathbf{k}_1;\beta_1\mathbf{k}_1)\bar{A}_\lambda(\alpha\mathbf{k};\beta\mathbf{k}) I^e(\beta_1\mathbf{k}_1;\beta\mathbf{k})\, I^h(\alpha_1\mathbf{k}_1;\alpha\mathbf{k}), \quad (2.47)$$

where we have defined

$$\begin{aligned} I^e(\beta_1\mathbf{k}_1;\beta\mathbf{k}) &= \int \mathrm{d}\mathbf{r}_e\, \psi^{W*}_{\beta_1,\mathbf{k}_1}(\mathbf{r}_e)\, \psi^W_{\beta,\mathbf{k}}(\hat{S}^{-1}\mathbf{r}_e), \\ I^h(\alpha_1\mathbf{k}_1;\alpha\mathbf{k}) &= \int \mathrm{d}\mathbf{r}_h\, \psi^W_{\alpha_1\mathbf{k}_1}(\mathbf{r}_h)\, \psi^{W*}_{\alpha\mathbf{k}}(\hat{S}^{-1}\mathbf{r}_h). \end{aligned} \quad (2.48)$$

We now compute $I^e(\beta_1\mathbf{k}_1;\beta\mathbf{k})$ by using the definition of $\psi^W_{\beta\mathbf{k}}$, Eq. (2.43), obtaining

$$I^e(\beta_1\mathbf{k}_1;\beta\mathbf{k}) = \frac{1}{N}\sum_{\mathbf{R}\mathbf{R}_1} e^{-i\mathbf{k}_1\cdot\mathbf{R}_1} e^{i\mathbf{k}\cdot\mathbf{R}} \int \mathrm{d}\mathbf{r}_e\; w(\mathbf{r}_e - \mathbf{R}_1 - \tau_{\beta_1}) w(\hat{S}^{-1}\mathbf{r}_e - \mathbf{R} - \tau_\beta). \quad (2.49)$$

As the Wannier functions w used in this system have a $2p_z$ character, they transform according to

$$w(\hat{S}^{-1}\mathbf{r}_e - \mathbf{R} - \tau_\beta) = w(\mathbf{r}_e - \hat{S}\mathbf{R} - \hat{S}\tau_\beta) \quad (2.50)$$

if $\hat{S}$ leaves unchanged the out-of-plane variable z. Defining the index β_S and the lattice vector $\mathbf{R}_{\beta_S}$ such that $\hat{S}\tau_\beta = \mathbf{R}_{\beta_S} + \tau_{\beta_S}$, we find

$$\int \mathrm{d}\mathbf{r}_e\; w(\mathbf{r}_e - \mathbf{R}_1 - \tau_{\beta_1}) w(\hat{S}^{-1}\mathbf{r}_e - \mathbf{R} - \tau_\beta) = \delta_{\beta_1,\beta_S}\delta(\mathbf{R}_1 - \hat{S}\mathbf{R} - \mathbf{R}_{\beta_S}), \quad (2.51)$$

where the orthonormality properties of MLWFs have been used. Therefore, by direct substitution in the definition of $I^e(\beta_1\mathbf{k}_1;\beta\mathbf{k})$ and using the identity $\sum_R e^{i\mathbf{k}\cdot\mathbf{R}} = N\delta_{\mathbf{k},\mathbf{0}}$, valid for any $\mathbf{k}$ vector in the BZ, we obtain

$$I^e(\beta_1\mathbf{k}_1;\beta\mathbf{k}) = \delta_{\beta_1,\beta_S} e^{-i\mathbf{k}_1\cdot\mathbf{R}_{\beta_S}}\, \delta_{\mathbf{k}_1,\hat{S}\mathbf{k}}. \quad (2.52)$$

Proceeding in an analogous way we find

$$I^h(\alpha_1\mathbf{k}_1;\alpha\mathbf{k}) = \delta_{\alpha_1,\alpha_S} e^{i\mathbf{k}_1\cdot\mathbf{R}_{\alpha_S}} \delta_{\mathbf{k}_1,\hat{S}\mathbf{k}}, \quad (2.53)$$

with α_S and $\mathbf{R}_{\alpha_S}$ such that $\hat{S}\tau_\alpha = \mathbf{R}_{\alpha_S} + \tau_{\alpha_S}$. Finally, by substitution of Eqs. (2.52) and (2.53) in Eq. (2.47) we obtain

$$\chi_S^\lambda = \sum_{\alpha\beta\mathbf{k}} \bar{A}^*_\lambda(\alpha_S\hat{S}\mathbf{k};\beta_S\hat{S}\mathbf{k})\bar{A}_\lambda(\alpha\mathbf{k};\beta\mathbf{k}) e^{-i(\hat{S}\mathbf{k})\cdot\mathbf{R}_{\beta_S}}\, e^{i(\hat{S}\mathbf{k})\cdot\mathbf{R}_{\alpha_S}} \quad (2.54)$$

We point out that Eq. (2.54) gives meaningful results only if the coefficients c used to compute the $\bar{A}$ functions are exactly the same used in the construction of the BSE kernel from which the envelope function $A_\lambda(v\mathbf{k};c\mathbf{k})$ is obtained by

	E	$2C_6$	$2C_3$	C_2	$3\sigma_v$	$3\sigma_d$
χ	2	1	-1	-2	0	0

Table 2.2: Characters χ, evaluated for each class of symmetry operations of the point group C_{6v}, considering the bright degenerate excitons $e_{4,5}$ of pristine ML-C_3N. Direct comparison with character table of C_{6v} indicates that this excitonic doublet transforms as the representation E_1.

diagonalization. If different coefficients are used, phase-inconsistency problems can arise.

We start by discussing the degenerate excitons $e_{4,5}$ of pristine C_3N. In order to understand which is the irreducible representation of C_{6v} which transforms as these excitons, for each symmetry operator $\hat{S}$ representing a class of C_{6v} we have computed the corresponding characters using Eqs.(2.41) and (2.54). The obtained characters are summarized in Tab. 2.2. From these results, we can associate the doublet $e_{4,5}$ to the irreducible representation E_1 of C_{6v}, consistently with their bright nature. In fact, an exciton λ is bright only if the matrix element $\langle 0|\hat{\mathbf{D}}|\lambda\rangle$ is non-zero, being $|0\rangle$ the excitonic vacuum, $\hat{\mathbf{D}}$ the exciton dipole operator (here assumed as constrained in the ML plane). The operator $\hat{\mathbf{D}}$ behaves like an in-plane vector, which, in turns, transforms as the E_1 irreducible representation of C_{6v}, while the excitonic vacuum belongs to the fully symmetric representation A_1. Therefore, the matrix element $\langle 0|\hat{\mathbf{D}}|\lambda\rangle$ will be different from zero only for the excitons transforming according to irreducible representations Γ of C_{6v} such that the direct product $E_1 \otimes \Gamma$ contains the representation A_1. Straightforward application of group theory rules [74] for direct product between irreducible representations of the same group indicates that the only representation satisfying this constraint is E_1, in agreement with our numerical results summarized in Table 2.2.
Considering the presence of uniaxial strain, the pair of excitons $e_{4,5}$ transforming as E_1 in unstrained C_3N will now be split into two excitons as there are no irreducible representations with dimension larger than one in C_{2v}, in agreement with our numerical findings. In order to classify these two excitons, we can apply the "Great orthogonality theorem" of group theory [74] to decompose the E_1 representation of C_{6v} into irreducible representations of C_{2v}. Each representation of C_{2v} contained in E_1 then corresponds to each exciton e_4 and e_5, as obtained in the presence of strain. Using the character tables of the C_{2v} group, we obtain $E_1(C_{6v}) = B_1(C_{2v}) \oplus B_2(C_{2v})$. We now associate exciton e_4 and e_5 to the irreducible representations B_1 and B_2. In order to do this, we could compute the characters for each exciton as discussed before for the degenerate pair $e_{4,5}$ in pristine C_3N. Instead, in this case we use a simpler approach, which consists in studying the wavefunction of these excitons in real space. Therefore, we compute the quantity $\Psi_\lambda^{\alpha,\beta}(\mathbf{R})$ defined as

$$\Psi_\lambda^{\alpha,\beta}(\mathbf{R}) = \langle \mathbf{r}_h = \tau_\alpha; \mathbf{r}_e = \tau_\beta + \mathbf{R}|\lambda\rangle \tag{2.55}$$

i.e. the probability amplitude to find, for the exciton λ, the electron localized in the $2p_z$ state on atom β in the unit cell $\mathbf{R}$ and the hole on the orbital $2p_z$ on atom α in the cell at $\mathbf{R} = \mathbf{0}$. Writing the real-space exciton wavefunction as in Eq.(2.44), it is possible to find

$$\Psi_\lambda^{\alpha,\beta}(\mathbf{R}) = \frac{1}{N}\sum_{\mathbf{k}} e^{i\mathbf{k}\cdot\mathbf{R}}\bar{A}(\alpha\mathbf{k};\beta\mathbf{k}). \tag{2.56}$$

$\bar{A}$ being defined as in Eq.(2.45). In Fig. 2.11 we show the excitonic wavefunction for the states e_4 and e_5 in the presence of a uniaxial strain of 2.0 % applied along the zig-zag (a,b) and armchair (c,d) directions. In all cases, we assume the position of the hole to be fixed on a Carbon atom denoted by the black dot and located on the symmetry plane σ_{yz} (represented by the dashed black line). Further, this function is generally complex valued: in this case we have properly chosen its global phase so that it assumes real values for all $\tau_\beta + \mathbf{R}$ (positive values red dots, negative values blue dots, diameter of a circle proportional to the modulus $|\Psi_\lambda^{\alpha,\beta}(\mathbf{R})|$). With zig-zag strain, the lowest exciton e_4 turns out to be odd w.r.t. the mirror reflection σ_{yz}, while the exciton e_5 is even: as $B_1(C_{2v})$ is odd and $B_2(C_{2v})$ is even under σ_{yz} operation, we can therefore assign e_4 to B_1 and e_5 to B_2 in the case of zig-zag strain. This can be also checked numerically, using the action of symmetry operators on excitonic wavefunctions, as given by Eq.(2.54). The situation is exactly the opposite in the case of armchair strain, where the lowest exciton e_4 is even under σ_{yz} while the exciton e_5 is odd, so that they can be respectively assigned to B_2 and B_1 irreducible representations of C_{2v}.
The evaluation of $\Psi_\lambda^{\alpha,\beta}(\mathbf{R})$ at fixed hole position is useful to properly understand the symmetry properties of e_4 and e_5, but it also underlines the strong spatial localization of the bright excitons in ML-C_3N under strain: this is especially apparent in the case of B_1 excitons (see Fig. 2.11 a and d), where, once the hole is fixed along the y axis, the electron is constrained in an effective one-dimensional stripe of the material, even for relatively small applied strains.
We complete this analysis on bright excitons in strained C_3N by pointing out the symmetry-breaking origin of the optical anisotropy observed in absorption spectra obtained by numerical solution of the BSE. We have just seen that for any applied strain (along the zig-zag or the armchair directions) the E_1 exciton of pristine ML-C_3N splits into two excitons transforming as the B_1 and B_2 irreducible representations of C_{2v}. Using group theory rules, we can verify that

$$\begin{aligned} &\langle 0|D_x|B_1\rangle \neq 0, \qquad && \langle 0|D_y|B_1\rangle = 0, \\ &\langle 0|D_x|B_2\rangle = 0, && \langle 0|D_y|B_2\rangle \neq 0, \end{aligned}$$

where D_x and D_y are the components along the x (zig-zag) and the y (armchair) axes. These selection rules are a direct consequence of the fact that D_x

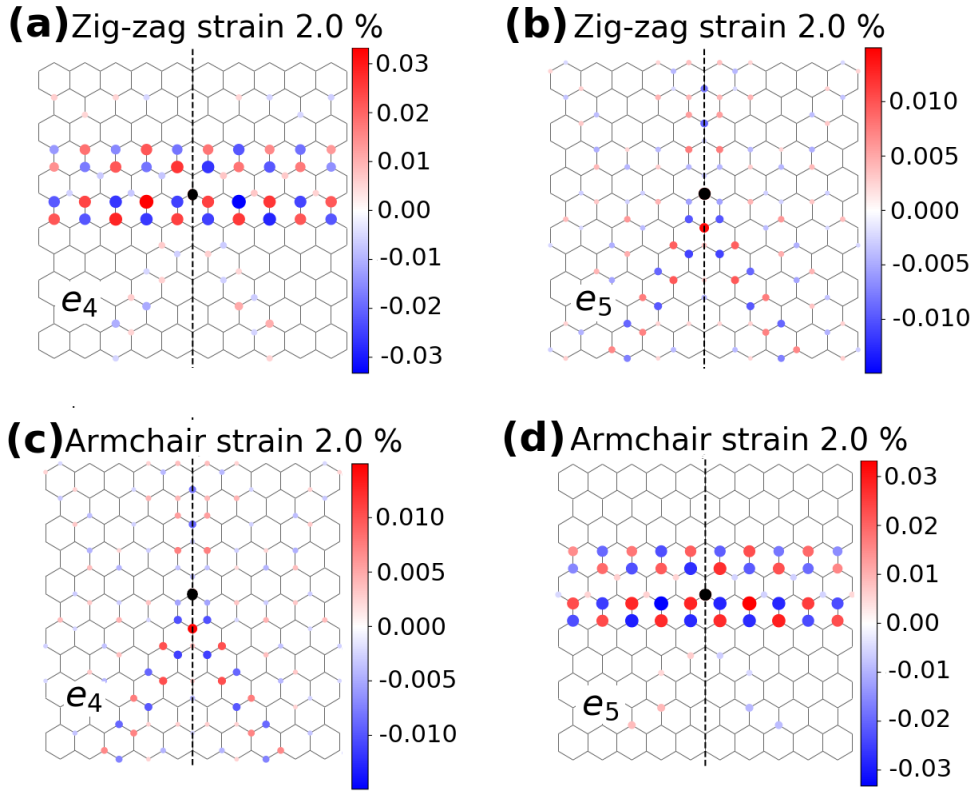

Figure 2.11: Excitonic wavefunctions $\Psi_{\lambda}^{\alpha,\beta}(\mathbf{R})$, as defined in Eqs. (2.55)-(2.56), computed respectively for the excitons e_4 (left) and e_5 (right), assuming a 2.0 % strain along the zig-zag direction (top, a and b) and the armchair direction (bottom, c and d). In all cases, we assume the hole to be fixed on the carbon atom marked by the black dot and positioned on the vertical dashed line, which represents the symmetry y=0 axis.

(D_y) transforms as the B_1 (B_2) irreducible representation of C_{2v}. Therefore, we have strong optical anisotropy in strained C_3N monolayer, with one exciton becoming dark for the light polarization direction at which the other exhibits its highest OS, simply because of the symmetry lowering effect induced by the strain. Thus, while the strength of the applied strain does not control this linear dichroism, it tunes the energy splitting between these two excitons.

2.4 Effect of strain on dark excitons

We now discuss the effect of strain on the lowest lying dark excitons in pristine ML-C_3N, denoted as $e_{1,2}$ and e_3 in Fig. 2.6. By a direct inspection of Fig. 2.7, one can realize that these excitons should remain dark or acquire a negligible OS in the presence of strain, as the spectra are dominated by excitons e_4 and e_5. To better clarify their optical behaviour, in Fig. 2.12 we present the absorption spectrum at photon energies slightly smaller than the energy of excitons e_4 and e_5 for different strains. In particular, Fig. 2.12(a) corresponds to zig-zag strains, Fig. 2.12(b) to armchair strains, while light polarization is kept fixed along the zig-zag direction in both cases. We note that the rapidly increasing signal for higher energies corresponds to the contribution of excitons e_4 and e_5 already discussed in the previous Section. For both strain directions, we notice the presence of a weak absorption feature in the tail of the main peak (not shown in Fig. 2.12), whose intensity progressively increases as a function of the applied strain. However, we point out that in the range of the considered strains (which are realistic values that can be efficiently applied to 2D materials experimentally) such an absorption peak is about two orders of magnitude smaller than the most intense absorption structure observed in Fig. 2.7. Such a feature comes from the dark exciton e_3 of pristine ML-C_3N, which acquires a small OS under the application of strain. Differently, the pair of degenerate excitons $e_{1,2}$ splits into two excitons e_1 and e_2 which remain dark even in the presence of strain.

We start our analysis of low-lying dark excitons focusing on the states coming from the degenerate pair $e_{1,2}$ in pristine ML-C_3N. Their $\mathbf{k}$-space $A(\mathbf{k})$ and real-space $\Psi_\lambda^{\alpha,\beta}(\mathbf{R})$ representations are given in Fig. 2.13(a-d), in the case of armchair strain equal to 1.5 %. Similarly to Sec. 2.3, we discuss these excitons starting from the symmetry properties of the degenerate pair $e_{1,2}$ in unstrained C_3N, from which they derive. Applying Eqs.(2.41)-(2.54), we find that the pair $e_{1,2}$ transforms as the irreducible representation E_2 of the point group C_{6v}. Since the only excitons in pristine C_3N which have a non-zero OS for in-plane polarization are those transforming according to E_1, excitons $e_{1,2}$ are dark by symmetry.

Uniaxial strain reduces the crystal point group from C_{6v} to C_{2v}, therefore $E_2(C_{6v})$ is a now a reducible representation of C_{2v}, which contains only the irreducible representations A_1 and A_2 of C_{2v}, i.e. $E_2(C_{6v}) = A_1(C_{2v}) \oplus A_2(C_{2v})$.

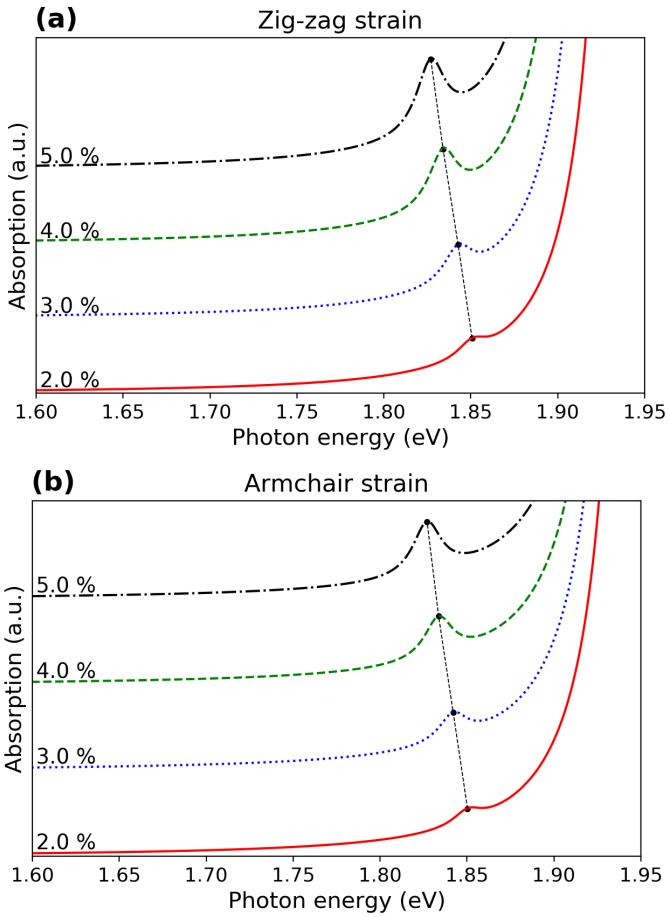

Figure 2.12: (a) Low energy tail of the absorption spectrum in ML-C_3N under uniaxial strain along zig-zag direction. (b) Same as (a), but considering an externally applied strain along the armchair direction. All the spectra were convoluted with a Lorentzian broadening of 10 meV. Curves corresponding to different strain values are rigidly shifted vertically to make the plot more readable.

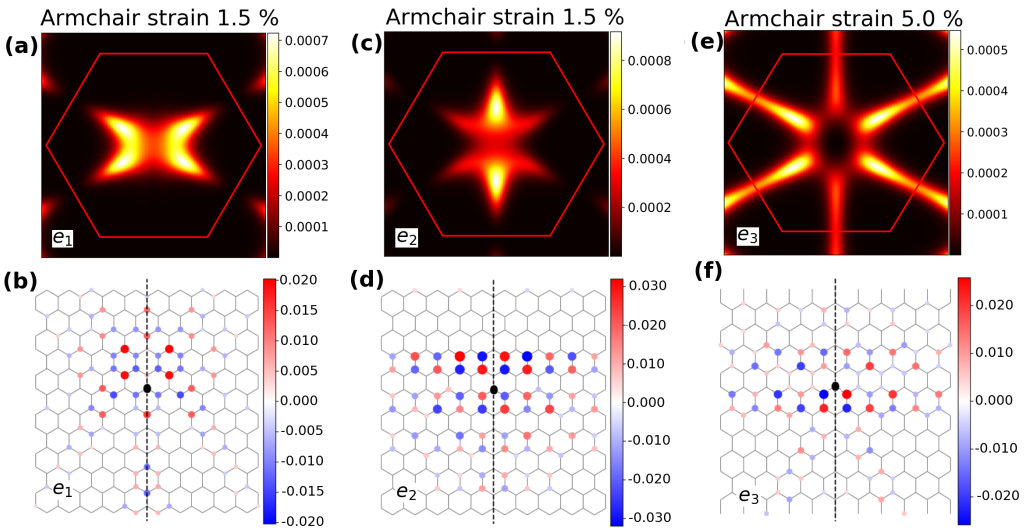

Figure 2.13: Functions $A(\mathbf{k})$ for excitons e_1, e_2 and e_3 are shown in panels (a), (c) and (e); the applied strain is fixed to 1.5 % (5.0 %) in the case of exciton e_1 and e_2 (e_3), and it is always assumed along the armchair direction. Real space representations $\Psi^{\alpha,\beta}(\mathbf{R})$ for the excitons e_1, e_2 and e_3 are displayed in panels (b), (d) and (f), computed for the same set of strain configurations.

As a consequence, the two split excitons e_1 and e_2 will transform as $\mathrm{A}_1(C_{2v})$ and $\mathrm{A}_2(C_{2v})$. This identification explains why these two excitons remain dark even in the strained crystal: considering that D_x and D_y respectively transform as the irreducible representations B_1 and B_2 of C_{2v}, all the possible direct products $\mathrm{B}_i \otimes \mathrm{A}_j$, with $i, j = \{1, 2\}$ do not contain the full symmetry representation A_1 of C_{2v}, so that the exciton dipole matrix element $\langle 0|\mathbf{D}|\lambda\rangle$ is always zero. As before, we can exploit the real space representation $\Psi^{\alpha,\beta}(\mathbf{R})$, as shown for example in Fig. 2.13(b,d), to assign $e_{1,2}$ to the irreducible representations $\mathrm{A}_{1,2}$. Looking at Fig. 2.13(b,d), in the case of armchair strain, the lowest exciton e_1 is even under the σ_{yz} mirror reflection, while e_2 is odd. Looking at the character table for C_{2v}, we can therefore assign e_1 to A_1 and e_2 to A_2. The same reasoning can be followed in the case of zig-zag strain: the only difference is that in this case, the exciton e_1 (e_2) transforms as the irreducible representation A_2 (A_1) of the point group C_{2v}.
We now discuss the properties of exciton e_3 and justify in terms of group theory arguments the reason why it acquires a finite OS in strained $\mathrm{C}_3\mathrm{N}$. In the discussion we focus on the 5.0 % strain case, though we note that the following comments remain qualitatively valid also for smaller strains. Looking at Fig. 2.13(e), we notice that the effect of strain along the armchair direction is to create an unbalance between the intensity of the $\mathbf{k}$-space wavefunction $A(\mathbf{k})$ along the $\Gamma\mathrm{M}$ and $\Gamma\mathrm{M}'$ directions (as those are no longer equivalent in the presence of strain, see also Fig. 2.6 for comparison with the pristine case). The application of the symmetry operators of the C_{6v} point group on the

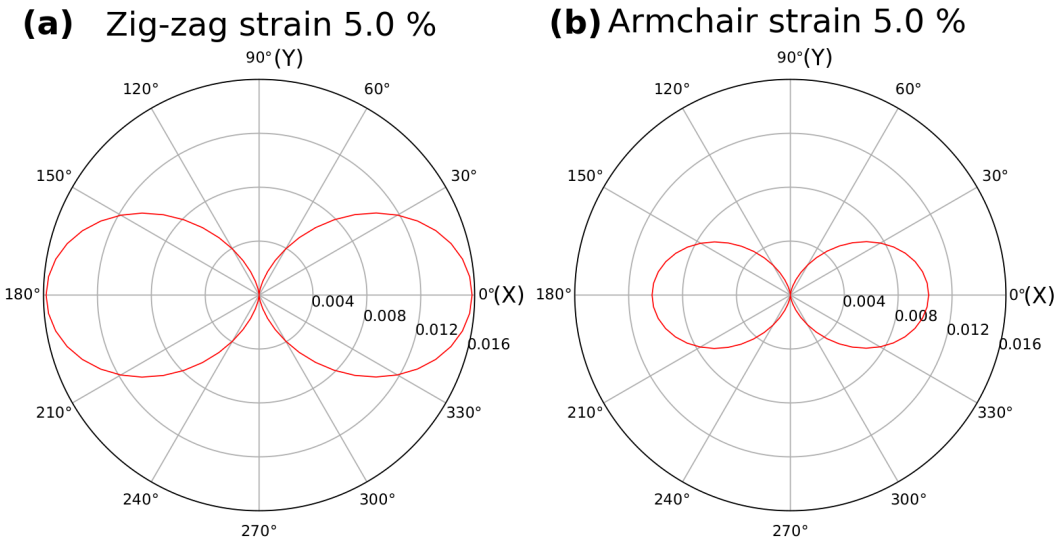

Figure 2.14: Oscillator strength D_λ, computed for exciton e_3 as a function of the light polarization direction (measured w.r.t. the zig-zag x axis), in the case of zig-zag (a) and armchair (b) strain equal to 5.0 %.The circles in both figures represent isovalues for the modulus of the exciton oscillator strength $|D_\lambda|$.

exciton wavefunction e_3 in unstrained C_3N enables us to assign it to the irreducible representation B_1 of C_{6v}, which is dark for planar polarization of the incoming light, in good agreement with the absorption spectrum shown in Fig. 2.6. Interestingly, B_1 of C_{6v} corresponds to B_1 of C_{2v}: in fact, by looking at Fig. 2.13(f), we see that the real space exciton wavefunction for e_3 is odd w.r.t. the mirror reflection about the yz plane, which is effectively the same behaviour of $B_1(C_{2v})$ under σ_{yz}. As already discussed in the previous Section, excitons transforming as $B_1(C_{2v})$ can have a non-zero oscillator strength for light polarized along the zig-zag direction. This justifies the appearance of a peak in the zig-zag polarized absorption spectrum of strained ML-C_3N due to the e_3 exciton.

To further confirm the agreement between the numerical results and the proposed symmetry analysis, in Fig. 2.14 we display the profile of the oscillator strength (OS) associated to the exciton e_3 as a function of the polarization direction under a zig-zag (a) and armchair (b) strain of 5.0 %. We notice that, independently of the direction of the applied strain, the e_3 exciton has an anisotropic OS, showing a nodal line along the armchair direction y. This is due to the fact that it transforms as B_1 of C_{2v} for both the considered uniaxial strains, and, since $\langle 0|D_y|B_1\rangle$ is zero by symmetry, such an exciton cannot absorb light polarized along y. This is confirmed by numerical results, which also indicate that the OS associated to exciton e_3 becomes more intense (of almost a factor 2) when strain is applied along the zig-zag rather than along

the armchair axis.

2.5 Exciton dispersion at small momenta

Up to now, we have discussed how excitons with null centre of mass momentum $\mathbf{Q}$ are modified via the application of tensile uniaxial strain. In this Section, we focus on the dispersion of exciton energies as a function of finite momentum $\mathbf{Q}$ [75]. A fully *ab initio* calculation of exciton band structure along high symmetry directions in the BZ for pristine C_3N has been already presented in Ref. [45]. Here, by taking advantage of the TB-BSE approach, we deepen that analysis by computing the excitonic dispersion in both pristine and strained C_3N at small momenta $\mathbf{Q}$. The evaluation of small-$\mathbf{Q}$ dispersions is very demanding (though possible [76]) within a fully ab initio approach, because of the limited $\mathbf{Q}$-points sampling accessible in practice. In this respect, in the present work we exploit the simplicity of our TB-BSE model to compute such a dispersion, which is known to strongly influence exciton dynamics and lifetimes [77, 78].

In the following, we evaluate the lowest excitonic bands $E_\lambda(\mathbf{Q})$, taking $\mathbf{Q}$ along the ΓM and ΓK′ directions along k-segments of length $|\Gamma M|/5$ and $|\Gamma K'|/10$, respectively. This dispersion is obtained by diagonalization of the finite-momentum excitonic Hamiltonian given in Eq.(2.4). In Fig. 2.15, we show the excitonic dispersion in the case of pristine ML-C_3N. Concerning the low energy excitonic bands, departing from the dark excitons at Γ, we notice that the bands branching out of the E_2 doublet (excitons $e_{1,2}$) are characterized by a negative concavity, while the band starting from the exciton B_1 (e_3) presents positive concavity, as also found by *ab initio* calculations. [45]

The most striking feature of the obtained band structure (not seen in the *ab initio* dispersion) is represented by the two bands which originate from the E_1 excitons at Γ ($e_{4,5}$), highlighted in Fig. 2.15 by red dots. We notice the presence of an almost flat band with negative concavity and of a V-shaped dispersion, with the latter well reproduced by a linear dispersion with slope of about 19.0 eV·Angstrom along both the ΓM and ΓK' directions (see the dashed red line in Fig. 2.15).

As discussed in the literature [76, 70, 79], this feature is due to the long range component ($\mathbf{G} = 0$) of the BSE exchange term, Eq. (2.32), in the excitonic Hamiltonian of 2D materials. In fact, this V-shaped dispersion combined with a slowly varying band is analogous to the dispersion discussed by Qiu *et al.* [76] for the excitonic bands departing from optically active 2-fold degenerate excitons in monolayer MoS_2. A similar analysis is also proposed in the work of Cudazzo *et al.* in Ref. [70], and in a recent work by Qiu *et al.* (Ref. [79]).

We now turn our attention to the effect of uniaxial strain on the excitonic dispersion. In order to do this, we compute the excitonic dispersion at small $\mathbf{Q}$ in the case of a strain equal to 1.0 % applied along the zig-zag and armchair

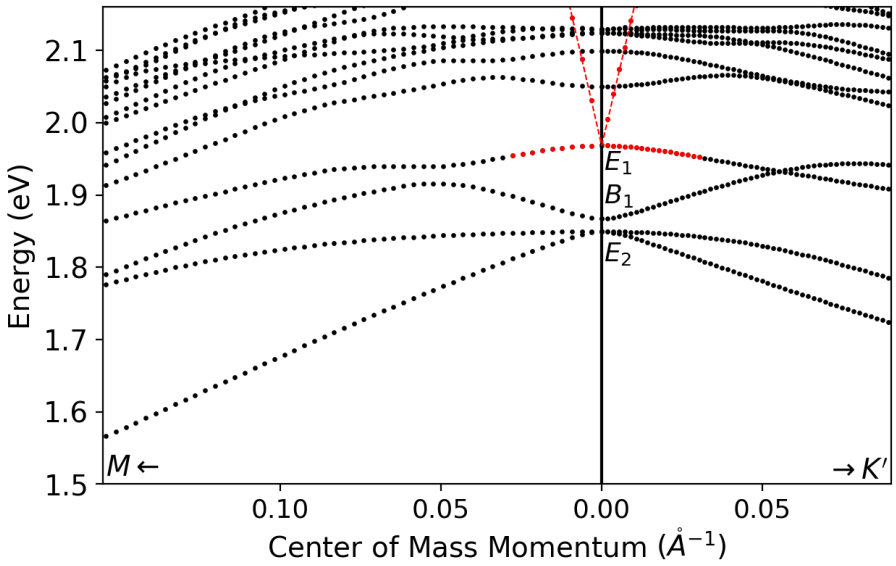

Figure 2.15: Exciton dispersion in pristine C_3N for $\mathbf{Q}$ in proximity of Γ and along the path M-Γ-K'. Red dots denote the excitonic bands departing from the bright excitons at Γ, transforming as E_1: the linear band dispersion of the highest band is also highlighted by dashed red lines, representing the obtained linear fits along the two high symmetry directions. For completeness, $|\Gamma M| = 0.746$ Å^{-1} while $|\Gamma K'| = 0.861$ Å^{-1}.

directions. Similar considerations can also be done in the case of different strain values. The resulting dispersions are shown in Fig. 2.16. As previously discussed, the pair of bright excitons E_1 in pristine C_3N will split into B_1 and B_2 excitons. In the case of zig-zag strain (Fig. 2.16a) the band originating from the lowest exciton B_1 is weakly dispersing along ΓM, while it has a linear trend along ΓK' (see blue dots in Fig. 2.16a). The situation is the opposite for the bands departing from the highest energy exciton B_2, which is linear along ΓM and almost flat (with negative concavity) along the orthogonal direction ΓK'. These bands are highlighted by red dots in the figure. Similar consideration can be done for the bands originating from B_1 and B_2 in the case of armchair strain (see Fig. 2.16b).
The observed behaviour is again due to the long range component of the exchange kernel of the excitonic Hamiltonian. Qiu *et al.* [79] demonstrated that in 2D materials the excitonic dispersion of a band λ at small $\mathbf{Q}$ can be written as

$$E_\lambda(\mathbf{Q}) = E_\lambda(\Gamma) + A_\lambda|\mathbf{Q}|\cos^2\theta_\mathbf{Q} + \frac{\hbar^2 Q_x^2}{2M_\lambda^x} + \frac{\hbar^2 Q_y^2}{2M_\lambda^y} \tag{2.57}$$

where $E_\lambda(\mathbf{Q} = \Gamma)$ is the energy of the non-degenerate exciton λ at null momentum and $\theta_\mathbf{Q}$ is the angle between $\mathbf{D}_\lambda$ (the exciton dipole) and the vector $\mathbf{Q}$. The terms showing a quadratic dependence on $\mathbf{Q}$ are determined by the single particle dispersions, the small-$\mathbf{Q}$ behaviour of the direct kernel and the

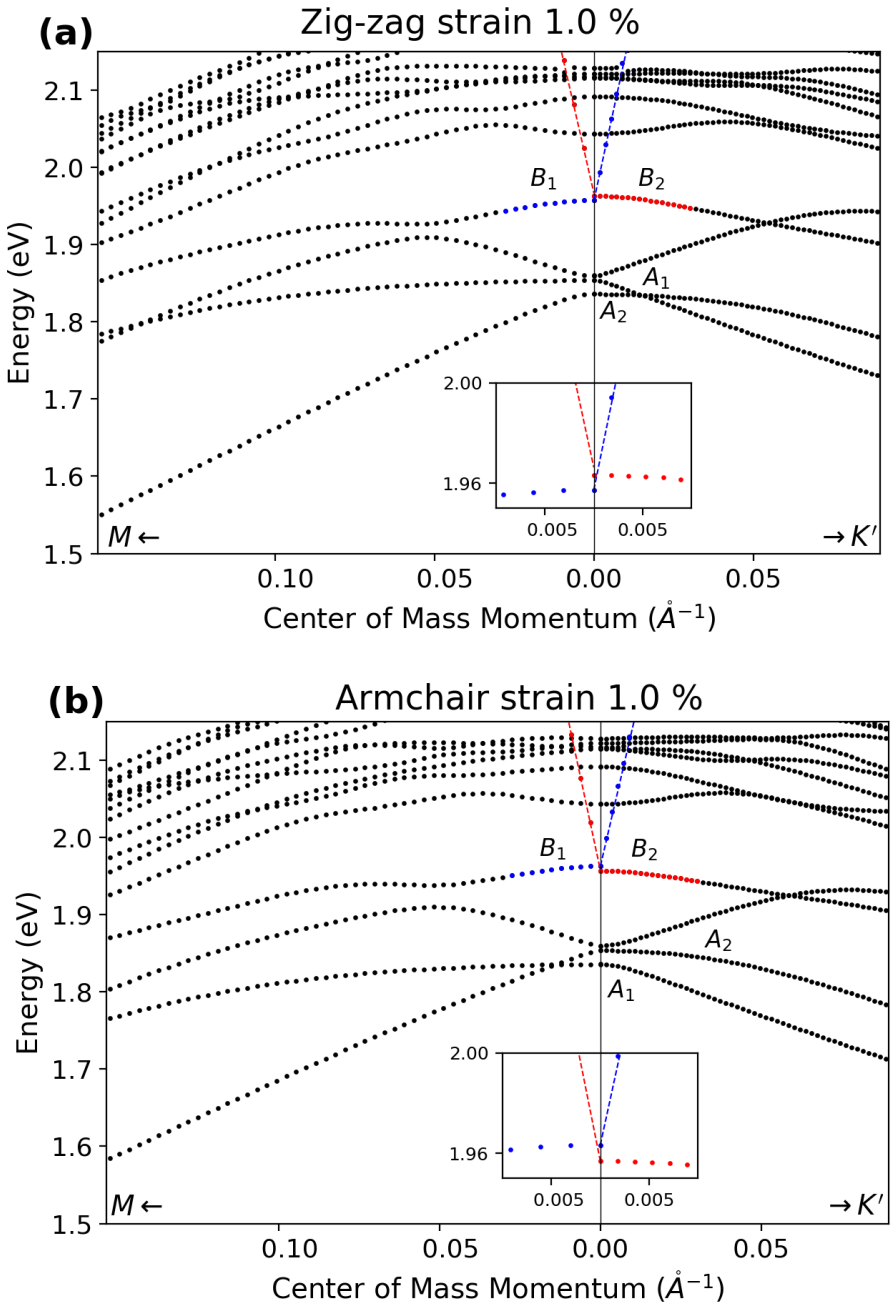

Figure 2.16: Exciton dispersion in C_3N for $\mathbf{Q}$ along the path M-Γ-K', in the case of zig-zag (a) and armchair strain (b). In both cases, the strain is fixed to 1.0 %. The red (blue) dots denote the excitonic band dispersing from the B_2 (B_1) exciton at Γ. The insets show the excitonic branches departing from the bright excitons B_1 and B_2 at Γ. For completeness, $|\Gamma M| = 0.748$ Å^{-1} and $|\Gamma K'| = 0.858$ Å^{-1}, in the case of zig-zag strain, while $|\Gamma M| = 0.739$ Å^{-1} and $|\Gamma K'| = 0.863$ Å^{-1} in the case of armchair strain.

short range part of the exchange kernel. These dependencies are captured by the exciton effective masses $M_\lambda^{x,y}$ which can be obtained by fitting ab initio results [76, 79]. On the other hand, the linear term is only due to the long range part of the exchange kernel, where A_λ is a coefficient proportional to the modulus of the exciton dipole $\mathbf{D}_\lambda$ at $\mathbf{Q} = 0$. Exploiting Eq. (2.57), we can give a rationale for the dispersions of the bands departing from the B_1 and B_2 excitons in strained C_3N. The exciton at Γ transforming as B_1 has a dipole $\mathbf{D}$ with null component along the y direction, as it can only have OS for light polarization along x. Therefore, the band originating from this exciton (depicted in blue in Fig. 2.16) will have a linear dispersion along ΓK', while it will be almost flat along ΓM. The reason is that if $\mathbf{Q} \parallel$ ΓM, the cosine function $\cos^2\theta_{\mathbf{Q}}$ is zero, so that the linear term in Eq. (2.57) does not contribute. Instead, the quadratic dispersion is due to the term proportional to Q_x^2 and Q_y^2, with the negative concavity determined by the dependence on $\mathbf{Q}$ of the difference $\epsilon_c(\mathbf{k}+\mathbf{Q}) - \epsilon_v(\mathbf{k})$. Conversely, the excitonic band originating from the exciton B_2 at Γ (highlighted by red dots in Fig. 2.16) will have a linear dispersion along ΓM and a quadratic one along ΓK', as the dipole for B_2 excitons is oriented along the y direction parallel to ΓM, so that only if $\mathbf{Q} \parallel$ ΓM the linear term in Eq. (2.57) gives contribution, while if $\mathbf{Q} \parallel$ ΓK' this term is zero as the dipole is perpendicular to the exciton center of mass momentum.

We further point out that such a linear dispersion is only possible for exciton branches originating from bright excitons at Γ. The reason why the band starting from the third exciton (i.e. the one non-degenerate in pristine C_3N) does not show linear dispersion is a direct consequence of the small dipole strength acquired by this exciton under strain, so that the quadratic term dominates on the linear one in Eq. (2.57), even if the latter may be non-zero. As a last comment concerning the excitonic bands shown in Fig. 2.16, we remark that the two low-energy bands departing from the excitons A_1 and A_2 at Γ are characterized by dispersions which are swapped passing from armchair to zig-zag strain. The reason is strictly related to the fact that with zig-zag strain the lowest exciton at Γ transforms as A_2 while the second exciton as A_1. The order is reversed in the case of armchair strain, and, as a consequence, also the bands are exchanged.

Finally, we can discuss our findings in view of the existing literature. In particular, our results concerning small-$\mathbf{Q}$ exciton dispersion in strained C_3N highlight a peculiar effect related to exciton propagation in mechanically strained C_3N. In fact, Qiu *et al.* [79] pointed out that in 2D materials where optically bright excitons with strongly anisotropic dipole strength can exist (like in single or few layer black phosphorous), it is possible to produce exciton wavepackets which propagate along a quasi 1D channel, whose direction is defined by the orientation of the excitonic dipole at null momentum. This has been proved in the ballistic regime, and it has been demonstrated to be a consequence of the linearity of exciton bands at small momentum, for $\mathbf{Q}$ parallel

to the excitonic dipole. Our results show that two bright excitons with intense oscillator strengths in orthogonal polarization directions are present in C_3N, at fixed uniaxial strain. As a consequence, in strained C_3N it should be possible to prepare exciton wavepackets which propagate along either the armchair or the zig-zag directions, according to the polarization of the incoming light beam which produce the wavepacket itself. This is not possible for example in black phosphorous, as, in that case, the crystal does not have two excitons at Γ which are close in energy and characterized by orthogonal dipoles.

2.6 Summary and perspectives

In this Chapter, we have discussed the effect of uniaxial strain on the excitonic properties of monolayer C_3N, adopting a model solution of BSE, based on a Tight Binding description of single particle properties. Such an approach allows us to investigate the effect of uniaxial strain on low-lying dark excitons and higher-energy active excitons in pristine C_3N, discussing the origin of strain-induced optical anisotropy, in terms of group theory and symmetry arguments. Furthermore, we have clarified the effect of strain on dark excitons, by demonstrating the strain-induced brightening of the lowest non-degenerate dark excitation.
Finally, the developed TB-BSE approach allows us to obtain the excitonic dispersion in both pristine and strained C_3N, in a range of centre-of-mass momenta $\mathbf{Q}$ which are hardly accessible using state-of-art fully *ab initio* calculations. Our results on excitonic dispersions show that mechanically strained C_3N displays a peculiar selectivity effect in the propagation direction of the exciton wavepackets along either the armchair or the zig-zag paths. We therefore believe that the dynamics of excitons in strained C_3N should deserve future experimental and theoretical investigation, in order to also clarify how other mechanisms affecting the exciton propagation (like exciton-phonon coupling [80, 81, 82, 83], discussed in Chapter 4) can be tuned by the applied mechanical strain.

Chapter 3

Low-energy optical absorption quenching in bilayer C_3N

3.1 Introduction

In Chapter 2, we have discussed the excitonic properties of monolayer C_3N and how they can be tuned by application of mechanical strain. In particular, we have found that the optical absorption of ML-C_3N is characterized by a single intense peak at about 1.96 eV, due to a pair of degenerate excitons characterized by a large binding energy (about 0.6 eV [45]).
In this Chapter we focus our attention on how electronic and optical properties of ML-C_3N are modified once two-layer systems are considered.
Vertical stacking of two layers of C_3N is a possible approach to tune electronic and optical properties of the isolated layer, as the coupling among the vertically stacked layers (held together by dispersive Van der Waals interaction) strongly affects both the optical [69, 84] and the electronic properties of the monolayers [85]. Few theoretical works have analysed the stability of bilayers C_3N (BL-C_3N) as a function of the possible stacking patterns [43, 2]: following the notation of Ref. [2], all these calculations obtain negative formation energies for AA′, AB and AB′ stackings.
Furthermore, BL-C_3N with AA′ and AB′ stackings have been also experimentally synthesized in Ref. [2], where a detailed investigation of the electronic properties using scanning tunnelling spectroscopy (STS) has been also provided: the obtained results indicate a strong change of the electronic-transport band gap passing from monolayer to bilayer together with relevant modifications of the electronic properties as a function of the stacking sequence.

Motivated by these experimental advances, we present a fully *ab initio* investigation of the optical properties of BL-C_3N, properly including excitonic effects which are known to play a fundamental role in the description of the absorption of 2D-materials. Our results indicate that, for all the considered stackings, the optical response does not exhibit low-energy features associated to discrete exciton states which instead characterize the absorption spectrum

of the isolated monolayer. Such behaviour is rather peculiar, as not observed in other common semiconducting bilayer homo-structures, e.g. BL-hBN[84], BL-MoS_2[86, 77] or BL-phosphorene[87]. The origin of low energy absorption quenching will be explained, focusing on the properties of the single particle states involved in the formation of the lowest-energy excitons with null momenta. Our analysis explains the observed optical quenching in terms of the negligible interband dipole matrix elements associated to the valence-conduction transitions involved in these excitations.

The content of this Chapter is reported in the manuscript *Quenching of low-energy optical absorption in bilayer C_3N polytypes.*

3.2 Computational details

We summarized here the main details about the computational methods used to describe electronic and optical properties of bilayer C_3N, presented in the following.
Ground state structural and electronic properties have been investigated using Density Functional Theory: in these calculations, we have used norm-conserving ONCV Pseudopotentials [63], with GGA-PBE approximation [10] for the exchange-correlation potential. Van der Waals interactions between layers have been taken into account, adding the dispersion correction proposed by Grimme [88] to the exchange-correlation energy computed at the PBE level (PBE-D2).
Equilibrium structural properties have been obtained, relaxing both the in plane unit cell and the atomic positions up to when the components of the forces acting on each atom were smaller than $5{\cdot}10^{-4}$ Ry/Bohr. In these ground state calculations, we have always used a 12x12x1 Monkhorst-Pack [14] **k**-grid to sample the Brillouin Zone (BZ) and a kinetic energy cutoff of 90 Ry for the plane wave basis set used to represent single particle wavefunctions.
Kohn-Sham wavefunctions, computed from the equilibrium ground state charge density, have been used to evaluate quasi-particle (QP) corrections to DFT energies, using single shot G_0W_0 approach as discussed in Chapter 1. The electron-electron screened interaction W has been obtained within Random Phase Approximation (RPA): converged QP gaps within a 10 meV threshold required the inclusion of 700 bands and a **G**-vector cutoff of 16 Ry in the construction of the screening matrix at the RPA level. The frequency dependence of W has been approximated using Godby-Needs plasmon-pole model [25], while 1000 bands have been included in the sum over states appearing in the correlation part of the electron self energy. In Figure 3.1a we show the value of the minimum indirect gap in AB-C_3N computed varying the **G**-cutoff of the inverse dielectric matrix and the number of bands included in the RPA polarizability. To reduce spurious interactions among different cells along the stacking direction, we have used a supercell length along z of 23.5

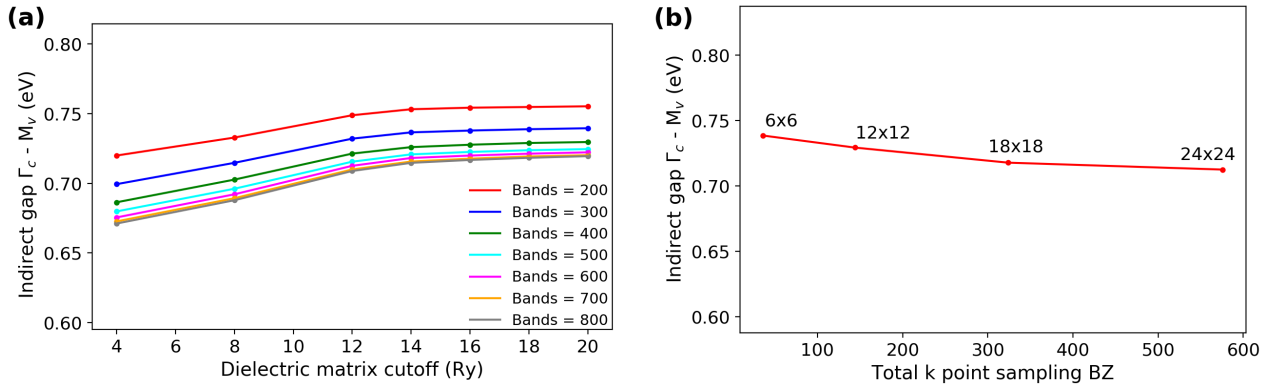

Figure 3.1: Convergence of parameters used in GW calculations. a) Indirect band gap in AB-C_3N as a function of the number of bands and the energy cutoff used in the RPA polarizability. Each color corresponds to a fixed number of bands. b) Indirect gap in AB-C_3N as a function of the **k**-grid used to sample the BZ, adopting the accelerated method of Ref. [27].

Å, together with a 2D cutoff for the Coulomb potential. Finally, to speed-up the convergence of QP gaps w.r.t. the **k**-point mesh, we have adopted the approach recently proposed by Guandalini *et al.* [27], verifying that, with this method, a 18x18x1 Monkhorst-Pack **k**-grid already provides converged gaps within the chosen threshold of 10 meV (see Fig.3.1b). Even if not shown, analogous convergence trends can be obtained in the case of AB′-C_3N bilayer.

Starting from QP corrected electronic energies, excitonic properties have been evaluated solving Bethe-Salpeter Equation in resonant approximation as discussed in Section 1.3. Converged exciton energies have been obtained including the two highest-occupied valence bands and the four lowest unoccupied conduction states in the construction of the excitonic Hamiltonian, while using a 48x48x1 Monkhorst-Pack **k**-grid to sample the BZ. We point out that, in the solution of the BSE, electron-electron screened interaction has been computed at the RPA level, in static approximation, using the same converged parameters adopted for the calculation of QP corrections. Furthermore, QP corrections have been approximated via a scissor-stretching operator, obtained via linear fitting of explicitly computed Quasi-Particle corrections at the G_0W_0 level. In Figure 3.2 we show the result of this linear fitting procedure in AB (Fig.3.2a) and AB′ (Fig.3.2b) stackings. The blue dashed lines represent the scissor-stretching fits, i.e. $E^v_{QP} = s_v E^v_{DFT}$ and $E^c_{QP} = s_0 + s_c E^c_{DFT}$, with s_0 the scissor term and s_v (s_c) the stretching coefficient for valence (conduction) states. For both stackings, QP energies of the last two occupied valence bands have been considered to evaluate s_v; on the other hand, the fitting of s_0 and s_c parameters has been done including only conduction states with energy smaller than 2 eV: in this way we have neglected the high energy σ^*-like states (not involved in the low-energy optical properties) in the fitting procedure,

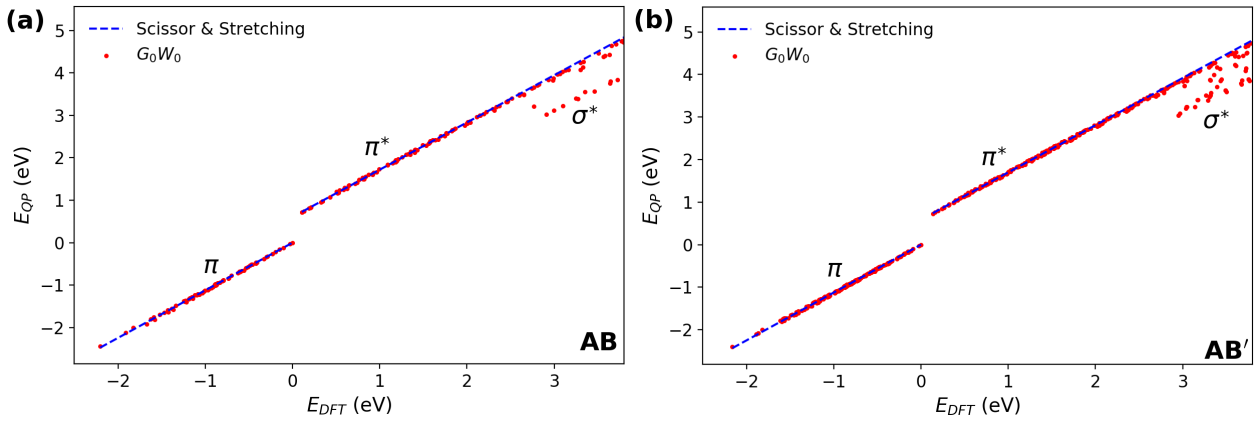

Figure 3.2: Fit of QP corrections using a scissor-stretching operator for both valence and conduction states in AB (a) and AB′ (b) C_3N. Notice that the higher-energy conduction states denoted as σ^* have not been included in the fitting procedure.

while considering only π-states.

3.3 Structural and electronic properties in bilayer C_3N with AB and AB′ stackings

We now discuss the structural and the electronic properties of Bilayer C_3N with AB and AB′ stackings. A similar discussion for the AA′ motif is presented in Section 3.7.

In Figure 3.3 we present the crystal structures of BL-C_3N with AB (upper panel) and AB′ (lower panel) stackings: yellow (light blue) spheres denote Carbon (Nitrogen) atoms and small (large) atoms are located on the upper (lower) layer, denoted from now on as L_1 (L_2).

For both stacking motifs, we have obtained an in-plane lattice parameter of 4.849 Å, slightly smaller than the one of the isolated monolayer (4.857 Å): the interlayer distance among the layers (evaluated as the separation along z between Carbon atoms with the same in-plane coordinates) has been found equal to 3.22 Å for the AB stacking and 3.21 Å in the AB′ structure. These values are in agreement with those obtained with PBE-D2 calculations in Ref. [2], while they are slightly smaller than the interlayer distances computed with VdW-functionals in Ref. [43].

We now briefly discuss the crystal symmetries of the two stackings. The point group of AB-C_3N is D_{3d}, and also includes non-symmorphic symmetries. Among the possible symmetries, this stacking possesses a spatial inversion center (red dot in the upper panel of Fig.3.3) together with two three-fold rotation axes parallel to z direction, whose in-plane position is denoted by a green dot in Fig.3.3. Furthermore, this stacking motif is invariant under mir-

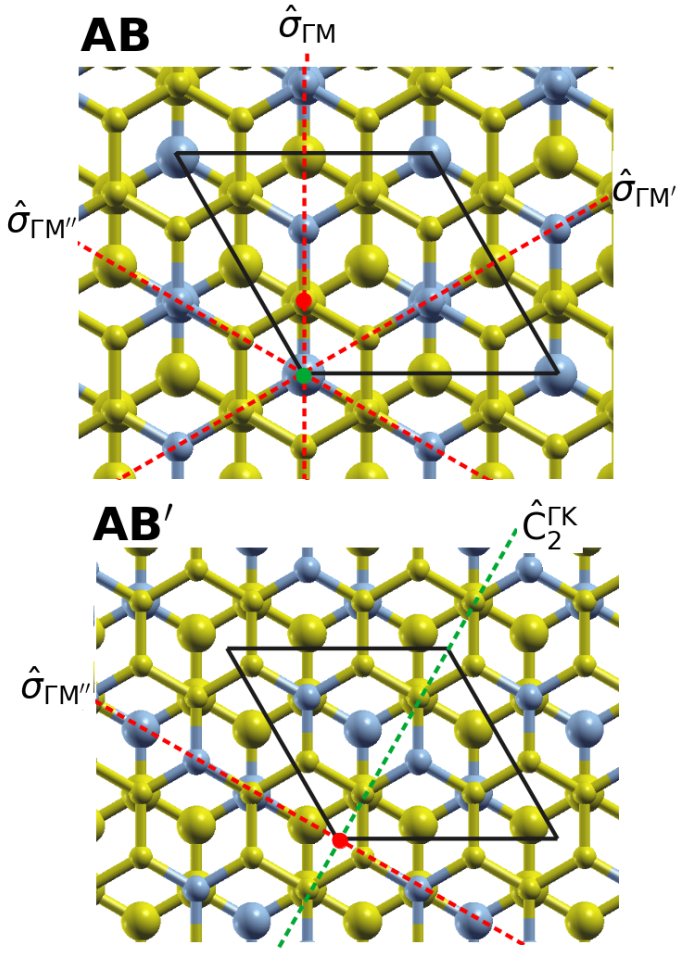

Figure 3.3: Crystal structures for bilayer C_3N with AB (upper panel) and AB′ (lower panel) stackings. Yellow (light blue) spheres indicate Carbon (Nitrogen) atoms, while small (large) radius spheres denote atoms located on the upper (lower) layer. The red dot indicates the in-plane position of the inversion symmetry center, while dashed red lines represent mirror symmetry planes parallel to the stacking direction. Finally, the green dot in the AB bilayer denotes the in-plane position of the two three-fold rotation axes parallel to the stacking direction, while the dashed green line in the AB′ bilayer corresponds to an in-plane C_2 rotation axis.

ror reflections w.r.t. planes parallel to the stacking direction and represented by dashed red lines in Fig.3.3: these planes are respectively denoted as $\hat{\sigma}_{\Gamma M}$, $\hat{\sigma}_{\Gamma M'}$ and $\hat{\sigma}_{\Gamma M''}$ as they are aligned to these high symmetry directions in the BZ.
AB′-C_3N has lower symmetry than the AB stacking pattern: its point group is C_{2h} and contains, apart from the trivial identity, the inversion symmetry, a two-fold in-plane rotation axis (represented by the green dashed line in the lower panel of Fig.3.3 and denoted as $\hat{C}_2^{\Gamma K}$) and a mirror symmetry plane

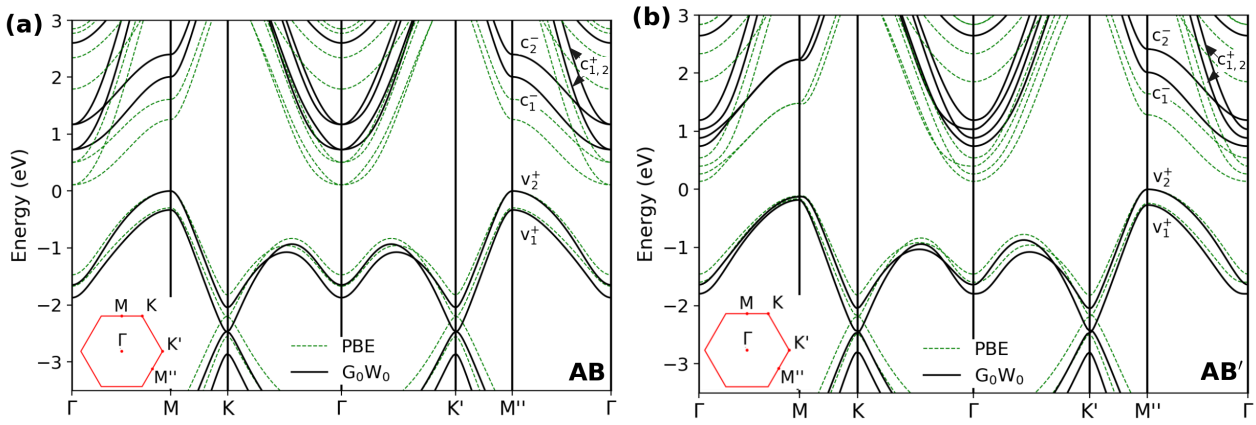

Figure 3.4: Electronic band structure computed at the DFT-PBE (green-dashed lines) and with G_0W_0 approximation (continuous black lines), for AB-C_3N (a) and AB′-C_3N (b). The insets represent the hexagonal Brillouin zone, together with the high symmetry points defining the paths where bands are computed. The parity of the topmost valence and the lowest conduction bands along ΓM″ direction w.r.t. mirror symmetry $\hat{\sigma}_{\Gamma M''}$ are indicated: the notation n_i^p indicates that band n_i has parity p, being $p = +(-)$ for even (odd) states and $n = \{v, c\}$. In both images, the top valence band energy is shifted to 0 eV.

$\hat{\sigma}_{\Gamma M''}$, parallel to the ΓM″ direction in the BZ.
In Figure 3.4 we present the electronic band structure for AB-C_3N (Fig. 3.4a) and for AB′-C_3N (Fig. 3.4b), computed both within DFT-PBE (dashed green lines) and including QP corrections at the G_0W_0 level (solid black lines). We note that both stackings are characterized by an indirect band gap, both at the DFT and GW level. In the case of AB stacking, the electronic band dispersions along ΓM and ΓM″ coincide, as a consequence of the three-fold rotational symmetry of this stacking; therefore, the highest-energy valence band has six equivalent maxima, obtained by symmetry from the $M = [0, \frac{1}{2}, 0]$ point, while the bottom of the conduction band is located at the Γ point. We also note that the presence of doubly degenerate bands at Γ is consistent with irreducible representations of dimension 2 in the D_{3d} point group: we have obtained an indirect gap of 0.108 eV at the PBE level, which is increased to 0.72 eV once QP corrections are taken into account. Finally, the direct band gap is found along the ΓM-equivalent directions, at a wavevector $\mathbf{k}$ located approximately in the middle of ΓM: the obtained G_0W_0 gap is approximately equal to 1.85 eV, as expected larger than the value obtained at the PBE level (1.12 eV).
In the case of AB′ stacking, the maximum of the valence band is found at the M″ point, while the lowest unoccupied conduction state is at Γ, as in the case of AB stacking motif. Our calculations gave an indirect gap of 0.136 eV at the DFT-PBE level, while we obtain a 0.73 eV indirect gap with inclusion of QP corrections. The obtained indirect gap for AB′-C_3N is slightly smaller

than the one measured experimentally with STS in Ref. [2] (0.85±0.03 eV), but it seems to be in better agreement with respect to the value obtained by other GW calculations [43], where the Hybertsen-Louie plasmon-pole approximation was used.
Because of the lack of three-fold rotational symmetry around z axis, the directions ΓM and ΓM″ are no more equivalent: as a result, the minimum direct gap is found approximately in the middle of ΓM″ direction, with a value around 1.79 eV (1.09 eV within DFT) while the indirect gap between the conduction at Γ and the top-valence at M is slightly larger than the one between Γ and M″: we obtain a $\Gamma_c - M_v$ gap of 0.87 eV (0.249 eV) with G_0W_0 (DFT-PBE) approximation.
Comparing band dispersions for AB and AB′ stackings, we notice that, for $\mathbf{k}$ along the ΓM direction, the lowest pair of unoccupied conduction bands are almost degenerate (splitting of about 1 meV) in the AB′ stacking, while they are well separated in the case of AB motif (splitting larger than 0.2 eV): a similar behaviour is also observed for the two topmost valence states, where the splitting is, however, not negligible also in the AB′ stacking (splitting of about 50 meV). In Section 3.6, we provide a qualitative explanation of this peculiar lack of splitting among the two lowest conductions, in AB′-C_3N, analyzing the quasi-symmetries of the sublattice where conduction states are localized once $\mathbf{k}$ is taken along ΓM direction.
The obtained results indicate that, despite keeping the same qualitative features (i.e. the minimum gap remains indirect), the electronic bandstructures of monolayer C_3N and bilayer C_3N are quantitatively different, as we observe a strong change of the electronic gaps. As an example, the minimum indirect gap in the studied bilayers is almost half the one obtained for the isolated monolayer, while the direct gap is about 0.8 eV smaller. Furthermore, we notice that the obtained gaps are only slightly different one from the other, once considering AB and AB′ stacking (in agreement with the hybrid-DFT results of Ref. [2]), but the electronic dispersions have differences because of the different symmetry properties of the two stackings.
We complete the analysis of the electronic properties of BL-C_3N with AB and AB′ stackings by reminding that both bilayers are invariant under mirror reflection $\hat{\sigma}_{\Gamma M''}$, therefore electronic states for $\mathbf{k}$ along this direction can be classified in terms of their parity w.r.t. such symmetry. We have found that, in both stackings, the two highest occupied valence bands are even w.r.t. $\hat{\sigma}_{\Gamma M''}$, so that we have denoted them as v_i^+ in Fig.3.4, with $i = 1, 2$; on the other hand, if $\mathbf{k}$ has modulus in the range $[\frac{|\Gamma M|}{3}, |\Gamma M|]$ the two lowest unoccupied conduction bands are $\hat{\sigma}_{\Gamma M''}$-odd, so we have indicated them as c_i^-. We also notice that for $\mathbf{k}$ close to Γ, the second and the third unoccupied conduction bands are instead even w.r.t $\hat{\sigma}_{\Gamma M''}$ and they exhibit a stronger dispersion with $\mathbf{k}$, if compared with odd conduction states. We point out that a similar analysis can be carried out also for electronic states along this direction in monolayer C_3N: in that case, the last occupied valence (lowest unoccupied

conduction) is even (odd) w.r.t. the mirror symmetry along ΓM″ direction, while the second unoccupied conduction is even.
In the case of AB stacking, the same parity analysis can be presented for the bands along the direction ΓM, as the crystal is invariant w.r.t. $\hat{\sigma}_{\Gamma M}$ mirror symmetry.
Such symmetry classification will be exploited to understand bilayers' optical properties in the following.

3.4 Optical absorption

In Figure 3.5 we show the absorption spectra computed for AB (Fig. 3.5a) and AB′ bilayer C_3N (Fig. 3.5b), both at the independent particle level (dotted black lines) and with inclusion of electron-hole interaction, by solving BSE as detailed in Section 3.2: green dashed (solid red) lines have been obtained assuming light polarization along $\Gamma\hat{K}$ ($\Gamma\hat{M}''$) direction (light polarization versors $\hat{\epsilon}$ are shown for clarity on top of the crystal structures in the insets).
The AB spectrum is dominated by an intense peak (denoted as C) at energy E≈1.70 eV, whose spectral position and intensity are not dependent on the polarization direction. Such peak is due to a close set of degenerate eigenstates of H_{exc}, characterized by relevant contributions from single particle transitions between the valence band v_1^+ and the conduction state c_1^- along ΓM and equivalent directions: among these, transitions with the highest weights are denoted by arrows on the band structure shown in Fig. 3.5c. We also point out that transitions between v_2^+ and c_2^- for $\mathbf{k}$ along the same direction also contribute to this absorption peak, even if with a smaller weight than $v_1^+ \rightarrow c_1^-$ transitions, therefore they are omitted for clarity in Fig. 3.5c.
The situation is slightly different in the case of AB′ C_3N: also for this stacking motif the absorption spectrum is dominated by a single intense peak, but its position in energy and its strength depend on the in-plane light polarization direction. In Fig. 3.5b, we have labelled as C_1 the main peak at 1.71 eV obtained for light polarization along $\Gamma\hat{K}$ and as C_2 the absorption maximum at 1.73 eV found for $\Gamma\hat{M}''$-polarized light.
The C_1 peak is mainly due to $v_1^+ \rightarrow c_1^-$ for $\mathbf{k}$ along ΓM″ direction, as depicted schematically by green arrows in Fig. 3.5d, with a smaller contribution coming from v_2^+ to c_2^- transitions for the same $\mathbf{k}$ points (not shown in Fig. 3.5d). On the other hand, the C_2 absorption peak derives from transitions between the two highest occupied valence states and the two lowest (quasi-degenerate) conduction bands along ΓM and ΓM′ directions (see red arrows in Fig. 3.5d).
The striking feature of bilayer C_3N optical spectra is the apparent absence of intense absorption peaks due to discrete bound excitonic states formed by single particle transitions close to the electronic direct gap. As shown in the insets of Fig. 3.5a and b, within the energy range between 1.25 and 1.5 eV, we actually observe two absorption structures (labelled in both cases as P_1

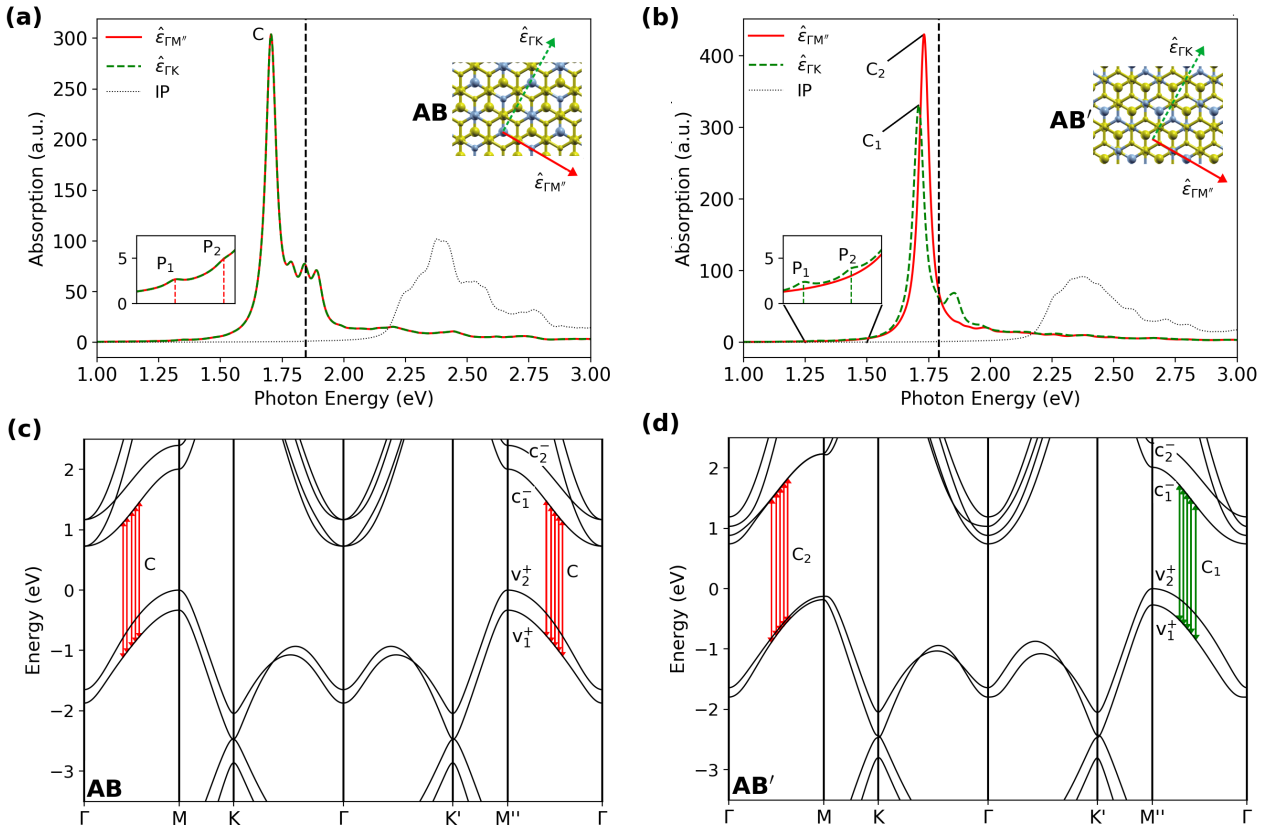

Figure 3.5: Optical absorption spectra for AB-C_3N (a) and AB′-C_3N (b). Solid red (dashed green) lines correspond to spectra computed with light polarization along the $\Gamma\hat{M}''$ ($\Gamma\hat{K}$) direction, while dotted lines are the independent particle spectra evaluated for polarization along $\Gamma\hat{M}''$. The insets represent low energy and quasi-dark peaks labelled as P_1 and P_2, while the vertical black dashed lines indicate the position of the direct QP band gap obtained within G_0W_0. The electronic structure of AB-C_3N is shown in c), with red arrows indicating the transitions mainly responsible for the C absorption peak in (a). Similarly, the single particle bands of AB′-C_3N are displayed in d): green (red) arrows underline the transitions mostly involved in C_1 (C_2) peaks labelled in b.

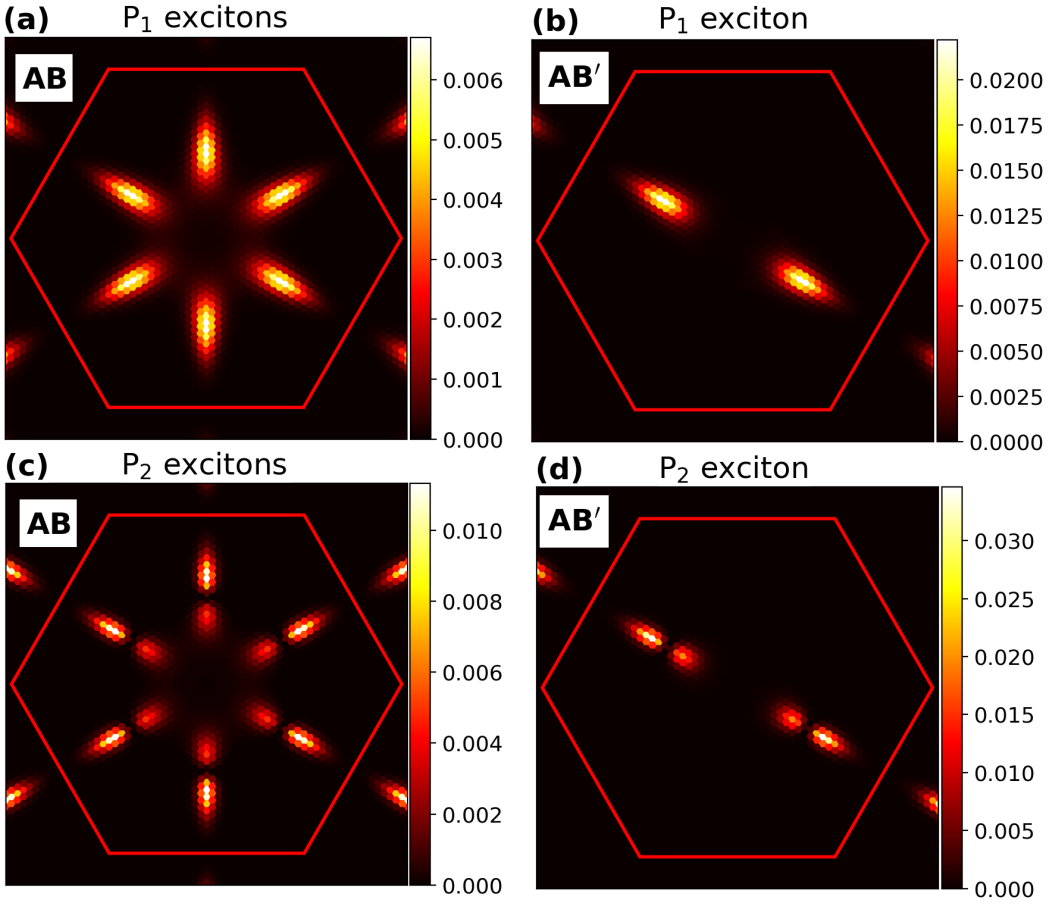

Figure 3.6: Contributions of single particle transitions between the last occupied valence and the lowest unoccupied conduction in the BZ to excitons P_1 and P_2 in AB-C_3N (a and c) and in AB′-C_3N (b and d), as defined by Eq.(3.1).

and P_2), but they exhibit optical strengths which are almost two orders of magnitude smaller than the most intense peaks. We now discuss in more detail such excitations for both stacking motifs.

In AB-C_3N, both P_1 and P_2 peaks are due to a pair of degenerate excitons, respectively at energies $E_{P_1} = 1.35$ eV and $E_{P_2} = 1.47$ eV, with oscillator strengths not dependent on the polarization direction. For completeness, we point out that diagonalization of the excitonic Hamiltonian also provides other excitonic resonances (the lowest with energy of 1.34 eV) which are characterized by null oscillator strength within numerical accuracy: such excitons, dark by strict symmetry reasons, will not be considered further in the following. P_1 and P_2 excitons are almost totally composed by electron-hole transitions between the last occupied valence v_2^+ and the lowest unoccupied conduction c_1^-, with wave-vectors $\mathbf{k}$ along ΓM and equivalent directions in the BZ; this is better clarified in Figure 3.6a and c, where we show for P_1 and P_2 excitons

respectively the quantity

$$A^{vc}(\mathbf{k}) = \sum_{\lambda} \left| A_{\lambda}(vc\mathbf{k}) \right|^2 \tag{3.1}$$

where v (c) is fixed to the last valence (first conduction) band and the sum over λ is performed over the pair of degenerate states responsible for P_1 and P_2 peaks respectively. We notice that single particle transitions forming the excitons P_1 are mainly localized in the middle of ΓM and equivalent directions, with $A^{vc}(\mathbf{k})$ having non-negligible values for $|\mathbf{k}|$ mainly in the interval $[\frac{1}{3}, \frac{2}{3}]|\Gamma\mathrm{M}|$. On the other hand, excitons P_2 (Fig. 3.6c) are still localized along ΓM directions, but the corresponding function $A^{vc}(\mathbf{k})$ has intense contributions from transitions slightly closer to the M point and exhibits a node for $\mathbf{k}$ points along this direction.
In the case of AB′ stacking, P_1 and P_2 peaks are related each to a single-nondegenerate exciton at energies $E_{P_1} = 1.30$ eV and $E_{P_2} = 1.42$ eV. Differently from the AB case, the oscillator strengths of these excitations are polarization dependent: this is apparent looking at the inset of Fig.3.6b, where we notice that both resonances are dark for light polarization along $\Gamma\hat{\mathrm{M}}''$ direction while they exhibit a small but non-zero optical activity for incoming light polarized along $\Gamma\hat{\mathrm{K}}$ versor. As in AB stacking, such excitons are mainly formed by transitions between the last occupied valence and the lowest conduction band: in Fig. 3.6b and d we show the functions $A^{vc}(\mathbf{k})$ computed respectively for exciton P_1 and P_2. We see that in both cases, the transitions involved in these excitations are strongly localized along the single ΓM″ direction of the BZ, with P_1 exciton having the main contributions coming from the middle of ΓM″, where the minimum direct electronic band gap is found and P_2 resonance characterized by a node along this direction.
The observed polarization dependence in the optical absorption of AB′-C_3N can be rationalized via symmetry arguments, similarly to Ref.[84] for Bilayer hBN. The point group of AB′-C_3N is C_{2h}, so the in-plane exciton dipole operator projected along $\Gamma\hat{\mathrm{M}}''$ ($\hat{\mathbf{D}}_{\Gamma\mathrm{M}''}$) will transform as B_u irreducible representation of C_{2h}, while $\hat{\mathbf{D}}_{\Gamma\mathrm{K}}$ will behave as A_u under symmetry. Therefore, the eigenstates $|\lambda\rangle$ of H_{exc} such that $\langle 0|\mathbf{D}|\lambda\rangle \neq 0$ (being $|0\rangle$ the excitonic vacuum transforming as the fully symmetric representation A_g) will transform as A_u or B_u if $\hat{\mathbf{D}}$ is projected along $\Gamma\hat{\mathrm{K}}$ or $\Gamma\hat{\mathrm{M}}''$ direction respectively: considering for example A_u states, these will have null optical activity by symmetry, once incoming light is polarized along $\Gamma\hat{\mathrm{M}}''$. Therefore, we can justify the presence of absorption peaks in AB′-C_3N which turn on and off according to the chosen polarization direction. Furthermore, following the presented analysis, we can assign P_1 and P_2 excitons to A_u representation, exactly as the eigenstates of H_{exc} responsible for the C_1 absorption peak, while C_2 is expected to be due to excitations transforming as B_u.
The situation is different for AB stacked C_3N: for simplicity, we discuss the brightness of excitonic eigenstates using the subgroup C_{3v} of D_{3d}, formed by

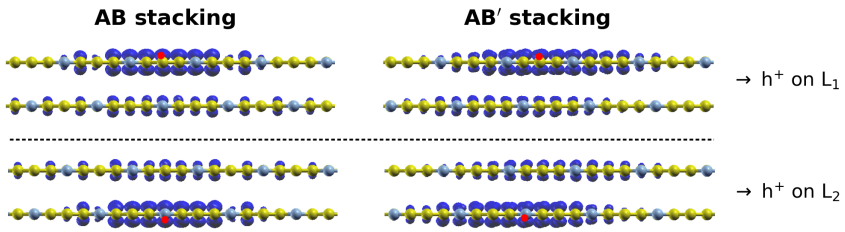

Figure 3.7: Wavefunctions for exciton P_1 computed in real space for AB (left) and AB′ (right) stackings. In each panel, the upper (lower) wavefunction has been computed assuming the hole localized on a Nitrogen atom on layer L_1 (L_2). The hole position along the stacking direction is indicated by the red circle.

the mirror planes σ along ΓM directions together with the two 3-fold rotations depicted in the upper panel of Fig.3.3. The in-plane exciton dipole operator $\mathbf{D}$ transforms as the two-dimensional irreducible representation E of C_{3v}: as a consequence, all bright excitons will behave as E of C_{3v}, so that they are expected to be twice degenerate and characterized by an isotropic oscillator strength, in agreement with the numerical results obtained *ab initio*.
We now turn our attention to the quasi-dark nature of the low-lying bound excitons P_1 and P_2 in both the considered stackings. We point out that such small optical activity cannot be related to an interlayer nature of these excitons, i.e. it is not due to a negligible spatial overlap between electron and hole wavefunctions. As an example, in Figure 3.7 we show the real space wavefunctions of exciton P_1 in AB (left panel) and AB′(right panel) stacked C_3N: for each stacking, the upper (lower) wavefunction has been obtained assuming the hole (represented by the red dot) fixed on layer L_1 (L_2) and located in the plane close to a Nitrogen atom. For both stacking motifs, the shown wavefunctions indicate the intralayer nature of such exciton: in fact, looking at the excitonic wavefunction isosurfaces, we notice that the electron has a high probability to be found on the same layer on which the hole is localized. The negligible dipole strength of these low-lying excitons is a consequence of the small interband dipole associated to the electron-hole single particle transitions involved in these excitations. This can be understood from the independent particle (IP) absorption spectrum shown in Fig.3.4a and 3.4b as dotted lines: we notice that in both cases, the optical signal is negligible for energies close to the direct QP gap, with the IP absorption onset located at higher photon energies.
In the following section we discuss more in detail the single particle states involved in these low-lying excitons and we propose a possible rationale for the observed IP absorption quenching.

3.5 Rationale for quenching of low energy absorption in AB and AB′ BL-C_3N

In this section we develop a model for the electronic bands in proximity of the direct gap to rationalize the small oscillator strength of the single particle transitions close to the direct electronic gap: as the following analysis is valid for both stackings, here we focus on the case of AB′-C_3N: at the end of this section analogous results will be presented for AB-C_3N. We will restrict our analysis to $\mathbf{k}$ along $\Gamma M''$, in the region where valence to conduction transitions giving the highest contribution to the low-energy quasi-dark excitons are located.

As already discussed in the literature [2, 43], the lowest lying conduction bands and the highest valence states have a π character: therefore, we can analyse them using a Tight-Binding (TB) Hamiltonian, obtained considering one $2p_z$ orbital for each atom; in the following we will denote as τ_α the position of both the atom α and the $2p_z$ orbital localized on that atom. In practice, we construct a TB hamiltonian

$$H^{2L}_{\alpha,\beta}(\mathbf{k}) = \sum_{\mathbf{R}} e^{i\mathbf{k}\cdot\mathbf{R}} t(\alpha 0, \beta \mathbf{R}) \tag{3.2}$$

where $\mathbf{R}$ is a lattice vector while $t(\alpha 0, \beta \mathbf{R}) = \langle \alpha 0 | \hat{H} | \beta \mathbf{R} \rangle$ are the hopping matrix elements between two $2p_z$ orbitals, respectively localized at sites τ_α and $\tau_\beta + \mathbf{R}$, which have been computed fully *ab initio* by Wannierization of DFT bands using `Wannier90` code. Starting from ground state charge density, we have computed Kohn-Sham states on a 18x18x1 $\mathbf{k}$-grid and we have used this set of wavefunctions to compute Maximally Localized Wannier Functions. MLWFs have been obtained considering as initial guesses one $2p_z$ orbital for each atom in the unit cell: the obtained functions exhibit a p_z character as expected, and they have a spatial spread of about 1 Å^2 (0.72 Å^2) if they are localized on a Carbon (Nitrogen) atom. In Figure 3.8 we present the comparison between DFT results (black dots) and Wannier-interpolated bands (red lines) for both AB (a) and AB′ (b) stackings. Green (blue) dashed lines represent the inner (outer) energy windows used in the disentanglement process.

As there are 16 atoms in the unit cell, at a general $\mathbf{k}$ the TB Hamiltonian can be written as a 16x16 hermitian matrix, in a block-like form, i.e.

$$\mathbf{H}^{2L}(\mathbf{k}) = \begin{bmatrix} \mathbf{H}^{L_1}(\mathbf{k}) & \mathbf{H}^{IL}(\mathbf{k}) \\ \mathbf{H}^{IL}(\mathbf{k})^\dagger & \mathbf{H}^{L_2}(\mathbf{k}) \end{bmatrix} \tag{3.3}$$

where $\mathbf{H}^{L_1}$, $\mathbf{H}^{L_2}$ and $\mathbf{H}^{IL}$ are 8x8 hermitian matrices. To obtain this separation, we have grouped together the orbitals localized on L_1 and on L_2, associating to each orbital α_1 localized at τ_{α_1} on layer L_1 an orbital α_2 at τ_{α_2} on layer L_2, such that $\tau_{\alpha_2} = \hat{I}\tau_{\alpha_2}$, being $\hat{I}$ the inversion symmetry operator.

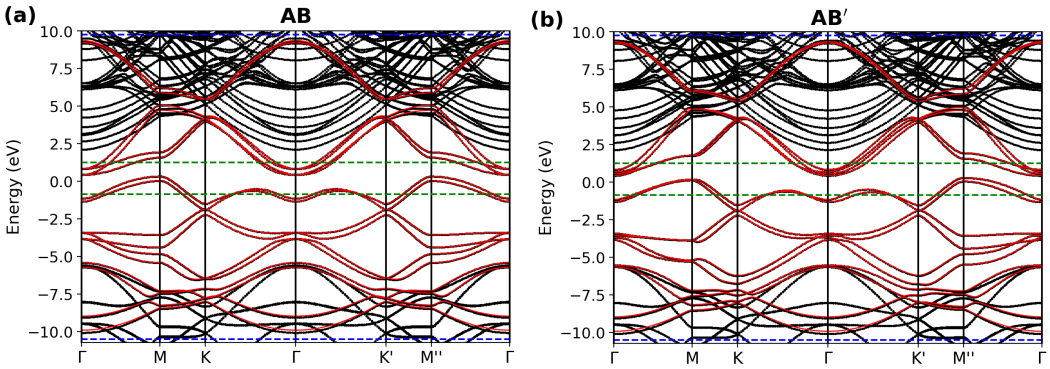

Figure 3.8: Comparison between DFT bands (black dots) and Wannier-interpolated bands (red lines) computed for AB-C_3N(a) and AB′-C_3N(b). Green (blue) dashed lines indicate the inner (outer) windows used in the disentanglement procedure.

Then $\mathbf{H}^{\mathrm{L}_1}$ ($\mathbf{H}^{\mathrm{L}_2}$) is the block of $\mathbf{H}^{\mathrm{2L}}$ which contains the intralayer hopping within layer L_1 (L_2), while $\mathbf{H}^{\mathrm{IL}}$ depends on the hopping integrals between orbitals on different layers. We can now write $\mathbf{H}^{\mathrm{2L}}(\mathbf{k}) = \mathbf{h}_{\mathrm{IN}}(\mathbf{k}) + \mathbf{h}_{\mathrm{IL}}(\mathbf{k})$, where $\mathbf{h}_{\mathrm{IN}}(\mathbf{k})$ is block-diagonal while $\mathbf{h}_{\mathrm{IL}}(\mathbf{k})$ is purely off-diagonal. We note that the subscripts 'IN' and 'IL' respectively stand for intralayer and interlayer.
We now consider the block diagonal hamiltonian $\mathbf{h}_{\mathrm{IN}}$. For each $2\mathrm{p}_z$ orbital on layer L_1 at position τ_{α_1} there is an analogous state localized at $\tau_{\alpha_2} = \hat{I}\tau_{\alpha_1}$ on layer L_2, because of the inversion symmetry of the Bilayer (with both AB and AB′ stacking). Therefore, it is possible to relate the diagonal blocks one to the other, i.e.

$$\begin{aligned} H^{\mathrm{L}_1}_{\alpha_1,\beta_1}(\mathbf{k}) &= \sum_{\mathbf{R}} e^{i\mathbf{k}\cdot\mathbf{R}} t(\alpha_1 0, \beta_1 \mathbf{R}) \\ &= \sum_{\mathbf{R}} e^{-i\mathbf{k}\cdot\mathbf{R}} t(\alpha_2 0, \beta_2 \mathbf{R}) \\ &= H^{\mathrm{L}_2}_{\alpha_2,\beta_2}(\mathbf{k})^* \end{aligned} \tag{3.4}$$

where we have used, the invariance of the hamiltonian under spatial inversion symmetry, the real character of the hopping integrals because of time reversal and $\hat{\mathrm{I}}|\beta_1\mathbf{R}\rangle = -|\beta_2\hat{\mathrm{I}}\mathbf{R}\rangle$. Equation (3.4) indicates that the matrix $\mathbf{H}^{\mathrm{L}_1}$ is the complex conjugate of $\mathbf{H}^{\mathrm{L}_2}$, therefore these matrices have the same eigenvalues. As the spectrum of $\mathbf{h}_{\mathrm{IN}}$ is the union of the spectra of $\mathbf{H}^{\mathrm{L}_1}$ and $\mathbf{H}^{\mathrm{L}_2}$, each eigenvalue $\varepsilon^0_{n\mathbf{k}}$ of $\mathbf{h}_{\mathrm{IN}}$ will be two fold degenerate, for each $\mathbf{k}$.
Furthermore, as $\mathbf{H}^{\mathrm{L}_1} = \mathbf{H}^{\mathrm{L}_2 *}$, we can associate to each eigenvalue $\varepsilon^0_{n\mathbf{k}}$ the pair of eigenstates

$$\begin{aligned} |\phi^{\mathrm{L}_1}_{n\mathbf{k}}\rangle &= \sum_{\alpha_1} c_{\alpha_1}(n\mathbf{k}) |\psi^W_{\alpha_1\mathbf{k}}\rangle \\ |\phi^{\mathrm{L}_2}_{n\mathbf{k}}\rangle &= \sum_{\alpha_2} c_{\alpha_2}(n\mathbf{k}) |\psi^W_{\alpha_2\mathbf{k}}\rangle \end{aligned} \tag{3.5}$$

where $|\psi^W_{\alpha\mathbf{k}}\rangle = \frac{1}{\sqrt{N}}\sum_{\mathbf{R}} e^{i\mathbf{k}\cdot\mathbf{R}}|\alpha\mathbf{R}\rangle$ and $c_{\alpha_2}(n\mathbf{k}) = c_{\alpha_1}(n\mathbf{k})^*$, being

$$\sum_{\beta_1} H^{\mathrm{L}_1}_{\alpha_1\beta_1}(\mathbf{k})c_{\beta_1}(n\mathbf{k}) = \varepsilon^0_{n\mathbf{k}}c_{\alpha_1}(n\mathbf{k}) \tag{3.6}$$

We notice that $|\phi^{\mathrm{L}_1}_{n\mathbf{k}}\rangle$ ($|\phi^{\mathrm{L}_2}_{n\mathbf{k}}\rangle$) is a Bloch function localized on layer L_1 (L_2) as it only involves $2\mathrm{p}_z$ orbitals localized on that layer. Further, defining the time inversion operator $\hat{\mathrm{T}} = \hat{\mathrm{K}}$, i.e. equal to the complex conjugate operator, we can realize that $|\phi^{\mathrm{L}_2}_{n\mathbf{k}}\rangle = -\hat{\mathrm{I}}\cdot\hat{\mathrm{T}}|\phi^{\mathrm{L}_1}_{n\mathbf{k}}\rangle$. In fact,

$$-\hat{I}\cdot\hat{T}|\phi^{L_1}_{n\mathbf{k}}\rangle = -\sum_{\alpha_1} c_{\alpha_1}(n\mathbf{k})^*\hat{I}\cdot\hat{T}|\psi^W_{\alpha_1\mathbf{R}}\rangle$$

Using the reality of $2\mathrm{p}_z$ orbitals together with $\hat{I}|\alpha_1\mathbf{R}\rangle = -|\alpha_2\hat{I}\mathbf{R}\rangle$ we find

$$\hat{I}\cdot\hat{T}|\psi^W_{\alpha_1\mathbf{R}}\rangle = -\frac{1}{\sqrt{N}}\sum_{\mathbf{R}} e^{i\mathbf{k}\cdot\mathbf{R}}|\alpha_2\mathbf{R}\rangle.$$

and reminding $c_{\alpha_2}(n\mathbf{k}) = c_{\alpha_1}(n\mathbf{k})^*$ we effectively obtain $|\phi^{\mathrm{L}_2}_{n\mathbf{k}}\rangle = -\hat{\mathrm{I}}\cdot\hat{\mathrm{T}}|\phi^{\mathrm{L}_1}_{n\mathbf{k}}\rangle$.

Before proceeding, we clarify the physical meaning of the splitting of $\mathbf{H}^{2\mathrm{L}}$ into $\mathbf{h}_{\mathrm{IN}}$ and $\mathbf{h}_{\mathrm{IL}}$. $\mathbf{h}_{\mathrm{IN}}$ can be thought as an intralayer Hamiltonian, where its diagonal blocks describe the two layers as separate, i.e. not interacting with each other; notice that the presence of the other layer is implicitly considered as the intralayer hopping integrals defining $\mathbf{H}^{\mathrm{L}_1}$ ($\mathbf{H}^{\mathrm{L}_2}$) are affected by the presence of layer L_2 (L_1). On the other hand, $\mathbf{h}_{\mathrm{IL}}$ describes the interlayer interaction between the layers and acts as a perturbation of $\mathbf{h}_{\mathrm{IN}}$ as interlayer hopping have smaller values than intralayer ones. With this interpretation, the states $|\phi^{\mathrm{L}_1}_{n\mathbf{k}}\rangle$ and $|\phi^{\mathrm{L}_2}_{n\mathbf{k}}\rangle$ can be thought as Bloch states with the same energy $\varepsilon^0_{n,\mathbf{k}}$ localized each on one of the two monolayers, once the interlayer coupling is assumed to be zero: we now define as $\varepsilon^0_{v,\mathbf{k}}$ ($\varepsilon^0_{c,\mathbf{k}}$) the energy of the highest occupied valence (lowest unoccupied conduction) band on these two non-interacting layers. The effect of the interlayer coupling will be to mix these layer-localized wavefunctions, to give the electronic states of the bilayer. The discussion presented so far is general and valid for each $\mathbf{k}$ point of the BZ: we now specialize to $\mathbf{k}$ vectors along $\Gamma\mathrm{M}''$ direction. For these wave-vectors, $\mathbf{H}^{2\mathrm{L}}$ commutes with $\hat{\sigma}_{\Gamma\mathrm{M}''}$ and the same is therefore valid for $\mathbf{h}_{\mathrm{IN}}$ and $\mathbf{h}_{\mathrm{IL}}$ separately. Therefore,

$$\begin{aligned}\hat{\sigma}_{\Gamma\mathrm{M}''}|\phi^{\mathrm{L}_i}_{v\mathbf{k}}\rangle &= |\phi^{\mathrm{L}_i}_{v\mathbf{k}}\rangle \\ \hat{\sigma}_{\Gamma\mathrm{M}''}|\phi^{\mathrm{L}_i}_{c\mathbf{k}}\rangle &= -|\phi^{\mathrm{L}_i}_{c\mathbf{k}}\rangle\end{aligned} \tag{3.7}$$

with $i = [1, 2]$: notice that these relations have been numerically verified, using the eigenstates of $\mathbf{h}_{\mathrm{IN}}$.

We now include the effect of $\mathbf{h}_{\mathrm{IL}}$ using first order degenerate perturbation theory, separately diagonalizing the matrix representation of $\hat{h}_{\mathrm{IL}}$ on the two

subspaces $\{|\phi^{L_1}_{v\mathbf{k}}\rangle, |\phi^{L_2}_{v\mathbf{k}}\rangle\}$ and $\{|\phi^{L_1}_{c\mathbf{k}}\rangle, |\phi^{L_2}_{c\mathbf{k}}\rangle\}$. With this procedure, we obtain the two highest-energy $\hat{\sigma}_{\Gamma M''}$-even valence bands $\{|\varphi_{v_1\mathbf{k}}\rangle, |\varphi_{v_2\mathbf{k}}\rangle\}$ and the two lowest-energy $\hat{\sigma}_{\Gamma M''}$-odd conduction states $\{|\varphi_{c_1\mathbf{k}}\rangle, |\varphi_{c_2\mathbf{k}}\rangle\}$ in the bilayer; such states have been respectively labelled as (v_1^+,v_2^+) and (c_1^-,c_2^-) in Figure 3.5b. They can be compactly written as

$$|\varphi_{n_j\mathbf{k}}\rangle \approx \frac{1}{\sqrt{2}}\left[|\tilde{\phi}^{L_1}_{n\mathbf{k}}\rangle + s_j|\tilde{\phi}^{L_2}_{n\mathbf{k}}\rangle\right] \tag{3.8}$$

with energy

$$E_{n_j\mathbf{k}} = \varepsilon^0_{n,\mathbf{k}} + s_j|\Delta_{n\mathbf{k}}| \tag{3.9}$$

In Eqs.(3.8)-(3.9), $n = \{v, c\}$, $j = \{1, 2\}$, $s_j = -1$ $(+1)$ for $j = 1$ $(j = 2)$, $\Delta_{n\mathbf{k}} = \langle\phi^{L_1}_{n\mathbf{k}}|\hat{h}_{IL}|\phi^{L_2}_{n\mathbf{k}}\rangle$ and

$$\begin{aligned} |\tilde{\phi}^{L_1}_{n\mathbf{k}}\rangle &= e^{i\frac{\gamma_{n\mathbf{k}}}{2}}|\phi^{L_1}_{n\mathbf{k}}\rangle \\ |\tilde{\phi}^{L_2}_{n\mathbf{k}}\rangle &= e^{-i\frac{\gamma_{n\mathbf{k}}}{2}}|\phi^{L_2}_{n\mathbf{k}}\rangle \end{aligned} \tag{3.10}$$

where $\gamma_{n\mathbf{k}} = \mathrm{Arg}[\Delta_{n\mathbf{k}}]$. Notice that $\gamma_{n\mathbf{k}}$ guarantees that the relative phase between the projections of a Bloch state $|\varphi_{n_j\mathbf{k}}\rangle$ on $2p_z$ orbitals localized on different layers is gauge invariant, i.e. it does not change under the transformation $c_{\alpha_1}(n\mathbf{k}) \to e^{i\eta}c_{\alpha_1}(n\mathbf{k})$, η being an arbitrary phase.

We point out that the zero-order expression given by Eq.(3.8) is a good approximation for the two lowest $\hat{\sigma}_{\Gamma M''}$-odd conduction bands and the two highest-energy $\hat{\sigma}_{\Gamma M''}$-even valence bands, for the considered $\mathbf{k}$ vectors along $\Gamma M''$ direction. In principle one should also consider other terms in the expression of the eigenstates, coming from higher orders of the perturbative series, describing the coupling between $|\phi^{L_i}_{n\mathbf{k}}\rangle$ and the eigenstates of $\mathbf{h}_{IN}$ with different eigenvalues. For $\mathbf{k}$ points around the middle of $\Gamma M''$ direction, these terms can be neglected in first approximation, as the other eigenstates of $\mathbf{h}_{IN}$ with the same $\hat{\sigma}_{\Gamma M''}$-parity of $|\phi^{L_i}_{n\mathbf{k}}\rangle$ have energies far from $\varepsilon^0_{n,\mathbf{k}}$ (w.r.t. to the interlayer coupling strength), so that the hybridization is negligible. Our numerical results indicate that these neglected terms become more relevant for $\mathbf{k}$ along this direction, but close to Γ point.

Therefore, looking at Eq.(3.8), we can understand that the lowest odd-conduction band and the highest even-valence can be seen, respectively, as antibonding and bonding combinations of the conduction and the valence states localized on the two monolayers; we remind that the states defined in Eq.(3.10) are still eigenstates of the intralayer hamiltonian $\hat{h}_{IN}$, with $|\tilde{\phi}^{L_2}_{n\mathbf{k}}\rangle = -\hat{\mathrm{I}}\cdot\hat{\mathrm{T}}|\tilde{\phi}^{L_1}_{n\mathbf{k}}\rangle$.

Starting from Eq.(3.8), we can evaluate the interband matrix element between the last occupied valence $|\varphi_{v_2\mathbf{k}}\rangle$ and the lowest unoccupied conduction $|\varphi_{c_1\mathbf{k}}\rangle$, $\mathbf{d}^{\epsilon}_{v_2c_1\mathbf{k}}$, as

$$\begin{aligned} \mathbf{d}^{\epsilon}_{v_2c_1\mathbf{k}} = \frac{1}{2}\Big[&\langle\tilde{\phi}^{L_1}_{v\mathbf{k}}|\hat{\epsilon}\cdot\mathbf{r}|\tilde{\phi}^{L_1}_{c\mathbf{k}}\rangle - \langle\tilde{\phi}^{L_2}_{v\mathbf{k}}|\hat{\epsilon}\cdot\mathbf{r}|\tilde{\phi}^{L_2}_{c\mathbf{k}}\rangle \\ &+ \langle\tilde{\phi}^{L_2}_{v\mathbf{k}}|\hat{\epsilon}\cdot\mathbf{r}|\tilde{\phi}^{L_1}_{c\mathbf{k}}\rangle - \langle\tilde{\phi}^{L_1}_{v\mathbf{k}}|\hat{\epsilon}\cdot\mathbf{r}|\tilde{\phi}^{L_2}_{c\mathbf{k}}\rangle\Big] \end{aligned} \tag{3.11}$$

being $\hat{\epsilon}$ the light polarization direction. To make the treatment simpler, we neglect the last two terms in Eq.(3.11) in the following, as they involve states localized on different layers, so that their value is generally small as a result of the reduced overlap among these wavefunctions.
In this way we obtain that the interband dipole is the difference between intralayer-interband dipoles

$$\mathbf{d}^{\epsilon}_{\mathrm{L}_i}(\mathbf{k}) = \langle \tilde{\phi}^{\mathrm{L}_i}_{v,\mathbf{k}} | \hat{\epsilon}\cdot\mathbf{r} | \tilde{\phi}^{\mathrm{L}_i}_{c,\mathbf{k}} \rangle \tag{3.12}$$

Intralayer-interband dipoles defined in Eq.(3.12) have been directly evaluated as

$$\begin{aligned} d^{\epsilon}_{\mathrm{L}_1} &= e^{\frac{i}{2}(\gamma_{c\mathbf{k}}-\gamma_{v\mathbf{k}})} \langle \phi^{\mathrm{L}_1}_{v\mathbf{k}} | \hat{\epsilon}\cdot\mathbf{r} | \phi^{L_1}_{c\mathbf{k}} \rangle \\ d^{\epsilon}_{\mathrm{L}_2} &= e^{-\frac{i}{2}(\gamma_{c\mathbf{k}}-\gamma_{v\mathbf{k}})} \langle \phi^{\mathrm{L}_2}_{v\mathbf{k}} | \hat{\epsilon}\cdot\mathbf{r} | \phi^{L_2}_{c\mathbf{k}} \rangle \end{aligned} \tag{3.13}$$

making use of Eq.(3.10) to express layer localized single particle states and evaluating $\gamma_{n\mathbf{k}}$ as the phase of

$$\Delta_{n\mathbf{k}} = \sum_{\alpha_1,\beta_2} c^*_{\alpha_1}(n\mathbf{k}) c_{\beta_2}(n\mathbf{k}) h^{\alpha_1,\beta_2}_{\mathrm{IL}}(\mathbf{k})$$

where index α_1 (β_2) runs over the $2\mathrm{p}_z$ states localized on Layer L_1 (L_2), while $h^{\alpha_1,\beta_2}_{\mathrm{IL}}(\mathbf{k})$ is the interlayer coupling matrix element, written in the basis of the Bloch states $|\psi^W_{\alpha\mathbf{k}}\rangle = \frac{1}{\sqrt{N}}\sum_{\mathbf{R}} e^{i\mathbf{k}\cdot\mathbf{R}} |\alpha\mathbf{R}\rangle$.
The matrix elements appearing in Eq.(3.13) have been evaluated following Refs.[89, 73],

$$\langle \phi^{\mathrm{L}_i}_{v\mathbf{k}} | \hat{\epsilon}\cdot\mathbf{r} | \phi^{L_i}_{c\mathbf{k}} \rangle = \frac{\hat{\epsilon}\cdot\langle \phi^{\mathrm{L}_i}_{v\mathbf{k}} | [\mathbf{r}, \hat{H}] | \phi^{L_i}_{c\mathbf{k}} \rangle}{\varepsilon^0_{c\mathbf{k}} - \varepsilon^0_{v\mathbf{k}}} = \frac{\sum_{\alpha_i\beta_i} c^*_{\alpha_i}(v\mathbf{k}) c_{\beta_i}(c\mathbf{k}) \hat{\epsilon}\cdot\mathbf{p}_{\alpha_i\beta_i}(\mathbf{k})}{\varepsilon^0_{c\mathbf{k}} - \varepsilon^0_{v\mathbf{k}}} \tag{3.14}$$

where, the index i runs over the two layers, $\varepsilon^0_{n\mathbf{k}}$ are the eigenvalues of the intralayer hamiltonian $\mathbf{h}_{\mathrm{IN}}$ and $\mathbf{p}_{\alpha_i\beta_i}(\mathbf{k})$ is defined as

$$\mathbf{p}_{\alpha_i\beta_i}(\mathbf{k}) = \sum_{\mathbf{R}} e^{i\mathbf{k}\cdot\mathbf{R}} t(\alpha_i 0, \beta_i \mathbf{R}) \Big(\tau_{\alpha_i} - \tau_{\beta_i} - \mathbf{R} \Big) \tag{3.15}$$

$t(\alpha_i 0, \beta_i \mathbf{R})$ representing the intralayer hopping matrix elements, within layer L_i.

If $\hat{\epsilon}$ is chosen along $\Gamma\mathrm{M}''$ direction, we immediately find that $\mathbf{d}^{\epsilon}_{\mathrm{L}_1}(\mathbf{k}) = \mathbf{d}^{\epsilon}_{\mathrm{L}_2}(\mathbf{k}) = 0$, because of the parity of layer resolved states, given by Eq. 3.7. However, if $\hat{\epsilon}$ is taken along the direction $\Gamma\mathrm{K}$, orthogonal to $\Gamma\mathrm{M}''$, we cannot justify the quenching by straightforward symmetry arguments. To clarify this point, in Figure 3.9a we show the modulus (upper panel) of the intralayer-interband dipoles $\mathbf{d}^{\Gamma\mathrm{K}}_{\mathrm{L}_1}(\mathbf{k})$ and $\mathbf{d}^{\Gamma\mathrm{K}}_{\mathrm{L}_2}(\mathbf{k})$, together with their relative phase (lower panel)

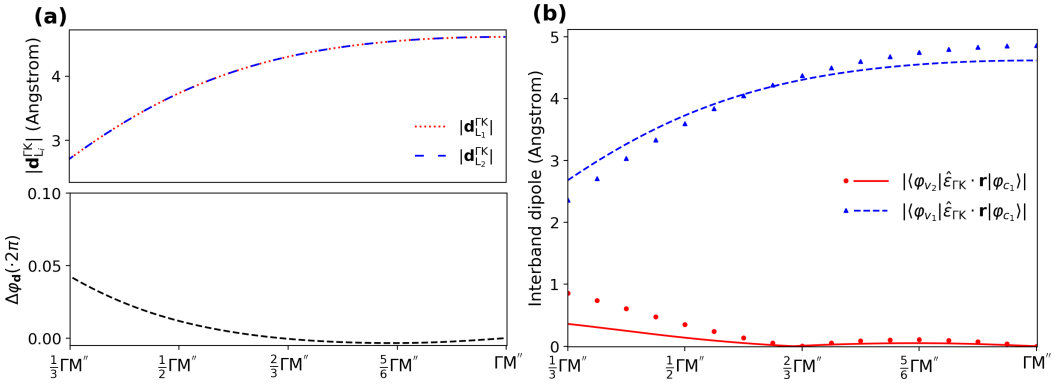

Figure 3.9: Interband dipole matrix elements for $\mathbf{k}$ along ΓM″ direction, in the interval $[\frac{|\Gamma M''|}{3}, |\Gamma M''|]$. In the upper panel of (a) we show the moduli of $\mathbf{d}^{\epsilon}_{L_i}$ for light polarization along ΓK for the two layers $i = 1, 2$, while in the lower panel the phase difference among $\mathbf{d}^{\epsilon}_{L_1}$ and $\mathbf{d}^{\epsilon}_{L_2}$ is presented. In (b) the red continuous (blue dashed) line corresponds to the interband dipole between $|\varphi_{v_2,\mathbf{k}}\rangle$ ($|\varphi_{v_1,\mathbf{k}}\rangle$) and $|\varphi_{c_1,\mathbf{k}}\rangle$ computed using the TB model. Dots and triangles represent the same quantities computed fully *ab initio* using `Yambo` code. Light polarization versor is assumed aligned along ΓK direction.

$\Delta\varphi_{\mathbf{d}} = \mathrm{Arg}[\mathbf{d}^{\Gamma K}_{L_1}(\mathbf{k})] - \mathrm{Arg}[\mathbf{d}^{\Gamma K}_{L_2}(\mathbf{k})]$. We notice that the moduli are equal while their relative phase is close to zero in the range of $\mathbf{k}$ points here considered, i.e. $|\mathbf{k}|$ in $[\frac{|\Gamma M''|}{3}, |\Gamma M''|]$. This means that the total interband dipole will be almost zero, as a consequence of the destructive interference of the two layer-resolved components. In other words, the transition probability from $|\varphi_{v_2,\mathbf{k}}\rangle$ to $|\varphi_{c_1,\mathbf{k}}\rangle$ due to ΓK polarized light can be interpreted as the quantum superposition of the interband scattering processes occurring on the two layers separately, whose probability amplitudes are out-of-phase, giving an overall negligible interband oscillator strength. In Figure 3.9b, the red line indicates the interband dipole between $|\varphi_{v_2,\mathbf{k}}\rangle$ and $|\varphi_{c_1,\mathbf{k}}\rangle$, computed using the perturbative solution of the TB model, while the red dots are the same quantities obtained *ab initio* with `Yambo`, to check the validity of our approximate treatment. We notice that, as this cancellation is not symmetry-constrained, the interband dipole is small, but not exactly zero. Such cancellation is exact only at M″ point, because of symmetry reasons. In fact, as M″ is invariant under spatial inversion $\hat{\mathrm{I}}$, we can assign inversion-parity labels to the states at this point. *Ab initio* results indicate that both $|\varphi_{v_2,\mathbf{k}}\rangle$ and $|\varphi_{c_1,\mathbf{k}}\rangle$ are odd under $\hat{\mathrm{I}}$ exactly as $\mathbf{d}_{\Gamma K}$, therefore the overall matrix element is zero.
We point out that the interband dipole is non-zero, once the transition between a pair of bonding or antibonding combinations is considered: for example, taking into account the scattering $|\varphi_{v_1,\mathbf{k}}\rangle \rightarrow |\varphi_{c_1,\mathbf{k}}\rangle$, the intralayer-interband transition amplitudes sum constructively giving an intense overall interband dipole. This is confirmed in Fig.3.9b, where this quantity is shown as computed using the model (dashed blue line) and fully *ab initio* using

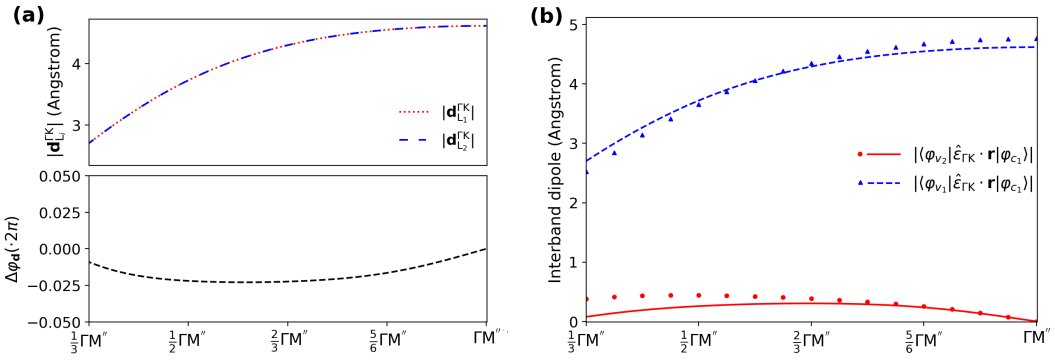

Figure 3.10: Interband dipole matrix elements computed for bilayer C_3N with AB stacking. This Figure in analogous to Figure 3.9, where the same quantities for AB′ stacking are shown.

`Yambo`(blue triangles). We further notice that the reasonable agreement between the model and the ab initio results is an *a posteriori* confirmation of the validity of Eq. (3.8) to describe single particle states along ΓM″.
To complete this analysis, in Figure 3.10 we present the interband dipoles in AB-C_3N, for $\mathbf{k}$ along the ΓM″ direction, in the interval $[\frac{|\Gamma M''|}{3}, |\Gamma M''|]$, assuming light polarization versor $\hat{\epsilon}$ along the ΓK direction, orthogonal to ΓM″. As in Figure 3.9a, the upper panel shows the modulus of both $\mathbf{d}^{\Gamma K}_{L_1}$ and $\mathbf{d}^{\Gamma K}_{L_2}$, while their phase difference is shown in the lower panel. In Fig. 3.10b we present as a red continuous (blue dashed) line the interband dipole matrix elements computed between $|\varphi_{v_2\mathbf{k}}\rangle$ ($|\varphi_{v_1\mathbf{k}}\rangle$) and $|\varphi_{c_1\mathbf{k}}\rangle$, again assuming light polarization along ΓK direction: dots and triangles correspond to the same quantities as computed with `Yambo` code.
We notice that these results are qualitatively analogous to those discussed for AB′ stacking motif. In other words, the intralayer-interband dipoles $\mathbf{d}^{\Gamma K}_{L_1}$ and $\mathbf{d}^{\Gamma K}_{L_2}$ have the same moduli, and a phase difference which is close to zero, in the interval of considered $\mathbf{k}$ points. Therefore, once we compute the interband dipole between $|\varphi_{v_2\mathbf{k}}\rangle$ and $|\varphi_{c_1\mathbf{k}}\rangle$, they are subtracted one from the other, giving an overall negligible interband dipole for the bilayer; on the other hand, if the interband dipole between $|\varphi_{v_1\mathbf{k}}\rangle$ and $|\varphi_{c_1\mathbf{k}}\rangle$ is computed, their contributions sum in phase, giving an intense optical strength.
Even if not shown, we underline that once $\hat{\epsilon}$ is chosen parallel to the ΓM″ direction, the dipole matrix elements are exactly zero: the reason is that, while the dipole operator is invariant under $\hat{\sigma}_{\Gamma M''}$ mirror symmetry, conduction and valence states have opposite parity, so that the resulting matrix element is constrained to be null for symmetry.
Finally, we point out that, because of the three-fold rotational symmetry of AB-C_3N, similar results can be obtained for interband dipoles computed considering $\mathbf{k}$ along ΓM and ΓM′ directions: in all these cases, if the polarization versor is parallel to $\mathbf{k}$, the interband dipole among the topmost valence and the lowest conduction is null by symmetry; instead, if light polarization is orthog-

onal to $\mathbf{k}$, these interband dipoles are not constrained to zero by symmetry, but they assume small values because of the cancellation of the intralayer contributions.

3.6 Conduction states quasi-degeneracy along ΓM direction in AB′ stacking

Before discussing the case of bilayer C_3N with AA′ stacking, in this Section we do a step backward and we provide a qualitative rationale for the negligible splitting among the two lowest unoccupied conduction bands along ΓM direction in bilayer C_3N with AB′ stacking. This quasi-degeneracy is rather peculiar and counterintuitive: in fact, taking multiple equivalent layers and letting them interact, one generally expects to observe energy separation between the resulting single particle states, as a direct consequence of the coupling among the layers themselves. This concept is usually referred to as Davydov splitting, and has been also observed in the case of vibrational modes in multilayer Transition Metal Dichalcogenides [90, 91]. Such splitting between the two lowest unoccupied conduction states is effectively observed AB′-C_3N once $\mathbf{k}$ is chosen along the ΓM″ direction.
Following the approach of Section 3.5, we consider the interlayer coupling as a perturbation of the intralayer terms in the Tight Binding Hamiltonian: as a consequence, we can express the splitting among the conduction states within first order degenerate perturbation theory as $\langle\phi^{L_1}_{c\mathbf{k}}|\hat{h}_{IL}|\phi^{L_2}_{c\mathbf{k}}\rangle$, being $|\phi^{L_1}_{c\mathbf{k}}\rangle$ and $|\phi^{L_2}_{c\mathbf{k}}\rangle$ the conduction eigenstates of $\hat{h}_{IL}$, localized on the two layers.
If we assume that the diagonal blocks of the intralayer Hamiltonian $\hat{h}_{IN}$ can be approximated with the Tight-Binding Hamiltonians of the two isolated layers, we can realize that they are both (approximately) invariant under mirror reflection w.r.t. planes parallel to $\hat{\sigma}_{\Gamma M}$ direction. This is clarified in Figure 3.11b, where we split the unit cell of AB′-C_3N (shown in Figure 3.11a) into two portions corresponding to the atoms on the two layers. We can see that each layer has its own mirror vertical symmetry plane (represented by black dashed lines in Fig. 3.11b) and that such planes are shifted one respect to the other as the two monolayers have a relative shift within the AB′ bilayer. As the lowest conduction band with $\mathbf{k}$ parallel to ΓM is odd under mirror symmetry in the isolated monolayer, we can understand that $|\phi^{L_1}_{c\mathbf{k}}\rangle$ and $|\phi^{L_2}_{c\mathbf{k}}\rangle$ will have non-zero projection only on the $2p_z$ states localized on the atoms marked by red squares in Fig. 3.11b: this happens because such functions must have a nodal line along the vertical direction, as a consequence of their odd-character w.r.t. to the vertical mirror plane (no contribution is observed from Nitrogen atoms as they are transferred into themselves under these in-layer mirror symmetry, apart from a lattice vector $\mathbf{a}_1$).
Therefore, the atoms where the conduction-eigenstates of $\hat{h}_{IN}$ are localized form a sublattice invariant under $\hat{\sigma}_{\Gamma M}$ mirror symmetry: this is clarified in

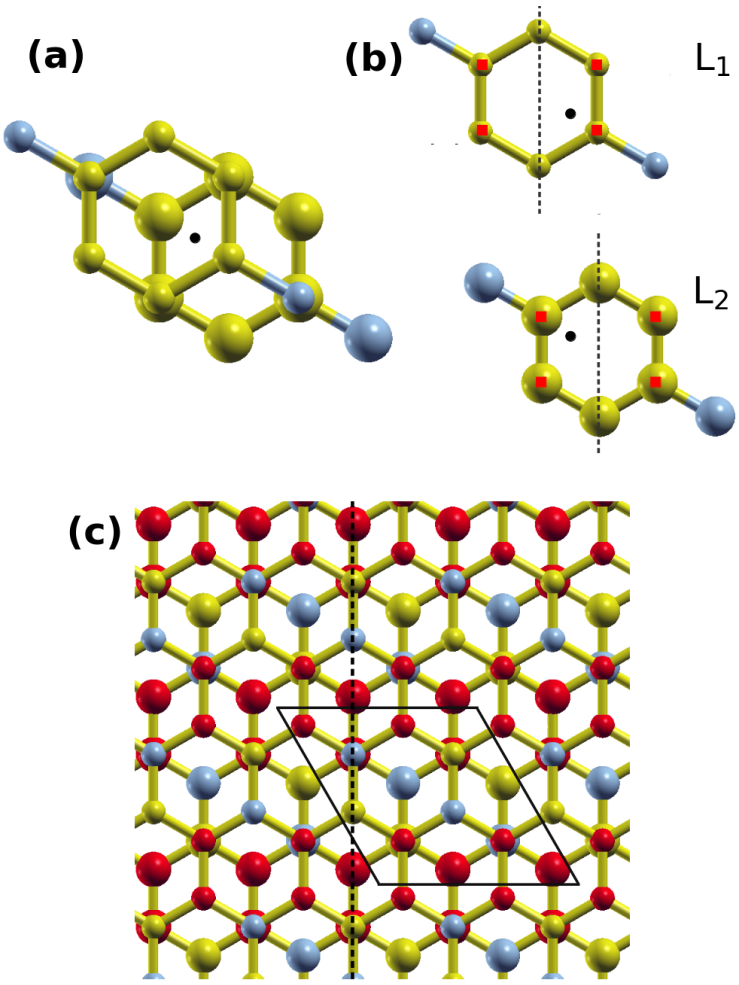

Figure 3.11: Unit cell of BL-C_3N with AB′ stacking is shown in a), with the black dot denoting the center of spatial inversion symmetry. The notation is analogous to the one used in Figure 3.3. b) represents the split unit cell, where the atoms on layer L_1 are separated from those on layer L_2. The dashed black lines represent mirror symmetry planes parallel to $\hat{\sigma}_{\Gamma M}$, within the separate layers, while the black dots indicate the in plane position of the inversion center of the whole bilayer. Notice that these mirror planes are shifted one w.r.t. the other. Atoms denoted by red squares are those where the states $|\phi^{L_1}_{c\mathbf{k}}\rangle$ and $|\phi^{L_2}_{c\mathbf{k}}\rangle$ are localized. c) Crystal structure of BL-C_3N with AB′ stacking, where the red spheres indicate the Carbon atoms forming the sublattice invariant w.r.t. $\hat{\sigma}_{\Gamma M}$; this symmetry is represented by the black dashed vertical line.

Figure 3.11c where the atoms forming the sublattice are shown in red, while the mirror plane is represented by the vertical dashed line. As this sublattice is $\hat{\sigma}_{\Gamma M}$ invariant, we can assume that the interlayer Hamiltonian which pairs the atoms within this sublattice on different layers is invariant w.r.t. $\hat{\sigma}_{\Gamma M}$: this is clearly not strictly exact, as the interlayer hoppings are affected by the fact that the overall bilayer lattice does not possess such symmetry, but it can be assumed as a reasonable working assumption.
Then, the state $|\phi^{L_1}_{c\mathbf{k}}\rangle$ is odd under $\hat{\sigma}_{\Gamma M}$ (as such plane coincide with the in-layer mirror plane, shown in 3.11b), while $|\phi^{L_2}_{c\mathbf{k}}\rangle$ is even, as each site on L_2 are transformed into themselves (apart from a lattice vector $\mathbf{a}_1$) by this symmetry operation. As a consequence, $\langle\phi^{L_1}_{c\mathbf{k}}|\hat{h}_{IL}|\phi^{L_2}_{c\mathbf{k}}\rangle \approx 0$ as the states have different parity w.r.t. $\hat{\sigma}_{\Gamma M}$, while $\hat{h}_{IL}$ is (approximately) invariant. Once we consider $\mathbf{k}$ close to Γ, the splitting increases, despite remaining less that 50 meV: this is beyond the presented reasoning, and can be justified, for example, via higher order terms of the perturbative expansion.
We also notice that this splitting appears for $\mathbf{k}$ along $\Gamma M''$ as $|\phi^{L_1}_{c\mathbf{k}}\rangle$ and $|\phi^{L_2}_{c\mathbf{k}}\rangle$ have the same parity under mirror symmetry $\hat{\sigma}_{\Gamma M''}$.

3.7 The case of AA′ stacking

As discussed in the Introduction, together with AB and AB′ stackings, another stable bilayer C_3N motif is AA′. The crystal structure of AA′-C_3N is shown in Figure 3.12a. This stacking has an inversion symmetry center (shown by the red dot in Fig. 3.12a), two mirror symmetry planes represented by red dashed lines and a two-fold rotation axis parallel to the stacking direction (indicated by the green dot). Interestingly, this stacking-motif is also invariant w.r.t. the nonsymmorphic symmetry operation $\{\sigma_{xy}|\vec{\tau}\}$, corresponding to $z \to -z$ mirror symmetry followed by fractional traslation of vector $\vec{\tau}$, represented by the red arrow.
Structural optimization within PBE-D2 provides an in-plane lattice parameter a = 4.849 Å, while the interlayer distance is equal to 3.22 Å, similarly to the other two stackings. The electronic bandstructure (shown in Fig.3.12b) exhibits a metallic character: the highest valence state (found at M′ point) has an higher energy than the lowest conduction state, occurring at the Γ point, with a corresponding negative "gap" of Γ_c - M'_v = -0.31 eV. Such metallicity (also found in Ref.[43]) is a problem related to PBE functional, as experimentally AA′-C_3N has been shown to have a finite gap of about 0.4 eV [2].
The use of such metallic ground state to compute both QP corrections and optical properties is problematic, as it would induce a fictitious over-screening effect once the electron-electron screened interaction is evaluated using RPA approximation, providing unaccurate values for electronic gaps and exciton binding energies.

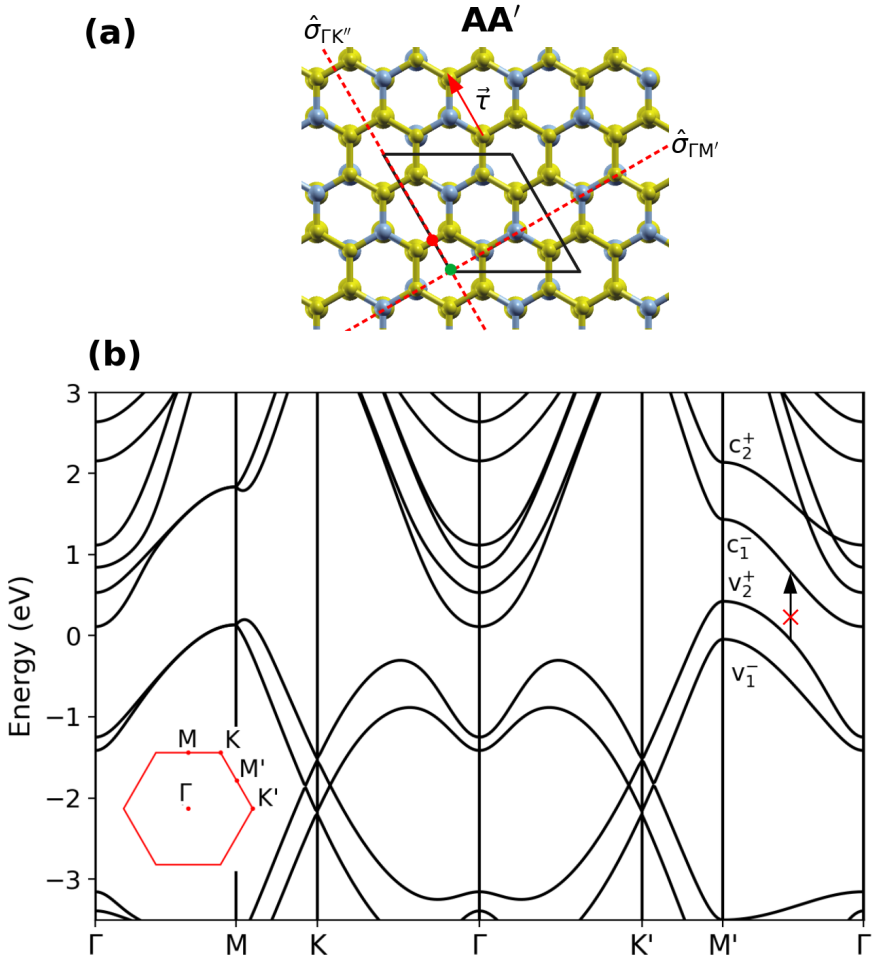

Figure 3.12: Crystal structure for bilayer C_3N with AA′ stacking is shown in a). The red dot indicates the in-plane position of the inversion symmetry center, the dashed red lines represent mirror symmetry planes parallel to the stacking direction and the green dot denotes the in-plane position of the two-fold rotation axis parallel to the stacking direction. Finally the red arrow represents the fractional translation $\vec{\tau}$ discussed in the main test. The DFT-PBE electronic structure is shown in b): along the direction ΓM′ the highest valence and the lowest conduction bands are labeled according to their parity w.r.t. $\{\sigma_{xy}|\vec{\tau}\}$ symmetry operation.

We now assume that the Kohn-Sham states computed at the PBE level are anyhow a good approximation for electronic wavefunctions, despite the values of the associated Kohn-Sham energies give a metallic ground state. With this assumption, we speculate about the fact that, also for this stacking, the low energy absorption will be quenched, in this case because of symmetry reasons and we will confirm our analysis via an approximate solution of the BSE.
Figure 3.12b indicates that the lowest direct band gap occurs almost in the middle of the $\Gamma M'$ direction: as a consequence, it is reasonable to expect that the low energy transitions which will contribute to the lowest energy excitons will come from this portion of the BZ. $\mathbf{k}$ points along this direction are invariant both under $\hat{\sigma}_{\Gamma M'}$ mirror symmetry and $\{\sigma_{xy}|\vec{\tau}\}$, therefore the electronic states can be properly labeled according to how they transform under these symmetries. Our DFT results indicate that the highest valence band is even under $\{\sigma_{xy}|\vec{\tau}\}$, while the lowest conduction is odd: these two states are respectively indicated as v_2^+ and c_1^- in Fig.3.12b. As the dipole operator $\mathbf{d}_\epsilon$ is invariant under $\{\sigma_{xy}|\vec{\tau}\}$ (assuming, as usual, incoming light with polarization direction $\hat{\epsilon}$ orthogonal to the stacking direction z), the matrix element $\langle\varphi_{v_2\mathbf{k}}|\hat{\epsilon}\cdot\mathbf{r}|\varphi_{c_1\mathbf{k}}\rangle$ will be zero, independently from the direction of the polarization versor $\hat{\epsilon}$. Therefore, we expect light-induced scattering between these bands to be forbidden by symmetry and consequently the low-energy excitons composed by these transitions to be optically dark.
To confirm these considerations, we solve BSE with a set of assumptions aimed at avoiding the spurious, DFT-induced metallicity. In practice:

- the static RPA electron-electron interaction in the direct part of the BSE kernel has been computed using Kohn Sham wavefunctions obtained from DFT-PBE, but applying a rigid shift s_0^W to all the empty states. Such parameter has been chosen so that the minimum gap Γ_c - M'_v of the resulting band-structure was positive but smaller than the one found experimentally, to avoid under-screening effects;

- in the independent-particle part of the excitonic hamiltonian we mimic quasi-particle corrections via a scissor operator applied to the DFT bands, manually chosen to obtain a minimum indirect band gap Γ_c - M'_v equal to the experimental one (0.4 eV). We underline that such scissor is therefore larger than the one introduced in the calculation of electronic screening.

The results of these calculations (performed on a 48x48x1 $\mathbf{k}$-grid as for the other stackings) are shown in Figure 3.13: in Fig.3.13a (Fig.3.13b) we display the results obtained for $s_0^W = 0.35$ eV ($s_0^W = 0.45$ eV). These absorption spectra (which exhibit small variations changing s_0^W) confirm the symmetry-based discussion just presented. In fact, in both cases, low energy excitons (whose positions are indicated by black vertical bars in the insets) are optically dark independently from the polarization direction, as no absorption structure

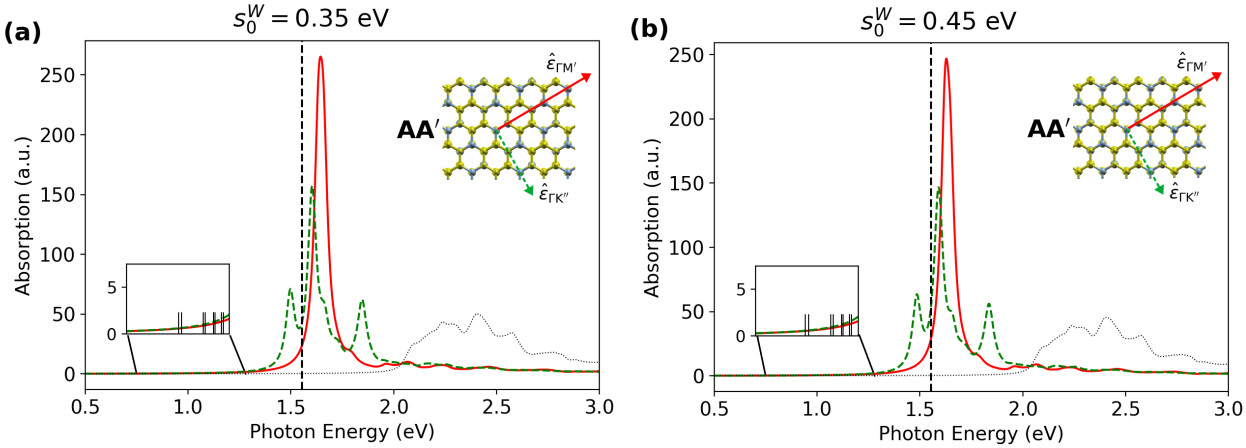

Figure 3.13: Absorption spectra for AA′-C_3N, computed using rigid shift parameters s_0^W equal to 0.35 eV (a) and 0.45 (b). In both graphs, polarization directions are shown on top of the crystal structure, while the vertical dashed line indicates the energy of the minimum direct gap. Finally, the black dotted line represents the independent particle absorption spectra.

is observed in the low energy region between 0.75 eV and 1.25 eV, where exciton-bound states are found. Such bound excitons are due to single particle transitions between bands v_2^+ and c_1^- along the Γ-M′ direction, as clarified in Figure 3.14, where we show the weights of single particle transitions between these bands for $\mathbf{k}$ in the full hexagonal BZ.

3.8 Summary and perspectives

In this Chapter, we have discussed electronic and optical properties of Bilayer C_3N with different stackigs motifs, using state-of-art fully *ab initio* calculations. Our results indicate a peculiar behaviour of BL-C_3N, i.e. a strong quenching of low-energy optical absorption due to the negligible oscillator strength of the discrete bound excitons composed by electron-hole transitions with energies close to the minimum electronic direct gap. These findings have been justified in terms of independent particle effects, i.e. as due to the negligible interband dipole between the lowest conduction and the topmost valence bands involved in the formation of these excitons. In AB and AB′ stackings we have demonstrated that the overall interband dipole assumes negligible values because of the destructive interference of the contributions coming from the two layers, while, in the case of AA′ stacking, the optical quenching is protected by the symmetries of the system.
This work could pave the way to future theoretical and experimental investigations on multilayer C_3N. On the one hand, it could be fascinating to investigate how optical properties of C_3N can be tuned varying the number of stacked monolayers or changing the twist angle between them. On the

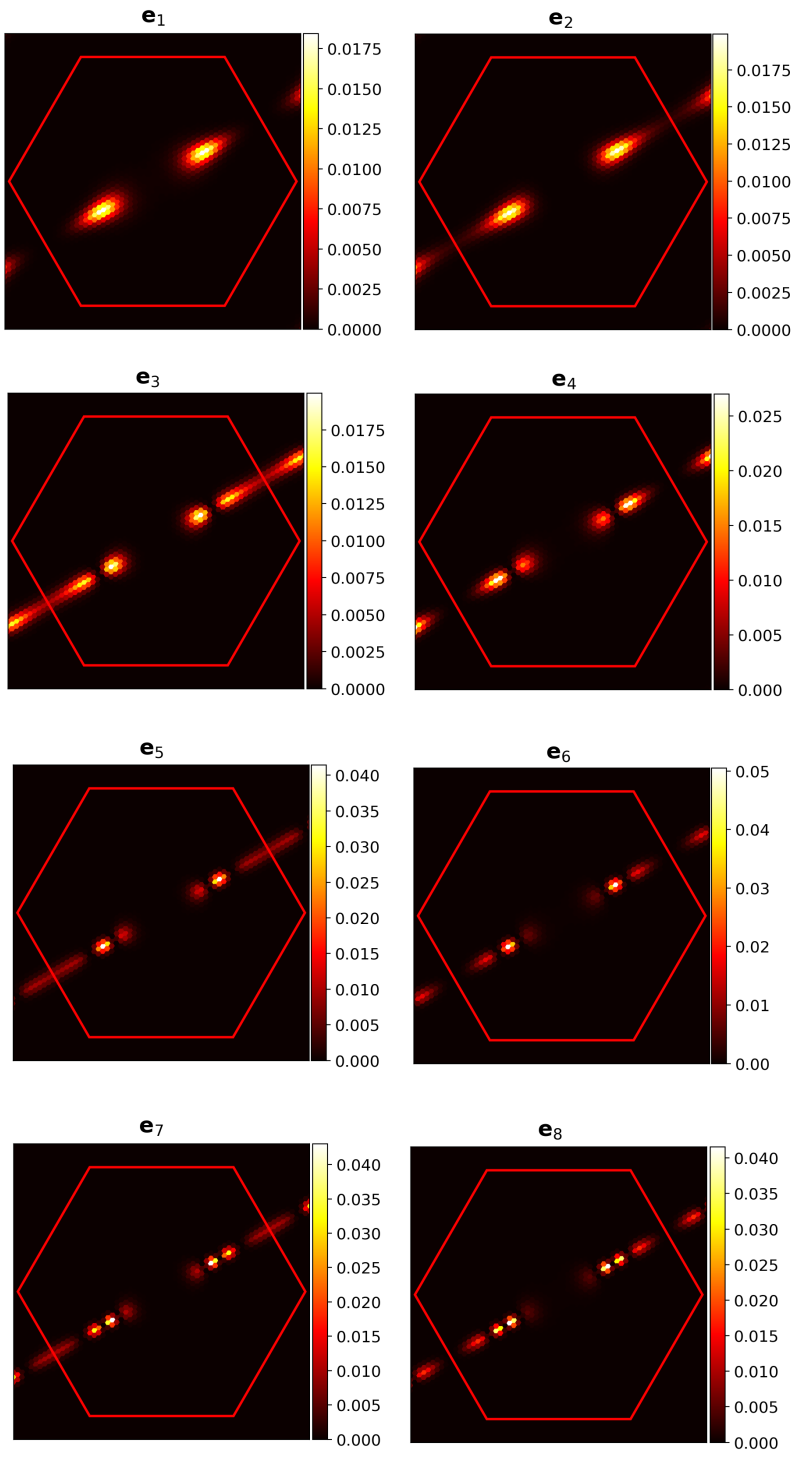

Figure 3.14: Exciton **k**-space distribution as defined in Eq.(3.1) (with v and c corresponding to the last occupied valence and the lowest unoccupied conduction respectively), for the eight lowest-energy excitations obtained fixing s_0^W = 0.35 eV. These states are labeled according to their increasing excitation energy.

other hand, the abundant presence of dark or quasi-dark low-energy excitons in BL-C_3N could have important effects on exciton lifetimes and dynamics.

Chapter 4

Phonon-assisted luminescence in rhombohedral Boron Nitride

In this Chapter we present an *ab initio* investigation of phonon-assisted light emission by finite-momentum excitons in rhombohedral boron nitride (rBN). In collaboration with the experimental group of Prof. Annick Louiseau and Prof. Julien Barjon, we have exploited our results to interpret the emission spectra experimentally measured via Cathodoluminescence in high quality rBN samples. Furthermore, by comparing experimental and theoretical results obtained for rBN and hexagonal boron nitride (hBN), we have demonstrated that phonon-assisted radiative emission from indirect excitons allows identifying different BN stackings.

The content of this Chapter is reported in part in the manuscript *Optical signatures of the rhombohedral polymorph of sp_2 boron nitride*.

4.1 Introduction

When sp_2 hybridized, boron and nitrogen atoms can form 1D nanotubes, 2D layers with a honeycomb lattice[92], or layered three-dimensional crystals. In 2D monolayers, these atoms form a regular hexagonal lattice, in which each hexagonal ring is composed by the same number of boron and nitrogen atoms. Bulk crystals are then formed by stacking these single-layers, which interact among themselves via weak and long-ranged Van der Waals interaction.
According to the relative orientations of the stacked layers, different sp_2-BN bulk crystals can be obtained. The most common (and also most thermodynamically stable) polytype is hexagonal boron nitride (hBN), firstly synthesized in high-quality and defect-free samples by Watanabe and co-workers [93, 94]: in this case, two consecutive BN single layers differ by a π rotation, resulting in the so-called AA$'$ stacking sequence, where boron and nitrogen atoms sit on top of each other.
Another possible stacking sequence is Bernal (or AB) boron nitride, recently

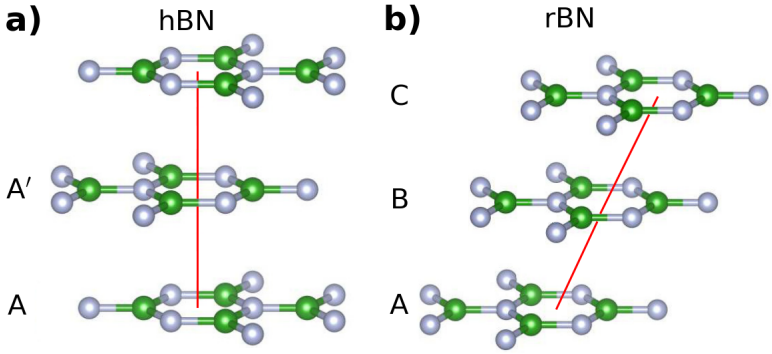

Figure 4.1: Stacking sequences of sp_2 BN considered in this Thesis: in a) Boron Nitride wih AA′ stacking is shown, while in b) the three shifted layers forming rBN unit cell are presented. Nitrogen and Boron atoms are respectively shown as green and gray spheres.

synthesized and studied via second harmonic generation and photoluminescence in Refs.[95, 96]. Its structure is obtained starting from two aligned BN monolayers and translating one of them by an in-plane BN interatomic distance, so that the centres of the hexagons of this layer are aligned with the atoms of the adjacent layers, along the stacking direction.
Finally, a different bulk BN polymorph is rhombohedral BN (rBN), in which the unit cell is composed by three BN monolayers, rigidly shifted along the same direction by the B-N planar interatomic distance, according to the so-called ABC stacking sequence [97, 98].
In the following, we will focus our attention on hBN and rBN crystals, whose stacking motifs are shown for completeness in Figure 4.1a and 4.1b, respectively.
Although composed by the same single layer building blocks, these stacking motifs are characterized by different electronic properties. Concerning this point, the fully *ab initio* work by Sponza and coworkers [99] demonstrated that Bernal BN is a direct gap insulator, while hBN and rBN are characterized by an indirect band gap. At the same time, as these polytypes only differ in the stacking sequence of the single layers, they can be hardly distinguished using crystallographic techniques. In addition, different BN stacking can coexist in the same crystal and the interaction with the substrate could also affect the relative abundance of the different phases in a given bulk BN sample[100, 101].
In this Chapter, we present a spectroscopic investigation of hBN and rBN using cathodoluminescence (CL) spectroscopy. By comparing CL spectra obtained for rBN with analogous results for hBN, we show that the stacking sequence affects the emission fine structure of rBN and hBN crystals, making CL an ideal experimental probe to discriminate between the two BN polytypes. The obtained experimental results are fully interpreted by *ab initio*

calculations of luminescence spectra for the two crystals, explicitly including exciton-phonon interactions.

4.2 Electronic properties of rBN

In this Section, we summarize the structural and electronic properties of rBN and we compare the obtained results with previous theoretical calculations available in the literature.
Rhombohedral boron nitride is modelled using a hexagonal lattice with six atoms per unit cell. Atomic positions and lattice parameters have been obtained fully *ab initio*, relaxing the structure up to when forces acting on atoms were smaller than 10^{-5} a.u. These ground states properties have been computed at the DFT level, using LDA approximation for the exchange-correlation potential, together with Pseudo-Potentials from the Pseudo-Dojo repository[102]. In all calculations, we have used a 100 Ry cut-off for the wavefunctions and the charge density has been computed using a 12x12x4 Monkhorst-Pack grid to sample the BZ.
The relaxation procedure gave an in-plane lattice parameter of 2.489 Å, and an out-of-plane cell dimension $c = 9.662$ Å. As expected, LDA tends to slightly underestimate experimental results ($a = 2.504$ Å, $c = 9.99$ Å[103]).
LDA electronic band structure has been computed starting from relaxed atomic positions: in Figure 4.2 we present the electronic bands for hBN (Fig. 4.2a) and for rBN (Fig. 4.2b), computed along the high symmetry path Γ-K-M-Γ-A. In agreement with the previous results by Sponza and collaborators, both stackings exhibit an indirect band gap, with the conduction minimum at the M point and the highest occupied valence state in proximity of the K point.
As DFT underestimates the band gap, we have computed QP corrections to KS energies within G_0W_0 approximation. The obtained QP corrections do not modify qualitatively the DFT electronic dispersion: their action has been included in the calculation of excitonic properties using a scissor-stretching operator, obtained by fitting QP corrections for π bands, which are the states involved in low energy excitons (see Fig. 4.2c and 4.2d). Inclusion of many body effects increase the electronic gap, which remain indirect in both stackings. In rBN (hBN) the minimum indirect gap has been found equal to 5.49 eV (5.66 eV), in reasonable agreement with G_0W_0 calculations of Ref.[99] (5.27 eV for rBN and 5.80 eV for hBN). The small discrepancies are probably due to the different structures used in Ref.[99], where experimental lattice parameters have been adopted.
The indirect gap nature of rBN (and analogously of hBN) strongly influences the excitonic dispersion in this material. In Figure 4.3 we present the energy of the lowest excitonic bands in rBN, assuming the exciton momentum $\mathbf{Q}$ aligned along the Γ-K direction of the hexagonal BZ (shown in the inset). The minimum-energy excitonic state available in the system has a non-zero

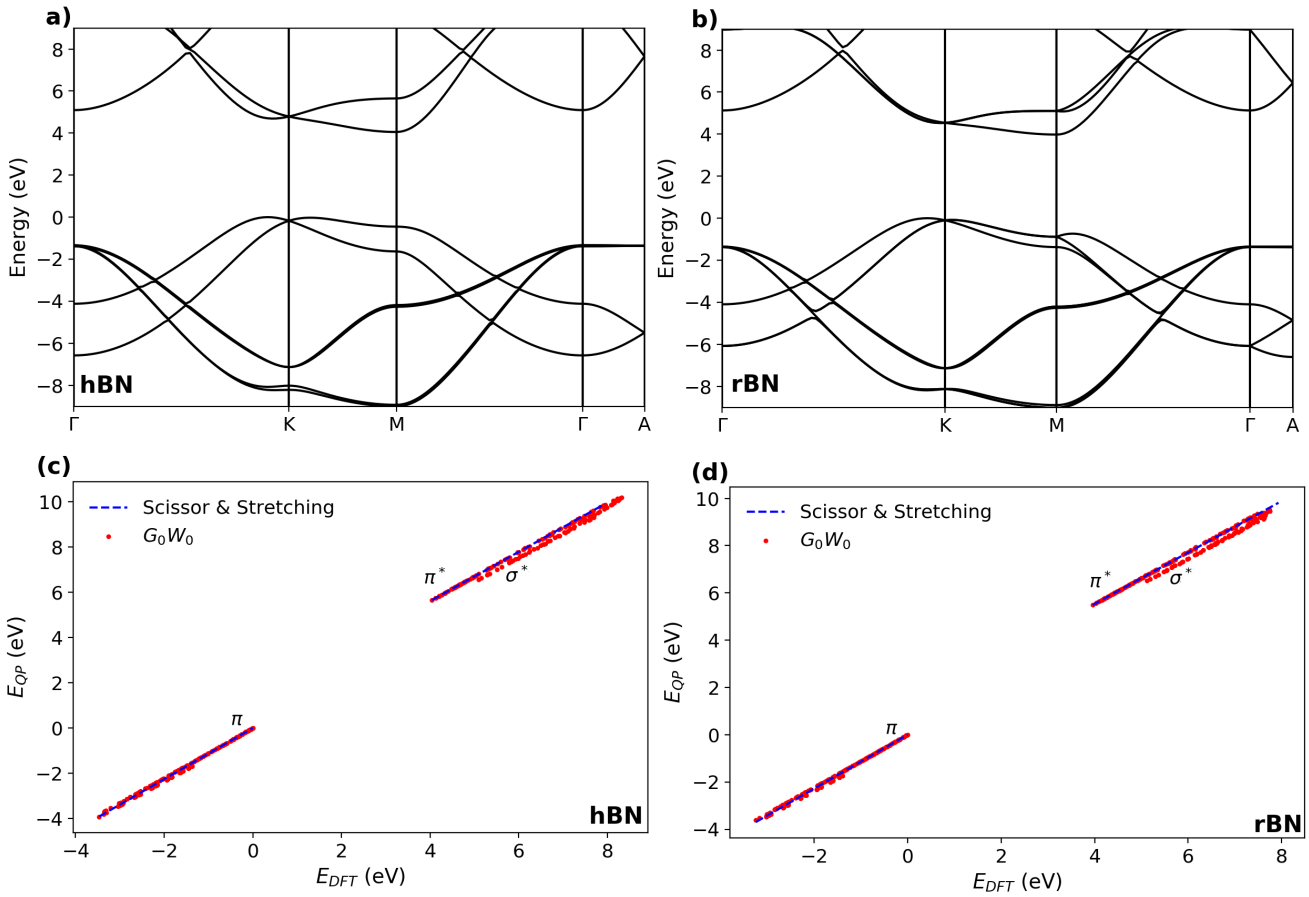

Figure 4.2: Electronic bandstructures for hBN (a) and rBN (b) computed within LDA-DFT. In panels c) and d) we show the linear scissor-stretching fits of the QP corrections obtained with G_0W_0 approach. Notice that σ^* states have not been included in the fitting procedure to obtain scissor-stretching parameters for the conduction bands.

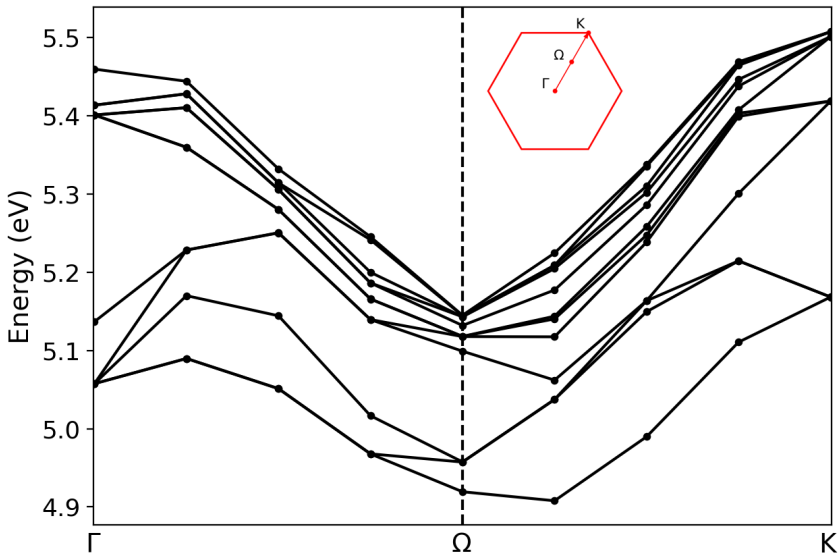

Figure 4.3: Exciton dispersion in rBN computed for exciton momentum $\mathbf{Q}$ along the in-plane Γ-K direction in the BZ.

momentum $\mathbf{Q}$: more precisely, the minimum energy is found at $\mathbf{Q} \approx \Omega$, being $\Omega = [\frac{1}{6}, \frac{1}{6}, 0]$ in reciprocal lattice units. Clearly, equivalent minima in the excitonic dispersion are found along the directions of the BZ equivalent to Γ-K, according to the symmetry operations of the C_{3v} point group of rBN.
These low energy excitons close to Ω are mainly composed by a hole located in proximity of K and an electron close to the M point. The reason why such electron-hole bound pairs have the lowest possible energy can be intuitively understood noting that these are the valence-to-conduction transitions with the lowest energy difference.
The obtained dispersion is in good agreement with the one proposed in the literature (see Figure 8 of Ref.[99]): furthermore, repeating analogous calculations for hBN, we have obtained an indirect excitonic dispersion, with minimum in the middle of Γ-K direction, similarly to Refs.[99, 83]
Having discussed the electronic and excitonic dispersions in hBN and rBN, we now discuss the theoretical approach we adopted to simulate luminescence spectra in these materials.

4.3 Theoretical model of finite-momentum exciton radiative emission

In cathodoluminescence (CL) experiments, the sample is excited by an external electron beam, which transfers energy to the material, with the subsequent creation of electron-hole bound pairs, i.e. excitons. The external beam is assumed to create a low density of electron-hole pairs, which can be therefore

treated as non-interacting bosonic particles[104]. By interaction with lattice phonon modes, these excitons will relax towards the states with the lowest possible energies: such states correspond to the minimum of the excitonic dispersion, shown in Figure 4.3 for rBN.
This mechanism of exciton creation and successive relaxation via coupling with the lattice is a complex and non-equilibrium process, whose fully *ab initio* description [105] is beyond the scope of this work. Therefore, in the following we model the quasi-equilibrium distribution of excitons close to the dispersion minima (resulting from the process just discussed) via a Boltzmann-like function, given by

$$N(E_\lambda(\mathbf{Q})) \propto e^{-\frac{E_\lambda(\mathbf{Q})-\mu}{k_B T_{exc}}} \tag{4.1}$$

which describes the occupation probability of the excitonic state $|\lambda, \mathbf{Q}\rangle$. In Eq.(4.1), μ is the excitonic chemical potential corresponding to the energy of the lowest accessible exciton, while T_{exc} is the excitonic temperature, controlling the excitonic distribution. This quantity has been measured by Cassabois and co-workers [106] as a function of the crystal temperature T (i.e. the temperature at which the experiment is performed). Experimental results indicate that for T smaller than 20 K, T_{exc} is constant and approximately equal to 50 K, while it increases almost linearly for larger T. In the following, as CL experiments were carried out at temperatures less than 10 K, we will fix T_{exc} to 20 K and 50 K, to demonstrate that our results are stable w.r.t. this parameter. We underline that, at the moment, T_{exc} is a fitting parameter which can be extracted only from experimental data.
This finite-momentum excitonic distribution cannot emit light via direct coupling with electromagnetic field, i.e. via a first order process, as a consequence of the mismatch between the nonzero exciton momentum and the photon wave-vector, which is almost zero for light frequency in the UV range (i.e. the frequencies emitted by BN samples). Therefore, the mechanism responsible for the emission is a second order process. An exciton $|\lambda\mathbf{Q}\rangle$ (close to the exciton dispersion minima) couples with the lattice and emits a phonon $(\nu\mathbf{Q})$, with subsequent scattering toward virtual excitonic states at Γ, from which photon emission can occur. An analogous process involving phonon absorption should also be taken into account. In the following, such processes are neglected as, in the range of considered T below 10 K, phonon emission processes dominate.
Calling $\Gamma_\lambda^{\nu\mathbf{Q}}(E)$ the probability of photon emission with energy E by an indirect exciton $|\lambda\mathbf{Q}\rangle$ assisted by phonon ν, we can model the CL spectrum as

$$I(E) \propto \sum_\lambda \sum_\nu \sum_{\mathbf{Q}} N(E_\lambda(\mathbf{Q}))\Gamma_\lambda^{\nu\mathbf{Q}}(E) \tag{4.2}$$

where λ is an index running over exciton bands at finite momentum $\mathbf{Q}$ and ν denotes the phonon branches. Finally, the occupation function N weights the contribution of different excitons, according to their occupation probability.

4.3.1 Calculation of phonon-assisted light emission probability by indirect excitons

The photon emission probability $\Gamma_{\lambda}^{\nu\mathbf{Q}}(E)$ is computed using second-order time dependent perturbation theory, similarly to the framework described in Cannuccia and co-workers[107].
In practice, we describe the system via the Hamiltonian

$$\hat{H} = \hat{H}_0 + \hat{H}' \tag{4.3}$$

$\hat{H}_0$ being the unperturbed Hamiltonian given by

$$\hat{H}_0 = \sum_{\lambda\mathbf{Q}} E_\lambda(\mathbf{Q}) a^\dagger_{\lambda\mathbf{Q}} a_{\lambda\mathbf{Q}} + \sum_{\nu\mathbf{q}} \hbar\omega_{\nu\mathbf{q}} b^\dagger_{\nu\mathbf{q}} b_{\nu\mathbf{q}} + \sum_{\varepsilon} \hbar\omega d^\dagger_{\omega\varepsilon} d_{\omega\varepsilon} \tag{4.4}$$

where $a^\dagger_{\lambda\mathbf{Q}}$ ($a_{\lambda\mathbf{Q}}$), $b^\dagger_{\nu\mathbf{q}}(b_{\nu\mathbf{q}})$ and $d^\dagger_{\omega\varepsilon}$ ($d_{\omega\varepsilon}$) are, respectively, bosonic creation (annihilation) operators for excitons in states $|\lambda\mathbf{Q}\rangle$, for ($\nu\mathbf{q}$) phonons and for photons with energy $\hbar\omega$ and polarization $\hat{\varepsilon}$.
The operator $\hat{H}'$ in Eq.(4.3) describes a perturbation to $\hat{H}_0$, corresponding to the sum of exciton-photon and exciton-phonon Hamiltonians, which are now derived for clarity.
The Hamiltonian describing the interaction between electrons and photons with frequency ω is given by

$$\hat{H}_{exc-pt} = \frac{1}{c}\mathbf{A}_\omega \cdot \Big[\sum_{vc\mathbf{k}} \mathbf{d}_{vc\mathbf{k}} c^\dagger_{v\mathbf{k}} c_{c\mathbf{k}} + \mathbf{d}_{cv\mathbf{k}} c^\dagger_{c\mathbf{k}} c_{v\mathbf{k}} \Big] \tag{4.5}$$

where $c_{n\mathbf{k}}$ ($c^\dagger_{n\mathbf{k}}$) is the annihilation (creation) operator for an electron in the single particle state ($n\mathbf{k}$), c and v indices run over conduction and valence bands respectively, $\mathbf{d}_{vc\mathbf{k}}$ is the interband dipole and $\mathbf{A}_\omega$ is the electromagnetic vector potential (here we are neglecting second order terms proportional to $\mathbf{A}^2_\omega$).
The vector potential is written in terms of photon creation-annihilation operators, i.e.

$$\mathbf{A}_\omega = \frac{C_1}{\sqrt{\omega}} \sum_{\varepsilon} \Big[d_{\omega\varepsilon} + d^\dagger_{\omega\varepsilon} \Big] \tag{4.6}$$

C_1 being a shorthand notation for a product of fundamental constants.
Defining creation and annihilation operators for excitons at Γ as in Ref. [82]

$$a^\dagger_{\lambda_2\mathbf{0}} = \sum_{vc\mathbf{k}} A^\Gamma_{\lambda_2}(vc\mathbf{k}) c^\dagger_{c\mathbf{k}} c_{v\mathbf{k}} \tag{4.7}$$

$$a_{\lambda_2\mathbf{0}} = \sum_{vc\mathbf{k}} A^{\Gamma *}_{\lambda_2}(vc\mathbf{k}) c^\dagger_{v\mathbf{k}} c_{c\mathbf{k}} \tag{4.8}$$

with $A^{\Gamma}_{\lambda_2}(vc\mathbf{k})$ the λ_2-exciton envelope functions and using the completeness property

$$\sum_{\lambda_2} A^{\Gamma *}_{\lambda_2 \mathbf{0}}(vc\mathbf{k}) A^{\Gamma}_{\lambda_2 \mathbf{0}}(v'c'\mathbf{k}') = \delta_{vv'}\delta_{cc'}\delta_{\mathbf{k}\mathbf{k}'} \tag{4.9}$$

it is possible to write, starting from Eqs.(4.7)-(4.8),

$$c^{\dagger}_{c\mathbf{k}} c_{v\mathbf{k}} = \sum_{\lambda_2} A^{\Gamma *}_{\lambda_2}(vc\mathbf{k}) a^{\dagger}_{\lambda_2 \mathbf{0}} \tag{4.10}$$

and

$$c^{\dagger}_{v\mathbf{k}} c_{c\mathbf{k}} = \sum_{\lambda_2} A^{\Gamma}_{\lambda_2}(vc\mathbf{k}) a_{\lambda_2 \mathbf{0}} \tag{4.11}$$

Substituting Eqs.(4.10) and (4.11) in Eq.(4.5) and using the second-quantized form of the vector potential given in Eq.(4.6), we obtain the exciton-photon Hamiltonian

$$\hat{H}_{exc-pt} = \frac{C}{\sqrt{\omega}} \sum_{\varepsilon} \sum_{\lambda_2}^{\Gamma_{exc}} \left[d^{\dagger}_{\omega\varepsilon} + d_{\omega\varepsilon} \right] \left[D^{\varepsilon}_{\lambda_2} a_{\lambda_2 \mathbf{0}} + D^{\varepsilon *}_{\lambda_2 \varepsilon} a^{\dagger}_{\lambda_2 \mathbf{0}} \right] \tag{4.12}$$

where the exciton dipole matrix elements have been introduced. Note that the quantity $C = \frac{C_1}{c}$ only depends on fundamental constants and does not affect the energy dependence of the luminescence spectra.

We now turn our attention to the coupling between excitons and phonons. The exciton-phonon Hamiltonian is obtained starting from the treatment of Chen and coworkers in Ref.[83]: part of the derivation is here repeated to make clearer the notation used in this Thesis to evaluate exciton-phonon interaction. Following [83], the exciton-phonon hamiltonian can be written as

$$\hat{H}_{exc-ph} = \sum_{mn} \langle m | \hat{\tilde{H}} | n \rangle a^{\dagger}_m a_n \tag{4.13}$$

where m and n are compact indexes running over excitonic bands and momenta and

$$\langle m | \hat{\tilde{H}} | n \rangle = \sum_{vcv'c'} A^{*}_m(vc) A_n(v'c') \left[\Delta^{*}_{cc'}(\varepsilon_c - \varepsilon_{c'})\delta_{vv'} + \Delta_{vv'}(\varepsilon_{v'} - \varepsilon_v)\delta_{cc'} \right]. \tag{4.14}$$

In Equation (4.14), c, c', v, v' are composite indexes for electronic states, denoting both bands and wave-vectors, A are the exciton envelope functions, ε_i correspond to single particle energies and

$$\Delta_{ij} = \frac{\langle j | \Delta \hat{V}_{KS} | i \rangle}{\varepsilon_i - \varepsilon_j} \tag{4.15}$$

$\Delta\hat{V}_{KS}$ being the variation of the Kohn-Sham potential due to atomic displacements from equilibrium positions, i.e.

$$\Delta\hat{V}_{KS} = \sum_{\alpha,s,\mathbf{R}} \left.\frac{\partial V_{KS}}{\partial u^{\alpha}_{\mathbf{R}s}}\right|_{eq} u^{\alpha}_{\mathbf{R}s} \tag{4.16}$$

where $u^{\alpha}_{\mathbf{R}s}$ is the displacement along direction α of atom s in the unit cell at $\mathbf{R}$. Equation (4.13) is obtained in Ref. [83] by evaluating the variation of the excitonic Hamiltonian due to the perturbation of single particle states caused by atomic displacements from equilibrium positions (in this procedure, the electron-electron interaction is assumed unmodified by the atomic displacements[108]).
Writing $u^{\alpha}_{\mathbf{R}s}$ in terms of phonon creation/annihilation operators, we have

$$\Delta\hat{V}_{KS} = \sum_{\alpha,s,\mathbf{R}} \sum_{\mathbf{q}_1\nu_1} \sqrt{\frac{\hbar}{2M_s\omega_{\nu_1\mathbf{q}_1}}} e^{i\mathbf{q}_1\cdot\mathbf{R}} \xi^{\alpha}_s(\nu_1,\mathbf{q}_1) \left.\frac{\partial V_{KS}}{\partial u^{\alpha}_{\mathbf{R}s}}\right|_{eq} \left[b_{\nu_1\mathbf{q}_1} + b^{\dagger}_{\nu_1-\mathbf{q}_1}\right] \tag{4.17}$$

By using the general definition Eq.(1.89), we can finally write

$$\Delta\hat{V}_{KS} = \sum_{\alpha s} \sum_{\mathbf{q}_1\nu_1} \sqrt{\frac{\hbar}{2M_s\omega_{\nu_1\mathbf{q}_1}}} e^{i\mathbf{q}_1\cdot\hat{\mathbf{r}}} \partial^{\mathbf{q}_1}_{s\alpha} V_{KS}(\hat{\mathbf{r}}) \xi^{\alpha}_s(\nu_1,\mathbf{q}_1) \left[b_{\nu_1\mathbf{q}_1} + b^{\dagger}_{\nu_1-\mathbf{q}_1}\right] \tag{4.18}$$

We remind that $\xi^{\alpha}_s(\nu_1,\mathbf{q}_1)$ is the normalized displacement of an atom s along the direction α within phonon $(\nu_1,\mathbf{q}_1)$ and $\partial^{\mathbf{q}_1}_{s\alpha} V_{KS}(\hat{\mathbf{r}})$ is a crystal periodic function defined according to Eq.(1.89).
Making explicit the single particle indices in the definitions of Δ we obtain

$$\Delta^{*}_{c\mathbf{k}_c,c'\mathbf{k}'_c} = -\frac{1}{\varepsilon_{c'\mathbf{k}'_c} - \varepsilon_{c\mathbf{k}_c}} \sum_{\nu_1\mathbf{q}_1} \left[b_{\nu_1\mathbf{q}_1} + b^{\dagger}_{\nu_1-\mathbf{q}_1}\right] \delta\Big(\mathbf{k}_c - \mathbf{k}'_c - \mathbf{q}_1\Big) g^{\nu_1}_{cc'}(\mathbf{k}'_c,\mathbf{q}_1) \tag{4.19}$$

and

$$\Delta_{v\mathbf{k}_v,v'\mathbf{k}'_v} = \frac{1}{\varepsilon_{v\mathbf{k}_v} - \varepsilon_{v'\mathbf{k}'_v}} \sum_{\nu_1\mathbf{q}_1} \left[b_{\nu_1\mathbf{q}_1} + b^{\dagger}_{\nu_1-\mathbf{q}_1}\right] \delta\Big(\mathbf{k}'_v - \mathbf{k}_v - \mathbf{q}_1\Big) g^{\nu_1}_{v'v}(\mathbf{k}_v,\mathbf{q}_1) \tag{4.20}$$

where we have introduced the electron-phonon coupling matrix elements[109]

$$g^{\nu}_{ij}(\mathbf{k},\mathbf{q}) = \sum_{s\alpha} \sqrt{\frac{\hbar}{2M_s\omega_{\nu\mathbf{q}}}} \xi^{\alpha}_s(\nu\mathbf{q}) \langle u_{i\mathbf{k}+\mathbf{q}} | \partial^{\mathbf{q}}_{s\alpha} V_{KS}(\hat{\mathbf{r}}) | u_{j\mathbf{k}} \rangle_{u.c.} \tag{4.21}$$

being i and j band indexes, while $|u_{i\mathbf{k}+\mathbf{q}}\rangle$ and $|u_{j\mathbf{k}}\rangle$ are the periodic parts of single particle states $|i\mathbf{k}+\mathbf{q}\rangle$ and $|j\mathbf{k}\rangle$.

By substitution of Eqs.(4.19) and (4.20) in Eq.(4.14) and making explicit the

excitonic indexes $m \to (\lambda_2 \mathbf{Q}_{\lambda_2})$ and $n \to (\lambda_1 \mathbf{Q}_{\lambda_1})$ we obtain

$$\langle \lambda_2 \mathbf{Q}_{\lambda_2} | \hat{\tilde{H}} | \lambda_1 \mathbf{Q}_{\lambda_1} \rangle = \sum_{\nu_1 \mathbf{q}_1} \Big(b_{\nu_1 \mathbf{q}_1} + b^{\dagger}_{\nu_1 - \mathbf{q}_1} \Big) \cdot \Bigg[\sum_{vcc'} \sum_{\mathbf{k}_c \mathbf{k}_v} A^{*}_{\lambda_2 \mathbf{Q}_{\lambda_2}}(v\mathbf{k}_v, c\mathbf{k}_c) A_{\lambda_1 \mathbf{Q}_{\lambda_1}}(v\mathbf{k}_v, c'\mathbf{k}_c - \mathbf{q}_1) g^{\nu_1}_{cc'}(\mathbf{k}_c - \mathbf{q}_1, \mathbf{q}_1) - \sum_{vv'c} \sum_{\mathbf{k}_v \mathbf{k}_c} A^{*}_{\lambda_2 \mathbf{Q}_{\lambda_2}}(v\mathbf{k}_v, c\mathbf{k}_c) A_{\lambda_1 \mathbf{Q}_{\lambda_1}}(v'\mathbf{k}_v + \mathbf{q}_1, c\mathbf{k}_c) g^{\nu_1}_{v'v}(\mathbf{k}_v, \mathbf{q}_1) \Bigg] \tag{4.22}$$

Momentum conservation has to be now considered: in other words, given an exciton with momentum $\mathbf{Q}$, the single particle transitions involved in this excitation must have wave-vectors constrained by the relation $\mathbf{Q} = \mathbf{k}_c - \mathbf{k}_v$: applying this reasoning to Eq.(4.22), it is possible to obtain

$$\begin{aligned} \mathbf{k}_c - \mathbf{k}_v &= \mathbf{Q}_{\lambda_2} \\ \mathbf{k}_c - \mathbf{k}_v &= \mathbf{Q}_{\lambda_1} + \mathbf{q}_1 \end{aligned}$$

from which we have $\mathbf{Q}_{\lambda_2} = \mathbf{Q}_{\lambda_1} + \mathbf{q}_1$ and $\mathbf{k}_c = \mathbf{k}_v + \mathbf{q}_1 + \mathbf{Q}_{\lambda_1}$. Calling $\mathbf{Q} \equiv \mathbf{Q}_{\lambda_1}$ and $\mathbf{k} \equiv \mathbf{k}_v$, we obtain

$$\langle \lambda_2 \mathbf{Q}_{\lambda_2} | \hat{\tilde{H}} | \lambda_1 \mathbf{Q} \rangle = \sum_{\nu_1 \mathbf{q}_1} \delta\Big(\mathbf{Q}_{\lambda_2} - \mathbf{Q} - \mathbf{q}_1 \Big) G^{\nu_1}_{\lambda_2 \lambda_1}(\mathbf{Q}, \mathbf{q}_1) \Big[b_{\nu_1 \mathbf{q}_1} + b^{\dagger}_{\nu_1 - \mathbf{q}_1} \Big] \tag{4.23}$$

$G^{\nu_1}_{\lambda_2 \lambda_1}(\mathbf{Q}, \mathbf{q}_1)$ being the exciton-phonon matrix elements, defined as

$$G^{\nu_1}_{\lambda_2 \lambda_1}(\mathbf{Q}, \mathbf{q}_1) = \sum_{vcc'} \sum_{\mathbf{k}} A^{*}_{\lambda_2 \mathbf{Q} + \mathbf{q}_1}(v\mathbf{k}, c\mathbf{k} + \mathbf{q}_1 + \mathbf{Q}) A_{\lambda_1 \mathbf{Q}}(v\mathbf{k}, c'\mathbf{k} + \mathbf{Q}) g^{\nu_1}_{cc'}(\mathbf{k} + \mathbf{Q}, \mathbf{q}_1) - \sum_{vv'c} \sum_{\mathbf{k}} A^{*}_{\lambda_2 \mathbf{Q} + \mathbf{q}_1}(v\mathbf{k}, c\mathbf{k} + \mathbf{q}_1 + \mathbf{Q}) A_{\lambda_1 \mathbf{Q}}(v'\mathbf{k} + \mathbf{q}_1, c\mathbf{k} + \mathbf{q}_1 + \mathbf{Q}) g^{\nu_1}_{v'v}(\mathbf{k}, \mathbf{q}_1) \tag{4.24}$$

In Equation (4.24), $G^{\nu_1}_{\lambda_2 \lambda_1}(\mathbf{Q}, \mathbf{q}_1)$ is the exciton-phonon coupling matrix element, which describes the scattering between excitons $|\lambda_1 \mathbf{Q}\rangle$ and $|\lambda_2 \mathbf{Q} + \mathbf{q}_1\rangle$ mediated by phonon $(\nu_1, \mathbf{q}_1)$. Finally, substituting Eq.(4.23) in Eq. (4.13) we obtain the exciton phonon Hamiltonian

$$\hat{H}_{exc-ph} = \sum_{\lambda_2 \lambda_1} \sum_{\mathbf{Q}} \sum_{\nu_1 \mathbf{q}_1} G^{\nu_1}_{\lambda_2 \lambda_1}(\mathbf{Q}, \mathbf{q}_1) a^{\dagger}_{\lambda_2 \mathbf{Q} + \mathbf{q}_1} a_{\lambda_1 \mathbf{Q}} \Big[b_{\nu_1 \mathbf{q}_1} + b^{\dagger}_{\nu_1 - \mathbf{q}_1} \Big] \tag{4.25}$$

Having defined the coupling between excitons, phonons and the electro-magnetic field, we evaluate the emission probability $\Gamma^{\nu \mathbf{Q}}_{\lambda}(E)$ as

$$\Gamma^{\nu \mathbf{Q}}_{\lambda}(E) = \frac{d |c_{|i\rangle \to |f\rangle}|^2}{dt} \tag{4.26}$$

i.e. as the scattering rate per unit time from an initial state $|i\rangle$ to a final state $|f\rangle$, both eigenstates of the unperturbed Hamiltonian $\hat{H}_0$.
The initial state $|i\rangle$ is given by

$$|i\rangle = |1_{\lambda\mathbf{Q}}\rangle_{exc} \otimes |n_{\nu\mathbf{q}}\rangle_{ph} \otimes |0\rangle_{pt} \tag{4.27}$$

and corresponds to one exciton in $|\lambda\mathbf{Q}\rangle$, n phonons of type $(\nu, \mathbf{q})$ and no photons ($|0\rangle_{pt}$ is the photon-vacuum).
Similarly, the $|f\rangle$ is chosen as

$$|f\rangle = |0\rangle_{exc} \otimes |1 + n_{\nu\mathbf{q}}\rangle_{ph} \otimes |1_{\omega\varepsilon}\rangle_{pt} \tag{4.28}$$

describing the state with one photon with energy ω and polarization $\hat{\varepsilon}$, $1+n$ phonons $(\nu, \mathbf{q})$ and no excitons ($|0\rangle_{exc}$ is the excitonic-vacuum).
Using second order perturbation theory[110], it is possible to obtain

$$\Gamma^{\nu\mathbf{Q}}_{\lambda}(E) = \frac{2\pi}{\hbar^2}\left|\sum_m \frac{\hat{H}'_{fm}\hat{H}'_{mi}}{\omega_{mi}}\right|^2 \delta\Big(E_f - E_i\Big) \tag{4.29}$$

where m runs over intermediate states (eigenstates of $\hat{H}_0$), $\omega_{mi} = \frac{1}{\hbar}\big(E_m - E_i\big)$ and E_i (E_f) is the energy of the initial (final) state. Using the definitions (4.27)-(4.28) for the initial and final states, we have $E_f - E_i = \hbar\omega_{\nu\mathbf{q}} + E - E_{\lambda\mathbf{Q}}$. By substitution of $\hat{H}' = \hat{H}_{exc-ph} + \hat{H}_{exc-pt}$ in Eq.(4.29), we find that the summation over m is restricted to states

$$|m\rangle = |1_{\lambda_2\mathbf{0}}\rangle_{exc} \otimes |1 + n_{\nu\mathbf{Q}}\rangle_{ph} \otimes |0\rangle_{pt} \tag{4.30}$$

λ_2 being an index running over excitons at $\mathbf{Q} = \Gamma$.
After some algebra, it is possible to obtain

$$\Gamma^{\nu\mathbf{Q}}_{\lambda}(E) \propto \delta\Big(\hbar\omega_{\nu\mathbf{Q}} + E - E_{\lambda\mathbf{Q}}\Big)\frac{1 + n_{\nu\mathbf{Q}}}{E}\left|\sum_{\lambda_2}^{\Gamma_{exc}} \frac{G^{\nu}_{\lambda_2\lambda}(\mathbf{Q}, -\mathbf{Q})D^{\varepsilon}_{\lambda_2}}{E_{\lambda_2} + \hbar\omega_{\nu\mathbf{Q}} - E_{\lambda}(\mathbf{Q})}\right|^2 \tag{4.31}$$

where we have taken $\mathbf{q} = \mathbf{Q}$ because of momentum conservation. In Equation (4.31), $n_{\nu\mathbf{Q}}$ is the Bose-occupation function for phonon mode $(\nu, \mathbf{Q})$, while $G^{\nu}_{\lambda_2\lambda}(\mathbf{Q}, -\mathbf{Q})$ is the exciton-phonon coupling matrix element, describing the scattering from an excitonic state $|\lambda\mathbf{Q}\rangle$ to a state $|\lambda_2\Gamma\rangle$. Starting from its general expression given by Eq. (4.24), we have

$$\begin{aligned} G^{\nu}_{\lambda_2,\lambda}(\mathbf{Q}, -\mathbf{Q}) = &\sum_{vcc'\mathbf{k}} A^*_{\lambda_2\Gamma}(v\mathbf{k}, c\mathbf{k})A_{\lambda\mathbf{Q}}(v\mathbf{k}, c'\mathbf{k} + \mathbf{Q})g^{\nu}_{cc'}(\mathbf{k} + \mathbf{Q}; -\mathbf{Q}) \\ &- \sum_{vv'c\mathbf{k}} A^*_{\lambda_2\Gamma}(v\mathbf{k}, c\mathbf{k})A_{\lambda\mathbf{Q}}(v'\mathbf{k} - \mathbf{Q}, c\mathbf{k})g^{\nu}_{v'v}(\mathbf{k}; -\mathbf{Q}) \end{aligned} \tag{4.32}$$

with g equal to the electron phonon coupling matrix elements given by Eq.(4.21).

As the available experimental CL signal is not polarization-resolved, in Eq.(4.31), we have substituted $D^{\varepsilon}_{\lambda_2}$ with the exciton-dipole D_{λ_2} averaged along all light-polarization directions perpendicular to the sample stacking sequence.

4.4 Computational workflow for computing phonon-assisted luminescence spectra

In this section, we now focus on the computational workflow we followed to predict the BN luminescence spectra. following the method described above to model the phonon-assisted radiative emission by indirect excitons.
Firs, we obtained a properly converged ground state charge density at the DFT level, using the parameters discussed in Section 4.2. With this charge density, phonon energies $\hbar\omega_{\nu\mathbf{q}}$ and eigen-displacements $\xi_s^\alpha(\nu\mathbf{Q})$ are computed using `ph.x` code from `Quantum Espresso` package, on a 24x24x2 $\mathbf{Q}$-grid. As discussed in Chapter 1, to compute phonon energies at point $\mathbf{Q}$, the variation of the KS potential $\partial_{s\alpha}^{\mathbf{Q}} V_{KS}$ is needed: in this step, we store these functions, as they will be used in the following to evaluate the electron-phonon coupling matrix elements. Notice that the calculation of vibrational properties is performed exploiting the symmetries of the system, therefore $\partial_{s\alpha}^{\mathbf{Q}} V_{KS}$ is computed only for $\mathbf{Q}$ points sampling the irreducible BZ.
Kohn Sham states have been then computed via a non-self-consistent calculation on a 24x24x4 Monkhorst-Pack grid without symmetries, i.e. sampling the full BZ. Such grid has been generated using the utility `kmesh.pl` of `Wannier90` [67]. These wavefunctions are then given as input to both `qe2pert.x` code from `Perturbo` package[111] and to `Yambo` code.
`qe2pert.x` makes possible an efficient evaluation of the matrix elements of the KS potential variation $\partial_{s\alpha}^{\mathbf{Q}} V_{KS}$ between the KS states , i.e.

$$\tilde{g}_{ij}^{\nu}(\mathbf{k},\mathbf{Q}) = \langle u_{i\mathbf{k}+\mathbf{Q}} | \partial_{s\alpha}^{\mathbf{Q}} V_{KS}(\hat{\mathbf{r}}) | u_{j\mathbf{k}} \rangle_{u.c.}$$

In practice `qe2pert.x` reads the local part of $\partial_{s\alpha}^{\mathbf{Q}} V_{KS}$ computed for $\mathbf{Q}$ in the irreducible BZ and, using the approach of Ref.[112] expands this function over the full BZ. Then, the non-local part of $\partial_{s\alpha}^{\mathbf{Q}} V_{KS}$ (due to the non-local term appearing in the pseudo-potentials) is evaluated for all $\mathbf{Q}$ points in the BZ using the analytical expression by Ref.[113]. Finally, the electronic KS states are read from disk and the matrix elements of $\partial_{s\alpha}^{\mathbf{Q}} V_{KS}$ are computed for all $\mathbf{k}$ and $\mathbf{Q}$ points sampling the BZ.
The electron-phonon coupling matrix elements are then evaluated according to Eq.(4.21), i.e.

$$g_{ij}^{\nu}(\mathbf{k},\mathbf{Q}) = \sum_{s\alpha} \sqrt{\frac{\hbar}{2M_s\omega_{\nu\mathbf{Q}}}} \xi_s^\alpha(\nu,\mathbf{Q}) \tilde{g}_{ij}^{\nu}(\mathbf{k},\mathbf{Q})$$

by combining the matrix elements evaluated by `qe2pert.x` with phonon energies and eigendisplacements obtained using `ph.x` code. This is done via an external `Python` script, which reads the `hdf5` file produced by `qe2pert.x`, containing $\tilde{g}$ and the dynamical matrices obtained for all $\mathbf{Q}$ points in the full BZ, as given by `ph.x`; then, after diagonalization of such matrices D, it

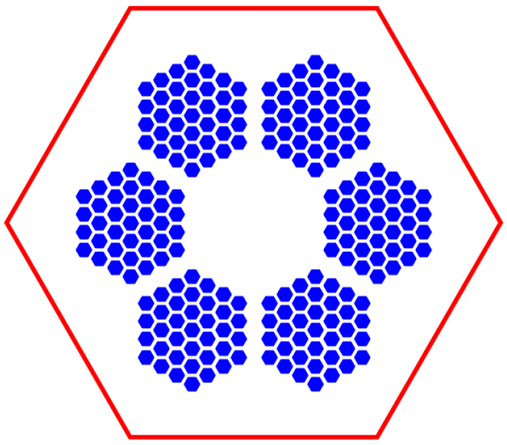

Figure 4.4: Grid of **Q**-points where finite-momentum excitons have been computed. The contribution to the luminescence spectra of excitons outside the selected regions is negligible because of the exponentially small occupation factor for the considered value of the effective excitonic temperature T_{exc}.

computes g as defined above, and stores the result to disk (again in a `hdf5` dataset).
Kohn-Sham states computed with the non-self-consistent calculation are then given as input to `Yambo`. Firstly, the electron-electron static interaction W_s is computed within RPA (in the specific case of BN, using 120 bands and a 10 Ry cut-off in the electronic polarizability). Then, using the obtained W_s, we have solved the BSE both for $\mathbf{Q} = \Gamma$ and at finite momentum, to obtain the excitonic properties, i.e. energies $E_{\lambda\mathbf{Q}}$ and envelope functions $A_{\lambda\mathbf{Q}}(v\mathbf{k}-\mathbf{Q},\mathbf{k})$). In the case of BN, we have included the two (three) topmost valence bands and the two (three) lowest unoccupied conduction bands in the solution of BSE for hBN (rBN), while QP corrections have been included using a scissor-stretching operator, as discussed in Section 4.2. Furthermore, the $\mathbf{Q} = \Gamma$ calculation has been done setting to zero the long-range component of the exchange kernel, while such contribution has been included in finite momentum calculations.
The luminescence spectrum, as provided by Eq.(4.2), would require the solution of finite momentum BSE for all **Q** points in the BZ, where electron-phonon matrix elements have been computed. We point out that this step is extremely time-consuming from a computational point of view. Furthermore, this is unnecessary, as the contribution to luminescence from excitons with momentum **Q** is weighted by the distribution function given in Eq.(4.1). This function is exponentially decaying far from the minima of the excitonic dispersion: therefore, if T_{exc} is small (e.g. below 50 K, as in our case), only states close to the minima have a non-negligible population. Therefore, in the calculation presented in the following we have restricted the sum over **Q** only to points of the 24x24x2 grid with $Q_z = 0$ and planar positions as shown in Fig.4.4 These points are chosen because they are located around the Ω

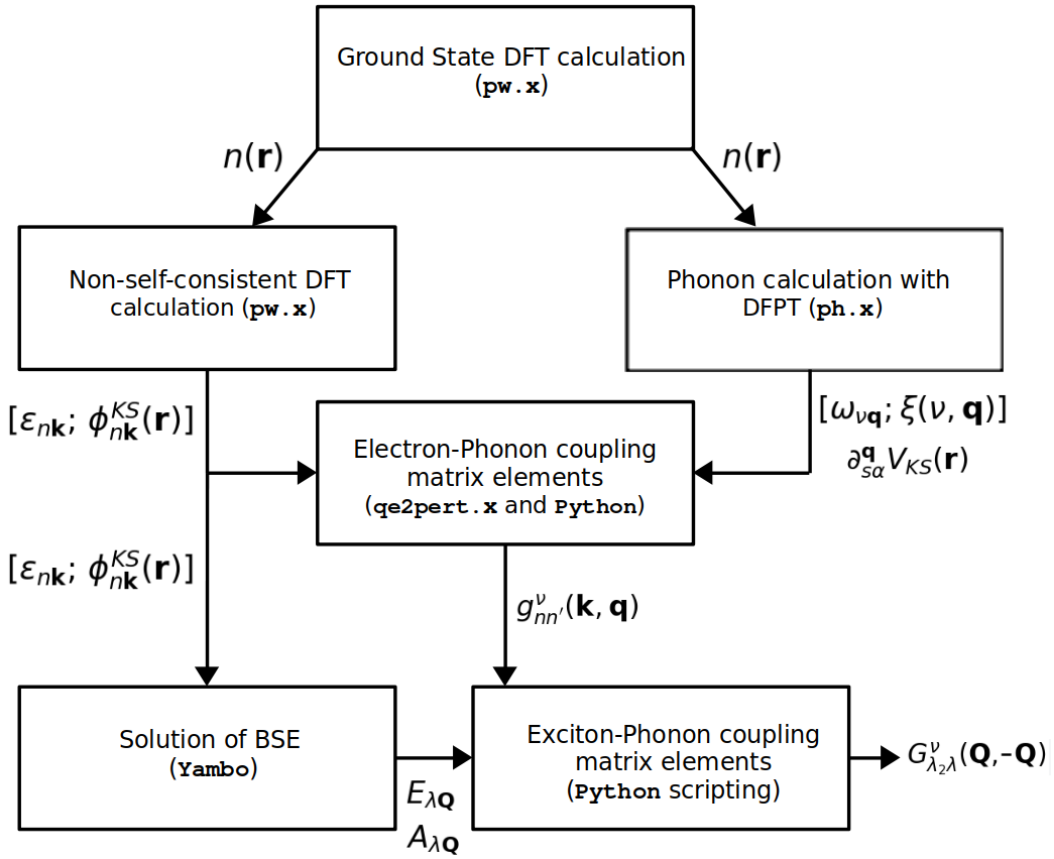

Figure 4.5: Schematic computational workflow followed in this Chapter to evaluate exciton-phonon coupling matrix elements, as given by Eq. (4.21).

point, i.e. in proximity of the minimum of the excitonic dispersion. We point out that exciton wavefunctions have been explicitly computed for all these $\mathbf{Q}$ points.
Exciton envelope functions $A_{\lambda\mathbf{Q}}(v\mathbf{k}-\mathbf{Q},\mathbf{k})$ and electron-phonon matrix elements g have been then combined using `Python` post-processing scripts to evaluate the exciton-phonon matrix elements as defined by Eq.(4.13). We stress the fact that with this procedure both A and g have been computed using the same set of single particle KS states: this is extremely important as both quantities are not gauge invariant (differently from their squared moduli), so that their phase depends on the (arbitrary) phase of the used electronic wavefunctions. With the approach just discussed, we are treating all phases consistently, avoiding possible phase-mismatch problems which could arise once using different KS states. The computational workflow followed to compute exciton-phonon coupling matrix elements is sketched in Figure 4.5.
Finally, known G, luminescence spectra are computed using Eq.(4.2) and Eq.(4.12), extracting from `Yambo` datasets exciton energies and exciton dipoles D_λ, for $\mathbf{Q}=\Gamma$.

As a last remark, the CL spectra shown in the following were obtained by convolution of the Dirac delta in Eq.(4.12) with a Lorentzian broadening

$$\delta\Big(E - E_{\lambda\mathbf{Q}} + \hbar\omega_{\nu\mathbf{Q}}\Big) \approx \frac{\eta}{\pi}\frac{1}{\Big(E - E_{\lambda\mathbf{Q}} + \hbar\omega_{\nu\mathbf{Q}}\Big)^2 + \eta^2}$$

where η has been fixed equal to 5 meV, to mimic the experimental resolution.

4.5 Comparison between experimental and theoretical luminescence in hBN and rBN

In Figure 4.6 we present the comparison between theoretical (solid green lines) and experimental (black dots) luminescence spectra for hBN (Fig.4.6a) and rBN (Fig.4.6c), where *ab initio* results have been obtained fixing $T_{exc} = 20$ K. In panels b and d, we show phonon dispersions for $\mathbf{Q}$ along Γ-K direction for hBN and rBN respectively, and we indicate the branches involved in the phonon-assisted light emission. For both stackings, theoretical spectra have been normalized to the maximum of the experimental data and they are rigidly shifted of 1.04 eV to match the position of the highest intensity peak. This shift (which is the same for both stackings) is a direct consequence of the band gap underestimation of G_0W_0 for bulk Boron Nitride. A solution to this problem could be a partial eigenvalue self-consistency in GW calculations, as suggested in Refs.[114, 115].
In Figure 4.7 we present the same quantities shown in Fig. 4.6, but with the *ab initio* spectra evaluated assuming an excitonic temperature $T_{exc} = 50$ K. The obtained spectra have the same qualitative features, once computed for these two temperatures; this demonstrates the stability of our results w.r.t. small variations of the T_{exc} parameter.
We find very good agreement between experimental and theoretical data. In both hBN and rBN, the spectra are dominated by the two peaks in the low-energy part of the spectrum. These are phonon-assisted satellites due to longitudinal optical phonons – denoted as LO_2-LO_3 modes in the phonon dispersion – and transverse optical ones (the almost-degenerate pair [116] TO_2-TO_3). These assignments for hBN are in good agreement with the results obtained in Refs. [115, 107], using a finite-difference approach.
Furthermore, the experimental intensity ratio between these peaks is well-reproduced by *ab initio* calculations, with the LO peak being less intense than the TO structure. The additional overtones appearing in this energy region are due to higher-order scattering processes [117] and are thus not captured by our theoretical approach, which is restricted to first-order exciton-phonon interaction.
The phonon branches involved in the emission process are explicitly labelled in Figs. 4.6b and 4.6d for the Ω point only.

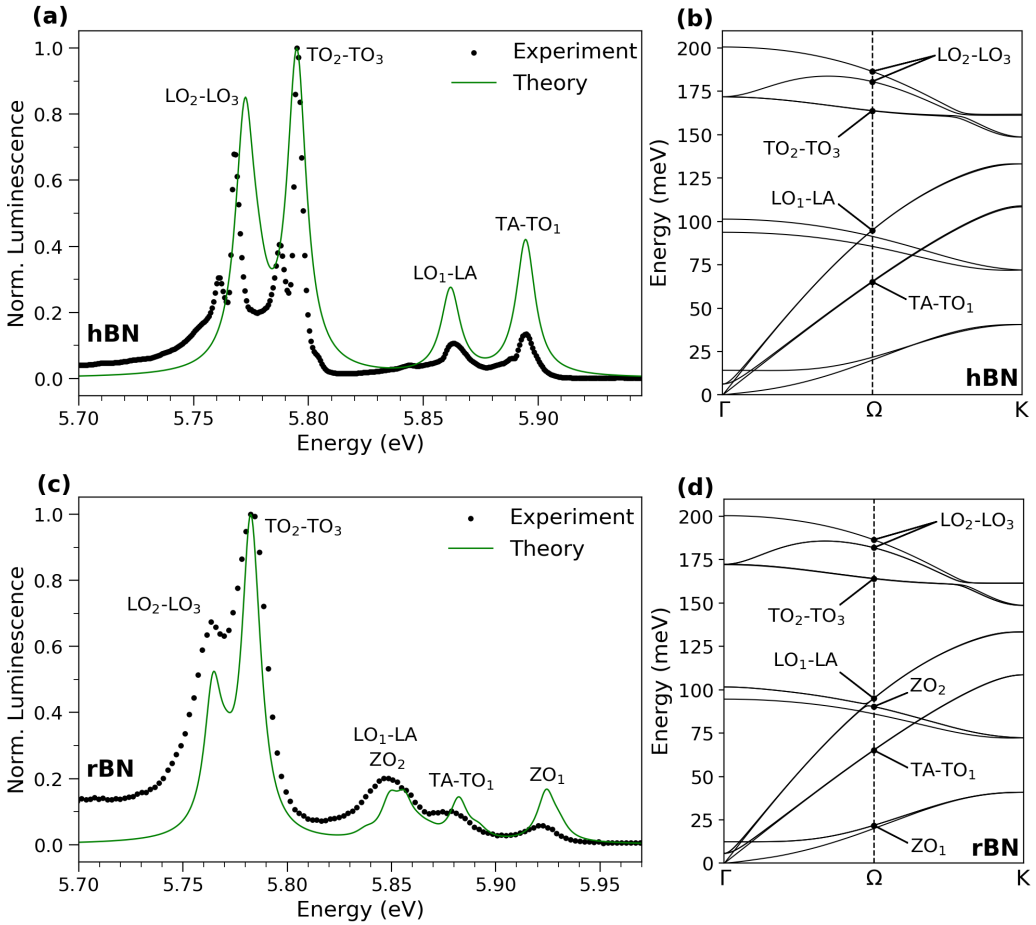

Figure 4.6: Experimental (black dots) and theoretical (green lines) luminescence spectra for hBN (a) and rBN (c). In both (a) and (c), theoretical spectra are blue shifted by 1.04 eV to match the position of the highest intensity peak in the experimental spectrum. Phonon dispersions in hBN (b) and rBN (d) along the Γ-K direction: phonon branches contributing to the luminescence spectra are highlighted at the Ω point, in the middle of the Γ-K direction. See the main text for the phonon mode labelling. Almost-degenerate phonon branches are paired with a hyphen. Theoretical spectra have been computed using $T_{exc} = 20$ K.

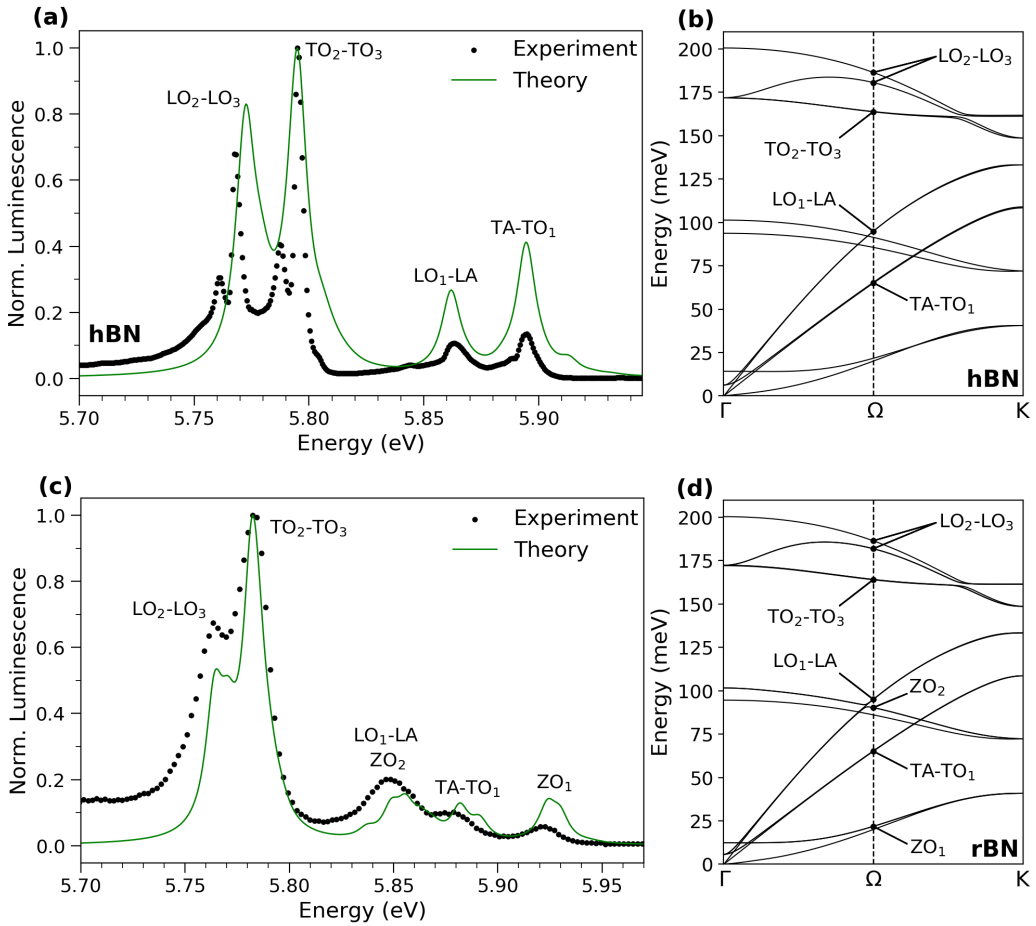

Figure 4.7: Same as Fig.4.6 but theoretical spectra were evaluated using $T_{exc} = 50$ K.

Luminescence spectra of hBN and rBN are qualitatively different at higher energies, as confirmed by *ab initio* results. In the case of hBN, we observe two main peaks: the first (at about 5.86 eV) corresponds to a replica of the LO-LA phonons, while the higher intensity structure at 5.89 eV is mainly due to TO phonons, with a small contribution from the almost-degenerate transverse acoustic mode (TA-TO_1). *Ab initio* results reproduce with great accuracy both the splitting between these peaks and their intensity ratio (the LO-LA peak being less pronounced than the TO-TA one), while they tend to overestimate their relative strengths, with respect to the dominant, low-energy satellites. The agreement may be further improved by increasing the $\mathbf{Q}$ grid used in the calculation of Eq.(4.2). We also note that, in agreement with the group theory analysis discussed in Ref.[115], no contributions from the out-of-plane phonon modes appear in the luminescence spectra.
In the case of rBN, the high-energy portion of the luminescence spectrum is qualitatively different from the hBN result. In this case, the CL spectrum shows three peaks, respectively at about 5.847 eV, 5.878 eV and 5.919 eV. They are also recovered in the *ab initio* results. The first structure is a combination of phonon-assisted replicas due to the almost-degenerate LA-LO_1 branches, albeit with a relevant contribution from optical out-of-plane modes (denoted as ZO_2). Conversely, the peak at 5.878 eV is associated to the TA-TO_1 phonons in analogy with the hBN case. Interestingly, *ab initio* results correctly reproduce the intensity ratio among these peaks. Finally, the highest-energy structure at 5.919 eV turns out to be due to the out-of-plane optical mode ZO_1, which is forbidden for the hBN luminescence because of symmetry reasons.
To complete the peak assignments, we also evaluate the functions

$$I_\nu(E) = \sum_\lambda \sum_{\mathbf{Q}} N(E_\lambda(\mathbf{Q}))\Gamma_\lambda^{\nu\mathbf{Q}}(E) \tag{4.33}$$

which correspond to the contributions of different phonon branches to the total luminescence spectra. These quantities are shown in Fig. 4.8 in the case of $T_{exc} = 20$K, showing as summed the contributions coming from phonon modes which are very close in energy in proximity of the Ω point. Phonon branches are labeled according to the same notation adopted in Fig. 4.6 and Fig. 4.7. Apart from confirming the phonon assignments just discussed, we can notice the relevant role of the out-of-plane phonon modes, which are instead totally absent in the case of hBN.

4.6 Summary and perspectives

In this Chapter we have presented an interpretation of experimental CL spectra of bulk boron nitride based on fully first-principle calculations, demonstrating how radiative emission in these indirect-gap materials is affected

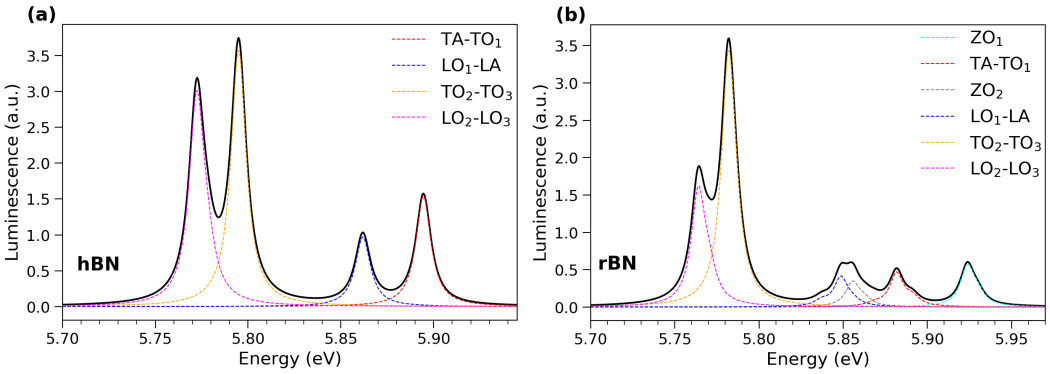

Figure 4.8: Phonon resolved contributions to luminescence as defined in Eq.(4.14), for hBN (a) and rBN (b). In both stackings, the luminescence spectra are blue shifted of 1.04 eV to match the position of the highest intensity experimental peak.

by the interaction between electronic and lattice excitations. We have also demonstrated how differences in the fine structure of the collected cathodoluminescence spectra allows distinguishing these two fundamentally similar BN polytypes, which are extremely difficult to discriminate using conventional crystallographic approaches. Furthermore, our *ab initio* results show the discriminating role of out-of-plane vibrations assisting excitonic radiative recombination for rBN, while they are totally silent in the case of hBN, due to symmetry reasons.

The methodology discussed in Sec.4.4 can be directly applied to discuss phonon-assisted luminescence from other indirect-gap materials, like for example Transition Metal Dichalcogenides bilayers. Clearly, a few technical improvements could be introduced, to improve both the accuracy and the efficiency of the presented methodology.

On the one hand, remarkable computational efficiency improvement would be obtained by computing the exciton-phonon coupling matrix elements G, by solving the BSE with the inclusion of symmetry operations, while preserving the phase-matching among exciton envelope functions and electron-phonon matrix elements.

On the other hand, the development of methods for interpolating the exciton-phonon matrix elements on denser $\mathbf{Q}$, similarly to what is done for electron phonon coupling, could strongly improve the accuracy of $\mathbf{Q}$ integration appearing in the definition of the luminescence spectra[118].

Finally, from a purely theoretical perspective, a great advancement could be a fully first-principles evaluation of the quasi-equilibrium excitonic distribution from which light emission occurs, using, for example, out of equilibrium approaches[105]. This would 'remove' the dependency of the theoretical results from the empirical parameter T_{exc}, which is not always available experimentally, increasing the predictive capabilities of this theoretical approach.

Chapter 5

Simulation of X-ray inelastic scattering in MoS_2 under ultra-high pressure

In this chapter, we present the results of a joint theoretical and experimental work aimed at characterising the low energy spectrum of bulk MoS_2 under pressure at room temperature by Inelastic X-Ray scattering (IXS) measurements.
This work is part of an ongoing collaboration with the group of Prof. Luigi Paolasini at the European Synchrotron Radiation Facility (ESRF).

5.1 Introduction

The search of the elusive excitonic insulator phase predicted by several pioneering studies[119, 120, 121] in the early sixties has catalysed many recent experimental and theoretical works[122, 123, 124].
In this context, fully *ab initio* calculations [125] have recently demonstrated that bulk MoS_2 should be characterized by an excitonic insulating phase at ultra-high external pressure and at cryogenic temperatures, below 10 K. Such electronic phase transition is expected to occur in a small range of pressure values around 34 GPa, before the appearance of a semimetallic phase at higher pressures.
External pressure affects MoS_2 electronic structure and, as a consequence, the excitonic dispersion. This is better clarified in Fig. 5.1, where we show the excitonic dispersion computed for three different pressure values.
Independently of the applied pressure, the exciton dispersion shows a minimum along the Γ-K direction of the hexagonal BZ, whose position in energy decreases by increasing pressure, becoming approximately zero at $P \approx 34$ GPa.
This exciton softening signals the possible spontaneous formation of electron-hole pairs with finite momentum, which are expected to create an excitonic

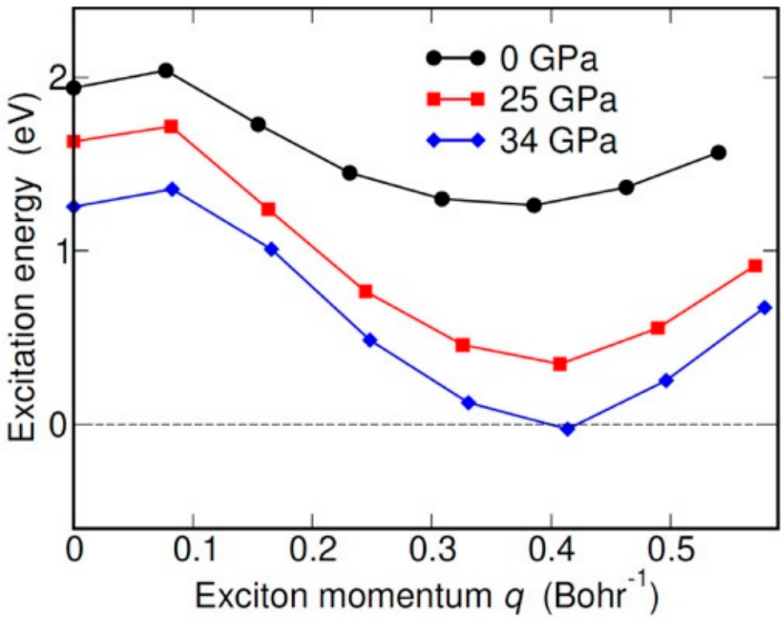

Figure 5.1: Lowest energy excitonic band for **Q** along Γ-K direction in bulk MoS_2 for different values of applied pressure. MoS_2 is assumed in the $2H_c$ phase. Figure adapted from Ref.[125].

condensate. Furthermore, as the involved excitons possess non-zero momenta, the electronic charge density characterizing the condensate should also exhibit a different periodicity with respect to the one of the underlying lattice. Mean field BCS-like calculations based on an *ab initio* modelling of electron-electron screened interaction indicate that the excitonic-insulating phase should be characterized by an anti-ferroelectric order, due to the inversion symmetry breaking effect associated to the excitonic condensate[125].
An intuitive way to probe this electronic phase transition consists on measuring the exciton-softening via IXS spectroscopy. In other words, by increasing the external pressure it could be possible to evaluate the progressive decrease of the energy of the lowest accessible excitons at finite momentum, similarly to what has been done by Kogar and co-workers[122] to probe exciton-softening in 1T-$TiSe_2$ via momentum-resolved electron energy loss spectroscopy.
These high-pressure IXS experiments clearly require a set of preliminary measurements, aimed both at testing the behaviour of bulk MoS_2 single crystals under high pressure and determining proper crystal orientations.
In the following, we will discuss a set of IXS measurements performed at room temperature, for different applied pressure values, i.e. 0.42, 11.47, 20.88 and 32.83 GPa.
In order to characterize the sample behaviour as a function of the external pressure, we have focused on the low energy part of IXS spectra, to probe the evolution of crystal phonon modes: IXS signals have been collected for a few high symmetry momenta in the BZ and compared with first-principle

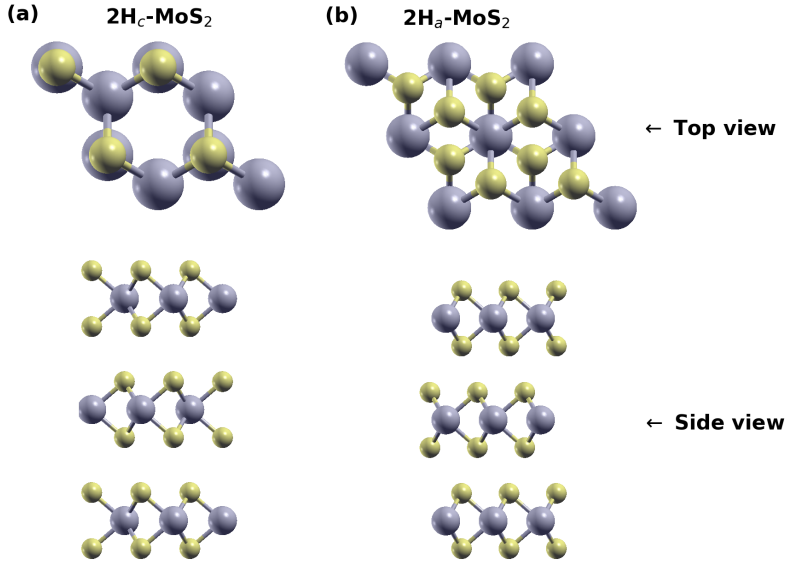

Figure 5.2: 2H$_c$ (a) and 2H$_a$ structures of bulk MoS_2. Upper panels represent the crystal top view, while lower panels correspond to the side view. Yellow (violet) spheres represent S (Mo) atoms.

calculations discussed in the following Sections.
Interestingly, first principles calculations by Tosatti *et al.* [126] and X-ray diffraction experiments [127] indicate that, at pressure $P \approx 20$ GPa, bulk MoS_2 should change its stacking motif, i.e. it presents a structural phase transition. At low pressure, single-layers MoS_2 are stacked together so that Mo atoms are aligned to S atoms on adjacent layers, while at pressure P larger than 20 GPa the most stable structure becomes the one in which Mo atoms on neighbouring layers are on top of each other. These two structures (called 2H$_c$ and 2H$_a$ respectively) are shown in Fig.5.2: both crystals have the same space group ($P6_3/mmc$) and they only differ according to the stacking motif of the single layers.
This structural phase transition has been studied with Raman spectroscopy [128, 129], probing changes under pressure of the Γ Raman active phonons. As the two crystals share the same point group, the Raman active modes are analogous in the two cases. In Raman experiments, the 2H$_c$ to 2H$_a$ transition is experimentally detected by frequency discontinuities as a function of pressure for $E^{1,2}_{2g}$ modes together with a slope change of the function $E_{A_{1g}}(P)$, representing the energy variation of mode A_{1g} w.r.t. pressure.
X-Ray Diffraction (XRD)[128, 127] has also been extensively used to study this phase transition. In this case, the 2H$_a$ phase is detected, looking at the behaviour of in-plane a and out-of-plane c lattice parameters as a function of pressure. More precisely, it is observed that a (c) increases (decreases) in a discontinuous way for pressure values around 20 GPa, signalling the transition from 2H$_c$ to 2H$_a$, in good qualitative agreement with the theoretical results of

Ref.[126]. Furthermore, we also point out that the pressure values at which the transition occur are different for single crystals and powders, with a lower transition pressure detected in the single crystal case (see for example Figure 5 of Ref.[127]).
To the best of our knowledge, the effect of $2H_c$ to $2H_a$ phase transition on finite momentum phonons has not been experimentally demonstrated yet. In the following, we will show results which show how IXS could close this gap, probing finite momentum phonons in few selected experimental configurations at high pressure.

5.2 First principles calculation of vibrational-IXS

In this joint experimental-theoretical effort, using DFPT calculations (see Sec.1.4 of Chapter 1) we have evaluated the phonon dispersion of bulk MoS_2 at different pressures and developed a computational post-processing tool to obtain vibrational IXS spectra to be directly compared with the experimental measurements performed at ESRF synchrotron.
IXS is a powerful technique to probe lattice vibrations at finite momenta in condensed matter systems: a complete introduction to this experimental methodology can be found in the review by Baron[130] and references therein.
IXS spectra are related to the dynamical structure function $S(\mathbf{Q}, E)$, which is proportional to the probability that an incoming photon with energy E_0 and momentum $\mathbf{Q}_0$ is found with energy $E_f = E_0 - E$ and momentum $\mathbf{Q}_f = \mathbf{Q}_0 + \mathbf{Q}$ after interacting with the sample. In other words, $\mathbf{Q}$ is the photon scattering momentum, while E is the energy lost by the photon in this process[1].
In the case of scattering with lattice vibrations, it is possible to derive the function S using first order perturbation theory as discussed by Tornatzky[131] and in Aschroft-Mermin book[132] in the case of neutron scattering.
Formally one obtains

$$S(\mathbf{Q}, E) \propto \sum_{\nu} Z_{\nu}(\mathbf{Q}) F_{\nu}(\mathbf{Q}, E) \tag{5.1}$$

where

$$Z_{\nu}(\mathbf{Q}) = \left| \sum_{j}^{N_{at}} \frac{1}{\sqrt{2M_j}} f_j(\mathbf{Q}) e^{-W_j(\mathbf{Q})} e^{i\mathbf{Q}\cdot\boldsymbol{\tau}_j} \left(\mathbf{Q} \cdot \boldsymbol{\xi}_j(\nu, \mathbf{q})\right) \right|^2 \tag{5.2}$$

and

$$F_{\nu}(\mathbf{Q}, E) = \left(1 + n_{\nu,\mathbf{q}}\right) \frac{1}{\hbar\omega_{\nu\mathbf{q}}} \frac{\gamma}{(E - \hbar\omega_{\nu\mathbf{q}})^2 + \frac{\gamma^2}{4}} \tag{5.3}$$

[1] In the following we only consider processes in which the incoming photon loses energy, i.e. $E > 0$.

In Equations (5.2) and (5.3), ν runs over phonon branches and j over the atoms in the unit cell, with positions $\boldsymbol{\tau}_j$. The scattering vector is given by $\mathbf{Q} = \mathbf{q} + \mathbf{G}_{hkl}$, where $\mathbf{G}_{hkl}$ is a reciprocal lattice vector identifying the $[h, k, l]$ Bragg diffraction indices selected experimentally, while $\mathbf{q}$ is a vector restricted to the crystal BZ.
The functions $f_j(\mathbf{Q})$ are the atomic scattering factors, defined as

$$f_j(\mathbf{Q}) = \int d\mathbf{r} n_j(\mathbf{r}) e^{i\mathbf{Q}\cdot\mathbf{r}} \tag{5.4}$$

n_j being the electronic charge density associated to the atom j[2].
Debye-Waller scattering factors $W_j(\mathbf{Q})$ are computed fully *ab initio* using [132]

$$W_j(\mathbf{Q}) = \frac{\hbar}{4M_j N_{\mathbf{q}}} \sum_{\nu_1 \mathbf{q}_1} \frac{\left|\mathbf{Q}\cdot\boldsymbol{\xi}_j(\nu_1, \mathbf{q}_1)\right|^2}{\omega_{\nu_1,\mathbf{q}_1}} \coth\left(\frac{\hbar\omega_{\nu_1\mathbf{q}_1}}{2k_B T}\right) \tag{5.5}$$

M_j being the mass of atom j and $\omega_{\nu_1\mathbf{q}_1}$ ($\boldsymbol{\xi}_j(\nu_1, \mathbf{q}_1)$) the frequency (the displacement of atom j) associated to phonon mode $(\nu_1\mathbf{q}_1)$. Notice that the evaluation of the Debye-Waller factors requires an integration over $\mathbf{q}_1$ points sampling the BZ.
Finally, $\frac{\gamma}{2}$ represents a Lorentzian broadening which accounts for the finite experimental resolution: in the following we have chosen $\gamma = 3$ meV, i.e. equal to the resolution in energy of the considered experimental setup.
Looking at Eqs.(5.1)-(5.3), it is simple to realize that, once fixed the scattering vector $\mathbf{Q}$, the IXS signal will be characterized by peaks at the energies of the phonon modes $(\nu, \mathbf{q})$, with $\mathbf{Q} = \mathbf{q} + \mathbf{G}_{hkl}$, if such modes are active. The phonon IXS activity is determined by the function $Z_\nu(\mathbf{Q})$ which depends both on the phonon displacements and on the chosen experimental scattering geometry.
Starting from Eq.(5.2), we see that a phonon mode is IXS-dark if the chosen $\mathbf{Q}$ is perpendicular to $\boldsymbol{\xi}$, but its IXS strength can be increased by choosing a scattering vector with non-zero projection along the phonon displacement. Furthermore, we also point out that choosing the scattering vector almost parallel to the atomic displacements does not guarantee to measure signal from the corresponding vibration in the IXS spectrum: factors $e^{i\mathbf{Q}\cdot\boldsymbol{\tau}_j}$ in Eq.(5.2) can determine destructive interference between the contributions from different atoms, making the phonon mode IXS-dark.
Presently, the implementation of Eq.(5.1) is not available within `Quantum Espresso` package. Therefore, to simulate $S(\mathbf{Q}, E)$, we have developed a `Python` package which works as an automatic interface to `Quantum Espresso`. In practice, it allows to automatically evaluate the IXS spectra for a set of different $\mathbf{Q}$ points provided in input, starting from the output of a usual phonon

[2]The derivation of Eqs.(5.1)-(5.3) assumes that the electronic charge density associated to each atom moves rigidly with the nucleus: even if such approximation is strictly true only for core electrons, deviations related to this approximations are neglected in the following.

dispersion calculation.
We now briefly discuss the steps we followed to compute the spectra shown in the next sections.

For a given pressure, we have relaxed atomic positions and lattice parameters of the hexagonal 3D unit cell, to minimize both the forces acting on atoms (the convergence threshold has been set to 10^{-5} a.u.) and the total enthalpy. In all DFT-ground state calculations we have used norm-conserving GGA-PBE Pseudo-Potentials, from Pseudo-Dojo repository, without including spin-orbit effects. A kinetic energy cutoff of 100 Ry and a Monkhorst-Pack grid 12x12x4 to sample the BZ have been used; in the case of the calculations at 32.83 GPa, we have increased the **k**-grid to 18x18x4 while using a Marzari-Vanderbilt smearing [133] of 0.01 Ry in the ground state calculation, because of the observed metallic character at the DFT level occurring at this value of the applied pressure[3].
Following Ref. [126], we have explicitly included van der Waals corrections within Grimme-D2 approach only in the calculations at P = 0.42 GPa: at higher pressure values, we have neglected these terms as we checked that for applied pressure higher than 5 GPa structural relaxation within pure PBE provides lattice parameters in better agreement with experimental data.
Dynamical matrices have been computed using DFPT (as described in Chapter 1) using a 12x12x4 Monkhorst-Pack grid to sample the BZ. Then, using inverse Fourier transform, the matrix of force constants in real space has been evaluated using the `q2r.x` code of the `Quantum Espresso` distribution.
Our developed package requires as inputs a list of $\mathbf{Q}$ points, together with the text file produced by `q2r.x` containing the force-constants in real space. In practice, our post-processing tool automatically calls `matdyn.x` code from `Quantum Espresso` to evaluate dynamical matrices at the chosen $\mathbf{Q}$ points[4], by Fourier transforming the real-space force constants; straightforward diagonalization of these matrices provides phonon energies and displacements at the chosen scattering vectors, which are then internally used to compute the dynamical structure factor via Eqs.(5.1)-(5.3). We note that the evaluation of Debye Waller factors for each $\mathbf{Q}$ (see Eq.(5.5)) requires phonon modes on a dense $\mathbf{q}$-grid sampling the BZ: such excitations are evaluated directly by `matdyn.x` and then read by our tool to obtain the Debye-Waller factors $W_j(\mathbf{Q})$ for each atom j.
Within this procedure, the atomic scattering factors given by Eq.(5.4) are obtained using the parametrization

$$f_j(\mathbf{Q}) = \sum_{\alpha}^{4} a_{\alpha}^{j} e^{-b_{\alpha}^{j} \frac{|\mathbf{Q}|^2}{16\pi^2}} + c^j \tag{5.6}$$

where a_{α}^{j}, b_{α}^{j} and c^j are 9 atomic-specific parameters taken from the Interna-

[3]Such metallicity is removed by inclusion of QP corrections, as discussed in Ref. [125].
[4]We remind here that $\omega_{\nu\mathbf{Q}} \equiv \omega_{\nu\mathbf{q}}$ and $\boldsymbol{\xi}_j(\nu, \mathbf{Q}) \equiv \boldsymbol{\xi}_j(\nu, \mathbf{q})$, if $\mathbf{Q} = \mathbf{q} + \mathbf{G}_{hkl}$

tional Table of Crystallography, and derived by fitting the results of Hartree-Fock atomic calculations, for each atomic specimen j. For completeness, we have also tested a different modelling for functions f_j (i.e. the one provided by Kirkland book[134]) and we have checked (at least for MoS_2) that IXS spectra were stable w.r.t. the chosen parametrization.
Finally, we point out that Debye-Waller factors have been computed by integrating Eq.(5.5) on a 33x33x7 $\mathbf{q}$ grid, again evaluating the phonon modes via automatic usage of `matdyn.x` code within our `Python` package. We note that for MoS_2, here discussed, Debye-Waller factors are nearly atom-independent, so that they do not strongly affect the obtained IXS spectra. Anyhow, they have been included in all the results presented in the following.

5.3 Vibrational IXS at low and intermediate pressure

In this section, we discuss IXS spectra obtained at low (P = 0.42 GPa) and intermediate pressure (P = 11.47 GPa). All measurements were performed on a MoS_2 single crystal cut by laser ablation. Pressure were applied using diamond anvil cell setup, adopting Helium as transmitting medium and checking the pressure value via Ruby fluorescence technique[135, 136, 137]. All the spectra shown in the following were collected at the ID28 beamline at ESRF. In Figure 5.3, we show the calculated phonon dispersions in MoS_2 at these two applied pressure values, assuming a $2H_c$ crystal structure in both cases.

The effect of pressure is two-fold: on the one hand, phonon frequencies harden by increasing pressure, as hydrodynamic compression reduces bond lengths between atoms resulting in a higher crystal stiffness. On the other hand, at P = 11.47 GPa, a larger splitting between Davydov pairs is observed: as the energy separation between them is proportional to the interlayer coupling, this increased splitting is directly related to the smaller separation between MoS_2 monolayers along the stacking directions, as expected due to the larger applied pressure.
In Figure 5.4 we present the comparison between theoretical (solid blue lines) and experimental (red dots) IXS spectra obtained at P = 0.42 GPa (left column) and at P = 11.47 GPa (right column). As representative results, we have chosen data collected at the same Bragg peak (i.e. at fixed $\mathbf{G}_{hkl}$, with $[h,k,l] = [1,1,0]$) taking $\mathbf{q}$ = K (upper panel), $\mathbf{q}$ = M′ (central panel) and $\mathbf{q} \approx -$A (lower panel). The elastic peak (centred at zero energy) is subtracted to all the shown experimental spectra.
Theoretical spectra are in good agreement with experimental data, in reproducing both the relative intensities of the IXS peaks and their positions in energy. In the case of P = 0.42 GPa, *ab initio* results match the position of the experimental peaks within less than 1 meV, while for P = 11.47 GPa, theoretical spectra systematically provide phonon structures which are slightly

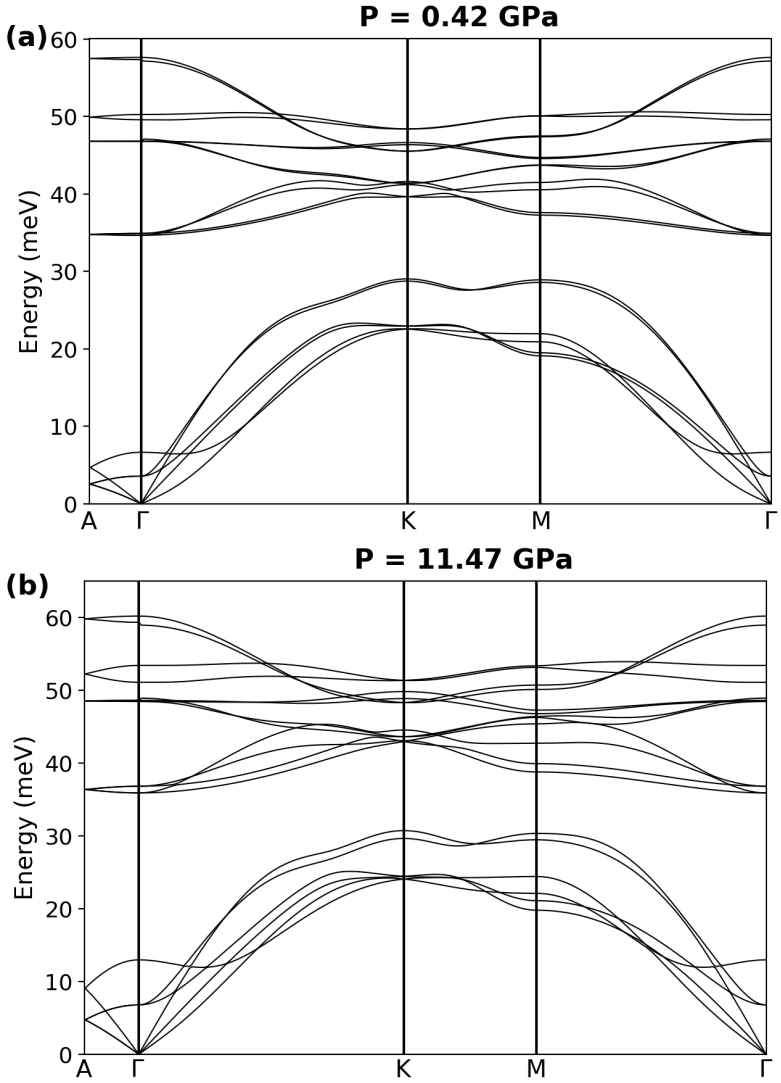

Figure 5.3: Phonon dispersion in MoS_2 with applied pressure values of 0.42 GPa (a) and 11.47 GPa (b). In both cases, we assume $2H_c$-MoS_2.

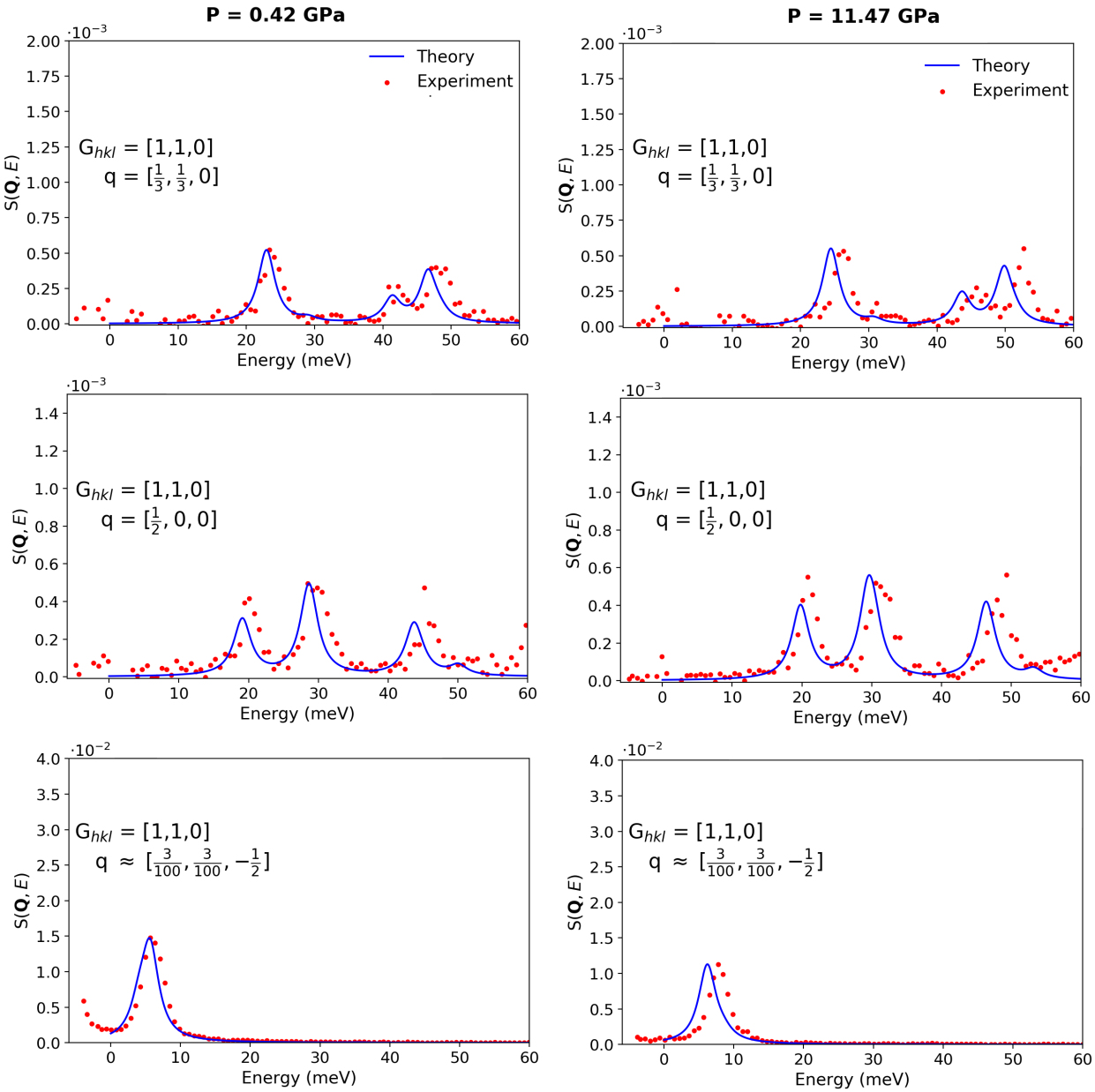

Figure 5.4: Comparison between experimental (red dots) and theoretical (solid blue lines) IXS spectra obtained for bulk MoS_2 under pressure values of 0.42 GPa (left column) and 11.47 GPa (right column). In all cases the reciprocal lattice vector $\mathbf{G}$ has been fixed to the Bragg point $[h, k, l] = [1, 1, 0]$, while the BZ vector $\mathbf{q}$ has been taken in proximity of the high symmetry points K (upper spectra), M′ (middle spectra) and A (lower spectra). In all cases, we have subtracted the fit of the elastic peak to the experimental data and we have normalized the theoretical spectra to the maximum of the experimental data.

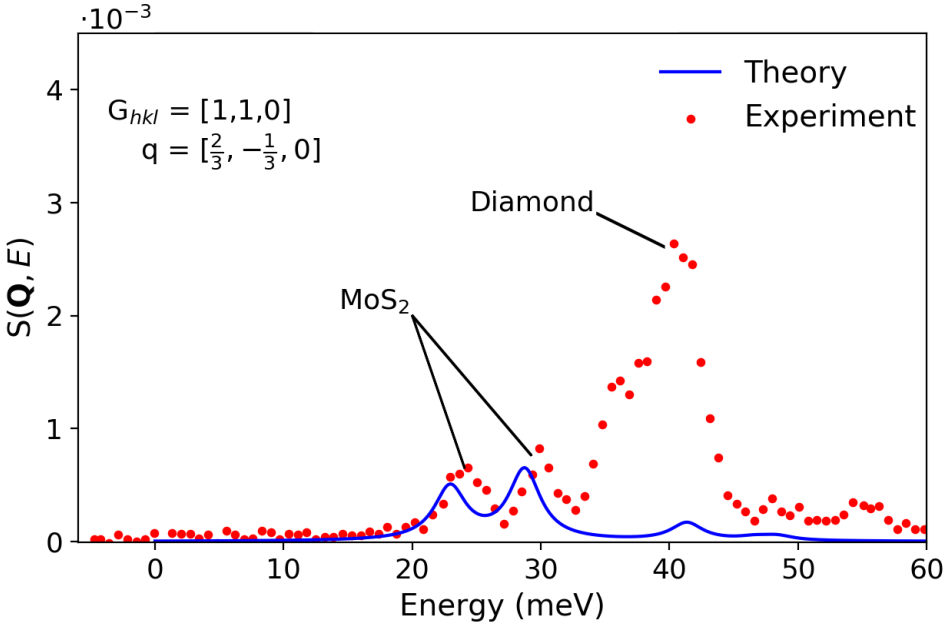

Figure 5.5: IXS experimental (red dots) and theoretical (red line) spectra computed at P = 0.42 GPa, fixing $\mathbf{Q} = \left[\frac{5}{3}, \frac{2}{3}, 0\right]$. The calculation permits to identify unambiguously the spurious peak due to the diamond anvil cell from the contribution coming from the MoS_2 sample.

red-shifted (of about 1.5 meV), w.r.t. the experimental data. Furthermore, we remark that such agreement is also observed for $\mathbf{q}$ wave-vectors not coincident with high symmetry points in the BZ. More precisely, we have also computed IXS spectra for $\mathbf{q}$ in a neighbourhood of high symmetry points: a measure of this type is shown in the lower panel of Fig.5.4, where the signal is collected close, but not exactly at $-$A. This is relevant from a practical point of view, as the IXS signal for $\mathbf{q}$ coincident with $-$A was dominated by the elastic contribution, masking the relevant inelastic features.
We complete this section noting that the diamond anvil cells were not pre-aligned and therefore, for some specific scattering vectors $\mathbf{Q}$, we observe spurious peaks due to diamond, which overlap with the MoS_2 signal of interest. As an example, we show in Figure 5.5 an IXS spectrum collected at $\mathbf{q} = \left[\frac{2}{3}, -\frac{1}{3}, 0\right]$ (again fixing $[h, k, l] = [1, 1, 0]$) assuming P = 0.42 GPa. By direct comparison between experimental and theoretical spectra, we can clearly identify the spurious diamond-peak, while recognizing the spectral features associated to MoS_2 phonons.

5.4 Fingerprints of $2H_c \rightarrow 2H_a$ transition in IXS spectra

In the following we will discuss a set of IXS spectra collected at high pressure values, i.e. P = 20.88 GPa and P = 32.83 GPa, close to and above the threshold-pressure for $2H_c \rightarrow 2H_a$ transition in bulk MoS_2.

In Figure 5.6 IXS experimental data are displayed as red dots: the left (right) column represents measurements obtained at P = 20.88 GPa (32.83 GPa), fixing $[h, k, l] = [1, 1, 0]$ while considering $\mathbf{q} = \left[\frac{1}{2}, 0, 0\right]$ (upper panel) and $\mathbf{q} = \left[\frac{1}{2}, -\frac{1}{2}, 0\right]$ (lower panel). The spectra are shown up to E = 40 meV, as at higher energies the experimental data are strongly affected by the spurious diamond peaks discussed in the previous section.

Despite having the same symmetry properties, $2H_c$-MoS_2 and $2H_a$-MoS_2 are characterized by different phonon dispersions, as one can understand from Figure 5.7, where phonons modes along a high symmetry path in the BZ are computed for the two structural phases at P = 32.83 GPa.
Even if a complete experimental evaluation of phonon dispersions in highly compressed MoS_2 is beyond the scope of these preliminary measurements, we notice that already at the chosen **Q** points shown in Fig.5.6, IXS spectra indicate the appearance of the $2H_a$ phase in the sample, at these considered pressure values.
In Fig. 5.6, dashed blue lines represent the IXS spectra computed assuming a $2H_c$ phase, while solid green lines correspond to calculations performed for a $2H_a$ structure. We note that, at fixed **Q**, both theoretical spectra are normalized with the same scaling factor.
Starting from the spectra at $\mathbf{q} = \left[\frac{1}{2}, 0, 0\right]$, we notice that the experimental spectrum is characterized by two intense peaks at about 25 and 32 meV for P = 20.88 GPa and at 26.5 and 33.4 meV for 32.83 GPa, with the lower spectral feature exhibiting an asymmetric tail toward smaller energies.
Focusing on P = 20.88 GPa, the theoretical spectrum obtained for the $2H_c$ phase capture reasonably well the higher energy peak, however with a redshift of about 2 meV. Conversely, the agreement is much worse at lower energies. In fact, the theoretical spectrum presents a single peak at about 20.5 meV (5 meV lower than the one observed experimentally): furthermore, the theoretical result does not capture the asymmetric tail observed in the measurement. The disagreement between experimental data and $2H_c$ results is even more pronounced at P = 32.83 GPa, where the theoretical low-energy peak is completely off w.r.t. the experimental data.
A much better agreement is observed considering the $2H_a$ phase. In this case, for P = 20.88 GPa, the lower-energy theoretical peak is closer to the experimental one (only redshifted of 1.5 meV) and, importantly, it is characterized by an asymmetric tail, suggesting the IXS-activation of a vibrational mode, dark in the $2H_c$ structure. Furthermore, similar considerations can be outlined at P = 32.83 GPa, where both intensity ratios and peaks' positions are

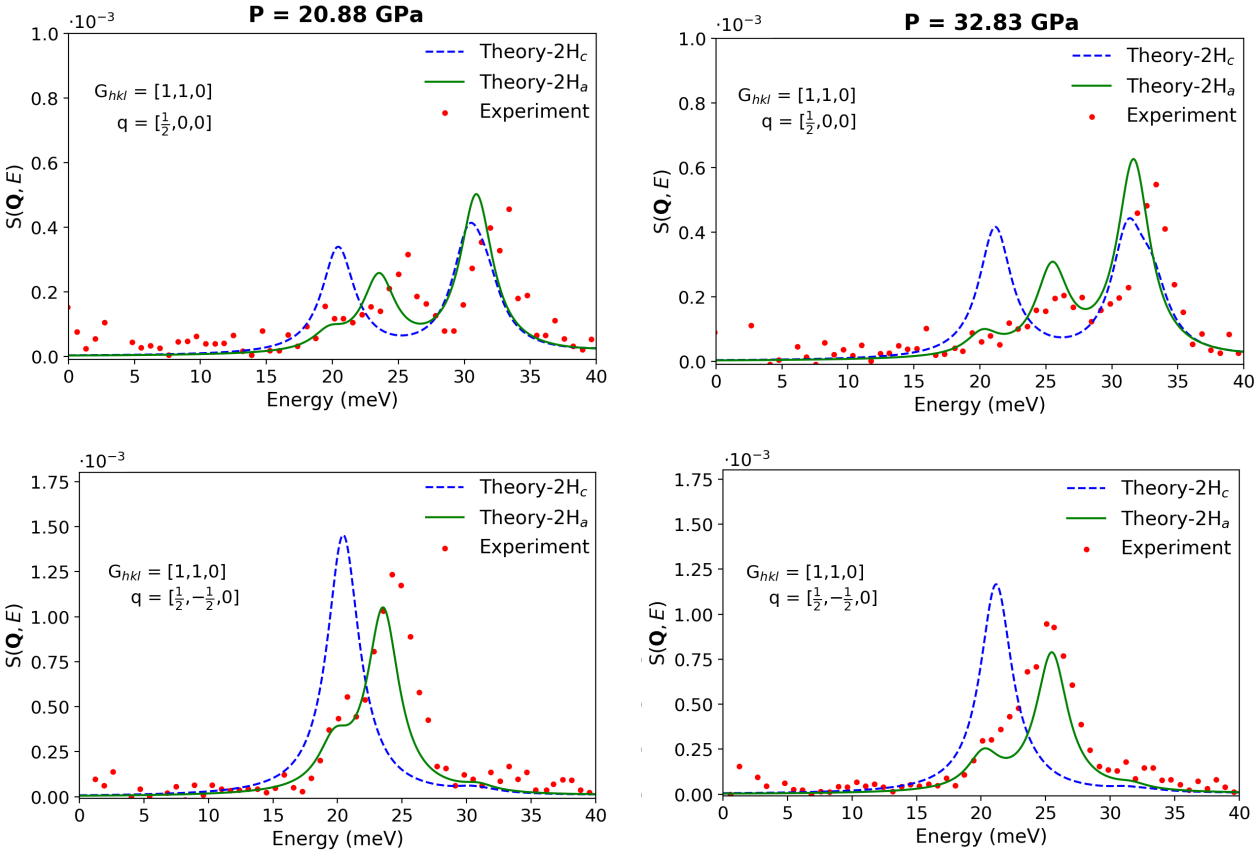

Figure 5.6: IXS spectra at pressure P = 20.88 GPa (left column) and P = 32.83 GPa (right column). All the spectra have been collected fixing $[h, k, l] = [1, 1, 0]$, while considering $\mathbf{q} = \left[\frac{1}{2}, 0, 0\right]$ (upper panel) and $\mathbf{q} = \left[\frac{1}{2}, -\frac{1}{2}, 0\right]$ (lower panel). In each graph, red dots are the experimental data (to which the elastic peak has been subtracted), while blue-dashed (green continuous) lines are the theoretical spectra obtained assuming a $2H_c$ ($2H_a$) phase for bulk MoS_2.

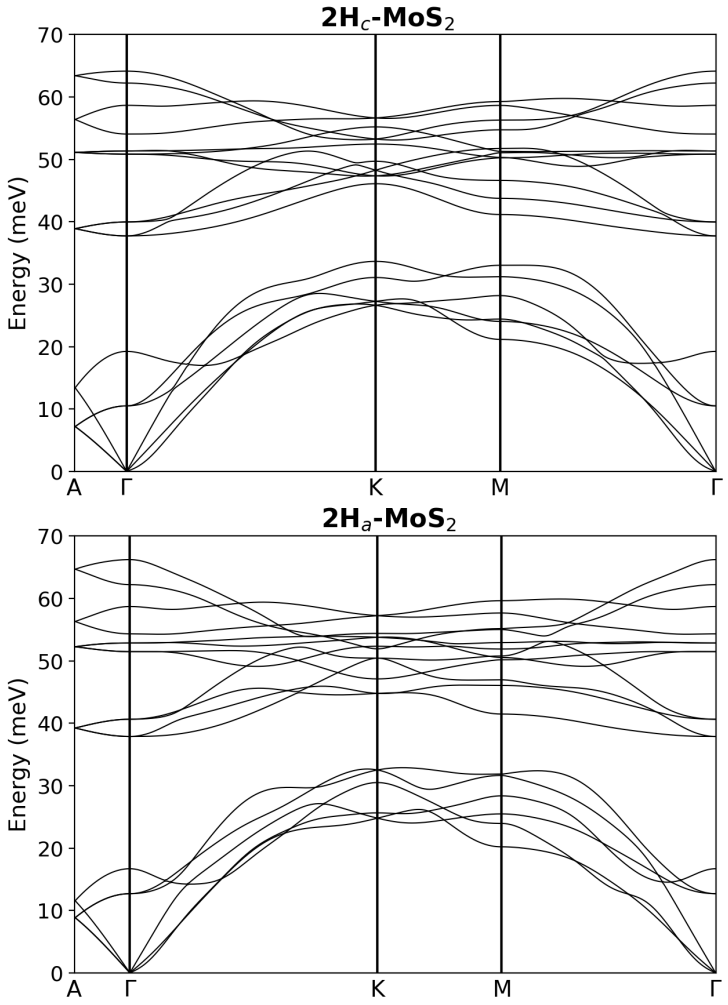

Figure 5.7: Phonon dispersions in MoS_2 at P = 32.83 GPa, in the $2H_c$ phase (upper panel) and in the $2H_a$ phase (lower panel).

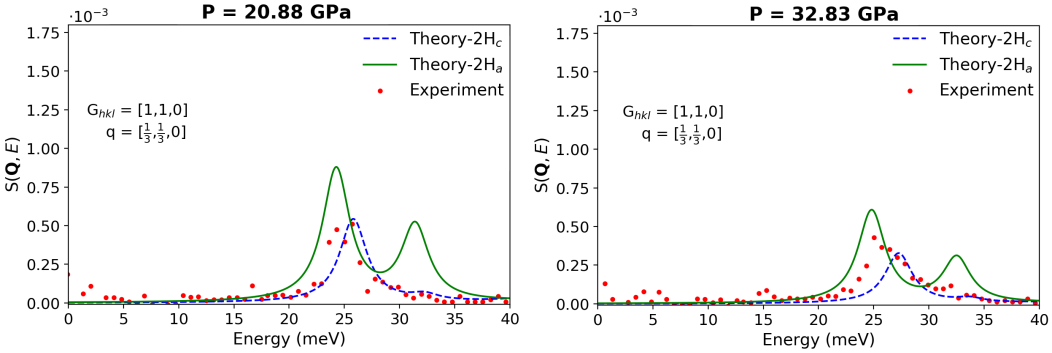

Figure 5.8: IXS spectra measured for Miller indices $[h, k, l] = [1, 1, 0]$ while fixing $\mathbf{q} = \mathrm{K}$ at P = 20.88 GPa (left panel) and P = 32.83 GPa (right panel).

properly reproduced: we notice that, at this pressure, the energy of the IXS main features agree within 1 meV.

The agreement between experimental and theoretical results for the $2\mathrm{H}_a$ phase indicates the presence of this structural phase in the sample at these applied pressure values. Furthermore, the fact that the experimental spectra are reproduced more accurately at P = 32.83 GPa than at P = 20.88 GPa could be justified in terms of $2\mathrm{H}_a$-$2\mathrm{H}_c$ phase coexistence in the lower pressure case, as also observed in XRD experiments [127]. This phase transition is even more apparent looking at the results shown in the lower panels of Fig.5.6. At P = 20.88 GPa, the experimental spectrum is dominated by a peak at about 24.2 meV, with a shoulder at lower energies (E = 20.9 meV). Analogous observations are possible for P = 32.83 GPa, where the main IXS spectral structure slightly hardens in energy, but keeps showing a shoulder at lower energies. Calculations assuming a $2\mathrm{H}_c$ phase do not capture neither the main peak position nor the observed low-energy shoulder, at both pressures. Differently, the $2\mathrm{H}_a$ results properly reproduce the experimental findings, even if the at P = 20.88 GPa, the theoretical spectra are still redshifted, as observed for $\mathbf{q} = \left[\frac{1}{2}, 0, 0\right]$.

The presented analysis indicates the appearance of the $2\mathrm{H}_a$ phase around 20 GPa. We are currently extending our study to other K-points, where the interpretation is not as straightforward and additional experiments and analysis are ongoing. Fig.5.8 shows the available IXS spectra measured for the same Bragg peak, but considering $\mathbf{q} = \left[\frac{1}{3}, \frac{1}{3}, 0\right]$, i.e. the K point. We see that at P = 20.88 GPa (left panel) the double peak structure expected for a $2\mathrm{H}_a$ crystal structure (green solid line) is not observed in the experimental spectrum, which is quite well reproduced by the $2\mathrm{H}_c$ result (dashed blue line). At 32.83 GPa (right panel), such main IXS-peak acquires a tail towards higher energies. This feature could be consistent with the double structure observed in the $2\mathrm{H}_a$ simulations, even if such peak seems to be experimentally damped in intensity. The interpretation of results at this $\mathbf{Q}$ scattering vector is still

an open problem which will be discussed in future experimental and theoretical investigations. A possible explanation of the discrepancies could be that the two $2H_a$ and $2H_c$ structures alone are not capable to properly describe phonon modes propagating along the $\Gamma - K$ direction in MoS_2 in this range of pressure values, while being reasonable for the vibrational modes at $\mathbf{q}$ points discussed in Fig.5.6. We stress that this hypothesis should be confirmed by comparing experimental and theoretical spectra acquired for different $\mathbf{q}$ along this direction to see if this deviation is systematically observed.

5.5 Summary and perspectives

In this chapter, we have discussed a set of recently acquired IXS measurements on bulk MoS_2 aimed at understanding the effect of ultra-high pressure on this layered material.

Vibrational-IXS spectra have been compared with theoretical results obtained from a fully *ab initio* description of lattice vibrations within DFPT. The computed spectra are generally in good agreement with experimental results, especially at low and intermediate applied pressure values.

We have also exploited our first principles results to interpret IXS signal measured for strains above 20 GPa. In particular, we have been able to identify features in the IXS spectra which cannot be justified assuming a $2H_c$ structure for bulk MoS_2, and which have been assigned to phonon modes of the high-pressure $2H_a$-MoS_2 phase. The very good agreement found e.g. at $\mathbf{q}$=M indicates that IXS could identify the structural phase transition. Still future work (already planned) is needed to clarify the inconsistencies observed along other momentum directions.

Finally, as the presented experiments indicate that bulk MoS_2 can sustain ultra-high applied pressure without structural failure, low-temperature measurement will be carried out to explore the existence of the excitonic-insulating phase proposed theoretically in highly compressed MoS_2.

Conclusions

In this Thesis, we have explored how excitonic properties of layered quasi-2D materials are affected by lattice degrees of freedom from a theoretical and computational perspective.

In fact, we have considered the effect of the strain, stacking geometries, lattice vibrations and pressure in a variety of challenging systems. In order to achieve a sound and comprehensive understanding of the physical mechanisms under investigation, we have joined highly accurate first-principles calculations with quantitative insightful models.

Recent advancements in experimental techniques allow for the controlled application of mechanical strain on 2D materials, leading to modified electronic and optical properties. This expanding research field, known as "straintronics", aims at developing innovative sensors and optoelectronic devices. In this context, the use of predictive techniques is crucial for understanding how external strain affects electronic and optical properties. Our study initially focuses on the electronic and optical properties of C_3N, a newly synthesized 2D material presenting an indirect gap, under applied strain. Focusing on low-lying excitons, we have demonstrated that uniaxial mechanical deformations can induce a pronounced optical anisotropy as a consequence of the symmetry-breaking effect of the applied strain. Such analysis has identified a possible future practical method to successfully tune ML-C_3N optical properties, making such material more attractive for integration in flexible opto-electronic devices. Furthermore, we have computed small-momenta excitonic dispersions under strain, with very dense sampling of exciton momenta, exploiting the computational simplicity of the approximate solution of BSE proposed in this work. These results could find application in future investigations of the dynamics of optically-bright excitons in strained C_3N.

To complete the analysis of optical properties in 2D polyaniline, we have considered excitonic properties in C_3N bilayers with different stacking motifs. Our calculations reveal a peculiar strong quenching of low energy optical absorption, not observed in other common homo-bilayers. Such singular behaviour has been rationalized in terms of a negligible interband dipole of valence-conduction transitions involved in the low-lying excitons.

Excitonic resonances in layered materials are strongly affected not only by external mechanical deformations, but also via their coupling with lattice vibrations. In this Thesis work, we have discussed the case of phonon-assisted

light emission by finite momentum excitons in different boron nitride polytypes, to interpret experimental Cathodoluminescence data.

Photoluminescence is widely utilized to investigate the behaviour of excited states in materials, however, the accurate first principles description of phonon-mediated light emission is still in its infancy due to the difficulty of consistently describing the coupling between excitons and phonons. In this Thesis, we have developed a robust computational scheme capable of overcoming the limitations present in some of the methodologies proposed in the literature, such as, for example, the phase mismatch between exciton wave functions and electron-phonon coupling elements.

Our results emphasize the importance of a proper description of exciton-phonon coupling to properly characterise the fine-structure observed in the light-emission spectra from these materials.

Our predictions successfully explain the variations in the CL signal fine structure among different polymorphs, attributing them to the activation of out-of-plane vibrations in rBN (which do not participate to light emission in hBN, because of symmetry constraints).

The methodology developed in this work, can be straightforwardly applied to other materials with indirect band gaps and could be further optimized (both theoretically and computationally) to obtain a fully *ab initio* description of other physical observables where exciton-phonon coupling plays a central role (e.g. exciton relaxation and lifetimes).

Finally, we have characterized the low energy excitation spectrum of bulk MoS_2 when subject to external pressures. We have developed a post-processing tool that allows to calculate the IXS intensities starting from phonon dispersions evaluated by first principles. Such a tool has allowed us to compare directly the vibrational-IXS spectra obtained at ESRF with theoretical predictions, indicating the presence of a structural transition at intermediate pressures around 20 GPa. Despite the fact that these calculations do not directly focus on the excitonic properties of layered MoS_2, we expect them to be relevant in forthcoming experiments of MoS_2-crystals under ultra-high pressure and cryogenic temperatures, i.e. at the conditions at which this material is predicted to behave as an ideal excitonic insulator.

We briefly summarize a few future developments of the work presented in this Thesis.
For BL-C_3N, a challenging issue concerns a precise description of the electronic ground state in the AA$'$ motif, to solve the metallicity problem associate to PBE-DFT. This will require the usage of more complex approximations for the exchange-correlation potential, to obtain single particle electronic energies and states from which more precise QP bandstructures and optical properties can be derived.

Ab initio calculation of exciton-phonon coupling matrix elements by first principles still remains a challenging task. Presently, a lot of efforts[118] are devoted to integrate in widely used first-principles codes (for example

`Yambo`) the evaluation of physical observables affected by the exciton-phonon interaction (e.g. phonon-assisted luminescence or exciton lifetimes), while implementing refined approaches as double-grid integrations. From a theoretical and computational perspective, important achievements will be the adoption of crystal-symmetries in the calculation of exciton-phonon matrix elements, while preserving the phase-matching among exciton wavefunctions and electron-phonon matrix elements. Furthermore, the possibility of interpolating exciton-phonon couplings on dense grids in reciprocal space similarly to what is currently done for electron-phonon matrix elements would further increase the accuracy of *ab initio* results, while decreasing the amount of needed computational resources.

The analysis of the behaviour of bulk MoS_2 under pressure is also an interesting topic both from a theoretical and an experimental perspective.
In particular, exploiting the high sensitivity of IXS spectroscopy, we plan to investigate the exciton-softening predicted via first principles calculations. At the same time, this technique can offer an accurate description of how phonon modes are modified by external pressure and how they can signal the structural phase transition $2H_c \rightarrow 2H_a$. *Ab initio* results will have an important role in future experiments, as they can provide support in defining the optimal experimental conditions at which such measurements should be carried out.
At the same time, inclusion of electron-phonon and phonon-phonon interaction (which has been neglected in the present implementation) could also provide a better agreement with experimental data, especially at high pressure.

Publications

The results of the present Thesis are reported in the following publications:

- **Matteo Zanfrognini**, Nicola Spallanzani, Miki Bonacci, Elisa Molinari, Alice Ruini, Marilia J. Caldas, Andrea Ferretti and Daniele Varsano, *Effect of uniaxial strain on the excitonic properties of monolayer C_3N: A symmetry-based analysis*, Physical Review B **107**, 045430 (2023).

- **Matteo Zanfrognini**, Miki Bonacci, Fulvio Paleari, Elisa Molinari, Alice Ruini, Andrea Ferretti, Marilia J. Caldas and Daniele Varsano, *Quenching of low-energy optical absorption in bilayer C_3N polytypes* arXiv:2302.09261 (2023).

- Miki Bonacci, **Matteo Zanfrognini**, Elisa Molinari, Alice Ruini, Marilia J. Caldas, Andrea Ferretti, and Daniele Varsano, *Excitonic effects in graphene-like C_3N*, Physical Review Materials **6**, 034009 (2022).

- Alexandre Plaud, **Matteo Zanfrognini**, Ingrid Stenger, Lorenzo Sponza, Léonard Schué, Fulvio Paleari, Elisa Molinari, Daniele Varsano, Ludger Wirtz, François Ducastelle, Annick Loiseau, Julien Barjon, *The optical signatures of the rhombohedral polymorph of sp_2 boron nitride* to be submitted.

Other publications:

- Angela Montanaro, Francesca Giusti, **Matteo Zanfrognini**, Paola Di Pietro, Filippo Glerean, Giacomo Jarc, Enrico Maria Rigoni, Shahla Y Mathengattil, Daniele Varsano, Massimo Rontani, Andrea Perucchi, Elisa Molinari and Daniele Fausti, *Anomalous non-equilibrium response in black phosphorus to sub-gap mid-infrared excitation* Nature Communications **13**, 2667 (2022).

- Ciro Guido, Enzo Rotunno, **Matteo Zanfrognini**, Stefano Corni and Vincenzo Grillo, *Exploring the spatial features of electronic transitions in molecular and biomolecular systems by swift electrons* Journal of chemical theory and computation, **17**, 4, 2364–2373 (2021).

- **Matteo Zanfrognini**, Enzo Rotunno, Jan Rusz, Rafal E Dunin Borkowski, Ebrahim Karimi, Stefano Frabboni, Vincenzo Grillo, *Dynamical diffraction effects in STEM orbital angular momentum resolved electron energy-loss magnetic chiral dichroism* Physical Review B **102**, 184420 (2020).

All the Python codes used within this Thesis are hosted on private Github repositories and are available upon reasonable request.

Ringraziamenti

Desidero ringraziare la Prof. Elisa Molinari per avermi permesso di svolgere questo Dottorato nell'ambito di un gruppo di ricerca e di collaborazioni estremamente stimolanti.
Sono molto grato a Daniele Varsano per la sua costante guida, disponibilità e pazienza durante tutto il lavoro di tesi, e per avermi incoraggiato a sviluppare alcune mie idee che ne sono diventate parte integrante.
Un ringraziamento particolare va a Fulvio Paleari per le tante illuminanti discussioni sull'accoppiamento eccitone-fonone e su come calcolare le quantità rilevanti utilizzando Yambo e Quantum ESPRESSO.
Desidero ringraziare Nicola Spallanzani, Andrea Ferretti, Alice Ruini e Miki Bonacci per la collaborazione nei lavori relativi alle proprietà eccitoniche di monolayer e bilayer C_3N.
Un particolare ringraziamento va anche a tutti gli altri ricercatori del gruppo di *ab initio* modelling di Modena, Alberto Guandalini, Pino D'Amico, Savio Laricchia, Simone Vacondio, Dario Leon Valido, Claudia Cardoso e Marco Gibertini.
I am indebted with Prof. Luigi Paolasini and Dr. Sofia Souliou for many useful discussions on IXS in compressed MoS_2. I also thank Prof. Annick Loiseau and Prof. Julien Barjon for sharing their experimental cathodoluminescence data on rBN and hBN with me.
Ringrazio infine Vincenzo Grillo, Stefano Frabboni ed Enzo Rotunno per le stimolanti discussioni su momento angolare, EELS e, più in generale, microscopia elettronica TEM prima dell'inizio di questo PhD.

Questo lavoro è stato possibile grazie al cofinanziamento del MUR attraverso il progetto PRIN Exc-Ins 2017BZPKSZ, e al supporto continuo dell'Istituto Nanoscienze del Consiglio Nazionale delle Ricerche (CNR-Nano), Modena.

MaX - Materials design at the Exascale, il Centro di Eccellenza Europeo per le applicazioni del supercalcolo, coordinato da CNR-Nano a Modena e finanziato dalla Unione Europea (H2020-INFRAEDI-2018-2020 n. 824143), ha contribuito a diversi aspetti computazionali indispensabili per questa tesi, in particolare con diversi sviluppi del codice Yambo.

Ringrazio il programma ISCRA per aver fornito le risorse computazionali su Marconi100 (CINECA) e EuroHPC Joint Undertaking per aver garantito l'accesso al cluster Meluxina.

Bibliography

[1] K. S. Novoselov, A. K. Geim, S. V. Morozov, D. Jiang, Y. Zhang, S. V. Dubonos, I. V. Grigorieva, and A. A. Firsov. Electric field effect in atomically thin carbon films. *Science*, 306(5696):666–669, 2004.

[2] W. Wei, S. Yang, G. Wang, T. Zhang, W. Pan, Z. Cai, Y. Yang, L. Zheng, P. He, L. Wang, A. Baktash, Q. Zhang, L. Liu, Y. Wang, G. Ding, Z. Kang, B. Yakobson, D. Searles, and Q. Yuan. Bandgap engineering of two-dimensional C_3N bilayers. *Nature Electronics*, 4:486–494, 2021.

[3] R. O. Jones and O. Gunnarsson. The density functional formalism, its applications and prospects. *Rev. Mod. Phys.*, 61:689–746, 1989.

[4] P. Hohenberg and W. Kohn. Inhomogeneous electron gas. *Phys. Rev.*, 136:B864–B871, 1964.

[5] W. Kohn and L. J. Sham. Self-consistent equations including exchange and correlation effects. *Phys. Rev.*, 140:A1133–A1138, 1965.

[6] D. M. Ceperley and B. J. Alder. Ground state of the electron gas by a stochastic method. *Phys. Rev. Lett.*, 45:566–569, 1980.

[7] F. Herman, J. P. Van Dyke, and I. B. Ortenburger. Improved statistical exchange approximation for inhomogeneous many-electron systems. *Phys. Rev. Lett.*, 22:807–811, 1969.

[8] A. D. Becke. Density-functional exchange-energy approximation with correct asymptotic behavior. *Phys. Rev. A*, 38:3098–3100, 1988.

[9] J. P. Perdew and Y. Wang. Accurate and simple analytic representation of the electron-gas correlation energy. *Phys. Rev. B*, 45:13244–13249, 1992.

[10] J. P. Perdew, K. Burke, and M. Ernzerhof. Generalized gradient approximation made simple. *Phys. Rev. Lett.*, 77:3865–3868, Oct 1996.

[11] P. Giannozzi, S. Baroni, N. Bonini, M. Calandra, R. Car, C. Cavazzoni, D. Ceresoli, G. Chiarotti, M. Cococcioni, I. Dabo, A. Dal Corso,

S. de Gironcoli, S. Fabris, G. Fratesi, R. Gebauer, U. Gerstmann, C. Gougoussis, A. Kokalj, M. Lazzeri, L. Martin-Samos, N. Marzari, F. Mauri, R. Mazzarello, S. Paolini, A. Pasquarello, L. Paulatto, C. Sbraccia, S. Scandolo, G. Sclauzero, A. P. Seitsonen, A. Smogunov, P. Umari, and R. M. Wentzcovitch. Quantum ESPRESSO: a modular and open-source software project for quantum simulations of materials. *J. Phys.: Condens. Matter*, 21(39):395502, 2009.

[12] P. Giannozzi, O. Andreussi, T. Brumme, O. Bunau, M. Buongiorno Nardelli, M. Calandra, R. Car, C. Cavazzoni, D. Ceresoli, M. Cococcioni, N. Colonna, I. Carnimeo, A. Dal Corso, S. de Gironcoli, P. Delugas, R. A. DiStasio, A. Ferretti, A. Floris, G. Fratesi, G. Fugallo, R. Gebauer, U. Gerstmann, F. Giustino, T. Gorni, J. Jia, M. Kawamura, H-Y. Ko, A. Kokalj, E. Küçükbenli, M. Lazzeri, M. Marsili, N. Marzari, F. Mauri, N. L. Nguyen, H-V. Nguyen, A. Otero de-la Roza, L. Paulatto, S. Poncé, D. Rocca, R. Sabatini, B. Santra, M. Schlipf, A. P. Seitsonen, A. Smogunov, I. Timrov, T. Thonhauser, P. Umari, N. Vast, X. Wu, and S. Baroni. Advanced capabilities for materials modelling with quantum ESPRESSO. *J. Phys.: Condens. Matter*, 29(46):465901, 2017.

[13] D. R. Hamann, M. Schlüter, and C. Chiang. Norm-conserving pseudopotentials. *Phys. Rev. Lett.*, 43:1494–1497, 1979.

[14] H. J. Monkhorst and J. D. Pack. Special points for brillouin-zone integrations. *Physical review B*, 13(12):5188, 1976.

[15] R. M. Martin, L. Reining, and D. M. Ceperley. *Interacting Electrons: Theory and Computational Approaches*. Cambridge University Press, 2016.

[16] G. Onida, L. Reining, and A. Rubio. Electronic excitations: density-functional versus many-body green's-function approaches. *Rev. Mod. Phys.*, 74:601–659, 2002.

[17] F. Bechstedt. *Many-Body Approach to Electronic Excitations*. Springer Berlin, Heidelberg, 2014.

[18] A. L. Fetter and J. D. Walecka. *Quantum Theory of Many-Particle Systems*. McGraw-Hill, Boston, 1971.

[19] E.K.U Gross, E. Runge, and O. Heinonen. *Many-Particule Theory*. Adam Hilger, 1986.

[20] M. S. Hybertsen and S. G. Louie. Electron correlation in semiconductors and insulators: Band gaps and quasiparticle energies. *Phys. Rev. B*, 34:5390–5413, 1986.

[21] L. Hedin. New method for calculating the one-particle green's function with application to the electron-gas problem. *Phys. Rev.*, 139:A796–A823, 1965.

[22] A. Marini, C. Hogan, M. Grüning, and D. Varsano. yambo: An ab initio tool for excited state calculations. *Comput. Phys. Commun.*, 180(8):1392–1403, 2009.

[23] D. Sangalli, A. Ferretti, H. Miranda, C. Attaccalite, I. Marri, E. Cannuccia, P. Melo, M. Marsili, F. Paleari, A. Marrazzo, G. Prandini, . Bonfà P, M. O. Atambo, F. Affinito, M. Palummo, A. Molina-Sánchez, C. Hogan, M. Grüning, D. Varsano, and A. Marini. Many-body perturbation theory calculations using the yambo code. *J. Phys.: Condens. Matter*, 31(32):325902, may 2019.

[24] F. Bruneval and X. Gonze. Accurate *gw* self-energies in a plane-wave basis using only a few empty states: Towards large systems. *Phys. Rev. B*, 78:085125, 2008.

[25] R. W. Godby and R. J. Needs. Metal-insulator transition in Kohn-Sham theory and quasiparticle theory. *Phys. Rev. Lett.*, 62:1169–1172, 1989.

[26] D. A. Leon, C. Cardoso, T. Chiarotti, D. Varsano, E. Molinari, and A. Ferretti. Frequency dependence in *GW* made simple using a multipole approximation. *Phys. Rev. B*, 104:115157, 2021.

[27] A. Guandalini, P. D'Amico, A. Ferretti, and D. Varsano. Efficient *GW* calculations in two dimensional materials through a stochastic integration of the screened potential, 2022.

[28] F. H. da Jornada, D. Y. Qiu, and S. G. Louie. Nonuniform sampling schemes of the brillouin zone for many-electron perturbation-theory calculations in reduced dimensionality. *Phys. Rev. B*, 95:035109, Jan 2017.

[29] C. A. Rozzi, D. Varsano, A. Marini, E. K. U. Gross, and A. Rubio. Exact coulomb cutoff technique for supercell calculations. *Phys. Rev. B*, 73:205119, 2006.

[30] S. Ismail-Beigi. Truncation of periodic image interactions for confined systems. *Phys. Rev. B*, 73:233103, 2006.

[31] G. Strinati. Application of the Green's functions method to the study of the optical properties of semiconductors. *La Rivista del Nuovo Cimento*, 11(12):1–86, 1988.

[32] M. Rohlfing and S. G. Louie. Electron-hole excitations and optical spectra from first principles. *Phys. Rev. B*, 62:4927–4944, 2000.

[33] D. Sangalli, P. Romaniello, G. Onida, and A. Marini. Double excitations in correlated systems: A many–body approach. *The Journal of Chemical Physics*, 134(3):034115, 2011.

[34] L. X. Benedict, E. L. Shirley, and R. B. Bohn. Optical absorption of insulators and the electron-hole interaction: An *ab initio* calculation. *Phys. Rev. Lett.*, 80:4514–4517, 1998.

[35] R. Del Sole and R. Girlanda. Optical properties of semiconductors within the independent-quasiparticle approximation. *Phys. Rev. B*, 48:11789–11795, 1993.

[36] S. Baroni, S. de Gironcoli, A. Dal Corso, and P. Giannozzi. Phonons and related crystal properties from density-functional perturbation theory. *Rev. Mod. Phys.*, 73:515–562, 2001.

[37] S. Baroni, P. Giannozzi, and An. Testa. Green's-function approach to linear response in solids. *Phys. Rev. Lett.*, 58:1861–1864, 1987.

[38] P. Giannozzi, S. de Gironcoli, P. Pavone, and S. Baroni. *Ab initio* calculation of phonon dispersions in semiconductors. *Phys. Rev. B*, 43:7231–7242, 1991.

[39] S. de Gironcoli. Lattice dynamics of metals from density-functional perturbation theory. *Phys. Rev. B*, 51:6773–6776, 1995.

[40] R. P. Feynman. Forces in molecules. *Phys. Rev.*, 56:340–343, 1939.

[41] J. Mahmood, E. K. Lee, M. Jung, D. Shin, H.-J. Choi, J. Min Seo, S.Min Jung, D. Kim, F. Li, M. Soo Lah, N. Park, H.Joon Shin, J. Hak Oh, and J.Beom Baek. Two-dimensional polyaniline (C_3N) from carbonized organic single crystals in solid state. *Proc. Natl. Ac. Sci.*, 113(27):7414–7419, 2016.

[42] S. Yang, W. Li, C. Ye, G. Wang, H. Tian, C. Zhu, P. He, G. Ding, X. Xie, Y. Liu, Y. Lifshitz, S.Tong Lee, Z. Kang, and M. Jiang. C_3N—A 2D crystalline, hole-free, tunable-narrow-bandgap semiconductor with ferromagnetic properties. *Adv. Mater.*, 29(16):1605625, 2017.

[43] Y. Wu, W. Xia, W. Gao, F. Jia, P. Zhang, and W. Ren. Quasiparticle electronic structure of honeycomb C_3N: from monolayer to bulk. *2D Materials*, 6(1):015018, 2018.

[44] Z. Tang, G. J. Cruz, Y. Wu, W. Xia, F. Jia, W. Zhang, and P. Zhang. Giant narrow-band optical absorption and distinctive excitonic structures of monolayer C_3N and C_3B. *Phys. Rev. Applied*, 17:034068, 2022.

[45] M. Bonacci, M. Zanfrognini, E. Molinari, A. Ruini, M. J. Caldas, A. Ferretti, and D. Varsano. Excitonic effects in graphene-like C_3N. *Phys. Rev. Materials*, 6:034009, 2022.

[46] B. Mortazavi. Ultra high stiffness and thermal conductivity of graphene like C_3N. *Carbon*, 118:25–34, 2017.

[47] A. Bafekry, S. Farjami Shayesteh, and F. M. Peeters. C_3N monolayer: Exploring the emerging of novel electronic and magnetic properties with adatom adsorption, functionalizations, electric field, charging, and strain. *J. Phys. Chem. C*, 123(19):12485–12499, 2019.

[48] L.B. Shi, Y.Y. Zhang, X.M. Xiu, and H.K. Dong. Structural characteristics and strain behavior of two-dimensional C_3N: First principles calculations. *Carbon*, 134:103–111, 2018.

[49] J. Xu, J. Mahmood, Y. Dou, S. Dou, F. Li, L. Dai, and J.B. Baek. 2d frameworks of C_2N and C_3N as new anode materials for lithium-ion batteries. *Adv. Mater.*, 29(34):1702007, 2017.

[50] G.C. Guo, R.Z. Wang, B.M. Ming, C. Wang, S.W. Luo, M. Zhang, and H. Yan. C_3N/phosphorene heterostructure: a promising anode material in lithium-ion batteries. *J. Mater. Chem. A*, 7:2106–2113, 2019.

[51] P. Bhauriyal, A. Mahata, and B. Pathak. Graphene-like carbon–nitride monolayer: A potential anode material for na- and k-ion batteries. *J. Phys. Chem. C*, 122(5):2481–2489, 2018.

[52] O. Faye, T. Hussain, A. Karton, and J. Szpunar. Tailoring the capability of carbon nitride (C_3N) nanosheets toward hydrogen storage upon light transition metal decoration. *Nanotechnology*, 30(7):075404, 2018.

[53] Meysam Makaremi, Sean Grixti, Keith T. Butler, Geoffrey A. Ozin, and Chandra Veer Singh. Band engineering of carbon nitride monolayers by n-type, p-type, and isoelectronic doping for photocatalytic applications. *ACS App. Mater. & Interf.*, 10(13):11143–11151, 2018.

[54] E. Blundo, M. Felici, T. Yildirim, G. Pettinari, D. Tedeschi, A. Miriametro, B. Liu, W. Ma, Y. Lu, and A. Polimeni. Evidence of the direct-to-indirect band gap transition in strained two-dimensional WS_2, MoS_2, and WSe_2. *Phys. Rev. Research*, 2:012024, 2020.

[55] E. Blundo, A. Surrente, D. Spirito, G. Pettinari, T. Yildirim, C. A. Chavarin, L. Baldassarre, M. Felici, and A. Polimeni. Vibrational properties in highly strained hexagonal boron nitride bubbles. *Nano Letters*, 22(4):1525–1533, 2022. PMID: 35107287.

[56] F. Carrascoso, R. Frisenda, and A. Castellanos-Gomez. Biaxial versus uniaxial strain tuning of single-layer MoS_2. *Nano Materials Science*, 4(1):44–51, 2022. Special issue on Graphene and 2D Alternative Materials.

[57] S. Latini, T. Olsen, and K. S. Thygesen. Excitons in van der Waals heterostructures: The important role of dielectric screening. *Phys. Rev. B*, 92:245123, 2015.

[58] F. Wu, F. Qu, and A. H. MacDonald. Exciton band structure of monolayer MoS_2. *Phys. Rev. B*, 91:075310, 2015.

[59] E. Ridolfi, C. H. Lewenkopf, and V. M. Pereira. Excitonic structure of the optical conductivity in MoS_2 monolayers. *Phys. Rev. B*, 97:205409, 2018.

[60] M. Zanfrognini, N. Spallanzani, M. Bonacci, E. Molinari, A. Ruini, M. J. Caldas, A. Ferretti, and D. Varsano. Effect of uniaxial strain on the excitonic properties of monolayer C_3N: A symmetry-based analysis. *Phys. Rev. B*, 107:045430, 2023.

[61] N. Marzari, A. A. Mostofi, J. R. Yates, I. Souza, and D. Vanderbilt. Maximally localized wannier functions: Theory and applications. *Rev. Mod. Phys.*, 84:1419–1475, 2012.

[62] P. Lechifflart, F. Paleari, and C. Attaccalite. Excitons under strain: light absorption and emission in strained hexagonal boron nitride. *SciPost Phys.*, 12:145, 2022.

[63] D. R. Hamann. Optimized norm-conserving Vanderbilt pseudopotentials. *Phys. Rev. B*, 88:085117, 2013.

[64] N. Marzari and D. Vanderbilt. Maximally localized generalized wannier functions for composite energy bands. *Phys. Rev. B*, 56:12847–12865, 1997.

[65] A. A. Mostofi, J. R. Yates, Y.S. Lee, I. Souza, D. Vanderbilt, and N. Marzari. wannier90: A tool for obtaining maximally-localised wannier functions. *Comput. Phys. Commun.*, 178(9):685–699, 2008.

[66] A. A. Mostofi, J. R. Yates, G. Pizzi, Y.S. Lee, I. Souza, D. Vanderbilt, and N. Marzari. An updated version of wannier90: A tool for obtaining maximally-localised wannier functions. *Comput. Phys. Commun.*, 185(8):2309–2310, 2014.

[67] G. Pizzi, V. Vitale, R. Arita, S. Blügel, F. Freimuth, G. Géranton, M. Gibertini, D. Gresch, C. Johnson, T. Koretsune, J. Ibañez-Azpiroz, H. Lee, J. Mo Lihm, D. Marchand, A. Marrazzo, Y. Mokrousov, J. I.

Mustafa, Y. Nohara, Y. Nomura, L. Paulatto, S. Poncé, T. Ponweiser, J. Qiao, F. Thöle, S. S Tsirkin, M. Wierzbowska, N. Marzari, D. Vanderbilt, I. Souza, A. A. Mostofi, and J. R Yates. Wannier90 as a community code: new features and applications. *J. Phys.: Condens. Matter*, 32(16):165902, jan 2020.

[68] I. Souza, N. Marzari, and D. Vanderbilt. Maximally localized wannier functions for entangled energy bands. *Phys. Rev. B*, 65:035109, 2001.

[69] K. Andersen, S. Latini, and K. S. Thygesen. Dielectric genome of van der Waals heterostructures. *Nano Letters*, 15(7):4616–4621, 2015.

[70] P. Cudazzo, L. Sponza, C. Giorgetti, L. Reining, F. Sottile, and M. Gatti. Exciton band structure in two-dimensional materials. *Phys. Rev. Lett.*, 116:066803, 2016.

[71] P. Cudazzo, I. V. Tokatly, and A. Rubio. Dielectric screening in two-dimensional insulators: Implications for excitonic and impurity states in graphane. *Phys. Rev. B*, 84:085406, 2011.

[72] Q.Y. Chen, M.Y. Liu, C. Cao, and Y. He. Anisotropic optical properties induced by uniaxial strain of monolayer C_3N: a first-principles study. *RSC Adv.*, 9:13133–13144, 2019.

[73] T. Galvani, F. Paleari, H. P. C. Miranda, A. Molina-Sánchez, L. Wirtz, S. Latil, H. Amara, and F. Ducastelle. Excitons in boron nitride single layer. *Phys. Rev. B*, 94:125303, 2016.

[74] M. Dresselhaus. *Group Theory: Application to the Physics of Condensed Matter*. Springer Berlin, Heidelberg, 2008.

[75] M. Gatti and F. Sottile. Exciton dispersion from first principles. *Phys. Rev. B*, 88:155113, 2013.

[76] D. Y. Qiu, T. Cao, and S. G. Louie. Nonanalyticity, valley quantum phases, and lightlike exciton dispersion in monolayer transition metal dichalcogenides: Theory and first-principles calculations. *Phys. Rev. Lett.*, 115:176801, 2015.

[77] M. Palummo, M. Bernardi, and J. C. Grossman. Exciton radiative lifetimes in two-dimensional transition metal dichalcogenides. *Nano Letters*, 15(5):2794–2800, 2015. PMID: 25798735.

[78] H.Y. Chen, V. A. Jhalani, M. Palummo, and M. Bernardi. *Ab initio* calculations of exciton radiative lifetimes in bulk crystals, nanostructures, and molecules. *Phys. Rev. B*, 100:075135, 2019.

[79] D. Y. Qiu, G. Cohen, D. Novichkova, and S. Refaely-Abramson. Signatures of dimensionality and symmetry in exciton band structure: Consequences for exciton dynamics and transport. *Nano Letters*, 21(18):7644–7650, 2021. PMID: 34463514.

[80] P. Cudazzo. First-principles description of the exciton-phonon interaction: A cumulant approach. *Phys. Rev. B*, 102:045136, 2020.

[81] F. Paleari and A. Marini. Exciton-phonon interaction calls for a revision of the "exciton" concept. *Phys. Rev. B*, 106(12):125403, 2022.

[82] G. Antonius and S. G. Louie. Theory of exciton-phonon coupling. *Phys. Rev. B*, 105:085111, 2022.

[83] H.Y. Chen, D. Sangalli, and M. Bernardi. Exciton-phonon interaction and relaxation times from first principles. *Phys. Rev. Lett.*, 125:107401, 2020.

[84] F. Paleari, T. Galvani, H. Amara, F. Ducastelle, A. Molina-Sánchez, and L. Wirtz. Excitons in few-layer hexagonal boron nitride: Davydov splitting and surface localization. *2D Materials*, 5(4):045017, aug 2018.

[85] J. He, K. Hummer, and C. Franchini. Stacking effects on the electronic and optical properties of bilayer transition metal dichalcogenides MoS_2, $MoSe_2$, WS_2, and WSe_2. *Phys. Rev. B*, 89:075409, 2014.

[86] K. F. Mak, C. Lee, J. Hone, J. Shan, and T. F. Heinz. Atomically thin MoS_2: A new direct-gap semiconductor. *Phys. Rev. Lett.*, 105:136805, 2010.

[87] V. Tran, R. Soklaski, Y.g Liang, and L. Yang. Layer-controlled band gap and anisotropic excitons in few-layer black phosphorus. *Phys. Rev. B*, 89:235319, 2014.

[88] S. Grimme. Semiempirical gga-type density functional constructed with a long-range dispersion correction. *Journal of Computational Chemistry*, 27(15):1787–1799, 2006.

[89] C. Delerue and M. Lannoo. *Nanostructures, Theory and Modeling*. Springer Berlin, Heidelberg, 2004.

[90] X. Luo, Y. Zhao, J. Zhang, Q. Xiong, and S.Y. Quek. Anomalous frequency trends in MoS_2 thin films attributed to surface effects. *Phys. Rev. B*, 88:075320, 2013.

[91] H. P. C. Miranda, S. Reichardt, G. Froehlicher, A. Molina-Sánchez, S. Berciaud, and L. Wirtz. Quantum interference effects in resonant raman spectroscopy of single- and triple-layer $MoTe_2$ from first-principles. *Nano Letters*, 17(4):2381–2388, 2017. PMID: 28199122.

[92] D. Golberg, Y. Bando, Y. Huang, T. Terao, M. Mitome, C. Tang, and C. Zhi. Boron nitride nanotubes and nanosheets. *ACS Nano*, 4(6):2979–2993, 2010. PMID: 20462272.

[93] Watanabe K., Taniguchi T., and Kanda H. Direct-bandgap properties and evidence for ultraviolet lasing of hexagonal boron nitride single crystal. *Nature Materials*, 3, 2004.

[94] Y. Kubota, K. Watanabe, O. Tsuda, and T. Taniguchi. Deep ultraviolet light-emitting hexagonal boron nitride synthesized at atmospheric pressure. *Science*, 317(5840):932–934, 2007.

[95] A. Rousseau, P. Valvin, W. Desrat, L. Xue, J. Li, J. H. Edgar, G. Cassabois, and B. Gil. Bernal boron nitride crystals identified by deep-ultraviolet cryomicroscopy. *ACS Nano*, 16(2):2756–2761, 2022. PMID: 35099926.

[96] A. Rousseau, P. Valvin, L. Xue, J. Li, J. H. Edgar, B. Gil, and G. Cassabois. Phonon-assisted broadening in Bernal boron nitride: A comparison between indirect and direct excitons. *Phys. Rev. B*, 106:035203, 2022.

[97] B. Gil, W. Desrat, A. Rousseau, C. Elias, P. Valvin, M. Moret, J. Li, E. Janzen, J. H. Edgar, and G. Cassabois. Polytypes of sp_2-bonded boron nitride. *Crystals*, 12(6), 2022.

[98] M. Moret, A. Rousseau, P. Valvin, S. Sharma, L. Souqui, H: Pedersen, H. Högberg, G. Cassabois, J. Li, J. H. Edgar, and B. Gil. Rhombohedral and turbostratic boron nitride: X-ray diffraction and photoluminescence signatures. *Applied Physics Letters*, 119(26):262102, 2021.

[99] L. Sponza, H. Amara, C. Attaccalite, S. Latil, T. Galvani, F. Paleari, L. Wirtz, and F. Ducastelle. Direct and indirect excitons in boron nitride polymorphs: A story of atomic configuration and electronic correlation. *Phys. Rev. B*, 98:125206, 2018.

[100] T. Sato. Influence of monovalent anions on the formation of rhombohedral boron nitride, rBN. *Proceedings of the Japan Academy, Series B*, 61(10):459–463, 1985.

[101] P. Sutter, J. Lahiri, P. Zahl, B. Wang, and E. Sutter. Scalable synthesis of uniform few-layer hexagonal boron nitride dielectric films. *Nano Letters*, 13(1):276–281, 2013.

[102] M.J. van Setten, M. Giantomassi, E. Bousquet, M.J. Verstraete, D.R. Hamann, X. Gonze, and G.-M. Rignanese. The Pseudodojo: Training and grading a 85 element optimized norm-conserving pseudopotential table. *Computer Physics Communications*, 226:39–54, 2018.

[103] R. S. Pease. An X-ray study of boron nitride. *Acta Crystallographica*, 5(3):356–361, 1952.

[104] B Laikhtman. Are excitons really bosons? *Journal of Physics: Condensed Matter*, 19(29):295214, jun 2007.

[105] Pedro Miguel M. C. de Melo and Andrea Marini. Unified theory of quantized electrons, phonons, and photons out of equilibrium: A simplified ab initio approach based on the generalized baym-kadanoff ansatz. *Phys. Rev. B*, 93:155102, Apr 2016.

[106] G. Cassabois, P. Valvin, and B. Gil. Hexagonal boron nitride is an indirect bandgap semiconductor. *Nature Photonics*, 10:262, 2016.

[107] E. Cannuccia, B. Monserrat, and C. Attaccalite. Theory of phonon-assisted luminescence in solids: Application to hexagonal boron nitride. *Phys. Rev. B*, 99:081109, Feb 2019.

[108] Z. Li, G. Antonius, M. Wu, F. H. da Jornada, and S. G. Louie. Electron-phonon coupling from ab initio linear-response theory within the *gw* method: Correlation-enhanced interactions and superconductivity in $ba_{1-x}k_xbio_3$. *Phys. Rev. Lett.*, 122:186402, 2019.

[109] Feliciano Giustino. Electron-phonon interactions from first principles. *Rev. Mod. Phys.*, 89:015003, Feb 2017.

[110] J. J. Sakurai and Jim Napolitano. *Modern Quantum Mechanics*. Cambridge University Press, 2 edition, 2017.

[111] Jin-Jian Zhou, Jinsoo Park, I-Te Lu, Ivan Maliyov, Xiao Tong, and Marco Bernardi. Perturbo: A software package for ab initio electron–phonon interactions, charge transport and ultrafast dynamics. *Computer Physics Communications*, 264:107970, 2021.

[112] Luis A. Agapito and Marco Bernardi. Ab initio electron-phonon interactions using atomic orbital wave functions. *Phys. Rev. B*, 97:235146, Jun 2018.

[113] Andrea Dal Corso. Density-functional perturbation theory with ultrasoft pseudopotentials. *Phys. Rev. B*, 64:235118, Nov 2001.

[114] Luis Artús, Martin Feneberg, Claudio Attaccalite, James H. Edgar, Jiahan Li, Rüdiger Goldhahn, and Ramon Cuscó. Ellipsometry study of hexagonal boron nitride using synchrotron radiation: Transparency window in the far-uvc. *Advanced Photonics Research*, 2(5):2000101, 2021.

[115] Fulvio Paleari, Henrique P. C. Miranda, Alejandro Molina-Sánchez, and Ludger Wirtz. Exciton-phonon coupling in the ultraviolet absorption and emission spectra of bulk hexagonal boron nitride. *Phys. Rev. Lett.*, 122:187401, May 2019.

[116] A. Molina-Sánchez and L. Wirtz. Phonons in single-layer and few-layer mos_2 and ws_2. *Phys. Rev. B*, 84:155413, Oct 2011.

[117] T. Q. P. Vuong, G. Cassabois, P. Valvin, V. Jacques, R. Cuscó, L. Artús, and B. Gil. Overtones of interlayer shear modes in the phonon-assisted emission spectrum of hexagonal boron nitride. *Phys. Rev. B*, 95:045207, Jan 2017.

[118] Pierre Lechifflart, Fulvio Paleari, Davide Sangalli, and Claudio Attaccalite. First-principles study of luminescence in hexagonal boron nitride single layer: exciton-phonon coupling and the role of substrate, 2022.

[119] L. V. Keldysh and Y. V. P Kopaev. Possible instability of the semimetallic state against coulomb interaction. *Sov. Phys.Solid State*, 6:2219–2224, 1965.

[120] J. des Cloizeaux. Excitonic instability and crystallographic anomalies insemiconductors. *J. Phys. Chem. Solids*, 26:259–266, 1965.

[121] D. Jérome, T. M. Rice, and W. Kohn. Excitonic insulator. *Phys. Rev.*, 158:462–475, 1967.

[122] A. Kogar, M. S. Rak, S. Vig, A. A. Husain, F. Flicker, Y. Il Joe, L. Venema, G. J. MacDougall, T. C. Chiang, E. Fradkin, J. van Wezel, and P. Abbamonte. Signatures of exciton condensation in a transition metal dichalcogenide. *Science*, 358(6368):1314–1317, 2017.

[123] D. Varsano, S. Sorella, D. Sangalli, M. Barborini, S. Corni, E. Molinari, and M. Rontani. Carbon nanotubes as excitonic insulators. *Nat. Commun.*, 8:1461, 2017.

[124] B. Sun, W. Zhao, T. Palomaki, Z. Fei, E. Runburg, P. Malinowski, X. Huang, J. Cenker, Y. Cui, J. Chu, X. Xu, S. Ataei, D. Varsano, M. Palummo, E. Molinari, M. Rontani, and D. Cobden. Evidence for equilibrium exciton condensation in monolayer WTe_2. *Nat. Phys.*, 18:94–99, 2022.

[125] S. Samaneh Ataei, Daniele Varsano, Elisa Molinari, and Massimo Rontani. Evidence of ideal excitonic insulator in bulk mos¡sub¿2¡/sub¿ under pressure. *Proceedings of the National Academy of Sciences*, 118(13):e2010110118, 2021.

[126] Liliana Hromadová, Roman Martoňák, and Erio Tosatti. Structure change, layer sliding, and metallization in high-pressure mos_2. *Phys. Rev. B*, 87:144105, Apr 2013.

[127] Alexander F. Goncharov, Maxim Bykov, Elena Bykova, Konstantin Glazyrin, Vitali Prakapenka, Zi-Yu Cao, and Xiao-Jia Chen. Structure and stability of $2H_a-Mos_2$ at high pressure and low temperatures. *Phys. Rev. B*, 102:064105, Aug 2020.

[128] Zhen-Hua Chi, Xiao-Miao Zhao, Haidong Zhang, Alexander F. Goncharov, Sergey S. Lobanov, Tomoko Kagayama, Masafumi Sakata, and Xiao-Jia Chen. Pressure-induced metallization of molybdenum disulfide. *Phys. Rev. Lett.*, 113:036802, Jul 2014.

[129] Zi-Yu Cao, Jia-Wei Hu, Alexander F. Goncharov, and Xiao-Jia Chen. Nontrivial metallic state of mos_2. *Phys. Rev. B*, 97:214519, Jun 2018.

[130] A.Q.R. Baron. Phonons in crystals using inelastic x-ray scattering. *Journal of The Spectroscopical Society of Japan*, 58:205–214, 2009.

[131] Hans Tornatzky, Roland Gillen, Hiroshi Uchiyama, and Janina Maultzsch. Phonon dispersion in mos_2. *Phys. Rev. B*, 99:144309, Apr 2019.

[132] N. Ashcroft and N. D. Mermin. *Solid state physics*. Saunders College Publishing, 1976.

[133] N. Marzari, D. Vanderbilt, A. De Vita, and M. C. Payne. Thermal contraction and disordering of the Al(110) surface. *Phys. Rev. Lett.*, 82:3296–3299, 1999.

[134] E. Kirkland. *Advanced Computing in Electron Microscopy*. Springer, 2014.

[135] S. M. Souliou, A. Bosak, G. Garbarino, and M. Le Tacon. Inelastic X-ray scattering studies of phonon dispersions in superconductors at high pressures. *Superconductor Science and Technology*, 33(12):124004, oct 2020.

[136] Guoyin Shen and Ho Kwang Mao. High-pressure studies with X-rays using diamond anvil cells. *Reports on Progress in Physics*, 80(1):016101, nov 2016.

[137] A. Jayaraman. Diamond anvil cell and high-pressure physical investigations. *Rev. Mod. Phys.*, 55:65–108, 1983.